The Faint Low-Frequency Radio Universe in Continuum: Exploitation of the Pre-SKA Deepest Survey

A thesis submitted in partial fulfilment of the requirements for the degree of

Doctor of Philosophy

in the

Faculty of Science
Department of Astronomy

UNIVERSITY OF CAPE TOWN

By: Emmanuel Francis Ocran

Supervisors: Prof. Russ Taylor and Prof. Mattia Vaccari

May 2020

Declaration of Authorship

I confirm that I have been granted permission by the University of Cape Town's Doctoral Degrees Board to include the following publication(s) in my PhD thesis, and where co-authorships are involved, my co-authors have agreed that I may include the publication(s).

I, **Emmanuel Francis Ocran**, declare that this thesis titled, **"The Faint Low-Frequency Radio Universe in Continuum: Exploitation of the Pre-SKA Deepest Survey"** and the work presented in it are my own. My PhD studies ended with the following peer-reviewed publications listed below:

- ***Deep GMRT 610 MHz observations of the ELAIS N1 field: catalogue and source counts***.
  E. F. Ocran*, A. R. Taylor, M. Vaccari, C.H. Ishwara-Chandra,I. Prandoni. 2020 MNRAS 1127, 1145*
- ***Cosmic evolution of star-forming galaxies to*** $z \simeq 1.8$ ***in the faint low-frequency radio source population***.
  E. F. Ocran*, A. R. Taylor, M. Vaccari, C.H. Ishwara-Chandra, I. Prandoni, M. Prescott, C. Mancuso. 2020 MNRAS 5911–5924*
- ***The evolution of the Low-Frequency Radio AGN Population to*** $z \simeq 1.5$.
  E. F. Ocran*, A. R. Taylor, M. Vaccari, C.H. Ishwara-Chandra, I. Prandoni, M. Prescott, C. Mancuso. Submitted to MNRAS*
- ***Investigating the infrared-radio correlation and radio spectral indices at*** μ***Jy fluxes with stacking***.
  E. F. Ocran*, J. Stil, A. R. Taylor, M. Vaccari, C.H. Ishwara-Chandra. To be submitted to MNRAS*

These publications, which I first-authored constitute the chapters of this thesis, and I confirm that I have my co-authors approval to include them.

I declare that no part of this thesis, **"The Faint Low-Frequency Radio Universe in Continuum: Exploitation of the Pre-SKA Deepest Survey"**, has previously been submitted for a degree or any other qualification at this University or any other institution.

Signature: **Date:**

Signed by candidate October 19, 2020

Student Name: **Student Number:**

Emmanuel Francis Ocran OCREMM001

Plagiarism Declaration

I, Emmanuel Francis Ocran , know the meaning of plagiarism and declare that all of the work in the document is my own and that works from other people have been properly cited and referenced.

Abstract

The Faint Low-Frequency Radio Universe in Continuum: Exploitation of the Pre-SKA Deepest Survey

This thesis presents a thorough and significant work on the properties of radio sources as derived from deep 610-MHz GMRT data and ancillary multi-wavelength data. The faint radio sources at 610-MHz are found out to distances such that the objects are seen as they were when the universe was less than half its current age. These data provide a first look at the faint radio sky at sensitivities that will soon be achieved by key programs on the South African MeerKAT radio telescope, and thus take a first step in the exploration of the radio universe that will be made by the Square Kilometre Array.

I report deep 610-MHz GMRT observations of the EN1 field, a region of 1.86 deg^2. We achieve a nominal sensitivity of 7.1 μJy beam^{-1}. From our 610 MHz mosaic image, we recover 4290 sources after accounting for multiple component sources down to a 5σ flux density limit of 35.5 μJy. From this data, I derive the 610 MHz source counts applying corrections for completeness, resolution bias and Eddington bias. The 610-MHz source counts show a flattening at flux densities below 1 mJy. The source counts are higher than previous observations at this frequency below this break. However, they are generally consistent with recent models of the low-frequency source population.

Using ancillary multi-wavelength data in the field, I investigate the key issue of source population classification using the deepest data at an intermediate-low frequency (higher than LOFAR and lower than JVLA), where previous work has not been sensitive enough to reach the μJy population. By cross-matching against the multi-wavelength data, I identify 72% of the radio sample having reliable redshifts, of which 19% of the redshifts are based on spectroscopy. From the classification, I obtain 1685 sources as Star-Forming Galaxies (SFGs), 281 sources Radio-Quiet (RQ) and 339 sources Radio-Loud (RL) Active Galactic Nuclei (AGN) for the sub-sample with redshifts and at least one multi-wavelength AGN diagnostic. SFGs are mostly low-power radio sources, i.e $L_{610\,\mathrm{MHz}} < 10^{25}\,\mathrm{W\,Hz^{-1}}$ while RQ AGN and RL AGN have radio powers $L_{610\,\mathrm{MHz}} > 10^{25}\,\mathrm{W\,Hz^{-1}}$. From cross-matching my sample with other radio surveys (GMRT at 325-MHz, FIRST at 1.4-GHz and JVLA at 5-GHz), I obtain the median spectral index from 325-MHz to 610-MHz to be -0.80 ± 0.29, 610-MHz to 1.4-GHz to be -0.83 ± 0.31 and 1.4-GHz to 5-GHz to be -1.12 ± 0.15. The main result is that the median spectral index appears to steepen at the highest frequency.

With the above catalogue in hand, I use the non-parametric V/V_{max} test and the radio luminosity function to investigate the cosmic evolution of different source populations. I study SFGs and derive their IR-radio correlation and luminosity function as a function of redshift. By integrating the evolving SFG luminosity functions I also derive the cosmic star formation rate density out to $z = 1.5$. I address the long standing question about the origin of radio emission in RQ AGN. I compare the star formation rate (SFR) derived from their far-infrared luminosity, as traced by Herschel, with the SFR computed from their radio emission. I find evidence that the main contribution to the radio emission of RQ

AGN is the star formation activity in their host galaxies. At high luminosities, however, both SFGs and RQ AGN display a radio excess when comparing radio and infrared star formation rates. The vast majority of our sample lie along the SFR − $M_\star$ "main sequence" at all redshifts when using infrared star formation rates. This result opens the possibility of using the radio band to estimate the SFR even in the hosts of bright AGN where the optical-to-mid-infrared emission can be dominated by the AGN. I investigate the evolution of radio AGN out to z ∼ 1.5 with continuous models of pure density and pure luminosity evolution with $\Phi^\star \propto (1+z)^{(2.25\pm0.38)-(0.63\pm0.35)z}$ and $L_{610\,\mathrm{MHz}} \propto (1+z)^{(3.45\pm0.53)-(0.55\pm0.29)z}$ respectively. I also constrain the evolution of RQ AGN and RL AGN separately with a continuous model of pure luminosity evolution. For the RQ and RL AGN, we find a fairly mild evolution with redshift best fitted by pure luminosity evolution with $L_{610\,\mathrm{MHz}} \propto (1+z)^{(2.81\pm0.43)-(0.57\pm0.30)z}$ for RQ AGN and $L_{610\,\mathrm{MHz}} \propto (1+z)^{(3.58\pm0.54)-(0.56\pm0.29)z}$ for RL AGN. The results reveal that the 610 MHz radio AGN population thus comprises two differently evolving populations whose radio emission is mostly SF-driven or AGN-driven respectively.

Finally, I probe the infrared-radio correlation and radio spectral indices of the faint radio population using stacking. I stack infrared sources in the EN1 field using the MIPS 24 micron mid-infrared survey and radio surveys created at 325 MHz, 610 MHz and 1.4 GHz. The stacking experiment shows a variation in the absolute strength of the infrared-radio correlation between these three different frequencies and the MIPS 24 micron band. I find tentative evidence of a small deviation from the correlation at the faintest infrared flux densities. The stacked radio spectral index analyses reveal that the majority of the median stacked sources exhibit steep spectra, with a spectral index that steepens with frequency between α_{610}^{325} and α_{1400}^{610}.

This work is particularly useful to pave the way for upcoming radio surveys with SKA pathfinders and precursors.

Acknowledgements

I would first like to thank my advisors, Prof. Russ Taylor and Prof. Mattia Vaccari, for being excellent instructors and a wonderful source of support over the years. They were always available to answer questions and offer advice, sometimes responding to emails at times when most people would be far from being able to discuss and explain scientific matters effectively and intelligently.

I would like to thank Prof. Ishwara Chandra, Prof. Isabella Prandoni and Prof. Jeroen Stil for their advice and dedication to my work. The research trips to India, Italy and Canada were one of the highlights of my PhD. Special thanks goes to Dr. Matt Prescott and the rest of academic staff, the South Africa-India MIGHTEE and superMIGHTEE collaboration both home and abroad. Their remarkable simplicity, humility and openness made my interaction whith them much easier, and the experience they shared with me has been very helpful.

I take this opportunity to record my sincere thanks to Astronomy Department of UCT. From the HoD Prof. Patrick Woudt and the entire staff, to the postdocs and fellow postgraduate students I express my thanks. The graduate students in this department deserve a huge thanks! There is a real community here that makes going through the trials and tribulations of a Doctorate program not only bearable, but fun. I have had such a great time my past 4 years here and I realize I am fortunate to have this experience. A huge thanks to all the friends I have made here along the way.

To Nicky and Annastine at the Inter-University Institute for Data Intensive Astronomy, and also Roslyn and Carol at the Astronomy Department of UCT, I would like express my profound gratitude. During these tiresome years, they have never stopped showing support and encouragement. Besides having to professionally handle paperwork issues, they have made themselves available to listen and discuss whenever I was feeling down. I would also like to express my appreciation to Siphelo Funani, apart from being there to offer IT support, he has also being a brother and a friend.

Last but not the least, I would like to thank my family: my mother and to my brothers and sister for supporting me throughout writing this thesis and my life in general.

Contents

List of Figures

List of Tables

Abbreviations

AGN	**A**ctive **G**alactic **N**uclei
SFG	**S**tar **F**orming **G**alaxy
MIR	**M**id- **I**nfrared
FIR	**F**id- **I**nfrared
GMRT	**G**iant **M**etrewave **R**adio **T**elescope
SKA	**S**quare **K**ilometre **A**rray
ASKAP	**A**ustralian **S**quare **K**ilometre **A**rray **P**athfinder
IRAC	**I**nfrared **A**rray **C**amera
HST	**H**ubble **S**pace **T**elescope
ISO	**I**nfrared **S**pace **O**bservatory
ISOPHOT	**I**SO **p**hoto-polarimeter
ISOCAM	**I**SO **C**amera
ELAIS	**E**uropean **L**arge **A**rea **I**SO **S**urvey
ACS	**A**dvanced **C**amera for **S**urveys
JVLA	**J**ansky **V**ery **L**arge **A**rray
LOFAR	**L**ow-**F**reqency **A**rray for radio **a**stronomy
HERMES	**H**erschel**M**ulti-tiered **E**xtragalactic **S**urvey
MIPS	**M**ultiband **I**maging **P**hotometer
SWIRE	**S**IRTF **W**ide-Area **I**nfrared **E**xtragalactic **S**urvey
SPIRE	**S**pectral and **P**hotometric **I**maging **R**eceiver
SERVS	**S**pitzer **E**xtragalactic **R**epresentative **V**olume **S**urvey

Physical Constants

Speed of Light	c	=	$2.997\,924\,58 \times 10^8$ ms^{-1} (exact)
Solar luminosity	$L_\odot$	=	$3.9\ 10^{33}$ erg s−1
Solar mass	$M_\odot$	=	$1.99\ 10^{33}$ g
Solar temperature	$T_\odot$	=	$5.780\ 10^3$ K

Symbols

a	distance	m
P	power	W (Js^{-1})
ω	angular frequency	$rads^{-1}$

I dedicate this thesis to my mother who taught me it is never too late to pursue my dreams.. . . .

Chapter 1

General Motivation and Overview

The study of the faint radio continuum universe and its properties has in recent times become a very active field of research due to the transformational capabilities of the Square Kilometer Array (SKA) in this field, as well as the major steps being taken and planned with SKA pathfinder and precursors. Because of their high sensitivity and coverage, future radio surveys with the South African SKA precursor MeerKAT and with the SKA1 will regularly detect radio emission from Star Forming Galaxies (SFG) and Active Galactic Nuclei (AGN) up to high redshifts over large areas of the sky. It is therefore hugely important to be able to predict which kind of sources these facilities will observe, and identify the key data in other spectral windows necessary to complement the radio information, to maximise the scientific outputs of these projects. In view of this, I embark on the exploitation of the deepest existing radio data from The Giant Metrewave Radio Telescope (GMRT) at 610 MHz. The radio data is complemented by multi-wavelength ancillary data. This DPhil thesis is to analyse this data to provide a better understanding of the faint low-frequency extragalactic radio-source population.

I will briefly review basic properties of the main components of the radio sky at the faint end. I will discuss the issue of their proper classification, their number counts, luminosity functions, and evolution. In particular, this Chapter reviews the present knowledge of the radio universe in continuum and of radio source populations. Then, I summarize the main topics that will be addressed in the various Chapters of this work.

1.1 Extragalactic radio sources and connection to other wavebands

Since the radio astronomy discipline begun to gain attention post World War II, astronomers have produced a large number of radio surveys. The last three decades have witnessed the conception and building of special telescopes and instruments, sometimes dedicated solely to conducting a specific survey. The advent of prospective new instruments and surveys that have been planned or about entering operations in the near future indicates that radio astronomy plays an important role for the advance of astrophysics.

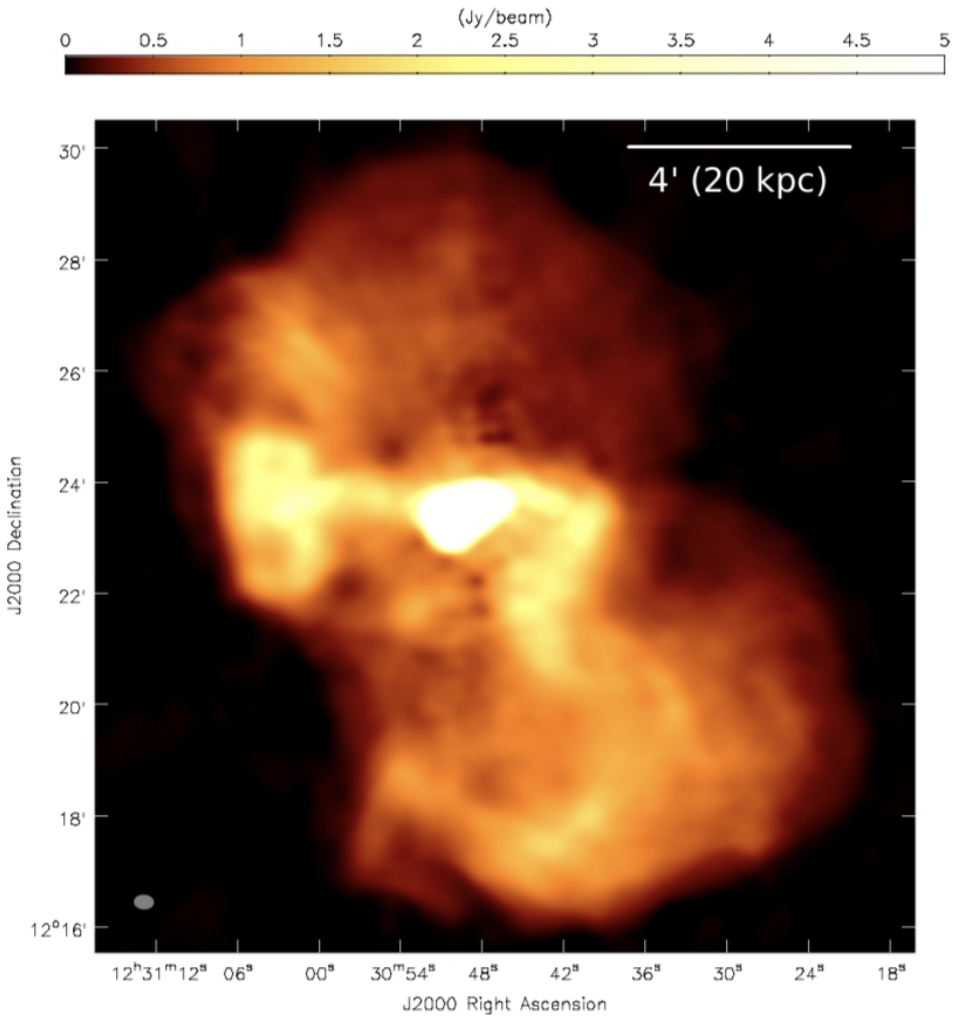

FIGURE 1.1: False colour image showing the M87 galaxy. LOFAR-HBA image of Virgo A at 140 MHz. The rms noise level is $\sigma = 20\,\mathrm{mJy/beam}$, the flux peak is 101 Jy/beam and the beam size is $21'' \times 15''$ (ellipse in the bottom-left corner). Some deconvolution errors are visible as small holes slightly above and below the bright core. The radio emission is shown in yellow/orange (LOFAR). At the centre, the radio emission has a very high surface brightness, showing where the jet powered by the supermassive black hole is located. Figure adapted from de Gasperin, F. et al. (2012).

Kiepenheuer (1950) attributed the strong radio emission from our Galaxy to synchrotron emission by cosmic rays accelerated by supernova shocks. It has been deduced that other normal galaxies also display this emission, which would be far weaker than the powerful radio galaxies. For this reason, fewer normal galaxies were therefore detected in preceding surveys. The 2C survey at Cambridge (Shakeshaft et al., 1955) was the first large (>1000 sources) radio survey which which catalogued 1936 discrete radio sources at 81 MHz. However, the 2C survey was later found to contain many spurious sources caused by strong radio sources detected in the outer sidelobes of the telescope point spread function (Mills, 1984). The Mills Cross interferometer near Sydney (Mills & Slee, 1957; Mills et al., 1958) whose 85 MHz catalogue showed a distribution of flux densities only slightly steeper than predicted by a Euclidean model was the first major survey without significant errors. Subsequently, surveys at Cambridge, notably the 3C by Edge et al. (1959) and Bennett (1962) agreed with the Sydney surveys.

In the last few years, deep radio observations have been undertaken in fields chosen because of their excellent multi-wavelength data. Due to new technologies enabling the construction of sensitive new telescopes, these surveys have resulted in a hundred-fold increase in the total number of known radio sources. With the increasing use of radio interferometric telescopes, large samples of radio galaxies have been matched with optical observations and used for cosmological studies. These surveys are designed to specifically to benefit from complementary imaging and spectroscopic observations. Figure 1.1 shows a false colour image showing the M87 galaxy. The radio emission is shown in yellow/orange (LOFAR, see de Gasperin, F. et al. 2012). At the centre, the radio emission has a very high surface brightness, showing where the jet powered by the supermassive black hole is located.

Extragalactic radio surveys remain the most powerful tool to probe the distant universe. Radio surveys that have been carried out at multi-radio frequencies include the work of Tasse et al. (2007) who used the low-frequency radio survey of the XMM Large-Scale Structure field (XMM-LSS; Pierre et al. 2004) to study the connection between extragalactic radio source populations and their environment as traced by X-ray and optical emission. They used the Giant Meterwave Radio Telescope (GMRT) for their radio survey at frequencies of 240 and 610 MHz. The same sample was also observed at the Very Large Array (VLA) at 74 MHz (Cohen et al., 2003) and at 325 MHz (Tasse et al., 2006). The nature of the low-frequency extragalactic source population is well constrained down to the micro-Jansky level (e.g. Padovani et al. 2009; de Zotti et al. 2010; McAlpine et al. 2013). The extragalactic radio source population ranges from normal galaxies with luminosities $\sim 10^{20}\mathrm{WHz}^{-1}$ to galaxies whose radio emission is as much as $10^4 - 10^7$ times greater owing to regions of massive star formation or to an AGN (see Padovani et al. 2009).

1.2 The faint radio sky population

Extragalactic radio sources exhibit a broad range of properties. Radio galaxies are unique structures which can extend to hundreds of kiloparsecs from a central active object, and they radiate energy over ten times that of normal galaxies. As such, these radio sources are considered to be amongst the most spectacular objects in the Universe. Normal galaxies, with typical radio powers $10^{20} - 10^{21}\,\mathrm{WHz}^{-1}$, are thought to have their radio emission dominated by synchrotron radiation from interstellar relativistic electrons (e.g. see Sadler et al. 1989; Phillips et al. 1997). Radio galaxies are instead associated with relativistic jets extending well beyond the host galaxy, which is often a giant elliptical and characterised by GHz radio powers $> 10^{22\mathrm{W}}\,\mathrm{Hz}^{-1}$ (Ledlow & Owen, 1996). Radio sources revealed in deep radio surveys at GHz frequencies exhibit the full range of properties.

1.2.1 Star forming galaxies

Building a comprehensive understanding of star formation processes covers several astrophysical areas. A star-forming galaxy (SFG) is a galaxy with a high rate of recent or ongoing formation of new stellar populations from the collapse of dense gas clouds.

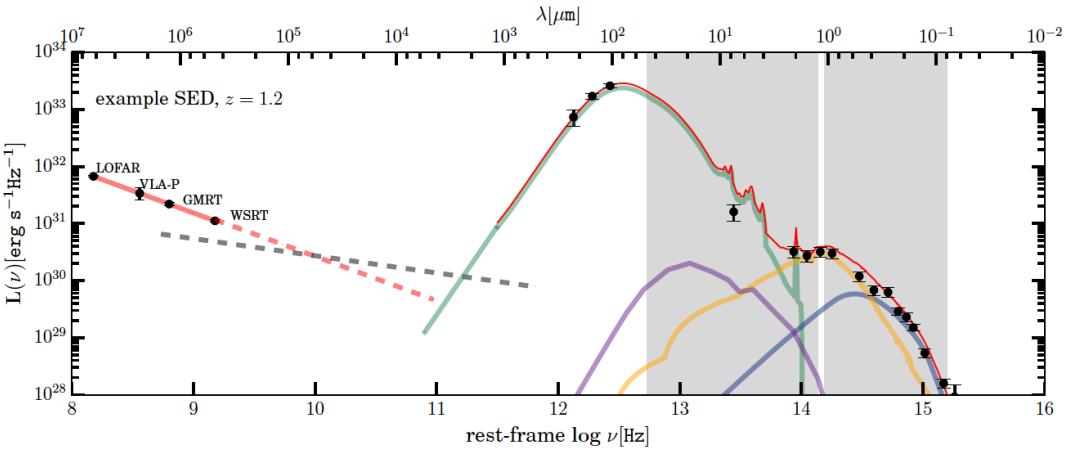

FIGURE 1.2: An example SED of dusty SF galaxy from our sample at z=1.2. The multi-wavelength coverage for this sample is shown from the low-frequency radio to the UV regime. For more details see the section on the classification into AGN and SF galaxies in Calistro Rivera et al. (2017). Figure adapted from Calistro Rivera et al. (2017)

SFGs are characterised by steep GHz radio spectra ($\alpha_r \approx 0.7$, where $S \sim \nu^{-\alpha_r}$) dominated by synchrotron emission of particles accelerated in supernova shocks. The emission also has a flat free-free component from HII regions of gas photo-ionized by massive stars, which becomes predominant at $\nu \gtrsim 30$ GHz (Condon, 1992). The radio luminosity is correlated with the star formation rate. The 1.4 GHz radio luminosities of SFGs range typically from from $10^{18} - 10^{23}$ WHz^{-1} (Mauch & Sadler, 2007). SFGs have typically disk-like morphology, with rotationally supported stellar kinematic. At higher redshift (z > 1), the SFG disks tend to be richer in gas than in the local Universe, and are often characterized by a clumpy structure (Genzel et al. 2011, and reference therein).

SFGs are rich of gas and dust, the materials from which stars form. Both stellar UV radiation and optical line emission can be absorbed by dust and never reach the observer. The appearance of a redder continuum with rest-frame optical colors similar to those of passive galaxies can be seen in the case of strong dust extinction. An example SED of a dusty SFG from our sample at z=1.2 is shown in Figure 1.2. The multi-wavelength coverage this sample is shown, from the low-frequency radio to the UV regime. The radio data points represent the radio SED from 150, 325, 610 MHz and 1.4 GHz. Calistro Rivera et al. 2016 used the code AGNFITTER to decompose the FIR-UV photometry into physical components of the host galaxy and the AGN.

1.2.2 Active Galactic Nuclei

Active Galactic Nuclei (AGN) are a class of highly luminous sources which emit from very compact regions in the centres of galaxies, whose emission is powered by accretion onto a super-massive black hole (SMBH) (Rees, 1984). Depending on the characteristics of their observed spectra AGNs are divided into a number of sub-classes. Basically, all sources with radio luminosities above $\sim 10^{24}$ WHz^{-1} are almost invariably associated with AGN (e.g., Condon 1992; Sadler et al. 2002; Best et al. 2005). At flux densities

greater than 1 mJy, the radio source population is dominated by AGN-driven emission generated from the gravitational potential associated with a supermassive black hole in the nucleus (see Fomalont et al. 2002; Padovani et al. 2009).

Most AGN classes can be described by the unified model of AGN (Osterbrock, 1978). In this model, the energy is produced by a hot accretion disk of matter infalling onto a super-massive (10^6 – $10^9 M_\odot$) (SMBH) black hole that is surrounded by an obscuring dusty torus (Antonucci, 1993). The accretion produces photo-ionising UV radiation, and gives rise to synchrotron radio emission and X-ray emission via Compton scattering. The high velocity dispersion of the gas clouds located within ~ 1 pc of the obscuring torus gives rise to broad line emission. A schematic visualization of the model is represented in Figure 1.3. The standard model for AGN proposes that the energy released is produced by the accretion of matter onto a SMBH. The AGN is powered by the conversion of gravitational potential energy into radiation, although the rotational kinetic energy of the SMBH may also serve as an important source of energy via the Blandford-Znajek mechanism (see e.g. Blandford & Znajek 1977).

AGN are observed over most of the electromagnetic spectrum, from 100 MHz radio waves to 100 MeV gamma rays (see Figure 1.4). In general, the difficulties in combining multi-wavelength datasets, has led to a confusing AGN terminology in early studies where the classification of various types of sources has been associated with the initial methodologies by which the objects where discovered, rather than physical properties of the different classes. Historically, Quasi-stellar objects (QSOs), or quasars, are the most luminous AGNs. Moreover, QSOs are considered the brightest objects in the Universe, except for the short-lived explosions related to supernovae and gamma-ray bursts. However, only $\sim 10\%$ of QSOs are radio loud sources. AGNs are often classified according to: (1) their *the ratio between radio luminosity and luminosity at other wavelengths* into radio-loud or radio-quiet AGN; and (2) *spectral features* into Type 1 or 2 AGN. The Type 1 AGN, broad-line, are viewed face-on to the opening of the torus whereas the Type 2 AGN, narrow-line, one faces the obscuring part of it. In a more realistic scenario, the covering factors of the torus differ for each individual AGN (see Villarroel & Korn 2014). Their classification into Type 1 or 2 depends on the presence or not of broad lines, and in turn on the observer line of sight with respect to the torus axis. However, the unified model of AGNs explains both radio-loud and radio-quiet AGN, as well as other classes, like e.g. Seyfert galaxies, and Blazars, with a reasonable explanation for the sources of the narrow line region (NLR) and the broad-line region (BLR) of AGN. There is a zoo of objects that are covered by this model; see Figure 1.3 for the basic ones mentioned.

While the standard unified model of AGN is remarkably successful at explaining a number of properties of individual AGN, the are different updated scenarios for explaining the different AGN zoology. The time-varying obscuration invoked in different models of SMBH-galaxy co-evolution predict different rates of mass accretion and star formation (see Di Matteo et al. 2005; Hopkins et al. 2008a; Alexander & Hickox 2012). These results indicate that the obscuring structure is directly heated by the AGN. Furthermore, they suggest that the covering factor of the obscuring material is broadly constant at a given AGN luminosity Also, these results are consistent with clumpy torus models (e.g., Nenkova et al. 2002, 2008b,a), which predict no inclination-angle dependence on the strength of the mid-IR emission dust in the narrow-line

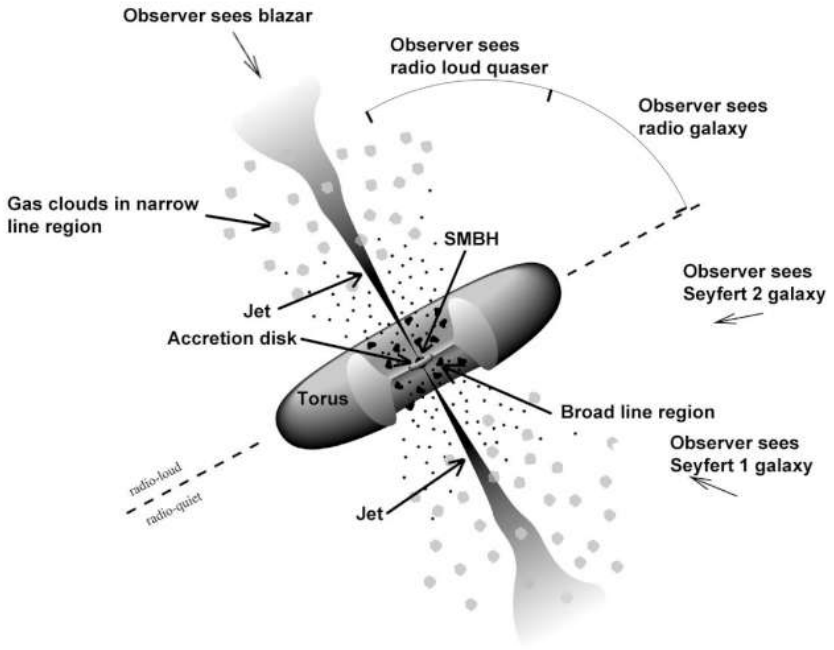

FIGURE 1.3: Schematic representation of the main elements of an AGN according to the unification scheme. Image courtesy of NASA's Fermi Gamma-ray Space Telescope: https://fermi.gsfc.nasa.gov/science/eteu/agn/

region can also lead to isotropic dust emission (e.g. see Efstathiou & Rowan-Robinson 1995; Schweitzer et al. 2008).

1.2.2.1 Radio-loud AGN

The radio emission in these systems is associated with particles accelerated by the central active nuclei. Compared to star forming galaxies, radio-loud AGN (RL AGN) are more powerful radio sources hosted by mostly elliptical galaxies. While at fainter flux densities (< 1 mJy) the contribution from star forming galaxies (SFGs) become increasingly important, the bright radio sky is dominated by the emission driven by radio-loud AGN (e.g., Prandoni et al. 2001; Smolčić et al. 2008; Seymour et al. 2008; Padovani et al. 2009). The bright end of the Euclidean-normalised source counts (151MHz flux densities > 100 mJy) is dominated by powerful radio-loud AGN (e.g. Willott et al. 2002).

1.2.2.2 Radio-quiet AGN

Radio quiet (RQ) AGN exhibit the presence of AGN activity in one or more bands of the electromagnetic spectrum (e.g., optical, mid-infrared, X-ray), and they are distinguished from RL AGN based on the ratio between the radio luminosity and the luminosity in another band. Kellermann et al. (1989) separated radio-loud and radio-quiet AGN based on their 5GHz to B-band flux density ratios. RQ AGN make up the majority (> 90%) of the AGN class and, until recently, they were normally found in optically, IR or X-ray selected samples, as they are characterised by relatively low radio-to-optical flux density ratios ($R \lesssim 10$)

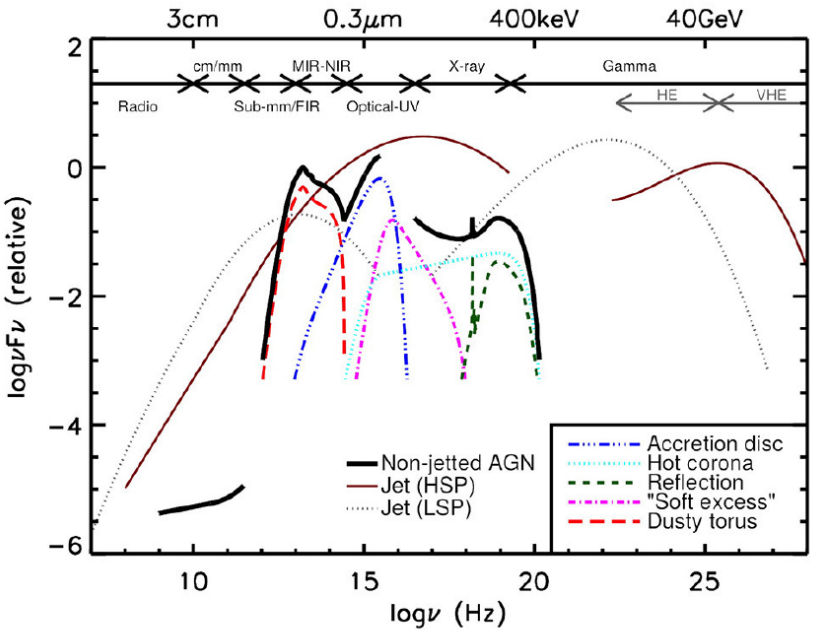

FIGURE 1.4: A schematic representation of an AGN spectral energy distribution (SED), loosely based on the observed SEDs of non-jetted quasars (e.g., Elvis et al. 1994; Richards et al. 2004). For details see Padovani (2017) and the section on the Faint Radio Sky for more details.

and radio powers ($P_{1.4\,GHz} \lesssim 10^{24}\,WHz^{-1}$) (Padovani 2016b). Nevertheless radio quiet (RQ) AGN are known to represent a significant fraction of sources in the faint radio sky, and the origin of their radio emission has been a matter of debate (Padovani et al. 2009). Some studies have proposed that RQ AGN represent scaled down versions of RL AGN with mini radio jets (e.g., Giroletti & Panessa 2009) or that their radio emission comes from star formation in the host galaxy (e.g., Padovani et al. 2011; Kimball et al. 2011). Separating the two emission mechanisms is important to investigate the circumstances under which they originate. This will help in understanding the host galaxy properties, and possibly to study the relation between AGN and star formation activity.

1.3 Radio Source classification

The range of properties radio sources display depending on observing frequencies and viewing angles presents an issue for the classification of individual sources. The availability of multi-wavelength minimizes the mis-classification of the radio-source population (Padovani, 2016b):

1. **X-ray power** : One precise method to select AGN is through X-ray surveys. X-ray surveys directly probe their high energy emission. However, it is more complex when dusty tori obscure the X-ray emission and reprocess it into infrared emission. Thus, the AGN detections through X-ray and infrared are somewhat complementary. Only AGN can have hard (2 - 10 keV) X-ray power $L_x \gtrsim 10^{42}\,erg\,s^{-1}$ (see Szokoly et al. 2004)

2. **MIPS 24 micron flux** : The Multiband Imaging Photometer (MIPS) (Rieke et al., 2004) $24_{\mu m}$ flux density, combined with the 1.4 GHz flux density can be used to calculate the so-called $q_{24\mu m}$ parameter, given by :

$$q_{24\mu m} = \log_{10}(S_{24\mu m}/S_{1.4GHz}) . \quad (1.1)$$

Bonzini et al. (2013) used this estimator to separate SFGs and radio-quiet AGN from radio-loud AGNs. The solid line in the top left panel of Figure 1.5 indicates the predicted $q_{24\mu m}$ value of M82 as a function of redshift, This is normalised by the local average value of $q_{24\mu m}$. Sargent et al. (2010b) defined this average value q_{240bs} as ($\langle q_{240bs} \rangle$) = $1.31^{+0.10}_{-0.05}$ for sources with $0.08 < z < 0.23$). The solid black curve shows the predicted value of M82 template, the dividing line between radio-quiet and radio-loud AGN with $\pm 2\sigma$ dispersion (dash black curve).

3. **Mid-Infrared diagnostics (IRAC colors)** : With the advent of the Spitzer Space Telescope (Werner et al., 2004), it has become possible to obtain MIR photometry for large samples of field galaxies, and thus to use MIR SEDs to identify specific populations of AGNs and star-forming galaxies. Studies have shown that the strong MIR continuum associated with AGNs provide a unique spectral signature that can be used to distinguish AGNs from starbursts and therefore the MIR bands can be used to select AGNs because the high energy radiation emitted by the accretion disk is absorbed by the surrounding dust and thermally re-emitted at longer wavelength. The IRAC color-color cuts most commonly adopted for AGN selection were defined by Lacy et al. 2004, 2007 and Stern et al. (2005) using shallow IRAC data to which additional flux cuts at $8\mu m$, $24\mu m$, or R band served to reject all but the brightest sources ($S_{8\mu m} \geq 1$ mJy, Lacy et al. 2004; R <21.5 and $S_{8\mu m} \geq 76$ μJy, Stern et al. 2005; $S_{24\mu m} \gtrsim 5$ mJy, Lacy et al. (2007). Lacy et al. (2004) used SDSS quasars to provide an empirical localization of the AGN population in the MIR color-color space. These initial color cuts effectively select luminous AGNs in samples containing only AGNs and bright, low-redshift star-forming galaxies (see also Sajina et al. 2005). The right panel of Figure 1.5 presents the IRAC color-color diagram showing the separation between AGNs (open red circles) and SFGs (black stars). The shaded region indicates the IRAC color cuts proposed by Donley et al. 2012 (the so-called Donley wedge).

4. **Optical indicators** : Baldwin, Philips, Terlevich (Baldwin et al., 1981) showed that it was possible to tell the difference between Type 2 AGN (see subsection 1.2.2) from normal star-forming galaxies by considering the intensity ratios of relatively strong emission lines. Veilleux & Osterbrock (1987) refined the approach and it has become a standard technique to classify objects according to where they reside on the BPT diagrams. Kewley et al. (2001) presented models used to derive a new theoretical classification scheme for starbursts and AGN based on the optical diagnostic diagrams. These models were built up on Dopita et al. (2000), who theoretically recalibrated the extragalactic H II region sequence using these line diagnostic diagrams and others, in order to differentiate and quantify the effects of abundance, ionization parameter, and continuous versus instantaneous burst models. Figure 1.6 (a), (b) and (c) shows the [OIII]/Hβ versus [NII]/Hα , [OIII]/Hβ versus [SII]/Hα and [OIII]/Hβ versus [OI]/Hα diagrams for the SDSS sample used in Kewley et al. (2006).

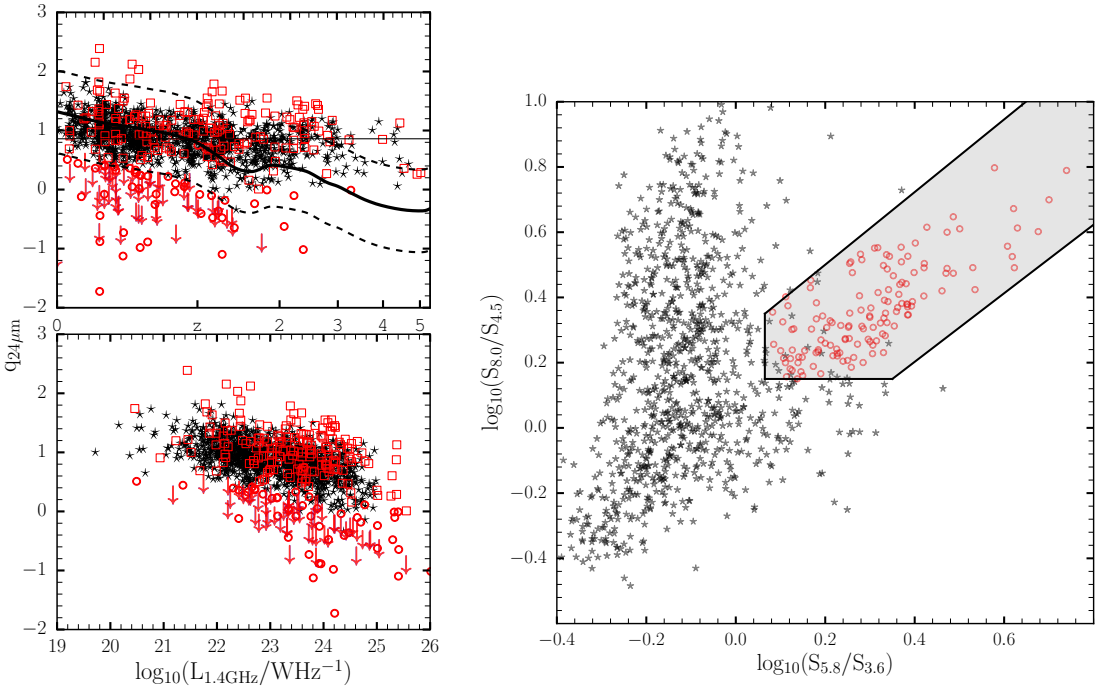

FIGURE 1.5: Left: The logarithm of the ratio between the mid-infrared and radio flux as a function of redshift (top) and 1.4 GHz radio luminosity (bottom). Different symbols refer to SFGs (black stars), RQ AGNs (open red squares) and RL AGNs (open red circles) The solid black curve shows the predicted value of M82 template, the dividing line between radio-quiet and radio-loud AGN with $\pm 2\sigma$ dispersion (dash black curve). Adapted from Ocran et al. (2017). Right: IRAC color-color diagram showing the separation between AGNs (open red circles) and SFGs (black stars). The shaded region indicates the so-called Donley wedge.

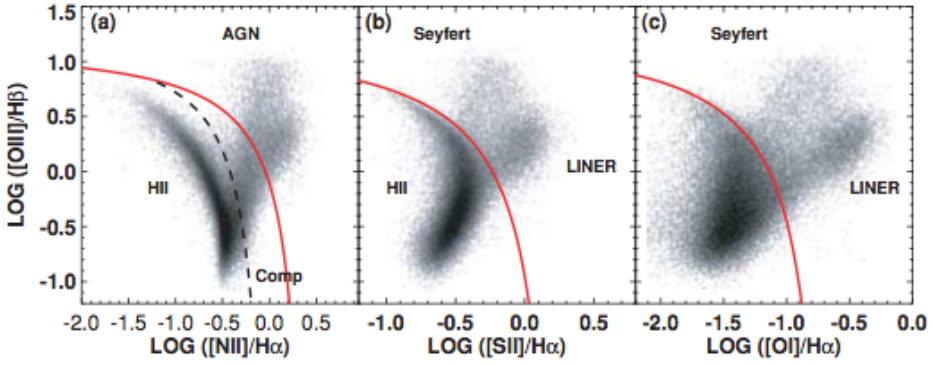

FIGURE 1.6: (a)The BPT [NII]/Hα versus [O III]/Hβ diagnostic diagram for SDSS galaxies with S/N>3 in all lines.The Kewley et al. (2001) extreme starburst line and the Kauffmann et al. (2003) classification line are shown as the solid and dashed lines, respectively. (b)The BPT [S II]/Hα versus [O III]/Hβ diagnostic diagram; (c) The BPT [O I]/Hα versus [O III]/Hβ diagnostic diagram. Adapted from Kewley et al. (2006).

1.4 Radio source counts

A powerful tool to study the statistical properties of radio sources is represented by the radio source counts. The cumulative distribution of the number of sources (N) brighter than a given flux density limit can be used also as a cosmological test. For instance evidence against the non-evolving, Steady State

cosmological models was provided by the slope of the source counts derived from early radio surveys (e.g. the Cambridge 2C survey; Shakeshaft et al. 1955 by Ryle & Scheuer 1955).

The source counts are usually tabulated in differential form: N(S)dS is the number of sources per steradian (sr) with flux densities between S and S + dS. In a static Euclidean universe, the flux density of any source at distance R is proportional to R^{-2}, and the volume enclosed by a sphere with radius *R* is proportional to R^3, therefore the number of sources stronger than any given flux density should be proportional to $S^{-3/2}$ and the differential number N(S) should be $dN/dS \propto S^{-5/2}$. Deviations from this form indicate evolution of number density or luminosity with distance. The radio source counts derived from a radio survey thus reflect the statistical properties of space and luminosity distribution of the radio source populations .

The relative contribution of different types of sources at every flux, which is the result of their luminosity functions at various redshifts (Prandoni et al., 2001) primarily determines the slope of the counts. The source counts therefore represent the most immediate observational constraint to evolutionary models of radio sources. An accurate determination of the source counts, their slope and normalization, is necessary in order to make this constraint helpful.

Differential source counts derived from deep 1.4 GHz surveys, and normalized to a non-evolving Euclidean model ($n\,S^{2.5}$), show a flattening below a few mJy (Windhorst 1984; Fomalont et al. 1984; Condon 1984). This change in slope was interpreted as the result of the emergence of a new population (namely SFGs), which does not appear at higher flux densities, where the counts are dominated by the classical powerful radio galaxies and quasars (99% of the sources above 60 mJy, Windhorst et al. 1990). The normalized source counts derived recently from a compilation of several deep radio surveys at 1.4 GHz is shown Figure 1.7. This plot illustrates very well the long-standing issue of the large scatter in the counts (exceeding Poisson fluctuations) present at flux densities $\lesssim 500\,\mu$Jy. The main causes for this considerable scatter can be either cosmic variance (source clustering) or survey systematics introduced by e.g. calibration, deconvolution and source extraction algorithms, or corrections applied to raw data to derive the source counts (see Prandoni et al. 2018). Cosmic variance certainly plays a role, as demonstrated by Heywood et al., 2013b. They compared the observed source counts with samples of matching areas extracted from the S3-SEX simulations (Wilman et al., 2008, 2010). Their simulated differential radio source counts are in good agreement with previously published values down to $\approx 50 - 100\,\mu$Jy and confirm the presence of a significant excess over a pure AGN model at $S < 500\,\mu$Jy. The effect of cosmic variance is also illustrated in Figure 1.7, where the shaded area represents the source counts' spread, expected from 400 samples of 0.5 deg^2 each, extracted from the simulated catalogue of Wilman et al. (2008).

It is important to stress that the observed spread prevent us from a robust comparison with source evolutionary models, and a robust determination of the relative contribution of SFGs and RQ AGN at sub-mJy fluxes.

Assessing the faint radio source population and characterizing their properties requires deep radio observations over large areas (to minimize cosmic variance), as well as a very good understanding of the multi-wavelength properties of both SFGs and AGNs (to reliably classify the sources).

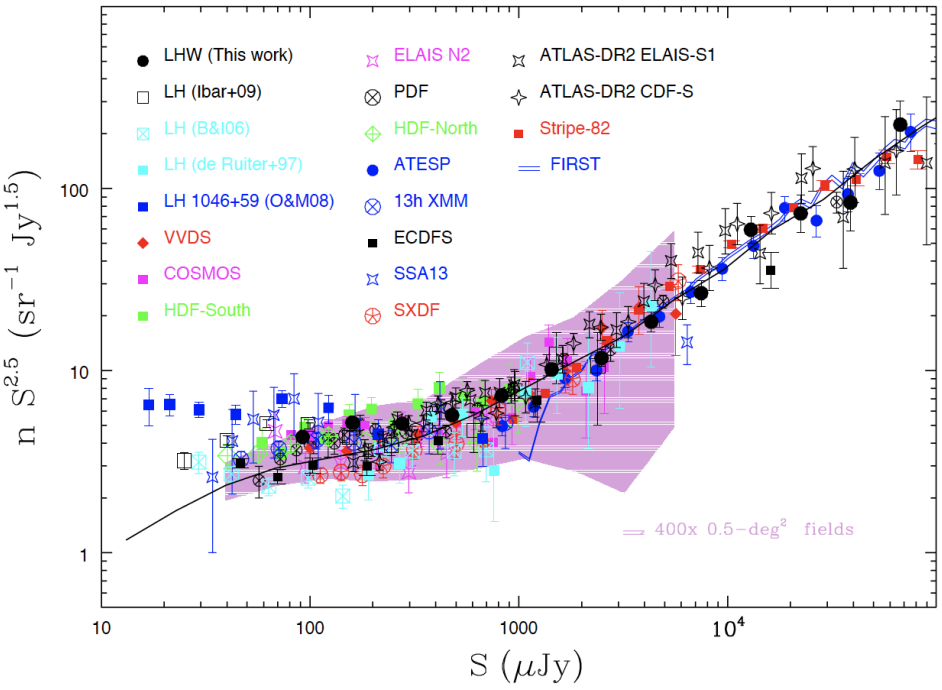

FIGURE 1.7: Normalized 1.4 GHz differential source counts for different samples (as indicated in the figure). For more details see text. Adapted from Prandoni et al. (2018).

1.5 The star-formation AGN connection

Understanding the relationships between different classes of sources composing the faint radio sky, as well as their cosmic evolution, is important for improving our understanding of the broad and complex relationships that exist between AGN and star-formation activity in the universe.

The observed correlation between AGN fraction and IR luminosity (and consequently with the SFR) of its host, is a well-known observational evidence supporting the idea of a connection between AGN and SF activities. While AGNs are a small fraction of the overall galaxy population at $L_{IR} < 10^{11}$, they are more than 50% in UltraLuminous InfraRed Galaxy (ULIRG) (e.g., Kartaltepe et al. 2010) suggesting that the AGN activity is linked to the strongest starburst events. A possible scenario explaining these observations has been proposed by Di Matteo et al. (2005) and Hopkins et al. (2008b). Both the AGN and the intense SF are triggered by a gas-rich major merger that provides fuel both to form new stars and to feed the black hole. In this phase, due to the large amount of dust present in the system, the AGN is often heavily obscured. Subsequently, the strong radiation from the AGN will clean the surroundings, quenching the star formation (this process is called AGN feedback), at the same time removing the obscuration of the AGN itself.

Galaxy formation simulations also invoke AGN feedback (e.g Springel et al. 2005). For example, the mass function (MF) of galaxies, i.e. the total number of galaxies with stellar mass in a certain mass bin as a function of mass, predicted by cosmological simulation shows an excess of galaxies at the high mass end

compared to the observed distribution (e.g., Ilbert et al. (2010, 2013)). Indeed, semi-analytic, hierarchical models of galaxy formation predict galaxies form in hot hydrostatic haloes where the radiative cooling time of the gas is much shorter than the age of the system. Therefore without further heating, cooling flows develop which channel gas to the centre of the galaxy triggering star formation and facilitating further accretion onto the supermassive black hole. In this scenario galaxies in the local universe should be more massive and have bluer colours and higher rates of star formation than is actually observed (White & Frenk, 1991). On the other hand, there are observational evidences of a coeval growth of the SMBH and their hosts. Amongst them is the tight correlation observed in the local Universe between the mass of the BH and the mass of its host galaxy bulge (see Kormendy & Ho (2013), for a review). Thus suggesting some mechanisms of AGN feedback that self-regulate the BH growth or influence the conversion of gas in stars, for example quenching or triggering the star formation. In the feedback scenario, the AGN may inject momentum and radiation in the inter-stellar medium (ISM) of massive galaxies, preventing the cold gas to further collapse and form stars, therefore reconciling theoretical predictions and observations.

1.6 Galaxy Luminosity Function

The luminosity function (LF), denoted by $\Phi(L)$ (in units of $Mpc^{-3}dex^{-1}$), provides one of the most fundamental tools to probe the distribution of galaxies over cosmological time. It describes the relative number of galaxies of different luminosities by counting them in a representative volume of the Universe thereby measuring the comoving number density of galaxies per unit luminosity, L, such that

$$dN = \Phi(L)dLdV \tag{1.2}$$

where dN is the observed number of galaxies within a luminosity range $[L, L + dL]$.

$$\int_0^\infty \Phi(L)dL = \rho \tag{1.3}$$

where ρ is the number of objects per unit volume V , and thus $\Phi(L)dL$ gives the number density of objects within a given luminosity range (see Choloniewski 1987). The density function can be defined by $\rho(x)$, where x represents the 3D spatial Cartesian coordinates such that the total number N of objects per unit volume (Mpc^{-3}) is

$$N = \int_V \rho(x) \tag{1.4}$$

For a given sample within a respective minimum and maximum redshift range z_{min} and z_{max} and solid angle Ω at a distance r it is possible to compute

$$N = \int_{z_{min}}^{z_{max}} \rho(z)\frac{dV'}{dz}dz \tag{1.5}$$

Luminosity functions are among the best tools for the study of galaxy evolution, as they allow to trace the changes in luminosity and/or density of a galaxy population as a function of redshift. The determination of

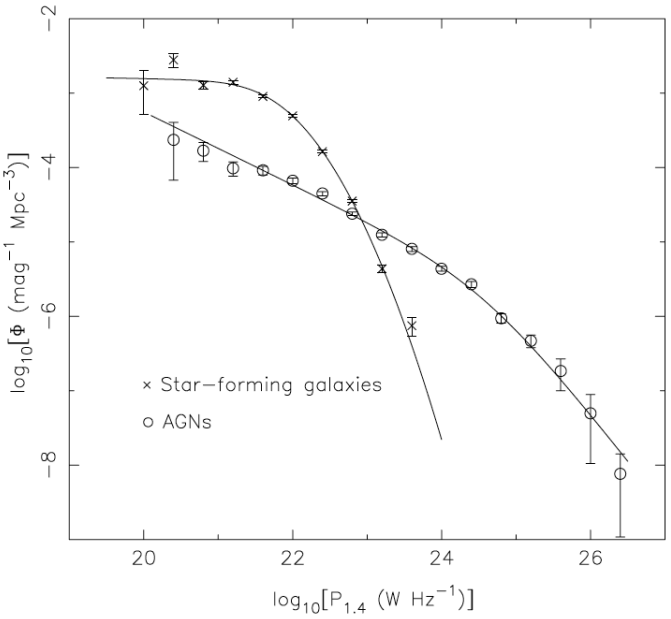

FIGURE 1.8: The local luminosity function at 1.4 GHz derived separately for the RL AGN (circles) and SF galaxies (crosses) in the 6dFGS-NVSS sample. Adapted from Mauch & Sadler (2007)

the LF requires a complete, flux density limited sample of sources, with redshift, at distances large enough that peculiar velocities cancel out ($z \gtrsim 0.003$) Padovani (2016b). New observational facilities have now reached incredible depth levels, enabling the characterisation of the faint-end of the LF to high precision levels, and providing estimates of the galaxy LF as far back as the first Gyr of universe lifetime (Bouwens et al. 2007; Ouchi et al. 2009; Oesch et al. 2010).

The LF provides a robust handle to compare the difference between different sets of galaxies i.e. at different redshifts, galaxy types, environment etc. It allows us to assess the statistical nature of galaxy formation and evolution and indeed, as soon as a new survey is carried out, the computation of the LF is one of the first actions (see e.g. Fried et al. 2001; Norberg et al. 2002; Blanton et al. 2003; Croom et al. 2004, 2009). Dunlop & Peacock (1990) provided the first comprehensive study of the radio luminosity function (RLF) using several complete samples selected at 2.7 GHz with flux density limits between 2.0 and 0.1 Jy. However, several fainter surveys have followed, like the Parkes Survey at 408 and 2700 MHz, and soon after the 6CE (Rawlings et al. 2001) and 7CRS samples, which display the most complete spectroscopic redshift follow-ups.

Figure 1.8 shows the local luminosity function at 1.4 GHz derived separately for the RL AGN (circles) and SF galaxies (crosses) in the 6dFGS-NVSS sample from Mauch & Sadler (2007). The two populations cross over at $P_{1.4} = 10^{23}$ WHz^{-1}, SFGs dominate the population of radio sources below this power and RL AGN dominate the population above it.

Schechter 1975, 1976 proposed an analytical equation to describe the general shape of a LF of optically-selected galaxies. However, this function turns over more steeply towards high luminosities than RLFs of SF galaxies. Instead the RLF is commonly fitted by the parametric form given by

$$\Phi_o(L) = \Phi_\star \left(\frac{L}{L_\star}\right)^{1-\alpha} \exp\left[\frac{-1}{2\sigma^2}\log^2\left(1+\frac{L}{L_\star}\right)\right] \tag{1.6}$$

proposed to fit the luminosity function of IRAS galaxies by Saunders et al. (1990) (see Mauch & Sadler 2007).

Equation 1.6 (is inadequate to describe the RLF of RL AGN and instead, RL AGN are fitted with a two power-law function analogous to the optical luminosity function of quasars (Dunlop & Peacock 1990; Brown et al. 2001)

$$\Phi_0(L) = \frac{\Phi^\star}{(L^\star/L)^\alpha + (L^\star/L)^\beta} . \tag{1.7}$$

Smolčić et al. (2009a) constrained well the evolution of the 1.4 GHz luminosity function for radio-selected SFGs in the VLA-COSMOS sample, using Equation 1.6 to describe the local LF (Figure 1.9). The top left panel of Figure 1.9 shows the local LF derived from Smolčić et al. (2009a). Although the 2deg^2 COSMOS field samples a relatively small comoving volume at the lowest redshifts, and only a photometric identification of SFGs has been used, the LF in the lowest redshift bin agrees remarkably well with the local LFs that were derived using all-sky radio surveys (NVSS, Condon 1989) (dashed grey lines) combined with good quality optical spectroscopic data (SDSS, 2dF Best et al. 2005) (open grey squares) to identify SFGs. A very good agreement is also found with the local 1.4 GHz LF for SF galaxies derived by Sadler et al. (2002) (yellow line). Smolčić et al. (2009b) used the VLA-COSMOS AGN sample of low luminosity radio sources (96% have $L_{1.4\,GHz} < 10^{25}$ WHz^{-1}) to comprehensively constrain the evolution of the low-power radio AGN out to z = 1.3. The right panel of Figure 1.9 compares the LFs of Smolčić et al. (2009b) with the Willott et al. (2001) model, after the latter has been converted to the current cosmology and the 151 MHz radio luminosities scaled to 1.4 GHz. It is worth noting that the VLA-COSMOS AGN data and the Sadler et al. (2002) AGN LF constrain the local radio LF more robustly at the faint end compared to the Willott et al. (2001) model for their less-powerful radio AGN.

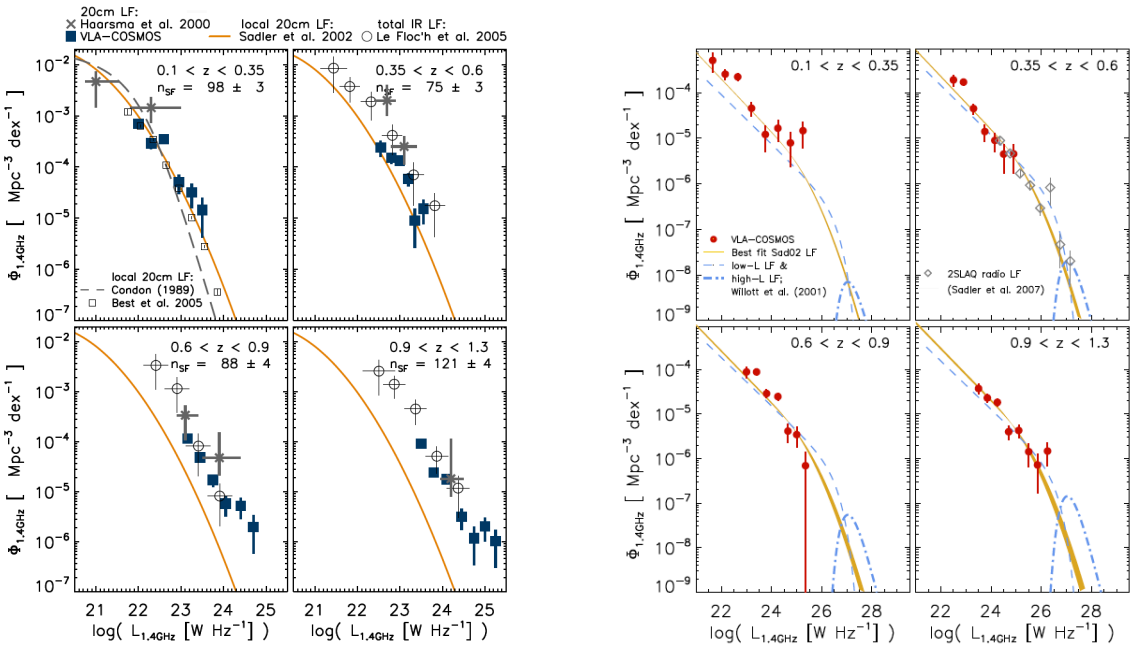

FIGURE 1.9: Left: 1.4 GHz luminosity functions (LFs) for star forming galaxies in the VLA-COSMOS survey, shown for four redshift ranges (filled blue squares) are presented in each panel. The number of galaxies in each redshift bin, statistically corrected for selection uncertainties (see text for details), is also indicated in each panel. Right: VLA-COSMOS AGN 1.4 GHz luminosity functions in four redshift ranges (red filled circles). For more details see Smolčić et al. (2009a) and Smolčić et al. (2009b).

1.7 Cosmic Star Formation History

The low-frequency emission arises mainly from SNe and as such, it is also related to the star formation rate (SFR). Its calibration as an SFR measurement is primarily empirical, example, based on the tight correlation observed between radio and FIR emission for IRAS-selected galaxies in the local Universe (e.g.,Yun et al. 2001). The infrared-radio correlation, together with insensitivity to dust extinction of radio surveys makes the radio emission an attractive wavelength for studying star formation.

Measurements of SFRs of many galaxies at different distances in large scale surveys, allows galaxies to be viewed at different times in the Universe. By comparing the average SFRs between local and distant galaxies, the evolution in the SFR of the Universe can be measured. Early studies by Lilly et al. (1996) and Madau et al. (1996) used ultraviolet (UV) measurements of galaxies to establish that evolution of the comoving space density of the global average SFR of the Universe has fallen by a factor of ~ 10 since $z \approx 1$ to the present day.

AGN also produce powerful radio emission. Locally, radio sources with $L_\nu\,(1.4\,\mathrm{GHz}) > 10^{23}\mathrm{WHz}^{-1}$ are predominantly AGN hence it is important to distinguish AGN from SFGs, by using different combinations such as radio spectral index, radio morphology, or infrared/radio correlation. However, these are difficult to measure, especially for very faint sources. Many studies have used the local radio LF to estimate the current star-formation rate density (SFRD) in the radio by carefully employed various criteria to separate

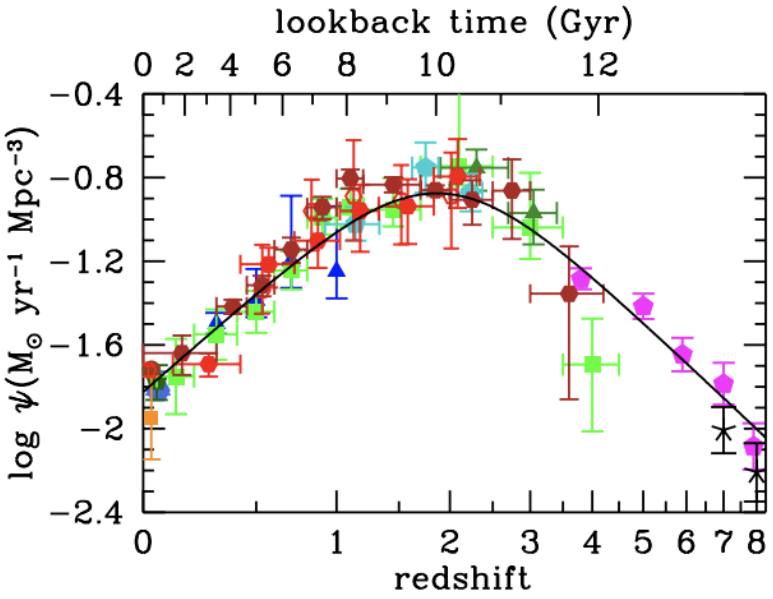

FIGURE 1.10: The history of cosmic star formation from FUV+IR rest-frame measurements taken from Madau & Dickinson (2014). Over-plotted are data from Wyder et al. (2005) (blue-gray hexagon), Schiminovich et al. (2005) (blue triangles), Cucciati et al. (2012) (green squares), Dahlen et al. (2007) (turquoise pentagons), Bouwens et al. (2012b,a) (magenta pentagons), Reddy & Steidel (2009) (dark green triangles), Gruppioni et al. (2013) (dark red filled hexagons) and Magnelli et al. (2013) (red filled hexagons).

AGN from star-forming galaxies.(see Machalski & Godlowski 2000; Condon et al. 2002; Sadler et al. 2002; Serjeant et al. 2002; Mauch & Sadler 2007). Haarsma et al. (2000) combined very deep VLA observations with spectroscopic and photometric redshift information to derive radio LFs and the cosmic SFRD at $0.3 < z < 0.8$. Seymour et al. (2008) identified AGN based on a combination of radio spectral indexes, radio morphology, and radio to NIR and MIR flux ratios and measured a peak SFRD at $z \approx 1.5$, albeit with large uncertainties by assuming pure luminosity evolution for the LF. All these studies found broad agreement between the radio SFRD evolution and optical and IR surveys, noting a steep decline from z = 1 to 0 (Madau & Dickinson, 2014). Figure 1.10 shows a recent compilation of multi-wavelength measurements of the SFRD from UV and IR data (Madau & Dickinson, 2014). There is a rising phase of the SFRD, scaling as $\Psi(z) \propto (1 + z)^{-2.9}$ at $3 \lesssim z \lesssim 8$, slowing and peaking at some point probably between z = 2 and 1.5, when the Universe was ~3.5 Gyr old (see Madau & Dickinson 2014).

While the SFRD from optical/UV surveys decrease from $z \sim 3$ going to higher redshift, the SFRD from studies using FIR (e.g. Liu et al. 2018; Loiacono et al. 2020; Gruppioni et al. 2020) and radio surveys, (e.g. Novak et al. 2017) shows a flat distribution over the whole redshift range. Gruppioni et al. 2020 noted that the difference between their results and the optical/UV surveys results increases with redshift, reaching a factor of about 10 at $z \sim 6$. The HST+near-IR dark galaxies contribute a significant fraction (about 17%) of the total SFRD at high redshift (i.e. $z > 3$). They concluded that at high redshifts, the surveys sampling the UV rest-frame can miss an increasing contribution of dust-obscured activity that cannot be recovered

even correcting the UV data for dust-extinction.

1.8 Science below the survey threshold

In preparation for the SKA, it is important for galaxy-formation and evolution studies to be able to investigate both faint AGN and star-formation activities (see e.g. Smolčić et al. 2008, 2009a,b; Bonzini et al. 2013; Padovani et al. 2014). Science at or below the survey threshold has expanded significantly in recent times. The techniques in this regime may be broadly defined as confusion or P(D) analyses (analyses of one-point statistics), and stacking, which accounts for the flux-density distribution of noise-limited images co-added at the positions of objects detected/isolated in a different waveband (e.g. see Glenn et al. 2010; Padovani et al. 2011; Heywood et al. 2013a; Zwart et al. 2014).

1.8.1 Stacking

Stacking is the co-addition of maps at the positions of sources detected in another map or catalogue (Zwart et al., 2015a). One makes a selection of sources in an often-deeper catalogue and measures the flux in a map, usually at another wavelength. Thus building up a distribution of map-extracted fluxes for that sample. Complications arises when the angular resolution of the map to be stacked is much coarser than in the selection band. Thus, for coarse-resolution maps, signal from more than one source can contribute to the net flux in a given pixel in the stacking band (e.g. see Webb et al. 2004; Greve et al. 2010; Zwart et al. 2015a). Hence due consideration must be given to this effect as a possible source of confusion noise.

1.9 Scope and Motivation of Thesis

Deep radio surveys probe both AGN and SFGs, and are becoming increasingly sensitive to the distant Universe. Hence, they represent a potentially very useful tool to address the role of AGN in galaxy evolution. However, several open issues remain to be understood. Are we probing a regime where AGN are less important? What can we learn about the relationship between AGN and SFGs by studying faint radio sources? The first step must be to determine the nature of the faint radio population. Multi-wavelength studies of the radio population in recent years have already made progress in addressing long-standing research questions such as the nature of the faint radio source population and how the number counts of deep radio surveys of the extragalactic sky change as a function of flux. Do we continue to see AGN dominated radio emission? This thesis presents additional insights into the characterization of the radio population, its evolution and relation to hosts galaxies, based on statistical properties of large samples of SFGs and AGN. I will be using analysis of deep imaging at 610 MHz with the GMRT and associated multi-wavelength data to explore the questions. This 610 MHz GMRT observations covering an area of $\sim 1.86\,\mathrm{deg}^2$ of ELAIS N1, explore the radio source population well below the regime dominated by

classical radio galaxies and Active Galactic Nuclei. A multi-wavelength approach is fundamental when dealing with deep radio images as most of the sources are unresolved and little information can be extracted from a single frequency catalog.

1.9.1 Thesis Outline

This thesis explores the faint radio sources using the multi-wavelength information to categorize the faint sources as AGN or SFG dominated, and with the aim of understanding their underlying properties. Below is an overview of the content of the next Chapters of this Thesis.

- **Chapter 2:** This Chapter presents the radio and the multi-wavelength source catalog used in this Thesis. The Giant Metrewave Radio Telescope (GMRT) observations of the ELAIS N1 are described, and particular attention is dedicated to the derivation of the radio source counts. The radio data is made up of 4290 sources down to a root mean square sensitivity of 10μJy and therefore represents one of the deepest radio samples available so far. Thus, these observations explore the radio source population well below the regime dominated by classical radio galaxies and Active Galactic Nuclei. A multi-wavelength approach is fundamental when dealing with deep radio images as most of the sources are unresolved and little information can be extracted from a single frequency catalog. Therefore, at the beginning of this Chapter, the wealth of multi-wavelength data available in the ELAIS N1 field, from the X-ray through to the Mid-Infrared is described. Also described are the details of the cross-matching of the radio sources with the multi-wavelength (Infrared, Optical and X-ray) source catalogs, and with new optical spectroscopic observations. I further study various diagnostics used to separate SFGs and AGNs in the faint radio sky. I then study of the radio spectral properties of this sample.

- **Chapter 3:** This chapter is focused on SFGs, which are mostly low power radio sources. I first analyse the SFGs through the far-infrared radio correlation. I make use of the non-parametric V/Vmax test and the radio luminosity function to investigate the cosmic evolution of the SFG sample. Then, I study the evolutionary properties of the radio population by comparing radio galaxies at different redshifts. I present new estimations of the radio luminosity function at 610 MHz for the SFGs. I convert the radio luminosities to SFR using a redshift dependent IR-radio correlation. By integrating LF fits in various luminosity limits estimated, I have derived the cosmic star formation history out to z = 1.5 for the SFG sample. Thus, this Chapter demonstrates the importance of using deep radio survey as a tool to study the cosmic star formation history.

- **Chapter 4:** This is direct a follow up of Chapter 3. The main topic of this Chapter is the evolution of AGN in the low-frequency faint radio source population. The AGN population comprises RQ AGN and RL AGN populations classified using multi-wavelength data. I study the radio-IR correlation for the RQ AGN and RL AGN populations comparing them to the SFGs population. I compare the well-established relation between SFR and main sequence (MS) of the various classes of AGN as

well as the SFGs discussed in Chapter 3 and also compare to literature. This is the so-called "star formation main sequence" (SFMS). I further constrained the evolution of the AGN population with continuous models of pure density and pure luminosity evolutions. I also present pure luminosity evolution fits for the RQ AGN and RL AGN.

- **Chapter 5:** In Chapter 5, I use stacking experiment, which is a commonly used technique to overcome confusion below the survey threshold. I investigate the infrared/radio correlation using this technique of source stacking, in order to probe the average properties of radio sources that are too faint to be detected individually. I stack infrared sources from the MIPS 24 micron mid-infrared survey in the ELAIS N1 field, using radio surveys created at 325 MHz, 610 MHz and 1.4 GHz. I investigate the mid-infrared radio (MIR) correlation at very low flux densities using the median stacks created at the frequencies mention. I also carry out radio spectral index analyses using the median stacked radio images.

- **Chapter 6:** In Chapter 6 a summary of the results and implications of this work are presented. Promising prospects for the development of this work are also proposed.

Chapter 2

Deep GMRT 610 MHz Observations of the ELAIS N1 Field : Catalogue and Source Counts

Abstract

The Faint Low-Frequency Radio Universe in Continuum: Exploitation of the Pre-SKA Deepest Survey

This is the first of a series of papers based on sensitive 610 MHz observations of the ELAIS N1 field using the Giant Metrewave Radio Telescope. We describe the observations, processing and source catalogue extraction from a deep image with area of 1.86 $\deg^2$ and minimum noise of ~7.1 μJy/beam. We compile a catalogue of 4290 sources with flux densities in the range 28.9 μJy - 0.503 Jy, and derive the Euclidean-normalized differential source counts for sources with flux densities brighter than 35.5 μ Jy. Our counts show a flattening at 610 MHz flux densities below 1 mJy. Below the break the counts are higher than previous observations at this frequency, but generally consistent with recent models of the low-frequency source population. The radio catalogue is cross-matched against multi-wavelength data leading to identifications for 92% and reliable redshifts for 72% of our sample, with 19% of the redshifts based on spectroscopy. For the sources with redshifts we use radio and X-ray luminosity, optical spectroscopy and mid-infrared colours to search for evidence of the presence of an Active Galactic Nucleus (AGN). We compare our identifications to predictions of the flux density distributions of star forming galaxies (SFGs) and AGN, and find a good agreement assuming the majority of the sources without redshifts are SFGs. We derive spectral index distributions for a sub-sample. The majority of the sources are steep spectra, with a median spectral index that steepens with frequency; $\alpha_{325}^{610} = -0.80 \pm 0.29$, $\alpha_{1400}^{610} = -0.83 \pm 0.31$ and $\alpha_{5000}^{610} = -1.12 \pm 0.15$.

2.1 Introduction

The study of the faint radio continuum universe and of its properties has recently become a very active field of research not only because of the planned transformational capabilities of the Square Kilometre Array (Braun et al., 2015) on this field, but also because of the major steps being taken and planned with SKA pathfinders and precursors. Deep radio observations of the extragalactic sky are a powerful means to probe the properties of diverse source populations over a variety of environments to high redshift (Condon, 1984; Becker et al., 1995; Gruppioni et al., 1999). Radio emission is important for galaxy population studies, as the synchrotron emission is a clear indicator of activity for both star formation galaxies (SFGs) and active galactic nuclei (AGN). Moreover, radio emission is not affected by dust obscuration, hence can probe astrophysical processes to large distances.

At faint radio flux densities star forming galaxies dominate. These are very different from the radio sources seen in the bright radio sky (Windhorst et al., 2011; Padovani, 2016b), which are dominated by Active Galaxies. Counts of radio galaxies versus flux density provide useful information, as the source count shape is directly related to the evolutionary properties of the galaxies (Prandoni et al., 2001; de Zotti et al., 2010; Padovani et al., 2011, 2015). Radio source counts represent the most immediate observational constraint to evolutionary models of radio sources (Prandoni et al. (2001). The now well-established flattening of the counts below 1 mJy is interpreted as the signature of the rise of star-forming galaxies (Rawlings & Jarvis, 2004; Seymour et al., 2008; Padovani et al., 2009).

Surveys at low frequencies, e.g. Garn et al. 2008; Sirothia et al. 2009; Williams et al. 2016, are an important complement to higher frequency observations. Low-frequency observations are powerful at detecting ultra-steep spectrum sources, which are often galaxies at high redshifts (e.g. Best et al. 1998, 2003; Miley & De Breuck 2008). Combining low- and high-frequency radio observations allows studies of the radio continuum spectra (e.g. Whittam et al. 2017; Mahony et al. 2016), providng a more precise characterization of the source properties (Riseley et al., 2016). Radio spectral indices can be used to identify GHz peaked sources (GPS) (Athreya & Kapahi 1998; O'Dea 1998; Snellen et al. 2000), ultra-steep spectrum sources (USS) (Roettgering et al. 1996; Jarvis et al. 2001), and core-dominated radio-quiet AGN (Blundell & Kuncic, 2007).

Star-forming galaxies are observed to have a mean spectral index between -0.8 and -0.7 at 1.4 GHz ($S(\nu) \propto \nu^{\alpha}$), with a relatively small dispersion of ±0.24 (Condon, 1992). Studies combining 610-MHz and 1.4-GHz data, have found evidence for flatter spectral indices (Bondi et al. 2007; Garn et al. 2008) and larger dispersions at sub-mJy radio flux densities (Magliocchetti et al., 2008), suggesting that core-dominated radio-quiet AGN are playing a key role in the sub-mJy radio population. Ibar et al. (2009) reported statistical analyses showing no clear evolution for the median spectral index, α_{1400}^{610}, as a function of flux density based on observations of the Lockman Hole using the Giant Metrewave Radio Telescope (GMRT). Their study found α_{1400}^{610} to be -0.6 to -0.7. They also analyse the spectral indices based independently on

GMRT and VLA selected samples, and found that a 610 MHz selected catalogue naturally tends to prefer the detection of steep-spectrum sources while selection at 1.4 GHz favours flatter spectra.

The European Large Area ISO Survey (ELAIS) N1 field has been observed at multiple radio frequencies. Sirothia et al. (2009) observed it at 325 MHz using the Giant Metrewave Radio Telescope (GMRT), with the objective of identifying active galactic nuclei and starburst galaxies and examining their evolution with cosmic epoch. Grant et al. (2010) observed 15 $\deg^2$ with the Dominion Radio Astrophysical Observatory synthesis telescope at 1420 MHz to a minimum rms of 55 μJy beam^{-1} in Stokes I and 45 μJy beam^{-1} in polarisation. Banfield et al. (2011) observed 10 $\deg^2$ at 1.4 GHz with the JVLA in B configuration to a minimum rms of 87 μJy beam^{-1} in total intensity. Taylor et al. (2014) observed a smaller region (0.13 $\deg^2$) at 5 GHz with the JVLA in B and C configuration to a minimum rms of 1.05 μJy beam^{-1}.

In this paper we present deep GMRT observations at 610 MHz of the ELAIS N1 field (ELAIS N1) covering 1.86 $\deg^2$. The ELAIS N1 field is a large northern field that has been targeted by surveys spanning the entire electromagnetic spectrum. Further building on the extensive radio coverage of ELAIS N1 and wealth of multi-wavelength observations that provides valuable insights into galaxy formation and evolution. In this work, we achieve a minimum noise of 7.1 μJy beam^{-1} and an angular resolution of 6 arcse $\times$ 6 arcsec.

The remainder of this paper is divided as follows: we first introduce the observations and data processing in Section 2.2. In Section 2.3, we present the 610-MHz source counts analysis. Section 2.4 provides the multi-wavelength cross-identifications and the nature of the source population. The multi-frequency spectral analysis of the sample is presented in Section 2.5. In this paper we assume a flat cold dark matter (ΛCDM) cosmology with $\Omega_\Lambda = 0.7$, $\Omega_m = 0.3$ and $H_o = 70$ km s^{-1} Mpc^{-1} .

2.2 Observations and data processing

2.2.1 Radio data

The ELAIS N1 field was originally chosen for deep extragalactic observations with the Infrared Space Observatory (ISO) due to its low infrared background (Rowan-Robinson et al., 2004; Vaccari et al., 2005). Since then, it has become one of the best-studied 1-10 $\deg^2$ extragalactic fields. GMRT observations of the ELAIS N1 field were obtained during several observing runs from 2011 to 2013. The observations were carried out for 7 positions arranged in a hexagonal pattern centred on $\alpha = 16^h\ 10^m\ 30^s$, $\delta = 54^\circ\ 35\ 00''$ (see Ocran et al. 2017). In this paper we present a deeper radio image, an improved radio data reduction and multi-wavelength analysis of the ELAIS N1 610 MHz Deep Survey first described by Ocran et al. (2017).

The survey consists of 7 closely-spaced GMRT pointings, with on source integration time of $\sim$ 18 hours per pointing. The pipeline was modified to restrict the flags, which resulted in slightly less data being flagged. The shallower pointings were added at the edges where the deep and shallow pointing had rms within

a factor of two. The weights used in the mosaic follows the same procedure as in Intema et al. (2017), Section 3.3. The weight is the inverse square of the local background rms noise (the inverse variance). The resolutions before mosaic, for each pointing were in the range 4.5 to 6 arcseconds. To reduce the noise around the edges of the mosaic image we included data from a set of pointings with 3 hours of observation each that are part of a wider but shallower study of ELAIS N1 (Ishwara-Chandra et al. 2020).

The data was analysed using CASA (Common Astronomy Software Applications) using standard procedures. The flux density scale was set using the primary calibrators 3C286 and 3C48, which were observed both at the start and at the end of each observing session. A phase calibrator was observed for 5 minutes every 30 minute of target observations for phase and gain calibrations. After initial flagging using `flagdata`, delay, bandpass and gain calibration was carried out. Post-calibration, the data was flagged again and re-calibrated. Channel averaging was done with post-averaging channel width of 0.78 MHz in order to keep the bandwidth smearing negligible. Split files from each pointing from different observing runs were combined using `concat` before imaging. We used `tclean` for imaging. Four rounds of phase-only self-cal and then 5 rounds of amplitude and phase self-cal was carried out on each pointing. The rms noise on the individual images were ~ 15 μJy/beam before mosaicing. The primary beam correction and mosaic was carried out in AIPS using the python script *make mosaic* (Intema, private communication) using a circular restoring beam of 6 arcsec.

An image of the mosaic is shown in Figure 2.1. There are a small number of bright classical radio galaxies with double-lobed and jet morphologies, however most of the sources are compact as typically found in faint (sub-) mJy radio fluxes. Figure 2.2 shows an image of the rms map created by PyBDSF, and Figure 2.3 shows the distribution of pixel amplitudes in the rms image. The minimum rms noise in the central region of the image is 7.1 μJy beam^{-1}. The median noise in the mosaic is 19.5μJy beam^{-1}. The higher noise values arise primarily due to enhanced rms in small regions around very bright sources and from the lower mosaic weights at the edge of the mosaic.

2.2.2 Source Finding and Cataloguing

The catalogue of radio sources was extracted using the PyBDSF source finder (Mohan & Rafferty, 2015). The rms map was determined with a sliding box `rms_box` = (80, 10) pixels (i.e. a box size of 80 pixels every 10 pixels), with a smaller box `rms_box_bright` = (40, 5) pixels in the regions around bright sources to account for the increase in local rms as a result of calibration artefacts. Figure 2.2 illustrates the variation in rms noise determined across the entire mosaic image.

PyBDSF extracts sources by first identifying islands of contiguous emission above a given threshold `thresh_isl`= 3σ, around pixels brighter than a given flux `thresh_pix`= 5σ. Then it decomposes the islands into Gaussian components. It then combines significantly overlapping Gaussians into sources, and determines the flux densities, shapes and positions of sources (Intema et al., 2011). We used the `group_tol` parameter with a value of 10.0 to allow more Gaussians to be grouped together and larger

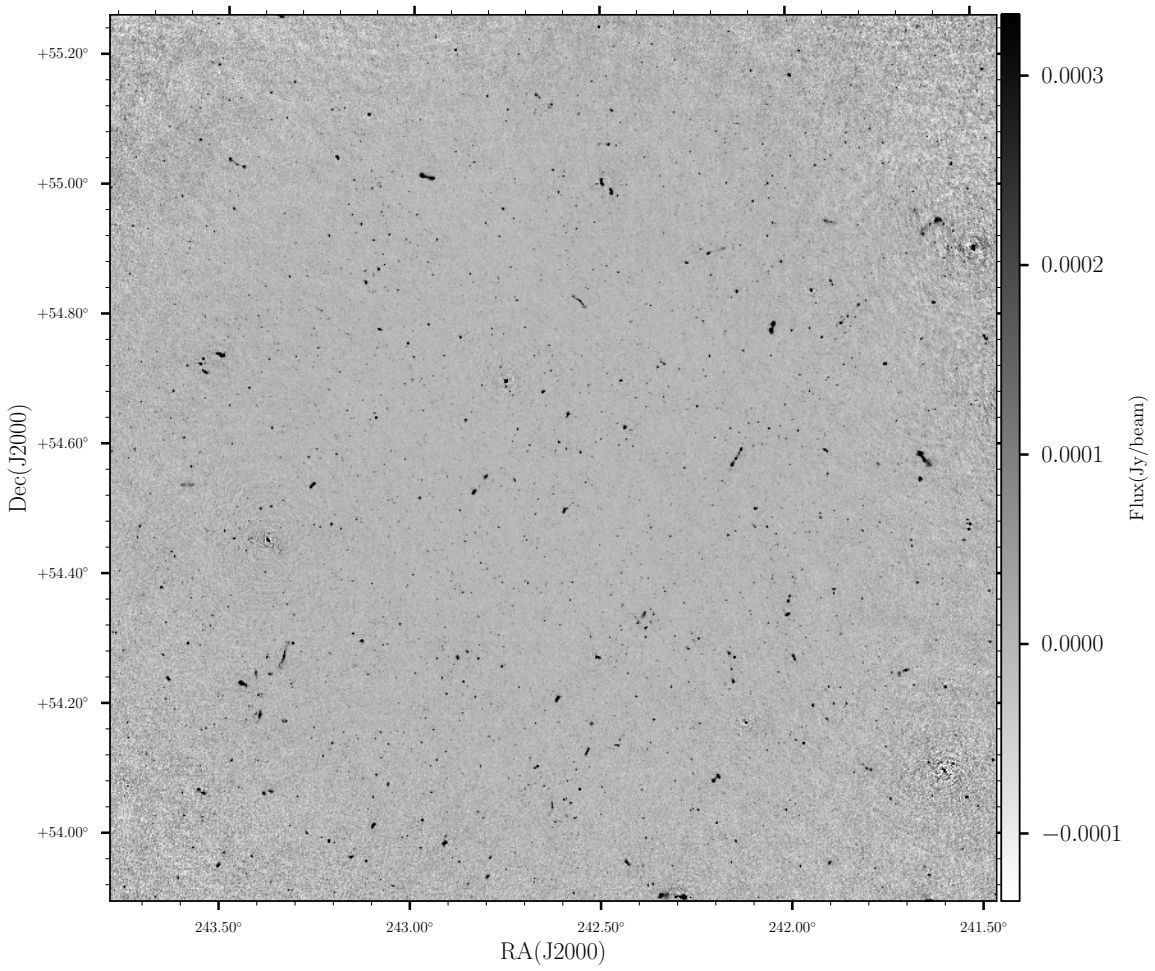

FIGURE 2.1: Image of the ELAIS N1 GMRT 610 MHz mosaic centered at $\alpha = 16^{h}\,10^{m}\,30^{s}$, $\delta = 54°\,35\,00''$ (J2000). This image is $47'$ on each side. The restoring beam is 6 arcsec circular and the RMS in the central region is $\sim 7.1\,\mu$Jy beam^{-1}. The grey-scale brightness stretch ranges between -0.1 and 0.3 mJy beam^{-1}.

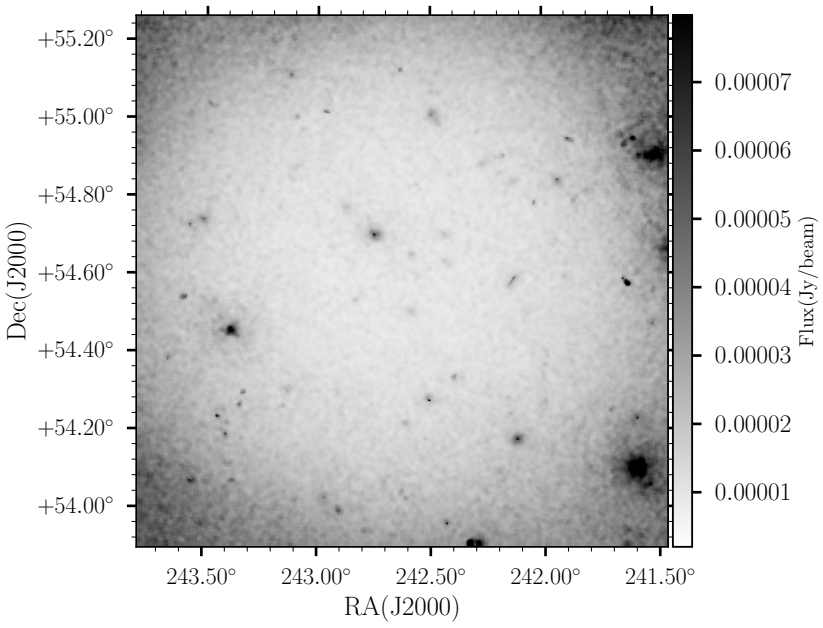

FIGURE 2.2: Greyscale image showing the local rms noise of the final mosaicked GMRT image, derived using PyBDSF (see Section 2.2.2). The grey-scale brightness stretch ranges between 0.01 and 0.07 mJy beam^{-1}.

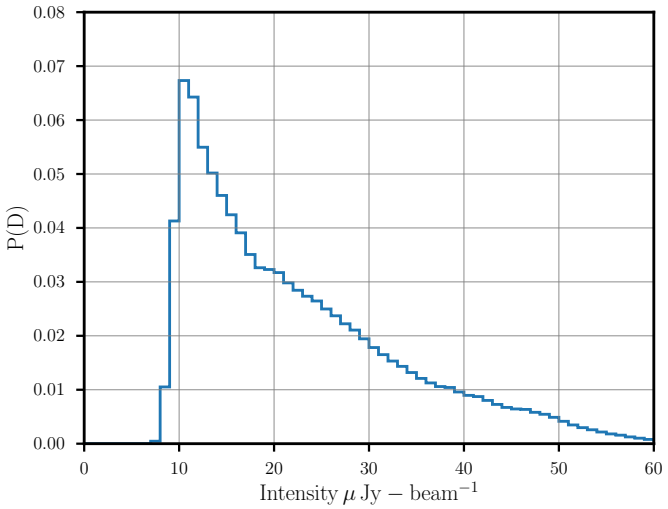

FIGURE 2.3: The distribution of the 610-MHz rms for the GMRT sample. The mean and median rms are 22.70 μJy and 19.50 μJy respectively.

sources to be formed. Sources are classified as *'S'* for single sources and *'M'* for multiple Gaussian sources. The total number of sources detected by PyBDSF in the image is 6605 comprising of 7919 Gaussian components of which 5682 were single component sources.

The catalogue consists of 4303 radio sources with signal to noise cut (SNR $= \frac{S_p}{rms}$) above the 5σ threshold and flux threshold cut $\geq 0.1 \times$ RMS. There are 128 sources included in the catalogue flagged as having poor Gaussian fits. In this case the integrated flux density is the total flux measured in the island instead of that defined by the Gaussian fit.

2.2.3 Multiple component sources

In order to generate a final source catalogue we need to identify multi-component sources that have not been recognised as such by `PyBDSF`, and therefore appear as distinct entries in the catalogue. This can happen when there is no significant radio emission between two radio lobes, or the local rms noise is overestimated because of large-scale faint radio emission (see Smolčić et al. 2017a), which affects the ability of `PyBDSF` to properly detect the source.

Figure 2.4 shows examples of such sources (typically radio galaxies or resolved star-forming disks). For the identification of these objects we make use of the Spitzer Extragalactic Representative Volume Survey (SERVS, Mauduit et al. 2012) which imaged 18 deg^2 using the IRAC1 3.6 μm and IRAC2 4.5 μm bands. SERVS overlaps with several other surveys from the optical, near- through far-infrared, sub-millimeter and radio. We first selected 12 likely multi-component sources visually by focusing on multiple bright and/or close `PyBDSF` detections with no SERVS counterparts. While it may not always be obvious how to discriminate (for example) between isolated compact sources that are apparently close and true double-lobe emission, the high identification rate of radio sources in infrared images thus allows us to do this rather robustly and to only carry out visual checks in a very small number of cases. We then overlaid radio contours on IRAC1 3.6 μm postage stamps. If a robust SERVS counterpart can be identified visually, i.e. at the centre of two radio lobes, we simply take the SERVS position to be the position of the radio source. Otherwise the radio source position was determined by averaging the positions of the different components detected by `PyBDSF` and we then visually match the radio source with a SERVS counterpart, if any. The total and peak flux densities were then estimated by summing the flux density inside regions enclosed by radio contours. Figure 2.5 shows examples of SERVS+radio cutouts of extended or otherwise complex sources in the catalogue (i.e. more examples of these sources are shown in Figure A.2 of Appendix A).

Following the above process we produced a curated catalogue of 4290 sources which we used for our scientific analyses.

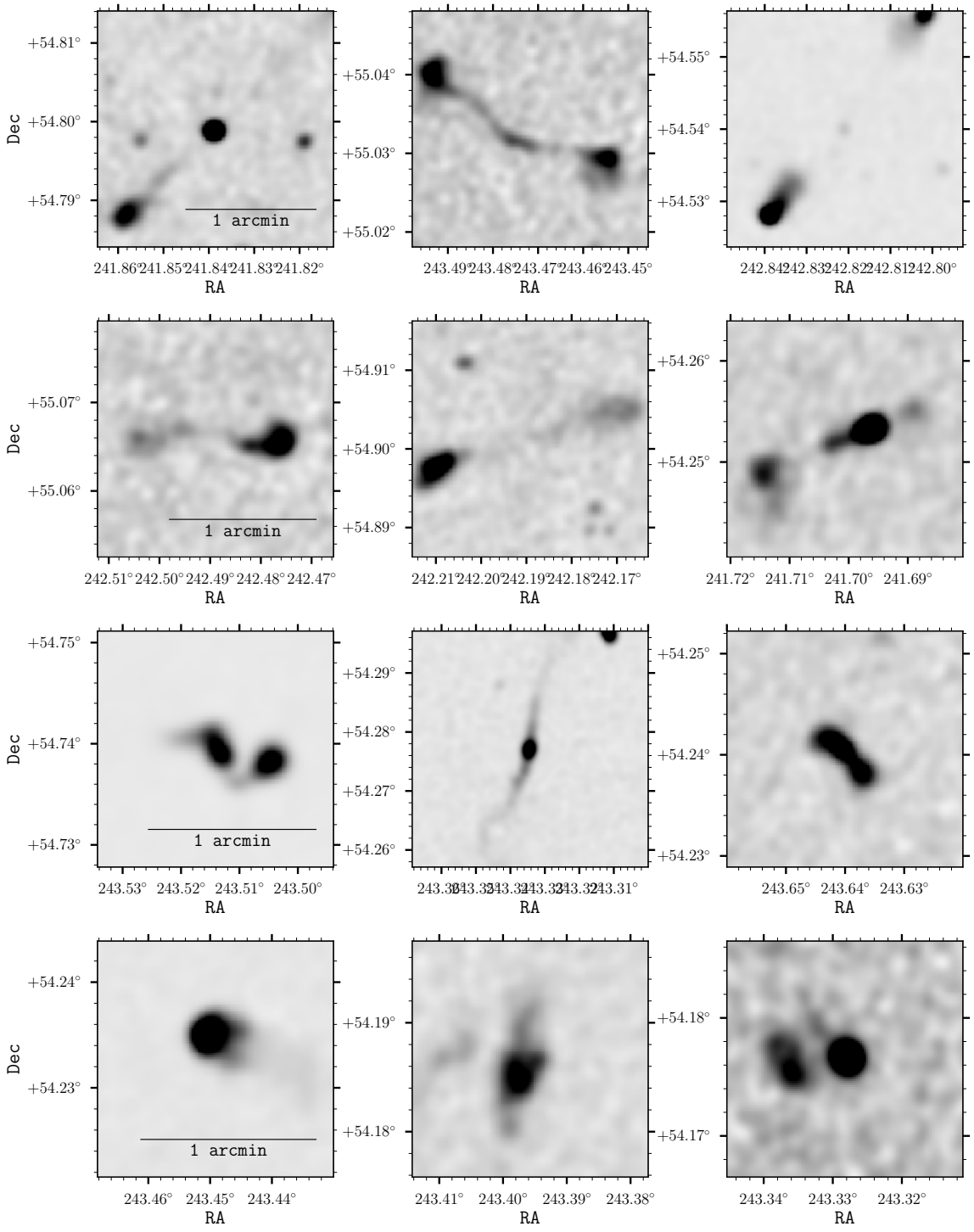

FIGURE 2.4: Postage stamps from the GMRT 610 MHz continuum mosaic image showing some extended radio sources.

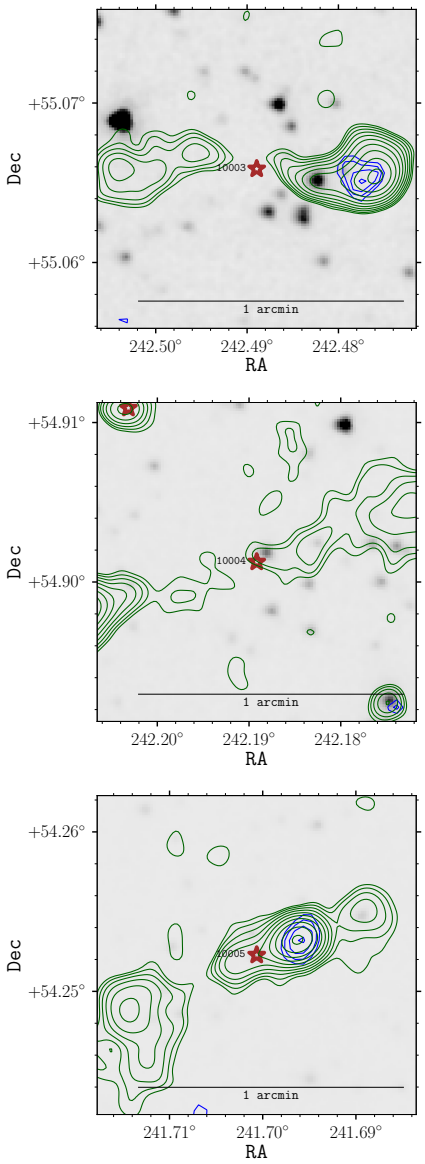

FIGURE 2.5: Postage stamps showing examples of multiple component sources in the GMRT 610 MHz catalogue. The greyscale shows IRAC band 1 and IRAC band 2 images respectively. The red stars show the central position of the GMRT source. The green contours represents the GMRT 610 MHz whereas the blue contours represents VLA FIRST. The contours levels are 1, 2, 3, 4, 5, and 6 σ.

2.3 Source Counts

We derived number counts in the ELAIS N1 using the curated catalogue shown in Table 2.2. The radio number counts require no additional data but nevertheless provide very useful information, as their shape is tightly related to the evolutionary properties of the sources and also to the geometry of the Universe Padovani (2016b). The differential number counts, dN/dS, were calculated using the observed number of sources per bin of flux density, N, corrected for the estimated number of false detections N_f, divided by the bin width (ΔS in Jy) and multiplied by the weight, w (which incorporates the efficiency, resolution bias C_R and Eddington bias C_{Edd})

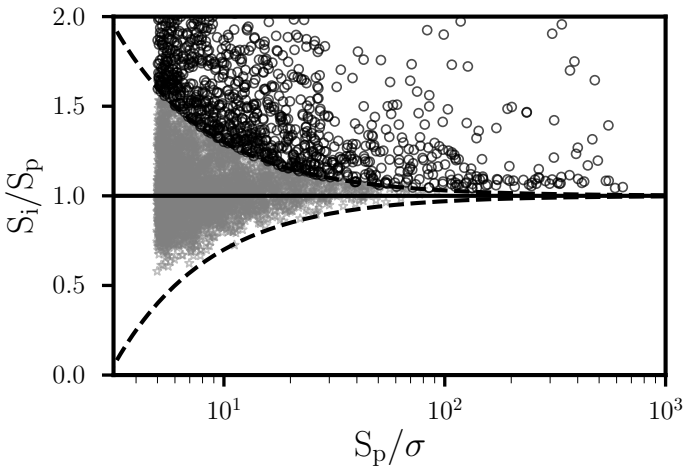

FIGURE 2.6: Ratio of the integrated flux density to peak flux density as a function of signal-to-noise ratio (S_p/σ). Sources which are classified as unresolved (grey stars) and resolved (open black circles) during the source-fitting procedure. The solid line is at $S_i/S_p = 1$.

$$\frac{dN}{dS} = \frac{N - N_f}{\Delta S} \times w \tag{2.1}$$

In this section, we discuss how we derive our source counts alongside our treatment of efficiency, resolution bias and Eddington bias.

2.3.1 Source sizes

The flux density ratio may be used to discriminate between point-like and extended sources (see Prandoni et al. 2001, 2006). The ratio of the integrated to peak flux densities is shown as a function of signal-to-noise ratio in Figure 2.6, with sources classified as point-like and extended shown separately. To select the resolved components, we determined the lower envelope of the points in Figure 2.6, by fitting a functional form that can be characterized by Equation 2.2. Almost all of the points with $S_i/S_p < 1$ lie above the curve. Reflecting this curve above the $S_i/S_p = 1$ line (upper envelope in Figure 2.6) gives a list of all the sources which lie above the upper envelope and can be considered to be resolved. This analysis shows that about 29% of the sources (1260/4290) are considered to be resolved.

$$\frac{S_i}{S_p} = 1.0 \pm \frac{3}{SNR} \tag{2.2}$$

where $SNR = \frac{S_p}{rms}$. Sources below this locus are considered to be unresolved. These resolved and unresolved components were flagged in the catalogue. We use the peak flux density as recovered by PyBDSF in place of the integrated flux density for unresolved sources when deriving the differential source counts.

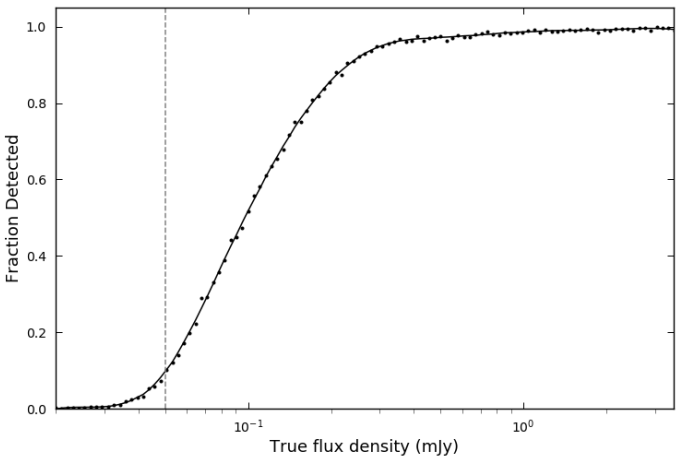

FIGURE 2.7: The fraction of simulated sources detected as a function of flux density illustrated by the blue solid curve. The solid line is a piece-wise polynomial spline interpolation of the data. The vertical dashed line shows the approximate 5σ detection level of 50 μJy/beam.

2.3.2 Reliability

The reliability of a source catalogue is defined as the probability that all detected sources in the survey area above a certain brightness detect limit are real sources and are not detections of artefacts or noise peaks (Williams et al. 2016; Whittam et al. 2017).

We investigate the effect these may have on the false detection rate by running the PyBDSF algorithm with the same parameters we use to compile the source catalogue on an inverted image in exactly the same way as described in Section 2.2.2. The source finding algorithm only detects positive peaks, therefore by inverting the image and running PyBDSF on the inverted map, any detections result from noise on the map Whittam et al. (2017). We detected 192 sources in the inverted image (compared to 6605 in the real image), giving a false detection rate of 2.5 per cent, which indicates, that the noise in the image is not entirely Gaussian. We corrected for false sources the source counts by subtracting the negative sources in each flux bin before calculating the counts.

2.3.3 Resolution bias

The underestimation of source counts in a given flux density bin due to a resolved component having a lower peak flux density than an unresolved component with equivalent integrated flux density is defined as resolution bias (e.g. see Kellermann & Wall 1987; Prandoni et al. 2001; Williams et al. 2016). We calculate the approximate maximum size $\theta_{\rm max}$ a source could have for a given integrated flux density before it drops below the peak flux detection threshold. Using the relation below:

$$\frac{S_{int}}{S_{peak}} = \frac{\theta_{maj}\theta_{min}}{b_{maj}b_{min}} \tag{2.3}$$

where b_{min} and b_{maj} are the synthesized beam axes, and θ_{min} and θ_{maj} are the deconvolved source axes, we estimate the maximum size a source of a given integrated flux density can have before falling below the peak flux detection threshold.

$$\theta_{max} = \left[(b_{maj}b_{min})\frac{S_{int}}{5\sigma}\right]^{0.5} \tag{2.4}$$

Combining the upper envelope for resolved sources defined in equation 2.2 (see Section 2.3.1) with equation 2.3 gives:

$$\theta_{min} = \left[(b_{maj}b_{min})\left(1 + \frac{3}{SNR}\right)\right]^{0.5} \tag{2.5}$$

where θ_{min} is the minimum angular size a source can have before it can be considered to be resolved as a function of its SNR (see Heywood et al. 2016). We estimate the fraction of sources with deconvolved angular sizes larger than this θ_{max} limit using the assumed true angular size distribution proposed by Windhorst et al. (1990).

$$h(>\theta) = \exp\left[-\ln 2\left(\frac{\theta_{lim}}{\theta_{med}}\right)^{0.62}\right] \tag{2.6}$$

where $\theta_{lim} = \max(\theta_{min}, \theta_{max})$ and $\theta_{med} = 2\,S^{0.3}_{1.4GHz}$ (S is the flux at 1.4 GHz density in mJy, we have scaled the 1.4 GHz flux densities to 610 MHz with a spectral index of -0.8).

The resolution bias correction factor c_R for the counts is then given by:

$$C_R = \frac{1}{1 - h(>\theta_{lim})} \tag{2.7}$$

The correction factors calculated using the median size distributions is plotted as a function of flux density in Figure 2.8.

2.3.4 Completeness and Eddington bias

Eddington (1913) showed that there was a significant bias in the measured number counts of stars even when the errors on the flux densities of the stars have the usual Gaussian distribution. This causes the apparent steepening of the observed source count by the intensity-dependent over-estimation of intensities, due to either system noise or confusion noise or both (Zwart et al., 2015a). This effect is more significant near the detection limit of a survey and could cause the number of observed sources to be slightly too high in the fainter bins. To quantify the effect that Eddington bias has on source counts, previous work at higher frequency have semi-empirical methods. For example, Moss et al. (2007) used the best-fitting population

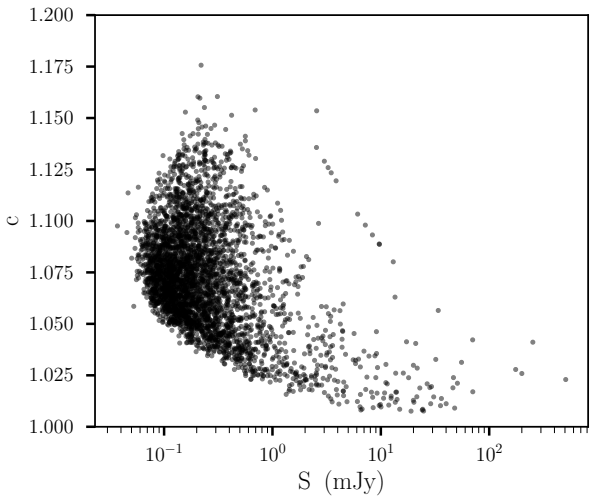

FIGURE 2.8: The resolution bias correction factor $c_R = 1/[1 - h(> max)]$ as a function of flux density.

model of the source count extrapolated to 60 μJy as a prediction of the source counts below the detection limit. They subsequently derive counts from this population and use the difference between the recovered population and input model to quantify the Eddington bias.

To correct for both Eddington bias and the detection efficiency as a function of flux density we followed the approach outlined in Ishwara-Chandra et al. (2020), which uses simulations to take into account the variation of the noise background of the mosaic image. The observed differential source counts can be related to the true source counts as

$$\frac{dN_o(s')}{ds'} = \int_0^\infty \frac{dN_t(s)}{ds}\,\epsilon(s)\,p(s,s')\,ds \tag{2.8}$$

Here $dN_o(s')/ds'$ is the observed count at observed flux densities s', and $dN_t(s)/ds$ is the true source count at the true flux s. The function $p(s,s')$ is the normalized probability density function that a source at observed flux s' is due to a source with true flux density s, and $\epsilon(s)$ is the probability that a source with true flux density, s, will result in a detection - the completeness of the source catalogue versus true flux density. We measured both function by inserting 3000 artificial point sources at a given true flux density at random positions into the residual map with the original sources removed. These sources populate the image with the same background noise and rms properties as the original source finding. The image was then searched for sources using the same parameters as for the real source list. Figure 2.7 shows the result for $\epsilon(s)$. The field of view effect dominates the curve in Figure 2.7 since the analysis is incorporating the varying sensitivity limit across the field of view due to the GMRT primary beam. The effect of Eddington bias is clearly seen in the fact that sources with true flux well below the detection threshold have significant probability to produce detections. The combined completeness and Eddington bias correction is derived by iteratively inverting Equation 2.8 to derive the correction factor that relates the true count to the observed count (see Ishwara-Chandra et al. 2020 for details).

2.3.5 The 610 MHz source counts

To compute the 610 MHz source counts, we used the integrated flux density if a source is classified as extended using the criteria described in Section 2.3.1. If a source is point-like, we instead use the peak flux density since this provides a better measure of the flux density of unresolved sources (Sirothia et al., 2009; Whittam et al., 2017) We compute the weight which take into account the efficiency ϵ(s), resolution bias,C_R, and Eddington bias C_{Edd} given by the equation below:

$$w = \frac{1}{\epsilon(s)} \times C_R \times C_{Edd}$$

Figure 2.9 illustrates the Euclidean-normalized differential source counts as derived from the catalogue discussed in this work (filled black points). The source counts are tabulated in Table 2.1. Uncertainties on the final normalized source counts are propagated from the errors on the reliability and resolution bias correction factors and the Poisson errors using the prescription of Gehrels (1986) on the raw counts per bin. We do not add uncertainties associated with the Eddington bias correction due to the computational expense of running the full required simulation. The bin sizes are in linear space and statistically independent. Each bin's upper limit is 1.34 times the lower limit. We note that for bins 75.264 - 100.854, 100.854-135.145 and 135.145-181.094 there are no sources in these bins hence the count is zero. Many studies have observed a flattening in the source counts below 1 mJy at 1.4 GHz (Windhorst 1984; Fomalont et al. 1984; Condon 1984). This flattening has been later observed also at other frequencies, including 610 MHz (Garn et al., 2008; Ibar et al., 2010; Whittam et al., 2017). This present work confirms this flattening $\sim$ 1 mJy down to at least 100 μJy (see Figure 2.9). Below 100 μJy our counts are probably less reliable, and we cannot entirely believe in the re-steepening we see. Our counts seems to be in better agreement with the later, but we caution that existing radio source count models are better constrained at higher frequency (1.4 GHz) and their extrapolation to much lower frequency heavily relies on the assumptions on the spectral index source distribution.

In this work we extend the number counts down to very faint 610 MHz flux densities whilst maintaining good agreement with simulations of previous studies at this frequency. Simulated counts by Massardi et al. (2010) are also shown in solid black curve in Figure 2.9. Mancuso et al. (2017) investigated the astrophysics of radio-emitting star-forming galaxies and active galactic nuclei (AGNs) and explained their statistical properties in the radio band including number counts. The dotted dashed black curve in Figure 2.9 show the Mancuso et al. (2017) models we compare to our work. The dashed green curve in Figure 2.9 shows the simulated 610 MHz counts from the Tiered Radio Extragalactic Continuum Simulation (T-RECS) by Bonaldi et al. (2019). This new simulation of the radio sky in continuum models two main populations of radio galaxies: Active Galactic Nuclei (AGNs) and Star-Forming Galaxies (SFGs), and corresponding sub-populations, over the 150 MHz - 20 GHz range.

TABLE 2.1: 610 MHz radio source counts within the ELAIS N1 1.864 deg^2 field, normalized to Euclidean geometry. We chose fixed (in linear space) bin sizes and non-overlapping (statistically independent) bins.

S_{range} (mJy) (1)	S_{width} (mJy) (2)	S_{mid} (mJy) (3)	Area (deg^2) (4)	C_{Edd} (5)	N (6)	Count ($Jy^{1.5}\ sr^{-1}$) (7)
0.067 - 0.090	0.023	0.078	0.667	3.041	559	$7.165^{+0.552}_{-0.538}$
0.090 - 0.120	0.030	0.105	1.009	1.981	612	$7.802^{+0.583}_{-0.571}$
0.120 - 0.161	0.041	0.141	1.313	1.326	670	$8.802^{+0.585}_{-0.572}$
0.161 - 0.216	0.055	0.189	1.546	1.148	566	$9.814^{+0.613}_{-0.596}$
0.216 - 0.289	0.073	0.253	1.705	1.032	447	$10.787^{+0.713}_{-0.686}$
0.289 - 0.388	0.098	0.339	1.783	1.016	316	$11.490^{+0.832}_{-0.796}$
0.388 - 0.520	0.132	0.454	1.807	0.926	234	$12.173^{+0.961}_{-0.909}$
0.520 - 0.696	0.177	0.608	1.818	0.987	150	$12.612^{+1.234}_{-1.141}$
0.696 - 0.933	0.237	0.815	1.831	1.105	90	$13.511^{+1.576}_{-1.426}$
0.933 - 1.251	0.317	1.092	1.840	1.000	68	$14.653^{+2.004}_{-1.767}$
1.251 - 1.676	0.425	1.463	1.846	1.000	49	$15.969^{+2.607}_{-2.281}$
1.676 - 2.246	0.570	1.961	1.848	1.000	32	$15.906^{+3.330}_{-2.784}$
2.246 - 3.009	0.764	2.627	1.854	1.000	31	$24.397^{+5.448}_{-4.582}$
3.009 - 4.032	1.023	3.521	1.859	1.000	31	$36.792^{+7.833}_{-6.539}$
4.032 - 5.403	1.371	4.718	1.864	1.000	16	$26.159^{+8.338}_{-6.539}$
5.403 - 7.240	1.837	6.322	1.864	1.000	13	$38.250^{+13.829}_{-10.592}$
7.240 - 9.702	2.462	8.471	1.864	1.000	14	$67.653^{+23.195}_{-17.879}$
9.702 - 13.001	3.299	11.351	1.864	1.000	14	$95.745^{+32.827}_{-25.304}$
13.001 - 17.421	4.420	15.211	1.864	1.000	10	$100.053^{+43.022}_{-31.017}$
17.421 - 23.344	5.923	20.382	1.864	1.000	8	$138.663^{+67.598}_{-48.532}$
23.344 - 31.281	7.937	27.312	1.864	1.000	8	$213.640^{+104.149}_{-74.774}$
31.281 - 41.916	10.635	36.598	1.864	1.000	4	$156.313^{+125.050}_{-74.249}$
41.916 - 56.168	14.251	49.042	1.864	1.000	4	$274.038^{+219.231}_{-130.168}$
56.168 - 75.264	19.097	65.716	1.864	1.000	2	$241.168^{+313.518}_{-156.759}$
75.264 - 100.854	25.590	88.059	-	-	-	-
100.854 - 135.145	34.290	118.000	-	-	-	-
135.145 - 181.094	45.949	158.119	-	-	-	-
181.094 - 242.666	61.572	211.880	1.864	1.000	1	$505.120^{+1161.775}_{-404.096}$
242.666 - 325.173	82.506	283.919	1.864	1.000	1	$685.387^{+1576.389}_{-548.309}$

[a] The listed counts were corrected for completeness and bias corrections (Resolution and Eddington Bias) (see text for details).

(1) the flux density bins.

(2) the width of the flux density bins.

(3) the central flux density of the bin.

(4) the effective area corresponding to the bin centre.

(5) the Eddington bias correction factor.

(6) the number of sources in each flux density bin.

(7) the corrected normalized source counts.

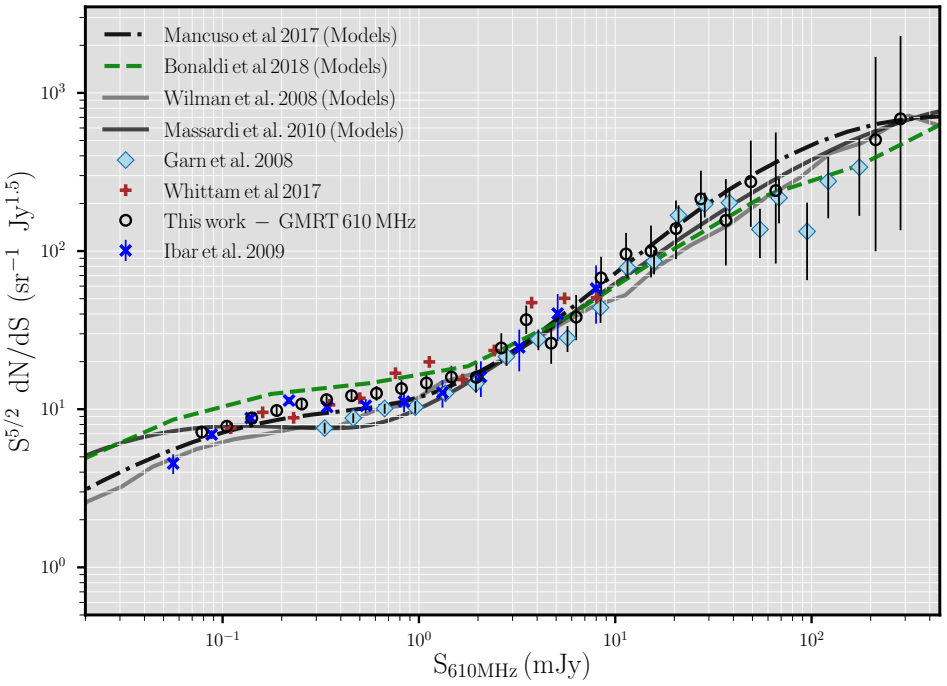

FIGURE 2.9: Normalized 610-MHz differential source counts as derived from the catalogue discussed in this work (black points). Vertical bars represent Poissonian errors on the normalized counts. We compare with results from previous observations at 610 MHz including: Garn et al. (2008) (filled blue diamonds), Ibar et al. (2009) (blue stars), Whittam et al. (2017) (brown pluses). We also compare against various models at 610 MHz including: Wilman et al. (2008) (solid grey curve), Massardi et al. (2010) (solid black curve), Mancuso et al. (2017) (dotted dashed black curve) and Bonaldi et al. (2019) (dashed green curve).

2.4 Multi-Wavelength Cross-Identification

2.4.1 Cross-matching

One advantage of the ELAIS N1 field is the wealth of multi-wavelength data publicly available in the field to study the properties of radio sources. Most of this public data has been homogeneized as part of the Spitzer Extragalactic Representative Volume Survey (SERVS) Data Fusion project* (Vaccari et al. 2010; Vaccari 2015) and of the The Herschel Extragalactic Legacy Project (Vaccari, 2016)†.

To determine their multi-wavelength counterparts, we first matched GMRT radio sources against the SERVS DR2 (Mauduit et al., 2012; Vaccari, 2015) positions using a variable search radius equal to three times the combined astrometric error. Where a SERVS match was not found, we used the UKIRT Infrared Deep Sky Survey (UKIDSS) Deep Extragalactic Survey (DXS) DR10Plus data release (Lawrence et al., 2007). Both the SERVS and UKIDSS catalogues were astrometrically calibrated against 2MASS, which

*http://www.mattiavaccari.net/df
†https://herschel.sussex.ac.uk

TABLE 2.2: Sample of the source catalogue of GMRT 610 MHz sources. The columns are described in the text.

ID	R.A	$\sigma_{R.A}$	Dec	σ_{Dec}	S_{int}	$\sigma_{S_{int}}$	S_{peak}	$\sigma_{S_{peak}}$	RMS	S_{code}	Type
	[deg]	[arcsec]	[deg]	[arcsec]	[mJy]	[mJy]	[mJy]	[mJy]	[mJy]		
(1)	(2)	(3)	(4)	(5)	(6)	(7)	(8)	(9)	(10)	(11)	(12)
1	243.801805	0.35	54.621228	0.36	0.2610	0.0555	0.2253	0.0290	0.0282	S	P
2	243.810522	0.04	54.993388	0.04	3.2388	0.0817	2.9474	0.0443	0.0435	S	E
3	243.797445	0.12	54.588408	0.10	0.7786	0.0478	0.6214	0.0237	0.0228	S	E
4	243.798035	0.40	54.594328	0.57	0.1594	0.0460	0.1432	0.0245	0.0242	S	P
5	243.802174	0.46	54.764238	0.74	0.2206	0.0654	0.1583	0.0298	0.0283	S	P
6	243.787447	0.18	54.310108	0.16	0.9742	0.0871	0.7077	0.0404	0.0383	S	E
7	243.801123	0.36	54.782338	0.30	0.1354	0.0379	0.1773	0.0260	0.0283	S	P
8	243.793715	0.34	54.539598	0.30	0.1761	0.0438	0.2095	0.0283	0.0297	S	P
9	243.808151	0.43	55.138628	0.64	0.7233	0.1393	0.3626	0.0488	0.0461	S	E
10	243.795284	0.46	54.718948	0.45	0.2611	0.0627	0.1945	0.0296	0.0280	S	P

The catalogue columns are:
(1) - GMRT 610 MHz Source ID.
(2) and (3) - flux-weighted right ascension (RA) and uncertainty.
(4) and (5) - flux-weighted declination (Dec.) and uncertainty.
(6-7) - integrated source flux density and uncertainty.
(8-9) - peak flux density and uncertainty.
(10) - the average background rms value of the island.
(11) - Code that defines the source structure. S - a single-Gaussian source that is the only source in the island. M - a multi-Gaussian source.
(12) - defines a source as extended (E) or point source (P).

provide a dense and accurate astrometric reference frame. Radio positional errors for individual sources from PyBDSF source finder (Mohan & Rafferty, 2015) are typically a few a tenths of an arcsecond. We computed the median astrometric offsets between the GMRT and SERVS catalogues to be $+0.539 \pm 0.420$ arcsec and -0.327 ± 0.422 arcsec in RA and DEC respectively from an initial cross-matching. We applied these corrections to the radio positions before performing a second cross-matching. We measured a median astrometric offsets for the second cross-matching to be $+0.055 \pm 0.447$ in RA and -0.026 ± 0.435 in DEC (see Figure A.3 in Appendix A). This correction was then applied to the radio positions for a final cross-matching. The radio positions within our final catalogue in Table 2.2 were corrected following this procedure are are thus ultimately also registered against 2MASS.

Virtually all cases where a match was found resulted in a unique identification, given the sub-arcsecond accuracy of the positions. For all GMRT sources with a match in SERVS/UKIDSS we determined multi-wavelength properties using the SERVS Data Fusion workflow, i.e. matching all ancillary catalogues with a search radius of 1 arcsec against the SERVS/UKIDSS position. This ancillary data include IRAC1234 and MIPS 24 μm photometry from SWIRE (Lonsdale et al., 2003), PACS and SPIRE photometry from HerMES (Oliver et al., 2012) and redshift information. Table 2.2 shows a sample of ten rows and a few selected columns from the curated catalogue with multi-wavelength properties, which is available electronically in its entirety.

TABLE 2.3: GMRT cross-matching statistics.

Category	Size	Fraction (%)
GMRT	4290	100%
Matched	3689	92%
SERVS	3689	86%
UKIDSS	3542	83%
SWIRE IRAC1234	1623	43%
MIPS 24 μm	2714	63%
X-RAY	149	3%
SPEC-Z[a]	834	19%
PHOTZ-HSC[b]	2885	67%
PHOTZ-SWIRE[c]	907	21%
PHOTZ-HELP[d]	1834	43%
REDSHIFT[e]	3105	72%
CLASS [f]	3490	81%
REDSHIFT & CLASS[g]	2304	54%

[a] spectroscopic redshifts
[b] Hyper Suprime-Cam (HSC) Photometric Redshift Catalogue (Tanaka et al., 2018a).
[c] SWIRE Revised Photometric Redshift Catalogue (Rowan-Robinson et al., 2008, 2013).
[d] HELP Photometric Redshift Catalogue (Duncan et al., 2018)
[e] The union of SPECZ, PHOTOZ-HSC, PHOTOZ-SWIRE and PHOTOZ-HELP.
[f] All sources with at least one multi-wavelength classification diagnostic.
[g] All sources with at least one multi-wavelength classification diagnostic and redshift association.

Table 2.3 summarizes the multi-wavelength and redshift information available for the cross-matched GMRT sources, included in the SERVS Data Fusion catalogue. Accounting for multiple sources the final number of our GMRT 610 MHz sources is 4290. The redshift information is discussed in more detail in the following section.

2.4.2 Redshifts

We have combined the spectroscopic redshift compilations from the Spitzer Data Fusion[‡] and HELP[§] projects to collect spectroscopic redshifts. The majority of the spectroscopic redshifts for our sample were obtained with the Baryon Oscillation Spectroscopic Survey (BOSS) (Eisenstein et al., 2011). This is supplemented by a small number of redshifts available from the literature and from SWIRE/HerMES spectroscopic follow-up programmes. For sources where a spectroscopic redshift was not available, we

[‡] http://mattiavaccari.net/df/specz
[§] http://hedam.lam.fr/HELP/dataproducts/dmu23/

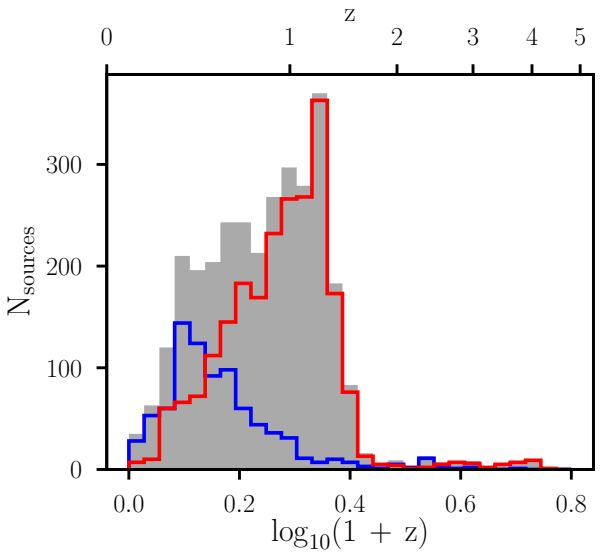

FIGURE 2.10: Redshift distribution for the GMRT 610 MHz sources. The grey histogram represents all the redshifts (i.e. both spectroscopic and photometric redshifts). The blue and red histograms represents spectroscopic and photometric redshifts respectively.

use photometric redshift estimates from the Hyper Suprime-Cam (HSC) project (Tanaka et al., 2018a), the SWIRE project (Rowan-Robinson et al., 2008, 2013) and the HELP project (Duncan et al., 2018).

The redshift distribution is shown in Figure 2.10 with the blue histogram representing spectroscopic redshifts and red histogram for photometric redshifts. We estimate the precision of the photometric redshifts using the normalized median absolute deviation (i.e. $\sigma_{\rm NMAD}$) (Hoaglin, 2003) given by $1.48 \times \text{median}(|\Delta z|)/(1 + z_{\rm spec})$. The second metric we estimate is the outlier fraction, O_f, defined as $|\Delta z|/(1 + z_{\rm spec}) > 0.2$ (see Brammer et al. 2008; Dahlen et al. 2013; Laigle et al. 2016; Duncan et al. 2018). We use these metrics to explore the performance of the photometric redshift estimates relative to the measured spectroscopic redshift. Figure 2.11 (upper panel) compares the photometric and spectroscopic redshift for different bins of $i_{\rm AB}$ magnitude for the GMRT sample. The bottom panel of Figure 2.11 presents $(z_{\rm phot} - z_{\rm spec})/(1 + z_{\rm spec})$ as a function of $z_{\rm spec}$. The horizontal line in indicates where $(z_{\rm phot} - z_{\rm spec})/(1 + z_{\rm spec}) = 0$. This plot clearly shows that the fraction of outliers increases significantly towards higher values of $z_{\rm spec}$ as a function of $i_{\rm AB}$ magnitude. The fraction of catastrophic failures varies from 3 to 9% and the scatter, NMAD is nearly constant with an average value of NMAD = 0.049 for the entire spectroscopic sample. The scatter does increase above $z_{\rm spec} > 1.5$, where $\sigma_{\rm NMAD} = 0.075$. Systematic deviations from the $z_{\rm phot} = z_{\rm spec}$ line are very small at most redshifts, with the exception that $z_{\rm phot}$ underestimates $z_{\rm spec}$ at $z = 1.0 - 1.4$ by $\sim 5\%$.

2.4.3 AGN/SFG Diagnostics Overview

Following Ocran et al. (2017), we have carried out a multi-wavelength study using optical, X-ray, infrared and radio diagnostics to search for evidence of AGN-driven activity in our sample. The total number of

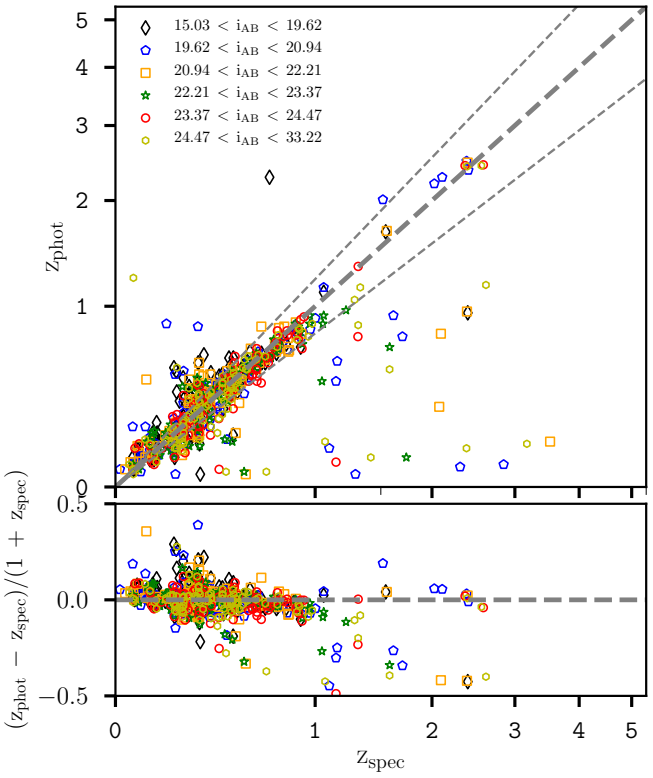

FIGURE 2.11: Comparison between photometric and spectroscopic redshifts as a function of i_{AB} magnitude in top panel. The dashed grey line corresponds to $z_{spec} = z_{phot}$. The double dashed lines show $z_{phot} = z_{spec} \pm 0.2(1 + z_{spec})$. The lower panel show $(z_{phot} - z_{spec})/(1 + z_{spec})$ vs z_{spec} as a function of i_{AB} magnitude.

TABLE 2.4: Photometric Redshift Performance for GMRT radio sources as a function of i_{AB} optical magnitude.

i_{AB}	$\sigma_{\rm NMAD}$	O_f
[15.03, 19.62]	0.054	0.075
[19.62, 20.94]	0.047	0.017
[20.94, 22.21]	0.063	0.121
[22.21, 23.37]	0.044	0.035
[23.37, 24.47]	0.052	0.070
[24.47, 33.22]	0.035	0.098

sources with redshifts for which we can define at least one AGN indicator is 2305 (i.e. $\sim$ 54% of the whole sample and $\sim$ 74% of the subsample with redshifts). The AGN diagnostics we employed are described below:

1. Radio power: we classify sources as RL AGNs based on a radio luminosity cut of $L_{1.4\,\rm GHz} \geq 10^{25}$ W Hz^{-1} (e.g. Sajina et al. 2007; Jiang et al. 2007; Sajina et al. 2008). We converted the 610 MHz radio flux densities to rest-frame 1.4 GHz effective luminosities assuming a radio spectral index of $\alpha = -0.8$ (i.e. $S(\nu) \propto \nu^{\alpha}$) (Ibar et al., 2010). [¶]

[¶] $L_{1.4\,\rm GHz} = 4\pi d_{\rm lum}^2 \frac{S_{1.4\,\rm GHz}}{(1+z)^{1+\alpha}}$, where $S_{1.4\,\rm GHz} = \left(\frac{1.4}{0.61}\right)^{\alpha} S_{0.6\,\rm GHz}$

2. Mid-Infrared to radio flux ratio: following the Bonzini et al. (2013), we compute $q_{24\mu m}$ for the radio sources with MIPS 24μm detections and redshifts. This is then compared to the redshifted $q_{24\mu m}$ value for the M82 local standard starburst galaxy template. If $q_{24\mu m}$ is lower than the one expected for M82 (i.e. below -2σ, $\sigma = 0.35$ average spread for local sources by Sargent et al. (2010b)), the sources are considered as a RL AGN.

3. X-ray luminosity: we classify a source as an AGN when $L_x > 10^{42}$ erg s^{-1} following e.g. Szokoly et al. (2004). ‖

4. BOSS AGN spectroscopic classification: we use the BOSS CLASS and SUBCLASS parameters, as detailed by Bolton et al. (2012), to classify the GMRT sources with BOSS identifications. The breakdown of the BOSS CLASS and SUBCLASS parameters is outlined in Ocran et al. (2017).

5. IRAC colours: we use the IRAC four-band colour-colour AGN diagnostic proposed by Donley et al. (2012)

$$x = \log_{10}\left(\frac{f_{5.8\mu m}}{f_{3.6\mu m}}\right), \quad y = \log_{10}\left(\frac{f_{8.0\mu m}}{f_{4.5\mu m}}\right) \tag{2.9}$$

$$\begin{aligned} x \geq 0.08 \wedge y \geq 0.15 \\ \wedge\, y \geq (1.21 \times x) - 0.27 \\ \wedge\, y \leq (1.21 \times x) + 0.27 \\ \wedge\, f_{4.5\mu m} > f_{3.6\mu m} > f_{4.5\mu m} \wedge f_{8.0\mu m} > f_{5.8\mu m} \end{aligned} \tag{2.10}$$

Using these AGN/SFG indicators, we classify the 610 MHz sources as follows:

1. RL AGN: these are sources with redshift information and $L_{1.4\,\mathrm{GHz}} > 10^{25}$ W Hz^{-1} or $q_{24\mu m}$ below the M82 locus.

2. RQ AGN: sources with redshifts and above the M82 locus threshold for selecting RL AGN. Furthermore, these sources are classified as AGN by at least one of the AGN diagnostics listed above.

3. SFG: these are sources with redshifts that do not show evidence of AGN activity in any of the diagnostics.

4. Unknown: these sources include those that are unmatched to SERVS IRAC12 positions, sources with no redshift and sources with redshift but no information on the parameters needed for the AGN classification.

‖ $L_x = 4\pi S_x d_L^2 (1+z)^{2-\gamma}$, where we fixed the the photon-index to the commonly observed value of $\gamma = 1.8$ (Dadina, 2008; Vito et al., 2014).

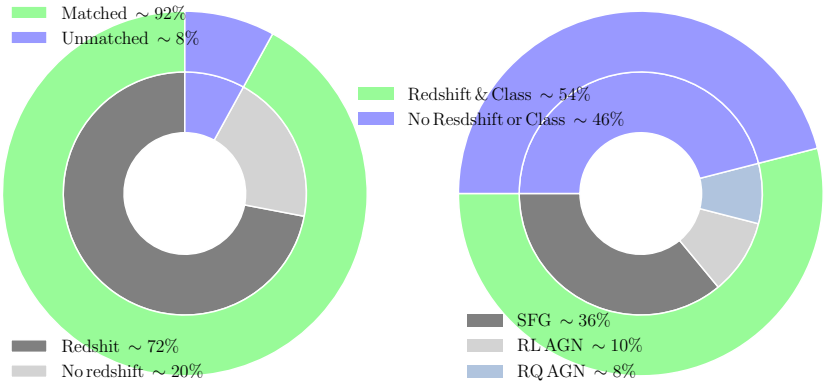

FIGURE 2.12: Left: Nested donut chart with two groups illustrating the GMRT sample that is matched (92%, green) and unmatched (8%, violet) to SERVS/UKIDSS positions. The three subgroups represents the GMRT sample with redshift (72%, dark grey), no redshift (20%,light grey) and the unmatched (8%, violet). Right: Nested donut chart with two groups illustrating the GMRT sample with redshift and at least one AGN indicator (54%, green), redshift and no AGN indicator (46%, violet). The four subgroups represents the fraction classified as SFG (36%, dark grey), RL AGN (10%,light grey), RQ AGN (8%, violet) and redshift and no AGN indicator (46%, violet).

TABLE 2.5: Total number of SFGs, RQ AGN and RL AGN from the selection criteria.

Class	Number	Fraction (%) (Sub-Sample with Redshift and Class)	Fraction (%) (Full Sample)
SFG	1685	73%	39%
RQ AGN	281	12%	7%
RL AGN	339	15%	8%
No Redshift or Class	1986	-	46%

The top panel of Figure 2.12 shows a nested donut chart with two groups illustrating the GMRT sources matched (92%, lime) and unmatched (8%, violet) to SERVS/UKIDSS positions. The three subgroups represents the GMRT sources with redshift (72%, dark grey), no redshift (20%,light grey) and unmatched (8% ,violet). The bottom panel represents a nested donut chart with two groups illustrating the GMRT sources with redshift and AGN classification possible for at least one AGN diagnostics (54%, green), redshift but no AGN classification possible (46%, violet). The four subgroups represents the fraction classified as SFG (36%, dark grey), RL AGN (10%, light grey), RQ AGN (8%, violet) and redshift and no AGN classification possible (46%, violet).

The substantial number of objects in our sample allows us to study how the faint radio source population changes with flux density. The left panel of Figure 2.13 shows the fraction of objects in each class in our sample as a function of limiting flux density. For a given flux density, $S_{610\,\mathrm{MHz}}$, the plot shows the fraction of objects that are classified as SFG, RL AGN, and RQ AGN in the sample of objects above that flux density. The green curves show the fraction for the total AGN population. The curves highlight the dramatic change in population over this flux density range. The SFG fraction exhibits a monotonic increase with decreasing flux density from $\sim$ 10% to 72%. RL AGNs decrease rapidly from being the dominant population above $\sim$ 1 mJy to the smallest fraction below $\sim$ 0.3 mJy. The fraction of RQ AGNs remains

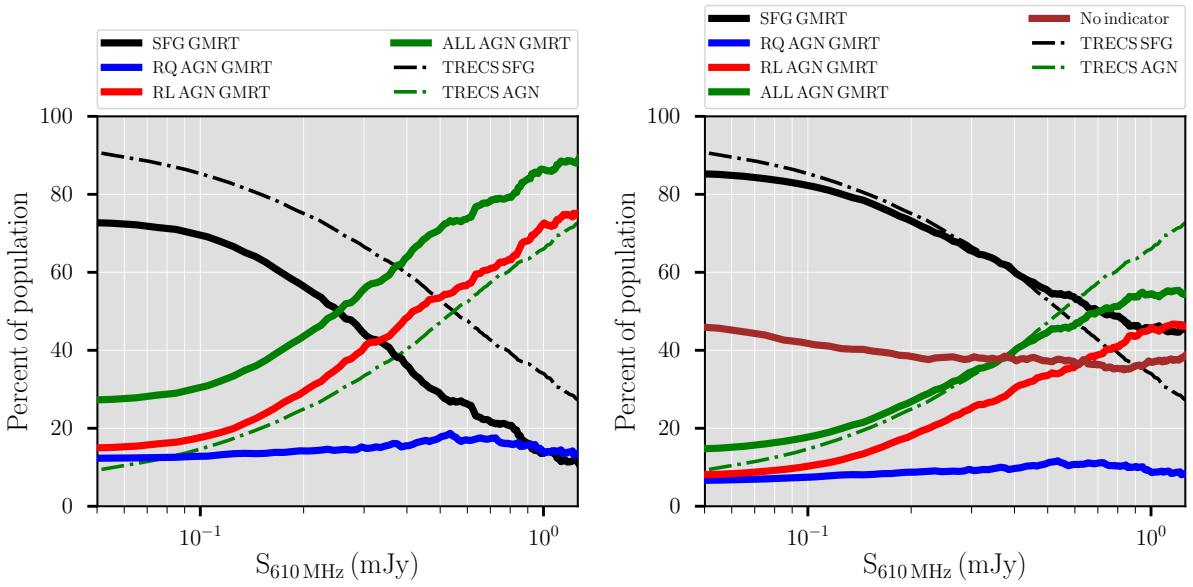

FIGURE 2.13: The relative fraction of AGNs and SFGs as a function of minimum flux density. The solid lines show the fraction of the sample with a flux density greater than $S_{610\,\mathrm{MHz}}$ which is classified as RQ AGN (blue), RL AGN (red), all AGN (green) and SFG (black). The dashed dotted green and black lines in both panels represents the relative fraction of AGN and SFG predicted by T-RECS (Bonaldi et al., 2019). The left panel compares the relative fraction of AGNs and SFGs for our classified sources only. The brown solid line in the right panel shows the relative fraction for sources with redshift but no multi-wavelength diagnostic classification. This is added to the classified SFGs fraction in the right panel

.

roughly constant with flux density just above ∼ 10%. Above ∼ 0.7 mJy, the fraction of RQ AGNs is higher than that of SFGs. Padovani et al. (2015) identied 626 radio sources with redshifts and classified 55%, 25% and 20% as SFGs, RQ AGNs and RL AGNs respectively from a deep 1.4 GHz sample reaching a 32.5 μJy flux limit over 0.29 deg^2 of the ECDFS VLA image. They further confirmed the main results of Padovani et al. (2011) that AGNs dominate at large flux densities ($\gtrsim$ 1 mJy) but SFGs become the dominant population below ≈ 0.1 mJy. Bonzini et al. (2013) reported that SFGs represent 57 ± 3% of the sub-millijansky sample, are missing at high flux densities but become the dominant population below ≈ 0.1 mJy, reaching 61% at the survey limit. Radio-quiet AGNs represent 26 ± 6% (or 60% of all AGNs) of sub-millijansky sources but their fraction appears to increase at lower flux densities, where they make up 73% of all AGN and ≈ 30 % of all sources at the survey limit, up from ≈ 6% at ≈ 1 mJy. These results from previous observations are in good agreement with what we report. The fact that we find more SFGs at faint flux densities can be attributed to our survey going deeper than previous surveys. We compare our results to the relative fraction of AGN and SFG computed for T-RECS by Bonaldi et al. (2019), specifically run using a prescription that satisfies the depth and area coverage of our observations (see dashed dotted green and black lines in both panels of Figure 2.13) and find that the fraction of our classified sources do not agree with T-RECS. When we add the fraction of sources that have no classification to the SFGs fraction, we see that below ∼ 0.6 mJy our computed AGN and SFGs fraction agrees well with T-RECS (see the right panel in Figure 2.13). Table 2.5 presents the total number of AGNs (including RL and RQ AGNs) and SFGs with respect to sources with redshifts and AGN classification possible as well as the full

GMRT sample.

2.5 Multi-Frequency Radio Spectral Indices

Radio spectral energy distributions (SEDs) provide useful information that can be used to differentiate between sources types according to their dominant emission mechanisms (Marsden et al., 2014). We computed the spectral index between 325 - 610 MHz, 610 - 1400 MHz and 610 - 5000 MHz for our ELAIS N1 sample using the GMRT 325 MHz deep survey by Sirothia et al. (2009), the Faint Images of the Radio Sky at Twenty Centimeters (FIRST) 1400 MHz survey (Becker et al., 1995) and the JVLA 5000 MHz Ultra Deep Survey by Taylor et al. (2014). Since the images mentioned above have different resolutions (see Table 2.6), special care must be taken when we analyse results based on different frequency-selected samples.

From the commonly used simple power law model, a negative α is indicative of sources dominated by synchrotron emission, such as radio galaxies. An $\alpha \sim 0$ may indicate either a star-forming galaxy dominated by free-free emission optically thin or optically thick synchrotron emission in core-dominated AGNs. Inverted $\alpha > 0$ spectra in the GHz regime can be associated to very young compact sources (Gigahertz Peaked Sources, GPS) or to Advection-Dominated Accretion Flow (ADAF) sources (see e.g. Narayan & Yi 1994). Thus, radio spectra are useful in unveiling the physical processes in radio sources (Prandoni et al., 2010; Argo et al., 2013).

2.5.1 Radio Spectral Index vs Flux Analysis

We investigate the spectral index properties of 610 MHz low-frequency selected sources. We estimated the median and the error on the median using the median absolute deviation estimator as this is a more robust measure of the variability of a univariate sample of quantitative data than the standard deviation (Rousseeuw & Croux, 1993). Table 2.6 summarizes the number of matches between the 610 MHz catalogue and the samples at other frequency. Figure 2.14 shows the 610 - 325 MHz, 610 - 1400 MHz and 610 - 5000 MHz colour-flux diagrams. The distribution of the spectral index between each frequency pair is shown as blue histogram in each panel. For the top panel of Figure 2.14, we note that only 479 of our GMRT 610 MHz sources have a counterpart at 325 MHz, therefore, α_{325}^{610} estimates are available only for 13 per cent of our radio-detected sources at 610 MHz. We find that α_{325}^{610} estimates range from -2.7 to 1.8 with a median value of -0.80 ± 0.29. Sirothia et al. (2009) reported a median spectral index between α_{325}^{610} to be 1.28 from 325 MHz studies of ELAIS N1 using the GMRT. They attributed their median value to an extra contribution of exceedingly steep diffuse emission being detected at the lower frequency. In the middle panel, only 99/4290 ($\sim 2.3\%$) of our 610 MHz detected sources have counterparts at 1.4 GHz. The α_{1400}^{610} estimates range from -2.5 to 1.1 with a median value of -0.83 ± 0.31. The bottom panel has the second highest number of sources since the JVLA 5000 MHz Deep only covers an area of 0.12 deg^2

TABLE 2.6: The radio surveys that were used to form the multi-frequency samples through cross-matching with the 610 MHz catalogue.

Survey	Frequency (MHz)	Resolution (arcsec)	Area covered (deg^2)	rms (μJy)	Number of Sources	Number of matches
ELAIS N1 GMRT Deep	325	10	1.5	70	901	479
VLA FIRST (All Sky)	1400	5	10575	150	946,000	99
ELAIS N1 JVLA Deep	5000	2.5	0.12	1	387	204

(see Table 2.6) and this is only a small region of the 610 MHz image. Only 204/4290 ($\sim 4.8\%$) of our 610 MHz sources have counterparts at 5 GHz with a median value of -1.12 ± 0.15.

At the lowest fluxes we are only sensitive to increasingly steeper (top and middle panels) or flatter sources (bottom panel), hence the median values that we derive can be biased and unreliable. We therefore restrict our statistical analyses to a much brighter sub-sample and measure the median spectral index, where the red lines (see Figure 2.14) are not biasing too much the median spectral indices. We find that the median spectral index for α_{325}^{610} for a flux range corresponding to $S_{610\,\mathrm{MHz}} > 0.5$ mJy represented by the vertical black dash line in the top panel of Figure 2.14 is -0.71 ± 0.27 (see the horizontal blue solid line). In the middle panel, we measure a median spectral index for α_{1400}^{610} over a flux range corresponding to $S_{610\,\mathrm{MHz}} > 1.9$ mJy to be -0.89 ± 0.28 (see the horizontal blue solid line). For the bottom panel, we measure a median spectral index for α_{5000}^{610} over a flux range corresponding to $S_{610\,\mathrm{MHz}} > 0.15$ mJy to be -1.23 ± 0.12 represented by the horizontal blue solid line.

The median spectral index α_{325}^{610} as a function of flux densities > 0.5 mJy is found to be approximately -0.71 from the original -0.80. This can be attributed to the fact that above the imposed flux density limit, most of the sources we select are AGNs and thus increases the median spectral index we measure. The median spectral index α_{1400}^{610} is found to be approximately -0.83 to -0.89, based on an almost unbiased sources with flux densities > 1.9 mJy. Statistical analyses of Ibar et al. (2009) showed no clear evolution for the median spectral index, α_{1400}^{610}, as a function of flux density and that α_{1400}^{610} was found to be approximately -0.6 to -0.7 based on an almost unbiased 10σ criterion, down to a flux level of $S_{1.4\mathrm{GHz}} \gtrsim 100\,\mu$Jy. Katgert & Spinrad (1974) found from a small sample of sources with $S_{610\mathrm{MHz}} \gtrsim 10$mJy a spectral index distribution of $\alpha_{1400}^{610} = -0.52 \pm 0.39$ using the Westerbork Synthesis Radio Telescope (WSRT). With respect to higher frequency surveys with a broad distribution, this was an unusual result. However, Katgert (1979) using a much larger sample presented similar result of $\alpha_{1400}^{610} = -0.68 \pm 0.31$. A detailed spectral index analysis using the other available radio data and adding the upper/lower limits for each source to get reliable estimates of median spectral indices through survival analysis is deferred to later works.

For the remaining 419/901 ($\sim$ 47 per cent, for 325 MHz), 688/818 ($\sim$ 84 per cent, for 1400 MHz), 170/330 ($\sim$ 52 per cent, for 5000 MHz) detected with no counterparts in the GMRT 610 MHz we derive the nominal detection limit in 325, 1400 and 5000 MHz (see Table 2.6) respectively represented by the solid red line in each panel.

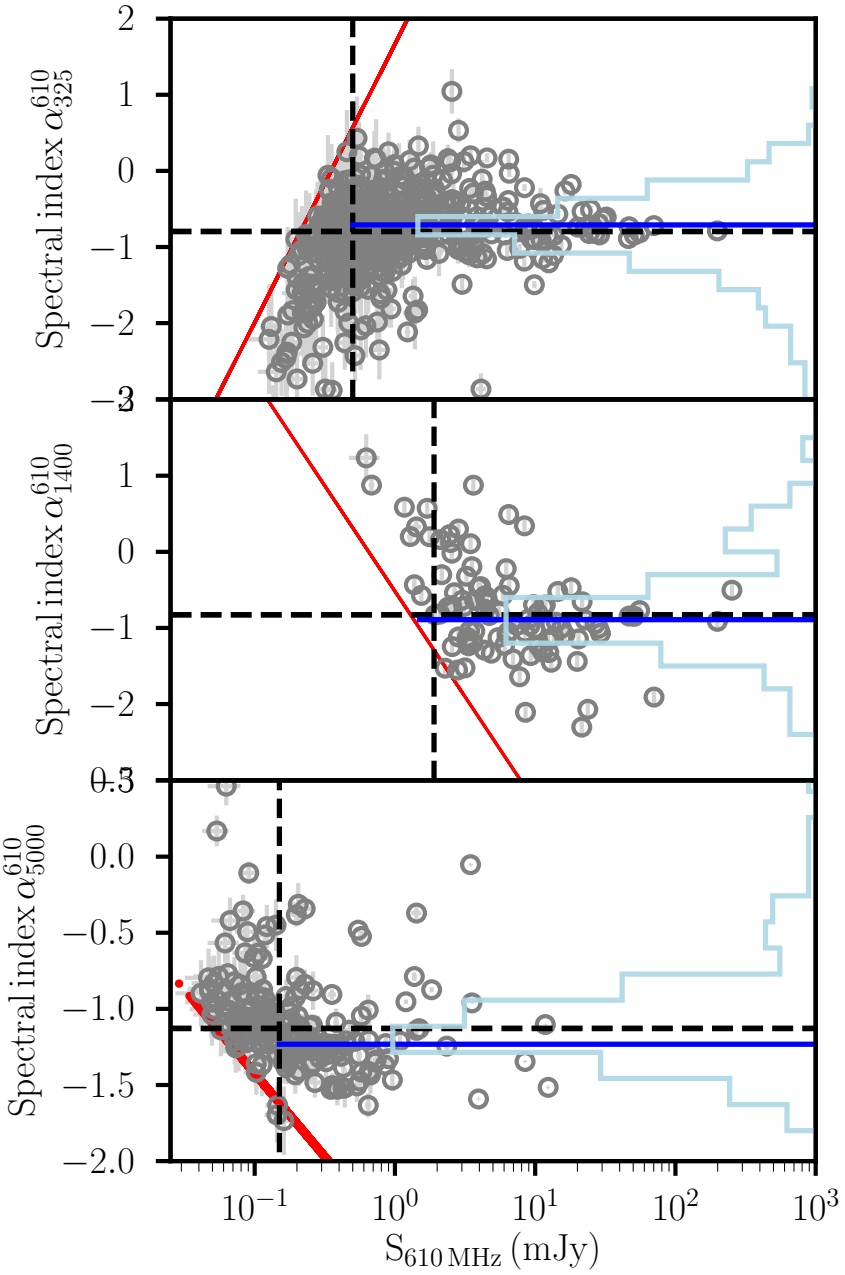

FIGURE 2.14: colour-flux diagrams comparing the 325-610 MHz (top), 1400- 610 MHz (middle), and 5000-610 MHz (bottom) spectral indices for ELAIS N1 GMRT Deep 610 MHz cross-identified sources. The solid red sloping line in each panel marks the flux density traced by the nominal detection limit of 325, 1400 and 5000 MHz respectively(see Table 2.6). The distribution of the spectral index between each frequency is shown as blue histogram in each panel. The dashed vertical lines in each panel represents the flux limit we impose when restricting our statistical analyses to a much brighter sub-sample. The blue horizontal lines in each panel represents the median spectral indices we measure for sources above the imposed flux limits.

2.5.2 Radio colour-colour plot

Figure 2.15 shows radio colour - colour plots for the ELAIS N1 GMRT 610MHz Deep sample. The spectral indices of the sample between 325 and 610 MHz against the spectral indices between 1400 and 610 MHz (i.e using the spectral indices measure in the middle panel of Figure 2.14) is shown in the left panel. The right panel show the spectral indices of the sample between 325 and 610 MHz against the spectral indices between 5000 and 610 MHz. We divide the radio colour-colour plot into four quadrants.

1. Steep and flat spectrum sources: where(α_{1400}^{610} | $\alpha_{5000}^{610} \leq 0$ & $\alpha_{325}^{610} \leq 0$)
2. Peaked spectrum sources: where (α_{1400}^{610} | $\alpha_{5000}^{610} \leq 0$ & $\alpha_{325}^{610} > 0$)
3. Inverted spectrum sources: where (α_{1400}^{610} | $\alpha_{5000}^{610} > 0$ & $\alpha_{325}^{610} > 0$)
4. Upturn spectrum sources (α_{1400}^{610} | $\alpha_{5000}^{610} > 0$ & $\alpha_{325}^{610} \leq 0$)

It is evident that the majority of our GMRT 610 MHz sources lie in the steep and flat spectrum quadrant in both panels. Moreover, the scatter around the diagonal line is asymmetric for the first panel (i.e α_{1400}^{610} vs α_{325}^{610}) of Figure 2.15 with relatively more number of sources lying below the lower left side of the diagonal line (i.e at $\alpha_{1400}^{610} < \alpha_{325}^{610}$), indicating a steepening of the spectrum at higher frequencies (despite the fact the α_{1400}^{610} MHz sample is biased towards flat spectrum sources). This is consistent with the RL AGN classification of most such sources.

The right panel show a slight scatter around the diagonal. It is interesting to note that sources lying below the diagonal line (i.e. $\alpha_{325}^{610} < \alpha_{5000}^{610}$) are mostly SFGs or RQ AGNs. This sample has more SFGs as it is created from the deep, narrow 5000 MHz survey (see Table 2.6). In the first case the flattening of the spectrum going at higher frequency may be due to an increase of the free-free emission contribution at high frequency; in the case of RQ AGN the flattening may be due to the emergence of core-dominated emission.

2.5.3 SFG and AGN spectral indices

The distribution of the spectral index between α_{325}^{610} and α_{1400}^{610} for SFG and AGN is shown as black and green histograms in Figure 2.16. The distribution for α_{325}^{610} is computed over a flux range corresponding to $S_{610\,\mathrm{MHz}} > 0.5$ mJy and that of α_{1400}^{610} is computed over a flux range corresponding to $S_{610\,\mathrm{MHz}} > 1.5$ mJy respectively. From Figure 2.16, the median and median absolute deviation (MAD) computed over $S_{610\,\mathrm{MHz}} > 0.5$ mJy is $\langle\alpha_{325}^{610}\rangle = -0.81 \pm 0.23$ for SFGs and $\langle\alpha_{325}^{610}\rangle = -0.69 \pm 0.22$ for AGNs. RL and RQ AGNs have a median and MAD of $\langle\alpha_{325}^{610}\rangle = -0.67 \pm 0.27$ and $\langle\alpha_{325}^{610}\rangle = -0.71 \pm 0.22$ respectively.

We computed $\langle\alpha_{1400}^{610}\rangle = -0.81 \pm 0.26$ over $S_{610\,\mathrm{MHz}} > 1.9$ mJy for AGNs (see bottom panel of Figure 2.16). In addition, RL and RQ AGNs have a median and MAD of $\langle\alpha_{1400}^{610}\rangle = -0.89 \pm 0.28$ and

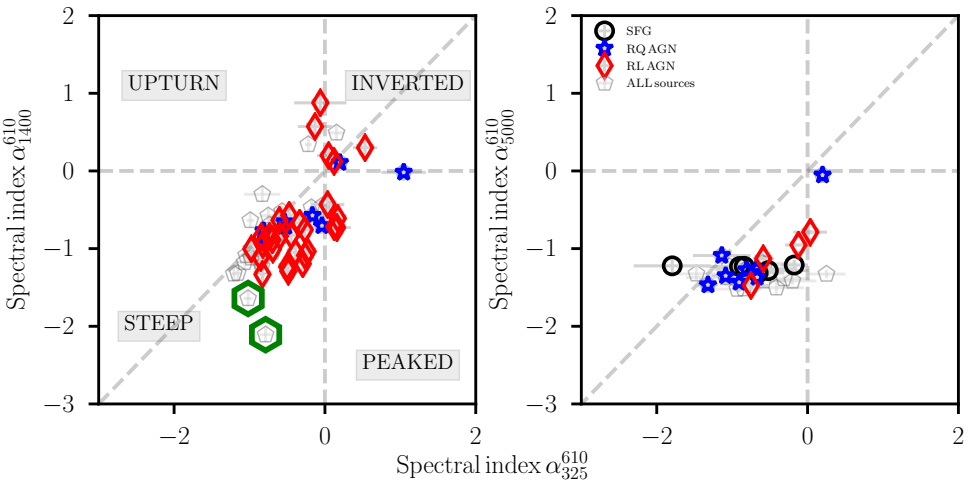

FIGURE 2.15: Radio colour - colour plots for sources the ELAIS N1 GMRT 610MHz Deep sample. Left: the spectral indices of the sample between 325 and 610 MHz against the spectral indices between 1400 and 610 MHz. Right: the spectral indices of the sample between 325 and 610 MHz against the spectral indices between 5000 and 610 MHz. SFG, RQ AGN, RL AGN and all sources indicator are represented with black, red, blue and dimgrey colours respectively. The green hexagon in the left panel shows ultra very steep sources (i.e. α^{610}_{1400} < -1.5).

$\langle\alpha^{610}_{1400}\rangle = -0.68 \pm 0.10$ respectively. The number of SFGs having α^{610}_{1400} associations is only one and not included in this analysis. Table 2.7 shows the breakdown of the number of SFGs, RL AGN, RQ AGN and sources with no classification that have a spectral index.

2.5.4 Ultra steep spectrum sources

Ultra steep spectrum sources (USS) radio sources are often associated with radio galaxies at high redshift (HzRGs z $>$ 2) (e.g. see Blumenthal & Miley 1979; Miley & De Breuck 2008). HzRGs are located in overdense regions in the early Universe and are frequently surrounded by protoclusters (Roettgering et al. 1996; Pascarelle et al. 1996; Knopp & Chambers 1997). Studies have shown USS are good candidates for high redshift radio galaxies (Riseley et al., 2016) which are among the most luminous and massive galaxies (e.g. Reuland et al. 2004; Bornancini et al. 2007; Singh et al. 2014) and are believed to be progenitors of the massive elliptical galaxies in the local Universe. Their extremely steep spectrum is generally attributed to radiation losses of relativistic electrons in the radio lobes, meaning they are most luminous at lower radio frequencies (Mahony et al., 2016).

In the literature, USS radio sources are commonly defined as those with spectral index values $\alpha < -1.3$ (Argo et al. (2013)). We selected sources that had spectral indices between 610 MHz and 1.4 GHz steeper than $\alpha^{610}_{1400} = -1.2$. Using this criterion, we find two sources with ultra-steep spectra in the GMRT 610 MHz sample. The 610 - 325 MHz spectral index for the first USS candidate (i.e source with GMRT ID 713) is $\alpha^{610}_{325} = -1.01$ whereas the 610 - 1400 MHz spectral index is $\alpha^{610}_{1400} = -1.65$. The second USS candidate (i.e source with GMRT ID 2388) has a 610 - 325 MHz spectral index of $\alpha^{610}_{325} = -0.79$ and a 610 - 1400 MHz spectral index of $\alpha^{610}_{1400} = -2.10$. This source is at the detection of threshold of the NRAO

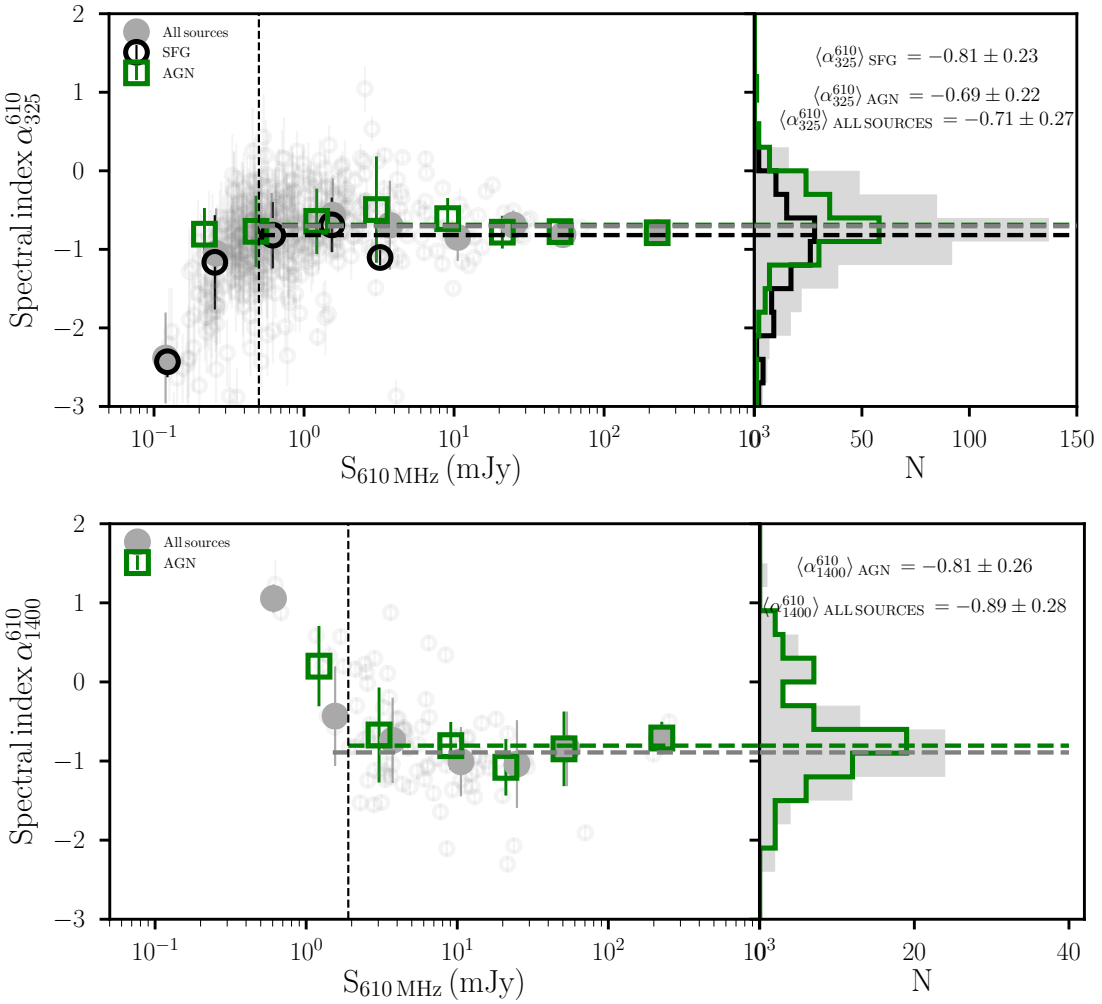

FIGURE 2.16: Top panel: The distribution for α^{610}_{325} is computed over a flux range corresponding to $S_{610\,\rm MHz}$ > 0.5 mJy. The filled grey circles, open black circles and open green squares represents all sources, SFGs and AGNs respectively in logarithmic bins of 0.4. Bottom panel: The distribution for α^{610}_{1400} is computed over a flux range corresponding to $S_{610\,\rm MHz}$ > 1.9 mJy. The filled grey circles and open green squares represents all sources and AGNs respectively in logarithmic bins of 0.4. The number of SFGs having α^{610}_{1400} associations is only one and not included in the plot.

VLA Sky Survey (NVSS) (Condon et al., 1998) and has flux density of 2.1±0.4 mJy at 1.4 GHz. If we use this flux, then 610 - 1400 MHz spectral index is $\alpha^{610}_{1400} = -1.6$.

Both candidate USS sources do not have redshift associations in our catalogue, hence these sources are more likely to be HzRGs.

Figure 2.17 shows the flux density as a function of frequency for the two very steep spectrum sources identified in Figure 2.15, the two-point spectral index values are also printed on the Figure. Postage stamp images of these sources are presented in Figure 2.18.

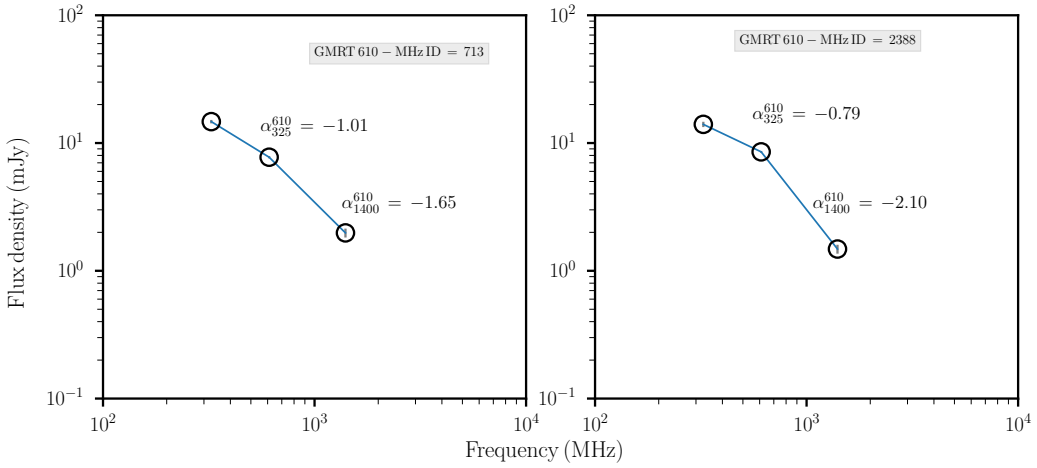

FIGURE 2.17: Flux density as a function of frequency for the two ultra steep spectrum sources identified in Figure 2.15. The radio SED for the two USS is from 325 MHz to 1400 MHz. Also shown are the spectral indices measured between data available for this source at various radio frequencies.

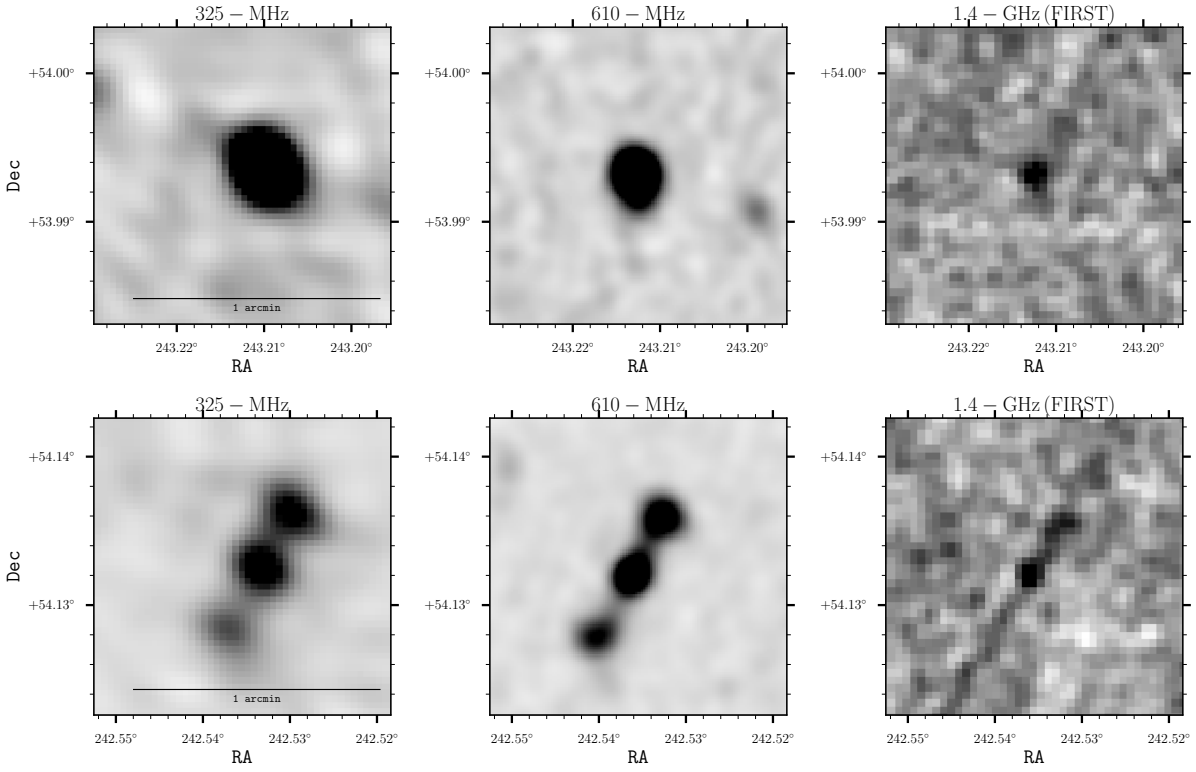

FIGURE 2.18: Candidate USS radio sources at three different frequencies from 325 MHz , 610 MHz and 1.4 GHz (FIRST) respectively for the two sources.

TABLE 2.7: Number of SFGs, RL AGN, RQ AGN and sources with no classification that have a spectral index.

α	SFG	RL AGN	RQ AGN	No classification
α^{610}_{325}	122	125	48	184
α^{610}_{1400}	1	53	10	35
α^{610}_{5000}	73	12	23	96

2.6 Summary and Conclusions

We report deep 610 MHz GMRT observations of the ELAIS N1 field, a region of 1.864 $\deg^2$. We achieve a nominal sensitivity of 7.1 μ Jy beam^{-1}. From our 610 MHz mosaic image, we recover 4290 sources after accounting for multiple component sources down to a 5σ flux density limit of 35.5 μ Jy.

From this data, we derive the 610 MHz source counts applying corrections for completeness, resolution bias and Eddington bias. The counts are within the scatter of most previous source counts from other surveys at 610 MHz and with extrapolated models of the low-frequency source population; the most obvious exception is the Wilman et al. (2008) source counts. The counts show a flattening below $\sim$ 1 mJy as a result of the increasing contribution of SFGs (Rawlings & Jarvis 2004; Padovani et al. 2015; Padovani 2016b).

Our radio catalogue was cross-matched against SERVS, UKIDSS and other multi-wavelength datasets. Using the different radio, mid-infrared, optical and X-ray AGN indicators explored in Ocran et al. (2017), we have efficiently separated the radio source population with redshift into three classes: SFGs, RQ AGNs and RL AGNs. The relative contribution of the three classes of sources to the subsample of radio sources with redshifts and at least one multi-wavelength diagnostic is as follows: $\sim$73% SFGs, $\sim$12% RQ AGNs and $\sim$15% RL AGNs. Compared to our previous analysis over a smaller area at 610 MHz in the same field, our results indicate a continued increase in the relative fraction of SFGs with decreasing flux density. Ocran et al. (2017) reported that RQ AGNs dominate the AGN population but in this work spanning a larger area of the same field we conclude that RL AGNs actually dominate. The significantly higher fraction of SFGs in our sample may also partially arise from the selection at lower frequency, where at a given flux density threshold flat-spectrum AGN cores are preferentially detected at 1.4 GHz.

We matched our 610 MHz catalogue and compared with catalogues from other surveys at different frequencies. In this regard, we form a sample with which to study the spectral index properties of low-frequency radio sources. We measure the median spectral index between 610 - 325 MHz, 610 - 1400 MHz and 610 - 5000 MHz. Our sample is dominated by steep-spectrum sources as expected for low-frequency selected sources. We measure a median spectral index of $\alpha^{610}_{325} = -0.80 \pm 0.29$, $\alpha^{610}_{1400} = -0.83 \pm 0.31$ and $\alpha^{610}_{5000} = -1.12 \pm 0.15$. We note that the median spectral index we measure at other frequencies for our sample is currently severely limited by the sensitivity of the high-frequency reference. The radio colour-colour plot (i.e α^{610}_{1400} vs α^{610}_{325}) reveals a steepening which is consistent with our RL AGN classification. Massardi et al. (2011) showed that a spectral index of $\alpha = 0.5$ provides a clean way of distinguishing flat-spectrum/compact sources from steep-spectrum/extended sources. These extended sources emit synchrotron radiation at relatively high frequencies where they are optically thin, implying the existence of fast electrons moving in a magnetic field which is a signature of RL AGN (see, Padovani (2016b)). Thus, the steepening of our RL AGN sources can be attributed to the systematic increase in the synchrotron age of the relativistic jets extending well beyond the host galaxy, i.e. an increase from the lobes' head towards their flaring ends (see, Sadler et al. 1989; Machalski et al. 2010).

Restricting our statistical analyses to a much brighter sub-sample, $S_{610\,MHz} > 0.5$ mJy for α_{325}^{610} and $S_{610\,MHz} > 1.9$ mJy for α_{1400}^{610}, we measure a -0.71 and -0.89 respectively. The median spectral indices between 610 - 325 MHz of the bright sample for SFGs and AGNs is -0.81 ± 0.23 and -0.69 ± 0.22 respectively. We also measure a median spectral index between 610 - 1400 MHz of -0.81 ± 0.26 for AGNs over $S_{610\,MHz} > 1.9$ mJy.

By adopting the definition of a USS object as a radio source with $\alpha < -1.3$, we find a total of two USS radio sources. The two candidate USS sources have no corresponding redshift association (both spectroscopic and photometric) from the multi-wavelength catalogue (see Section 2.4 and Section 2.4.2) and therefore remain unclassified. Saxena et al. (2018a) defined a sample of USS radio sources from the TGSS ADR1 at 150 MHz to search HzRGs. They used the TGSS along with FIRST and NVSS at 1.4 GHz to select sources with spectral indices steeper than -1.3 resulting in a final sample consisting of 32 sources. Currently, most powerful distant radio galaxy is at z = 5.7 (Saxena et al., 2018b) with an ultra-steep spectral index, $\alpha_{1.4\,GHz}^{150\,MHz} = -1.4$ (see Saxena et al. 2018a). Although we have no redshift estimates for our two candidate USS sources, chances of them being HzRGs is very high. However, there is also the possibility of their being dust obscured radio AGNs at lower redshifts, low luminosity RQ AGNs which are pretty much indistinguishable from SFGs in terms of the radio emission at lower redshifts present in our sample. Follow-up observations are essential to confirm that the two USS sources are HzRGs.

A detailed and more complete analysis of the evolutionary properties of the different classes of sources in our GMRT sample, in comparison with other observational and modeling work will be the subject of forthcoming papers. Upcoming large radio continuum surveys with the SKA pathfinders and precursors (Norris et al., 2013), such as the MeerKAT International GHz Tiered Extragalactic Exploration (MIGHTEE) Survey (Jarvis et al., 2016) with MeerKAT (Jarvis et al., 2016), will detect millions of radio sources down to fainter flux limits than we explored in this paper. It is therefore extremely important to be able to predict which kind of sources these facilities will observe and what are the key data in other spectral windows necessary to complement the radio information to maximise the scientific outputs of these projects. This work is particularly useful for paving the way to upcoming radio surveys that these new radio facilities will provide.

Chapter 3

Cosmic evolution of star-forming galaxies to $z \simeq 1.8$ in the faint low-frequency radio source population

Abstract

The Faint Low-Frequency Radio Universe in Continuum: Exploitation of the Pre-SKA Deepest Survey

We study the properties of star-forming galaxies selected at 610 MHz with the GMRT in a survey covering ~1.86 deg^2 down to a noise of ~7.1 μJy / beam. These were identified by combining multiple classification diagnostics: optical, X-ray, infrared and radio data. Of the 1685 SFGs from the GMRT sample, 496 have spectroscopic redshifts whereas 1189 have photometric redshifts. We find that the IRRC of star-forming galaxies, quantified by the infrared-to-1.4 GHz radio luminosity ratio q_{IR}, decreases with increasing redshift: $q_{IR} = 2.86 \pm 0.04(1 + z)^{-0.20\pm0.02}$ out to $z \sim 1.8$. We use the V/V_{max} statistic to quantify the evolution of the co-moving space density of the SFG sample. Averaged over luminosity our results indicate $\langle V/V_{max} \rangle$ to be 0.51 ± 0.06, which is consistent with no evolution in overall space density. However we find V/V_{max} to be a function of radio luminosity, indicating strong luminosity evolution with redshift. We explore the evolution of the SFGs radio luminosity function by separating the source into five redshift bins and comparing to theoretical model predictions. We find a strong redshift trend that can be fitted with a pure luminosity evolution of the form $L_{610\,MHz} \propto (1 + z)^{(2.95\pm0.19)-(0.50\pm0.15)z}$. We calculate the cosmic SFR density since $z \sim 1.5$ by integrating the parametric fits of the evolved 610 MHz luminosity function. Our sample reproduces the expected steep decline in the star formation rate density since $z \sim 1$.

3.1 Introduction

Radio continuum observations provide dust unbiased information on mechanical feedback originating in star formation and AGN radio jets (Condon 1992; Merloni & Heinz 2007; Madau & Dickinson 2014). They thus underpin our understanding of galaxy evolution over cosmic time. Multi-wavelength analysis of the GMRT 610 MHz deep ELAIS N1 data down to flux densities of 50 μJy by Ocran et al. (2017) clearly shows the transition from an AGN dominated population to a star-forming galaxy (SFG) below flux densities of $\sim$ 300μJy. This is in line with what found in 1.4 GHz deep surveys. This flux depends on the frequency. (Condon 1989; Mauch & Sadler 2007; Padovani et al. 2015; Prandoni et al. 2018).

The synchrotron emission in SFGs is closely related to recent star formation, so that its emission is widely used as a star formation indicator. This is due to the short lifetime of the massive stars producing Type II and Type Ib supernovae (e.g. see Condon 1992; Bell 2003; Murphy et al. 2011). The total infrared luminosity of a galaxy and its total 1.4 GHz radio luminosity are known to be linearly and tightly correlated (e.g. see van der Kruit 1971; de Jong et al. 1985; Helou et al. 1985; Condon 1992; Bell 2003; Sargent et al. 2010b). This so called infrared-radio correlation (IRRC) is well established for SFGs (e.g. Ivison et al. 2010; Magnelli et al. 2010; Thomson et al. 2014).

The evolution of different radio populations conducted by using non-parametric V/V_{max} analysis (Schmidt 1968; Morris et al. 1991; Yun et al. 2001). Clewley & Jarvis (2004) used the V/V_{max} test to show that low luminosity radio sources evolve differently from their more powerful, predominantly Fanaroff-Riley type II (FRII). McAlpine & Jarvis (2011) used V/V_{max} test to investigate the cosmic evolution of low luminosity ($L_{1.4GHz} < 10^{25} W\,Hz^{-1}sr^{-1}$) radio sources in the XMM Large Scale Structure survey field (XMM-LSS). Their results indicates that the low luminosity sources evolve differently to their high luminosity counterparts out to a redshift of $z \sim 0.8$.

The bivariate luminosity function of an optical-radio matches sample describes the volume density of galaxies per unit interval of radio luminosity per interval of of optical luminosity in each redshift bin. The evolution of star-forming galaxies has been extensively studied over the years using optical and infrared surveys. Mid and far-infrared *Spitzer* observations indicate that the galaxy population undergoes pure luminosity evolution with $k_D \sim 3.4 - 3.8$ out to $z \sim 1.2$, where k_D is the pure density evolution (PDE) (e.g. Caputi et al. 2007; Magnelli et al. 2009; Rujopakarn et al. 2010; Magnelli et al. 2011). While far infrared luminosity functions from Herschel data result in slightly stronger evolution estimates with $L_\star \propto (1 + z)^{4.1\pm0.3}$ up to $z \sim 1.5$ (Gruppioni et al. 2010; Lapi et al. 2011). At low redshifts ($z < 0.5$) Herschel studies performed by Dye et al. (2010) suggested evidence of stronger evolution in star-forming galaxies with the total luminosity density evolving as $(1 + z)^{7.1}$.

At radio wavelengths there has been substantial work on AGN but SFGs only become significant at low flux densities, hence are becoming more accessible with deep surveys. Mauch & Sadler (2007) studied a sample of 7824 radio sources from 1.4 GHz NRAO Very Large Array (VLA) Sky Survey (NVSS) with galaxies brighter than $K = 12.75$ mag in the Second Incremental Data Release of 6dF Galaxy Survey (6dFGSDR2)

that spanned a redshift range $0.003 < z < 0.3$ and determined the local luminosity function at 1.4 GHz for their 60% star forming galaxies (SFGs) and 40% active galactic nuclei (AGN). Smolčić et al. (2009a) derived the cosmic star formation history (CSFH) out to $z = 1.3$ using a sample of ~350 radio selected star forming galaxies and determined an evolution in the 1.4 GHz luminosity function based on the VLA-COSMOS SFGs. Mao et al. (2012) used the Data Release 1 (DR1) from the Australia Telescope Large Area Survey (ATLAS) consisting of the preliminary data published by Norris et al. (2006) and Middelberg et al. (2008) et al. (2008) and reaching an rms sensitivity of 30 μ Jybeam^{-1} to derive radio luminosity functions. They constructed the radio luminosity function for star-forming galaxies to $z = 0.5$ and for AGN to $z = 0.8$ and found that radio luminosity function for star-forming galaxies appears to be in good agreement with previous studies. McAlpine et al. (2013) investigated the evolution of faint radio sources out to $z \sim 2.5$ by combinnig a 1 square degree VLA radio survey complete to a depth of $100\mu Jy$ with the following surveys: Visible and Infrared Survey Telescope for Astronomy Deep Extragalactic Observations and Canadian-France-Hawaii Telescope Legacy Survey. Novak et al. (2017) use of the deep Karl G. Jansky Very Large Array (VLA) COSMOS radio observations at 3 GHz to infer radio luminosity functions of star-forming galaxies up to redshift of $z \sim 5$ based on 6040 detections with reliable optical counterparts.

In the low-frequency regime, Willott et al. (2001) measure the radio luminosity function (RLF) of steep-spectrum radio sources using three redshift surveys of flux-limited samples selected at low (151 and 178 MHz) radio frequency, low-frequency source counts and the local RLF. Prescott et al. (2016) presented a measurement of the evolution of SFGs to z = 0.5, by matching a catalogue of radio sources measured at a frequency of 325 MHz from the Giant Metrewave Radio Telescope (GMRT) to their optical counterparts in the Galaxy And Mass Assembly (GAMA) survey. They found that the radio luminosity function at 325 MHz for SFGs closely follows that measured at 1.4 GHz.

The evolution of the global galaxy SFR density can be used as a robust constraint on various simulations and semianalytic models of galaxy evolution (e.g., Pei et al. 1999; Somerville et al. 2001; McCarthy et al. 2001). Total CSFH has been constrained using MIR (24/8μm) selected samples obtained by deep small area surveys (Zheng et al. 2006; Caputi et al. 2007; Bell et al. 2007). Smolčić et al. (2009a) used the VLA-COSMOS SFGs to derive the cosmic star formation history out to $z = 1.3$. In this paper, we present a measurement of the evolution of SF galaxies to $z \sim 1.5$, by matching a catalogue of radio sources measured at a frequency of 610 MHz from the (GMRT) to their optical counterparts in the SERVS Data Fusion* (Vaccari et al. 2010; Vaccari 2015). The 610 MHz GMRT survey covers a sky area of ~1.86 deg^2. The restoring beam is 6 arcsec circular and the RMS in the central region is ~ 7.1 μJy beam^{-1} making this survey the most sensitive low-frequency deep field to date. The SERVS Data Fusion provides reliable spectroscopic and photometric redshifts, allowing us to classify AGN and SFG. The layout of this paper is as follows: we first introduce the 610 MHz SFG data in Section 3.2. In Section 3.3, we present the sample properties of the selected SFGs. The estimation of the radio luminosity function is discussed in Section 3.4. In Section 3.5, we describe how we constrain the evolution of the SFG luminosity function out to $z \simeq 1.5$. The implications for the cosmic star formation density are presented in Section 3.6. We adopt

*http://www.mattiavaccari.net/df

throughout the paper a flat concordance Lambda cold dark matter (ΛCDM) ,with the following parameters: Hubble constant $H_0 = 70\,\mathrm{kms}^{-1}\,\mathrm{Mpc}^{-1}$, dark energy density $\Omega_\Lambda = 0.7$ and matter density $\Omega_m = 0.3$.

3.2 The 610 MHz GMRT data

The radio data we use in this paper, is taken from the GMRT at 610 MHz the covering ~1.86 deg^2 of ELAIS N1 field. The survey consisted of 7 closely-spaced pointings. The on source integration time was ~ 18 hours per pointing. The resolutions before mosaic, for each pointing were in the range 4.5 to 6 arcseconds. The minimum rms noise in the central region of the image is 7.1 $\mu\mathrm{Jy\,beam}^{-1}$. The radio data is fully described in Ocran et al. (2020a). Data analysis was carried out on the data intensive cloud at the Inter-University Institute for Data Intensive Astronomy (IDIA). A source catalogue was produced by extracting sources in the mosaic using the PyBDSF source finder (Mohan & Rafferty, 2015). This resulted in a final catalogue of 4290 radio sources. By matching to multi-wavelength data against SERVS IRAC12 positions Fusion[†] (Vaccari et al. 2010; Vaccari 2015), we obtain a redshift estimate for 72%, with 19% based on spectroscopy. The redshift estimates are a combination of spectroscopic and photometric redshifts from (i.e. the Hyper Suprime-Cam (HSC) Photometric Redshift Catalogue (Tanaka et al., 2018b), the revised SWIRE Photometric Redshift Catalogue (Rowan-Robinson et al., 2013) and the Herschel Extragalactic Legacy Project (Vaccari, 2016; Shirley et al., 2019, HELP)). For 3105 of the sources with redshifts we use radio and X-ray luminosity, optical line ratios, mid-infrared colors, and 24μm and IR to radio flux ratios to separate SFGs from AGN. In Ocran et al. (2020a), we outlined that total number of sources with redshifts for which we can define at least one AGN indicator was 2305 (i.e. ~ 54% of the whole 4290 sample and ~ 74% of the 3105 sources with redshifts). We classified 1685 sources as SFG constituting 73% of the 2305 sources for which we were able to define at least one AGN indicator for source classification. For sources with redshift, rest frame 610 MHz radio luminosities are calculated using equation 3.1 below:

$$L_{610} = 4\pi D_L^2 \frac{S_{obs}}{(1+z)^{1+\alpha}} \tag{3.1}$$

where L is the luminosity in WHz^{-1} at the frequency ν, D_L is the luminosity distance in metres. S_{obs} is the observed flux density at 610 MHz, and α is the spectral index and it is defined as $S \propto \nu^\alpha$. In Ocran et al. (2020a), we measured a median spectral index that steepens with frequency with $\alpha_{325}^{610} = -0.80 \pm 0.29$, for ~479 sources and $\alpha_{1400}^{610} = -0.83 \pm 0.31$ for ~99 sources. Hence, we use the canonical spectral index of $\alpha = -0.8$ often assumed for SFGs (Condon, 1992).

3.2.1 The SFG sample

From Ocran et al. (2020a), we have a multi-wavelength match for 92% of the sources and a redshift identification for 72% of the sources. But we have been able to classify 39% as SFGs and 15% as AGNs

[†] http://www.mattiavaccari.net/df

which adds up to 54%. If there is an indication of AGN activity in the source from any of the criteria adopted, then we inferred that the source is an AGN, regardless of the results from the other indicators. For our studies of the fractions of radio sources belonging to different classes and of the luminosity functions of different source classes, our sample is limited to radio sources with a SERVS/UKIDSS counterpart, a redshift and for which at least one of our AGN diagnostic criterion can be defined. A source within this sample is then classified as an SFG when none of the AGN diagnostic criteria we adopted are met. Conversely, if there is an indication of AGN activity in the source (i.e. any of the criteria 1 to 4 is met, see Ocran et al. (2020a)) then we inferred that the source is an AGN, regardless of the results from the other indicators. This may be considered as an upper limit to the population of sources in this flux density regime whose radio emission is powered by star formation processes.

Figure 3.1 shows the distribution of 610-MHz flux densities. The entire GMRT sample of 4290 sources (i.e. light gray histogram) is represented as S_{ALL}. Radio sources that have multi-wavelength identification (i.e black histogram) is represented as $S_{matched}$, whereas radio sources with redshifts (i.e. red histogram) is represented S_z. The sources with redshifts that also have at least one diagnostic for AGN activity (i.e. this sample is fully described in Ocran et al. (2020a) and Section 3.2, see blue histogram) is represented as $S_{AGN\,diagnostic}$. The SFG sample used for this analysis is drawn from the latter. We use these distributions to derive the redshift success C_z completeness which is outlined in subsection 3.4.2.

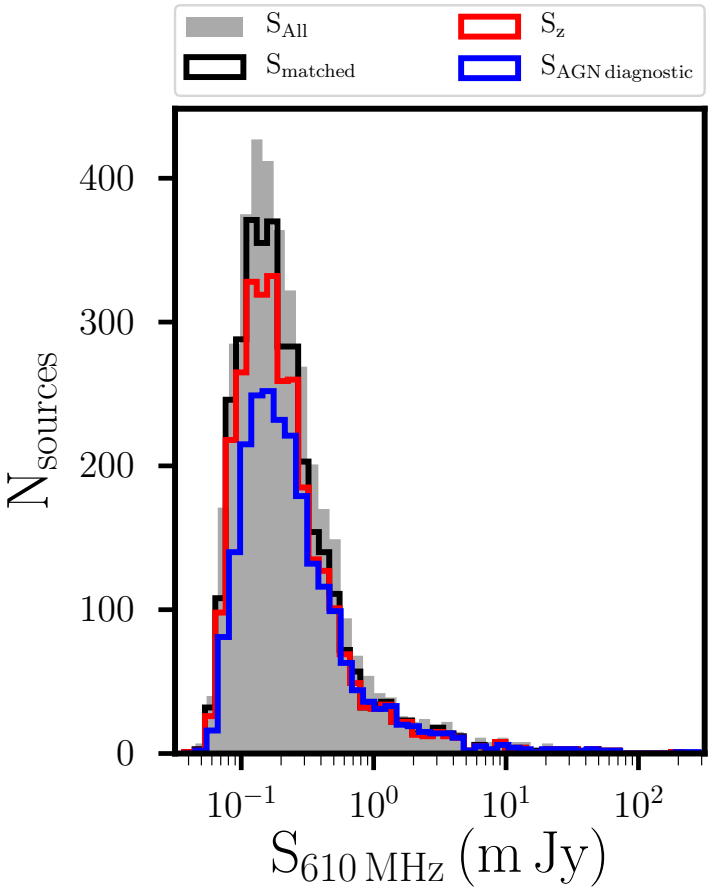

FIGURE 3.1: The distribution of 610-MHz flux densities for the entire GMRT sample of 4290 sources (light gray), radio sources that have multi-wavelength identification (black), radio sources with redshifts (red) and sources with redshifts that also have at least one diagnostic for AGN activity (blue).

3.3 SFG Properties

Figure 3.1 shows the distribution of the GMRT sources (grey histogram) with r_{mag} (left) and redshift (right). We over-plot the distribution of objects identified as SFG in black. The redshift distribution clearly shows that the sample is incomplete for $r_{mag} > 25$ and $z > 1.5$. This is driven by HSC/Subaru photometric redshifts, which start being incomplete at $z \sim 1.3$. Tanaka et al. (2018b) stresses that photometric redshifts should only be used at $z \lesssim 1.5$ and $i \lesssim 25$.

We note a secondary peak in our sample at $z \sim 1.1$ and $r \sim 25$. Swinbank et al. (2007) identified five candidate galaxy over densities at $z \sim 1$ across $\sim 1\,deg^2$ in the ELAIS N1 field by analysing deep field of the UK Infrared Deep Sky Survey (UKIDSS) Deep eXtragalactic Survey. They attributed these five overdense regions lying in a narrow redshift range as an indication of the presence of a supercluster in this field at $z \sim 1$. Our secondary peak may be due to this supercluster.

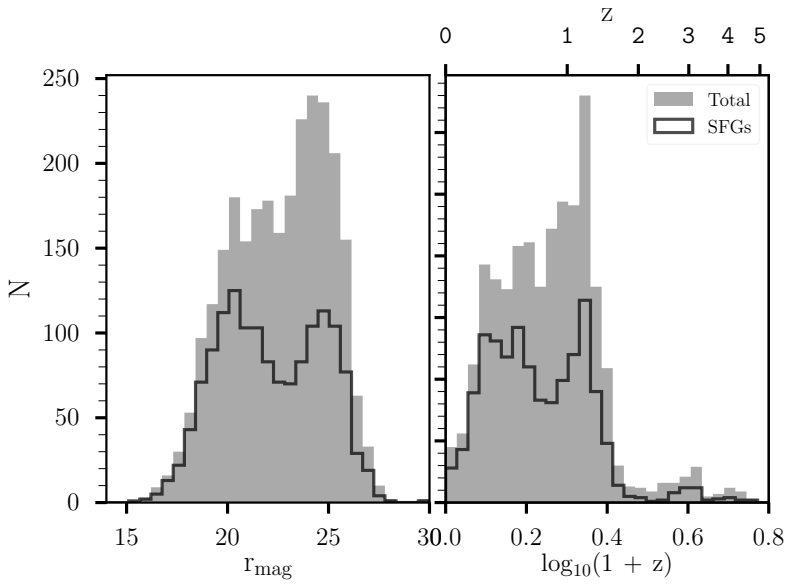

FIGURE 3.2: Distribution of the GMRT sources (grey histogram) with r_{mag} (left) and redshift (right). The distribution of SFG (black) are over-plotted.

3.3.1 The redshift evolution of the IRRC

We characterised the IR/radio correlation of our SFGs by the logarithmic ratio between the IR bolometric (8-1000 μm) luminosity and the radio luminosity q_{IR}(Helou et al., 1985).

$$q_{IR} = \log_{10}\left(\frac{L_{IR}}{3.75 \times 10^{12}\,W}\right) - \log_{10}\left(\frac{L_{radio}}{W\,Hz^{-1}}\right) \tag{3.2}$$

where L_{IR} is the total rest-frame infrared luminosity and L_{radio} is the luminosity at the radio frequency to be studied, in our case at 610 MHz and 1.4 GHz in W/Hz. The 1.4 GHz luminosities were computed from the $S_{610\,MHz}$ using a radio spectral index of -0.8. The far-Infrared luminosities, L_{IR}, were derived from rest-frame integrated 8 - 1000μm luminosities, estimated by Małek et al. (2018) using HELP photometry. They were obtained by performing SED fitting on the ultraviolet(UV)/near-infrared(NIR) to far-infrared(FIR) emission of 42,047 galaxies from the pilot HELP field: ELAIS N1. We corrected the luminosity values to our more accurate spectroscopic redshift by following the prescription presented by Ocran et al. (2017).

We investigate the evolution of the q_{IR} parameter with redshift which is quantified by the function $q_{IR} \propto (1 + z)^{\gamma}$

(Ivison et al., 2010; Calistro Rivera et al., 2017). We first analyse the 1.4 GHz behavior because this can be compared to the literature. Figure 3.3 shows q_{IR} vs redshift. The inset histogram shows q_{IR} is scattered in a distribution with an overall median value of $q_{IR} = 2.61^{+0.30}_{-0.28}$ (see the red horizontal solid line in Figure 3.3). This q_{IR} distribution agrees well with previous literature within the errors. Yun et al. (2001) measured a median $q_{IR} = 2.34 \pm 0.26$ (see the dashed horizontal line in Figure 3.3), by investigating the radio counterparts to the IRAS redshift survey galaxies that are also identified in the

TABLE 3.1: The number of sources, median value of z and q_{IR} for star-forming galaxies in each redshift bin.

z	median(z)	q_{IR}(1.4 GHz)
0.002 – 0.282	0.20	2.73 ± 0.03
0.282 – 0.562	0.44	2.71 ± 0.02
0.562 – 0.842	0.68	2.57 ± 0.02
0.842 – 1.122	0.97	2.54 ± 0.02
1.122 – 1.402	1.23	2.45 ± 0.03
1.402 – 1.682	1.46	2.48 ± 0.04
1.682 – 1.962	1.80	2.24 ± 0.07

NRAO VLA Sky Survey (NVSS) catalog. The horizontal shaded region represents the ±0.26 upper and lower bounds around the median value. Bell (2003) assembled a diverse sample of galaxies from the literature with far-ultraviolet (FUV), optical, infrared (IR), and radio luminosities to explore the origin of the radio-IR correlation and measured a median $q_{IR} = 2.64 \pm 0.02$ (see the dotted dashed horizontal line in Figure 3.3). We note that Bell (2003) used total infrared (TIR) luminosities, but Yun et al. (2001) value is based on far-infrared (FIR) luminosities . Delhaize et al. (2017) showed that this usually results in lower median values. We split the data into seven redshift bins, Table 3.1 presents the number of sources, median value of z and q_{IR} for star-forming galaxies in each redshift bin. By fitting a power-law function to the median values of q_{IR}, weighting by the uncertainty, we find a significant variation of q_{IR} with redshift: $q_{IR} = 2.86 \pm 0.04(1 + z)^{-0.20\pm0.02}$. The errors here are the 1σ uncertainty from the power-law fit. Our result is in good agreement with Delhaize et al. (2017), who carried out double-censored survival analysis (following Sargent et al. (2010b)) to calculate the median q_{IR} values (and associated 95% confidence intervals) for their samples in redshift bins. To get q_{IR} they converted their 3 GHz luminosities to 1.4 GHz ones using a spectral index of −0.7. They reported a slightly higher but statistically significant variation of q_{IR} with redshift: $q_{IR} = 2.88 \pm 0.03(1 + z)^{-0.19\pm0.01}$ from a highly sensitive 3 GHz observations with the Karl G. Jansky Very Large Array (VLA) and infrared data from the Herschel Space Observatory in the 2 deg^2 COSMOS field. Despite the fact that we do not follow the survival analysis approach (see Schmitt et al. 1993; Novak et al. 2017; Ceraj et al. 2018; Molnár et al. 2018), we nevertheless get results in good agreement, implying that our analysis is not significantly biased.

Magnelli et al. (2015) found a moderate but statistically significant redshift evolution $q_{IR}(z) = 2.35 \pm 0.08(1 + z)^{-0.12\pm0.04}$ using deep FIR luminosities from the *Herschel* Space Observatory (Pilbratt et al., 2010) and deep radio 1.4 GHz VLA observations. Calistro Rivera et al. (2017) measured the redshift evolution of the infrared-radio correlation (IRC) for SFG sample obtained with Low Frequency Array (LOFAR) at 150 MHz and found that the ratio of total infrared to 1.4 GHz data of the Bootes field decreases with increasing redshift given by: $q_{IR} = 2.45 \pm 0.04(1 + z)^{-0.15\pm0.03}$.

Under our assumption of a fixed spectral index $\alpha = -0.8$, q_{IR} (610 MHz) is given by the simple conversion $q_{610\,MHz} = q_{1.4GHz} - 0.29$. We thus report a median q_{IR} (610 MHz) = 2.32, and

$q_{610\,MHz} = 2.57 \pm 0.04(1 + z)^{-0.120\pm0.02}$ as a function of redshift.

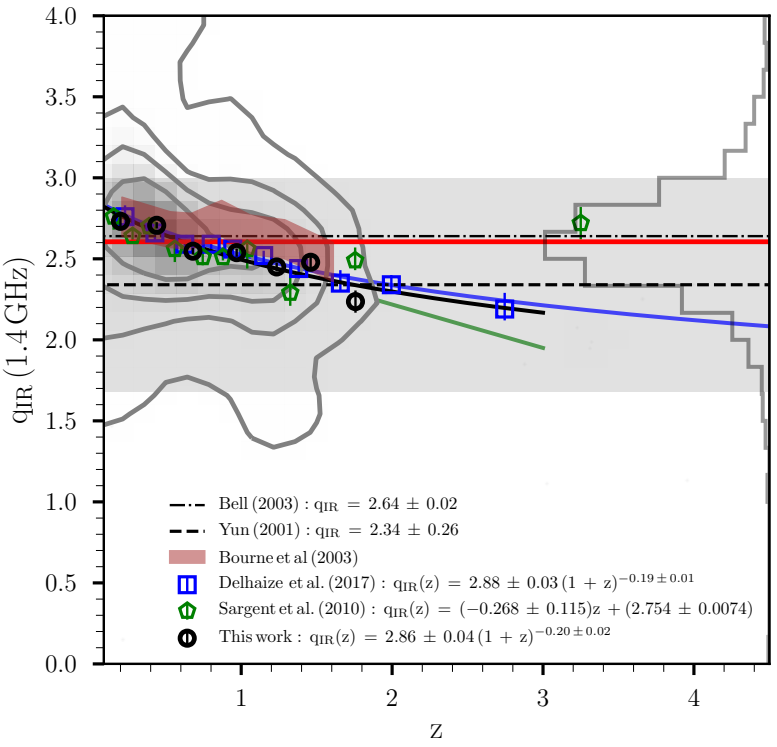

FIGURE 3.3: The q_{IR} versus redshift for SFGs. The background grey density contour represents the q_{IR} for SFGs with radio and IR detection, and redshift information. The contours levels are 1, 2, 3, and 4 σ. The inset histogram represents the q_{IR} distribution. The median q_{IR} within each redshift bin is indicated by the open black circle. Error bars show the 1σ dispersion calculated via bootstrap method. The solid black line shows the power-law fit to the our SFGs sample. The horizontal shaded region represents the ±0.26 upper and lower bounds around the median value of Yun et al. (2001).

3.4 Radio luminosity function

3.4.1 Sample selection

To study the evolution of the Radio Luminosity Function (RLF) we limit our sample to SFGs with r_{mag} lim = 25 and 0.002 < z < 1.5, making 1291 SFGs in total. We choose r_{mag} lim = 25 to maximise the number of sources that we can use to calculate the luminosity function. Table 3.2 presents a summary of the number and percentage of all the SFGs with spectroscopic and photometric redshifts (a). The number and percentage of the SFGs that satisfies the selection for computing the luminosity function (b). The r_{mag} versus redshift for the SFG sample with redshift estimates and r_{mag} limit of 25 (see the dashed horizontal red line) is plotted in the left panel of Figure 3.4. The right panel of this plot shows the 610 MHz luminosity versus redshift for the GMRT sample with redshift and limiting magnitude of r = 25.

(A) All SFGs (1685 sources).

	Number	Percentage
z_{phot}	1189	70.5
z_{spec}	496	29.5

(B) SFGs and selection criteria (1291 sources, i.e SFGs $\wedge$ r $<$ 25 $\wedge$ 0.002 $<$ z $<$ 1.5).

	Number	Percentage
z_{phot}	834	64.6
z_{spec}	457	35.4

z_{phot} - photometric redshift.
z_{spec} - spectroscopic redshift.

TABLE 3.2: Summary of the number and percentage of all the SFGs with spectroscopic and photometric redshifts (a). The number and percentage of the SFGs that satisfies the selection for computing the luminosity function (b).

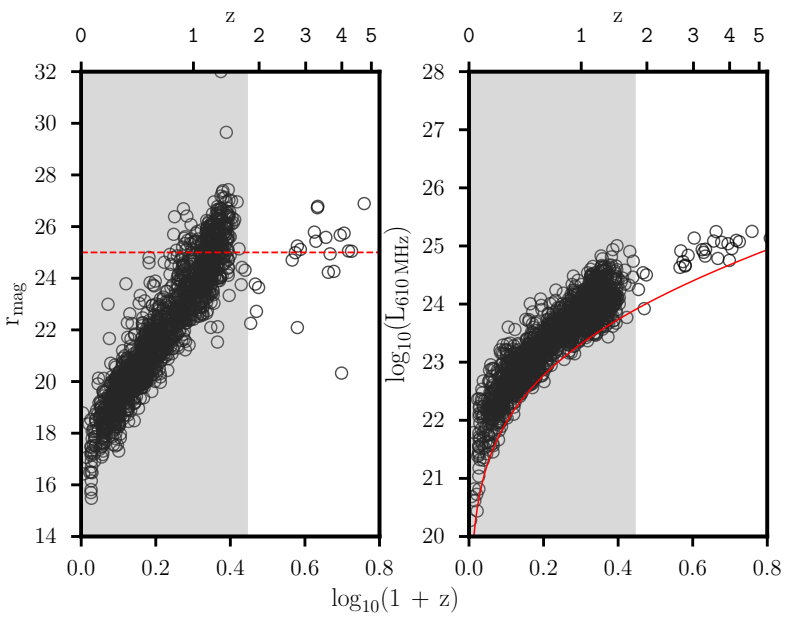

FIGURE 3.4: r_{mag} versus redshift for the SFG sample with redshift estimates and r_{mag} limit of 25 (the dashed horizontal red line) (left panel). 610 MHz luminosity versus redshift for the GMRT SFG (open black circles) sample with redshift and r_{mag} limit of 25 (right panel). The luminosity limit implied by the GMRT sensitivity is shown by the solid red curve.

3.4.2 V/V_{max} Statistic

In order to assess the evolution in the comoving space density of radio sources we use the non-parametric V/V_{max} method (Rowan-Robinson 1968; Schmidt 1968). V_{max} is the volume over which the galaxy could have been observed given the selection limits. It allows the incorporation of additional selection criteria.

For a uniform distribution, the value of V/V_{max} will be uniformly distributed between 0 and 1. Thus for such a sample the mean value is $\langle(V/V_{max})\rangle = 0.5 \pm (12N)^{-1/2}$, where N is the number of objects in the sample. $\langle(V/V_{max})\rangle > 0.5$ indicates that the sources are biased towards larger distances, or an increase of the space density with redshift. $\langle(V/V_{max})\rangle < 0.5$ indicates a deficiency in high redshift sources, or a decline in the space density with redshift. A constant comoving population is given by $\langle(V/V_{max})\rangle = 0.5$ (Clewley & Jarvis 2004; Tasse et al. 2008; McAlpine & Jarvis 2011; McAlpine et al. 2013; Prescott et al. 2016).

Our sample is a matched radio/optical sample, thus we take into account both the optical and radio limits of the surveys, where V_{max}, the final maximum observable volume, is taken as the minimum from the optical and radio V_{max} for each source:

$$V_{max} = \min(V_{max,radio}, V_{max,optical}) \tag{3.3}$$

Where $V_{max,radio}$ and $V_{max,optical}$ represent the maximum observable volumes of the source in the radio and optical surveys respectively and are shown below:

$$V_{max,radio} = \sum_{i=1}^{n} V_{max,radio,i}(z_{max,radio,i}) \times C_i \tag{3.4}$$

$$V_{max,optical} = \sum_{i=1}^{n} V_{max,optical,i}(z_{max,optical,i}) \times C_i \tag{3.5}$$

$V_{max,radio}$ and $V_{max,optical}$ were computed from $z_{max,radio}$ and $z_{max,optical}$ as shown in equations 3.4 and 3.5 above. This is in a single redshift bin and that the sum goes over all galaxies in a given redshift bin. The $z_{max,radio}$ and $z_{max,optical}$ represent the maximum observable redshifts of the source in the radio and optical surveys respectively. The k-correction to the $V_{max,radio}$ is a power law. We estimate $z_{max,optical}$ by running `kcorrect` (Blanton et al., 2003) which redshifts the best fitting SED template from the photometric redshift estimation procedure and determine the redshift where the template becomes fainter than our imposed a limiting magnitude of r = 25. The derivation of the radio completeness C_f is given by $\epsilon(s)$ (see Ocran et al. (2020a)). The $\epsilon(s)$ is the probability that a source with true flux density, s, will result in a detection. We measured this by inserting 3000 artificial point sources at a given true flux density at random positions into the residual map with the original sources removed. These sources populate the image with the same background noise and rms properties as the original source finding. We stressed in Ocran et al. (2020a)

that the field of view effect dominates the curve in the radio completeness correction (see Figure 7, Ocran et al. (2020a)) since the analysis is incorporating the varying sensitivity limit across the field of view due to the GMRT primary beam. This represents the completeness of the radio source catalogue versus true flux density (see Ocran et al. 2020a). In order to correct for the redshift incompleteness, we divided the distribution for the entire sample (i.e. light gray histogram see Figure 3.1) by the distribution for the sources with at least one diagnostic for AGN activity (i.e. blue histogram). We then corrected the RLF with this redshift success completeness, C_z. This redshift incompleteness in our sample is mostly due to sources not being detected in the optical wavelength range, so that we cannot compute a reliable (photometric) redshift. While this selection effect can in principle depend on the source class and redshift, since the correlation between optical and radio flux is not particularly tight for either SFGs and AGNs. We do not make any assumptions about the sources with no identifications or with no redshifts, but we do correct for the incompleteness associated with these selection effects with a constant correction factor equal to C_z. We define the completeness correction factor C_i (i.e see equations 3.4 and 3.5) as:

$$C_\rangle = C_z \times C_f \tag{3.6}$$

C_z is the redshift success completeness and C_f is the completeness of the radio catalog.

In Figure 3.5 and Table 3.3 we show the mean V/V_{max} statistic in bins of radio luminosity in the range $10^{20} < L_{610MHz} < 10^{25}\,WHz^{-1}$ for our SFG sample (see open black circles). For each bin we provide the number of sources (N) in the bin, mean $\langle V/V_{max}\rangle$, mean redshift ($\langle z \rangle$). The $\sigma = 1/\sqrt{12N}$ Avni & Bahcall (1980) are the statistical errors derived from the sample size. The dashed horizontal line shows the median $\langle V/V_{max}\rangle$. We calculate $\langle V/V_{max}\rangle$ to be 0.51 ± 0.06 for our SFGs. This value is not significantly different from 0.5, given the error of 0.06 thus averaged over luminosity there is no overall evidence for evolution in the number density of SFGs. However there is a clear trend of V/V_{max} with radio luminosity. At faint radio luminosities $L_{610MHz} < 10^{23}\,WHz^{-1}$ the values are below 0.5 indicating a higher space density at low redshift. Conversely for high luminosity, $L_{610MHz} > 10^{23}\,WHz^{-1}$ there is evidence for positive evolution or higher space density at higher redshift. The strong evolution of the high luminosity radio sources was also detected by Clewley & Jarvis (2004)). McAlpine & Jarvis (2011) also found evidence of this strong evolution at high luminosities although their result is at a lower statistical significance due to the small size of their sample. Taken together the results indicate strong luminosity evolution with overall number density constant with redshift but more high luminosity sources and fewer low-luminosity objects at higher redshift.

3.4.3 Derivation of the Radio luminosity function (RLF)

We derive the radio LF (Φ) for our GMRT sample in five redshift bins using the standard $\frac{1}{V_{max}}$ method (Schmidt, 1968).

TABLE 3.3: The V/V_{max} statistic as in radio luminosity bins for SFGs.

Median Luminosity $\log_{10}(L_{610\,MHz}\,[WHz^{-1}])$	Number (SFG)	V/V_{max} (SFG)	$1/\sqrt{12N}$ (SFG)
20.82	6	0.446	0.12
21.72	29	0.258	0.05
22.34	211	0.456	0.02
22.97	433	0.494	0.01
23.66	442	0.569	0.01
24.33	162	0.583	0.02
24.93	3	0.729	0.17

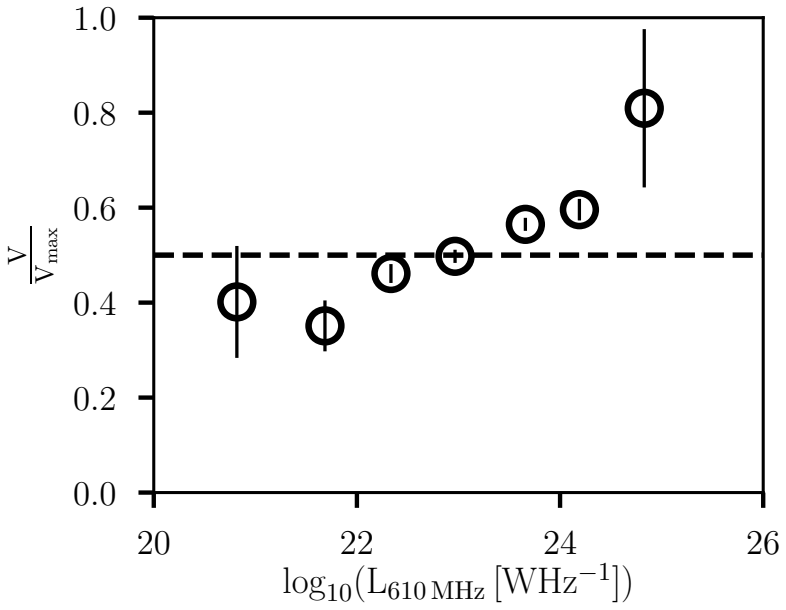

FIGURE 3.5: The V/V_{max} statistic as a function the radio luminosity for SFG out to $z = 1.5$ for the GMRT data (open black circles).

As the GMRT mosaics have non-uniform sensitivity, the effective area of the survey changes as a function of the flux limit. The volume of space available to a source of a given luminosity $V_{max,radio}$ (L) has to be calculated by taking into account the variation of survey area as a function of flux density limit (this correction has been already applied in Subsection 3.4.2). The RLF for a given luminosity bin is given by:

$$\Phi_z(L) = \sum_{i=1}^{n} \frac{1}{V_{max,i}} \pm \sqrt{\sum_{i=1}^{n} \frac{1}{{V_{max,i}}^2}} \tag{3.7}$$

where $\Phi_z(L)$ is the density of sources in $Mpc^{-3}dex^{-1}$.

3.5 Cosmic evolution of the SFG radio luminosity function

In this section we explain the reasoning behind adopting the analytic form of our local luminosity function at 610 MHz to fit our data. We further describe how the evolution of SFG luminosity function out to $z \sim 1.5$ is constrained.

3.5.1 The local RLF

Figure 3.6 presents the local 610 MHz SFG luminosity function shown as open black circles. The sample is truncated at $z < 0.1$ to minimize the effects of evolution. The yellow plus and blue stars represents Mauch & Sadler (2007) and Condon et al. (2002) SFG volume densities scaled to 610 MHz using an $\alpha = -0.8$. The dashed red line is the analytic fit to the local 610 MHz SFG data. We also show the 610 MHz RLF for SFGs in the redshift range $0.002 < z < 1.5$ shown in open black circles in Figure B.1.

An analytic function of the type described by Saunders et al. (1990)

$$\Phi_o(L) = \Phi_\star \left(\frac{L}{L_\star}\right)^{1-\alpha} \exp\left[\frac{-1}{2\sigma^2}\log^2\left(1+\frac{L}{L_\star}\right)\right] \tag{3.8}$$

where the $L_\star$ parameter describes the position of the turnover of the power-law plus log-normal distribution, $\Phi_\star$ is the normalization, α and σ are the faint and bright ends of the distribution, respectively.

To obtain the analytic form of the local luminosity function that is used throughout this work we use the best fit parameters from Novak et al. (2017), who combined data from both wide and deep surveys to properly constrain both the faint and the bright end of the local LF form Condon et al. (2002), Best et al. (2005), Mauch & Sadler (2007) data using the form given in equation 3.8. The best fit parameters obtained by Novak et al. (2017), which we use throughout this work are $\Phi_\star = 3.55 \times 10^3 \mathrm{Mpc}^{-3}\mathrm{dex}^{-1}$, $L_\star = 1.85 \times 10^{21} \mathrm{WHz}^{-1}$, $\alpha = 1.22$, $\sigma = 0.63$.

3.5.2 RLF as a function of z

We compare our results with literature values of SFG LF derived at 1.4 GHz and scaled down to 610 MHz assuming $\alpha = -0.8$ to check the robustness of our LF. Figure 3.7 presents the radio luminosity functions of SFGs at $\nu = 610$ MHz in different redshift bins (black open circles). Scaled down luminosity functions from 1.4 GHz to 610 MHz by Smolčić et al. (2009a), McAlpine et al. (2013) and Novak et al. (2017) are shown as green pluses, orange pentagons and blue diamonds respectively in each panel.

We compare with LFs derived from Wilman et al. (2008) semi-empirical simulation of the SKA and Mancuso et al. (2017) models. The Mancuso et al. (2017) models were obtained by following the model-independent approach by Mancuso et al. (2016a,b). These models are based on two main ingredients:

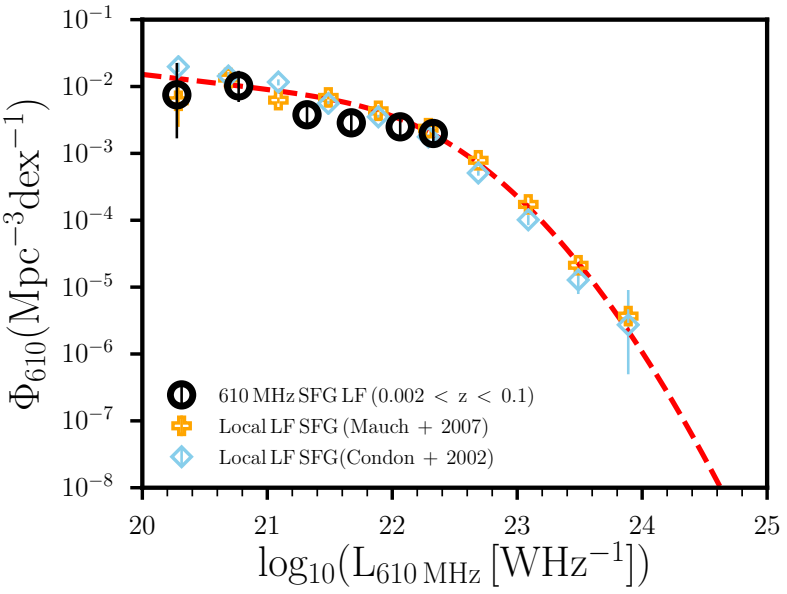

FIGURE 3.6: The local 610 MHz SFG luminosity function. The yellow plus and blue stars represents Mauch & Sadler (2007) and Condon et al. (2002) SFG volume densities scaled to 610 MHz using an $\alpha = -0.8$. The dashed red line is the combined analytic fit performed by Novak et al. (2017) to the local radio LF of SFGs from several surveys with different observed areas and sensitivities.

(i) the redshift-dependent SFR functions inferred from the latest UV/far-IR data from HST/Herschel and related statistics of strong gravitationally lensed sources, and (ii) deterministic tracks for the co-evolution of star formation and BH accretion in an individual galaxy, determined from a wealth of multiwavelength observations (see Mancuso et al. (2017)). We also compare to SFG models (see open brown hexagons in Figure 3.7) from the Tiered Radio Extragalactic Continuum Simulation (T-RECS) by Bonaldi et al. (2019) who modeled the corresponding sub-populations, over the 150 MHz - 20 GHz range. Our results concurs with the results of these models from literature, especially to the Mancuso et al. (2017) and Bonaldi et al. (2019) models at high luminosities. Note, however, that in the first two redshift bins the faint end of the Mancuso et al. (2017) models is lower than that of our SFG LF. Also, the faint end of the Bonaldi et al. (2019) and Wilman et al. (2008) models are higher than our measured SFG LF.

The breakdown of the luminosity, number density ($\Phi_{610}(\mathrm{Mpc}^{-3}\mathrm{dex}^{-1})$) and the number of sources in each redshift bin is presented in Table 3.4. Our data have small Poissonian error bars due to the relatively large number of sources in each bin and as such the errors do not reflect all possible systematic effects.

3.5.3 RLF Evolution

Following Novak et al. (2017), we assume that the shape of the LF remains unchanged at all observed cosmic times and only allow the position of the turnover and the normalization to change with redshift. We used the Markov chain Monte Carlo (MCMC) algorithm module EMCEE (Foreman-Mackey et al., 2013), implemented in the LMFIT Python package (Newville et al., 2014) to perform a multi-variate fit to the data.

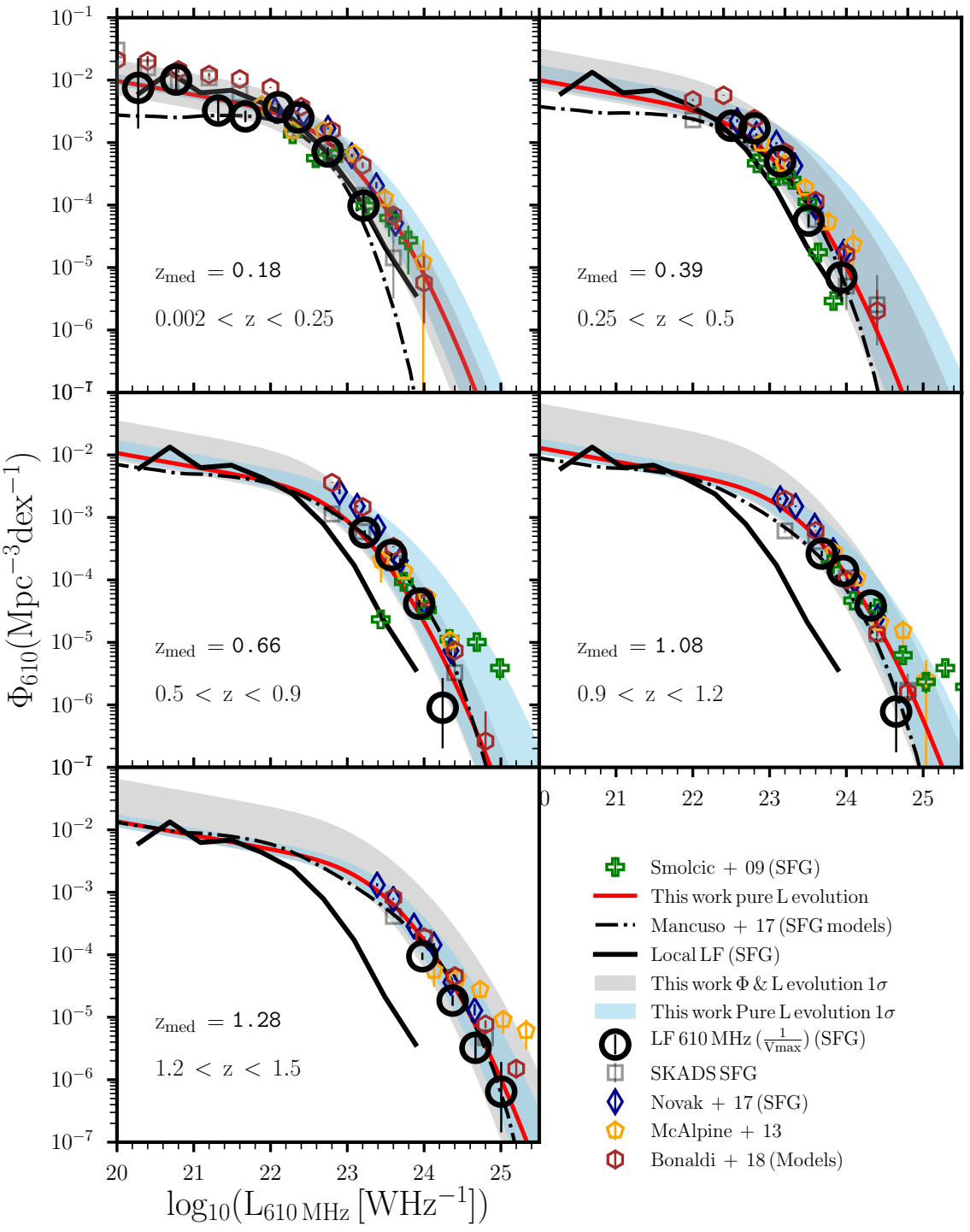

FIGURE 3.7: Radio luminosity functions of SFGs at $\nu = 610$ MHz in different redshift bins (black open circles). The black dashed lines in each panel are the SFG models from Mancuso et al. (2017). The black squares represent the total SFG LF from the semi-empirical simulation of the SKA (Wilman et al., 2008). Luminosity functions computed for SFGs from the T-RECS (Bonaldi et al., 2019) simulations are shown as open brown hexagons. The local radio luminosity function of Mauch & Sadler (2007) is shown for reference as a solid black line in each panel. Scaled down luminosity functions from 1.4 GHz to 610 MHz by Smolčić et al. (2009a), McAlpine et al. (2013) and Novak et al. (2017) are shown as green pluses, orange pentagons and blue diamonds respectively in each panel. The solid red lines in each panel corresponds to the median values of the MCMC samples. **The skyblue shaded region corresponds to the 68% confidence region of the MCMC samples for the independent PLE fits. The grey shaded region shows the 68% confidence region of the MCMC samples by combining PDE and PLE fitting.** The redshift range and the median redshift are shown in each panel. Error bars are determined using the prescription of Gehrels (1986).

TABLE 3.4: **Radio luminosity functions for the SFGs computed using the $1/V_{max}$ method for the different redshift bins of this study.**

Redshift z	Luminosity $\log_{10}(L_{610\,MHz}\,[WHz^{-1}])$	Number density $\Phi_{610}(Mpc^{-3}dex^{-1})$	Number N
$0.002 < z < 0.25$	20.28	$7.51^{+14.64}_{-5.70} \times 10^{-3}$	1
	20.77	$1.02^{+14.64}_{-5.70} \times 10^{-2}$	4
	21.32	$3.25^{+14.64}_{-5.70} \times 10^{-3}$	6
	21.67	$2.63^{+14.64}_{-5.70} \times 10^{-3}$	20
	22.10	$3.68^{+14.64}_{-5.70} \times 10^{-3}$	68
	22.36	$2.53^{+14.64}_{-5.70} \times 10^{-3}$	89
	22.74	$7.21^{+14.64}_{-5.70} \times 10^{-4}$	36
	23.21	$9.81^{+14.64}_{-5.70} \times 10^{-5}$	5
$0.25 < z < 0.5$	22.50	$1.86^{+0.24}_{-0.21} \times 10^{-3}$	58
	22.80	$1.69^{+0.16}_{-0.11} \times 10^{-3}$	176
	23.14	$5.01^{+0.44}_{-0.40} \times 10^{-4}$	113
	23.51	$5.63^{+1.53}_{-1.21} \times 10^{-5}$	16
	23.93	$6.98^{+7.95}_{-4.10} \times 10^{-6}$	2
$0.5 < z < 0.9$	23.23	$5.75^{+0.46}_{-0.42} \times 10^{-4}$	135
	23.57	$2.51^{+0.18}_{-0.17} \times 10^{-4}$	163
	23.94	$4.17^{+0.63}_{-0.54} \times 10^{-5}$	43
	24.24	$8.99^{+17.93}_{-6.98} \times 10^{-7}$	1
$0.9 < z < 1.2$	23.68	$2.64^{+0.30}_{-0.27} \times 10^{-4}$	71
	23.96	$1.39^{+0.12}_{-0.11} \times 10^{-4}$	117
	24.31	$3.89^{+0.54}_{-0.47} \times 10^{-5}$	49
	24.65	$7.81^{+0.16}_{-6.07} \times 10^{-7}$	1
$1.2 < z < 1.5$	23.98	$9.46^{+1.35}_{-1.18} \times 10^{-5}$	47
	24.37	$1.85^{+0.39}_{-0.32} \times 10^{-5}$	24
	24.67	$3.25^{+1.89}_{-1.24} \times 10^{-6}$	5
	25.00	$6.44^{+12.84}_{-5.00} \times 10^{-7}$	2

The listed luminosity values represent the median luminosity of the sources in the corresponding luminosity bin.

We fit all redshift slices for evolution assuming two scenarios for the LF, one in which the luminosity of the radio sources is fixed and undergoes pure density evolution parametrized (PDE) by

$$\Phi_z(L) = (1+z)^{k_D}\Phi_o(L) \tag{3.9}$$

and another in which the number density of radio sources is fixed and the population undergoes pure luminosity evolution:

$$\Phi_z(L) = \Phi_o\left(\frac{L}{(1+z)^{k_L}}\right) \tag{3.10}$$

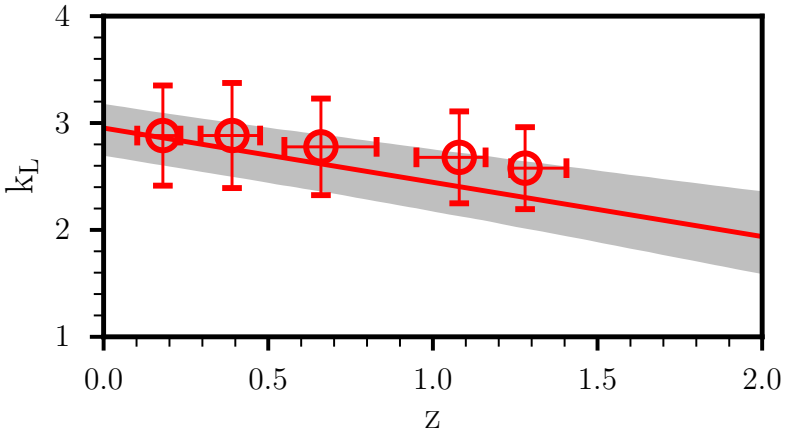

FIGURE 3.8: Parameters obtained from fitting PLE model to the SFG luminosity functions. Open red circles show the evolution parameters obtained from fitting the assumed analytic form of the luminosity function in five redshift bins assuming pure luminosity evolution scenario (see text for details). The vertical error bars represent the median absolute deviation (MAD) of the MCMC samples. The horizontal error bars denote the inter-quartile range (IQR) of reshift in each bin. The same color line shows the results from the continuous fit assuming that the PLE parameter evolves linearly with redshift.

where $\Phi_z(L)$ is the LF at redshift z, $\Phi_o(L)$ the normalization of the local LF, and k_D and k_L represent pure density and pure luminosity evolution parameters, respectively and denotes the strength of the evolution. Both the PLE and PDE models are common in the literature (e.g. see Condon 1984; Sadler et al. 2002, 2007; Gruppioni et al. 2013; McAlpine et al. 2013). Studies have shown that true evolution might be a combination of both of these extremes (see, e.g. Yuan et al. 2016a, 2017; Novak et al. 2017). The best fit evolution parameters for each redshift bin obtained with this procedure are presented in Table 3.5. The LMFIT Python package first does the fitting by performing a non linear least-squares χ^2 minimization to obtain the best fit k_L and k_D parameters. The EMCEE is then implemented to calculate the probability distribution for the parameters. From this we get the medians of the probability distributions and a 1σ quantile, estimated as half the difference between the 15.8 and 84.2 percentiles.

We also fit a continuous model the redshift dependence of the evolution parameters by adding a redshift dependent term to the k_L, and k_D parameters in Equation 3.9 and Equation 3.10 (e.g. see Novak et al. 2017; Smolčić et al. 2017b; Novak et al. 2018; Ceraj et al. 2018). We fit a simple linear redshift dependent evolution model to all SFG luminosity functions in all redshift bins simultaneously given by:

$$\Phi(L,z) = (1+z)^{(k_D+z\beta_D)} \times \Phi_0\left[\frac{L}{(1+z)^{(k_L+z\beta_L)}}\right]. \tag{3.11}$$

where k_D, k_L, β_D and β_L are the various evolution parameters. Equation 3.11 considers the case with both density and luminosity evolution combined plus redshift dependence (i.e four free parameters). We test pure density and pure luminosity evolution together via the procedure described above. The 68% confidence region by combining PDE and PLE fitting to the samples are shown with grey shaded are Figure 3.7.

Figure 3.8 presents best fit parameters obtained from fitting PLE model to the SFG luminosity functions. The second column of Table 3.5 presents values of the parameters (i.e. k_L) obtained from fitting PLE model to the SFG luminosity functions Open red circles show the evolution parameters obtained from independently fitting the assumed analytic form of the luminosity function in five redshift bins assuming pure luminosity evolution scenario whereas the same color line shows the results from the continuous fit (i.e. jointly fitting the RLF in the 5 redshift bins) assuming that the PLE parameter evolves linearly with redshift by using Equation 3.11. The vertical error bars represent the median absolute deviation (MAD) (Rousseeuw & Croux, 1993) of the MCMC samples. We derive $L_{610\,MHz} \propto (1+z)^{(2.95\pm0.19)-(0.50\pm0.15)z}$ (i.e. $k_L = 2.95 \pm 0.19$) for $0.002 < z < 1.5$. With no uncertainties associated with their estimated value, Haarsma et al. (2000) have found that a PLE with $k_L = 2.74$ is a good representation of the evolution of their radio-selected SF galaxies. Smolčić et al. (2009a) derived 2.1 ± 0.2 or 2.5 ± 0.1 for SFG depending on the choice of the local LF (i.e. Sadler et al. (2002) or Condon (1989) local LFs). Strazzullo et al. (2010) derived $k_L = 2.9 \pm 0.3$ by studying a sample of 1.4 GHz radio sources in the Deep SWIRE Field (DSF), reaching a limiting flux density $\sim 13.5\mu$Jy at the center of a $0.36\,deg^2$ area. We can therefore compare our results more directly with both Smolčić et al. (2009a) and Strazzullo et al. (2010), keeping in mind that both samples reach only $z = 1.3$. The evolution we measure is slightly higher than Smolčić et al. (2009a) but in good agreement with Strazzullo et al. (2010). However, our value is significantly weaker than found in the IR band for $z \leq 1.3$ by Magnelli et al. (2009), who modeled the evolution of infrared luminous star-forming galaxies as a PLE and found $k_L = 3.6 \pm 0.4$. McAlpine et al. (2013) studied the evolution of faint radio source out to $z \sim 2.5$. They found that the radio population experiences mild positive evolution out to $z \sim 1.2$ increasing their space density by a factor of ~ 3 with SFGs driving the more rapid evolution at low redshifts, $z < 1.2$. The McAlpine et al. (2013) translated to 610 MHz are shown in yellow symbols in Figure 3.7 and are in good agreement with our values of SFG luminosity functions out to $z < 1.5$. They reported k_L to be 2.47 ± 0.12 for their radio-selected star-forming population which is consistent with Smolčić et al. (2009a) but slightly below our measured value. Padovani et al. (2011) reported the radio power of SFGs evolves as $(1+z)^{2.5-2.9}$ up to $z \leq 2.3$, their maximum redshift in their sample, which in agreement with previous determinations in the radio, IR bands and this work. Although they also reported the evolution to be $k_L = 3.5^{+0.4}_{-0.7}$ for $z \leq 1.3$ or $k_L = 3.1^{+0.8}_{-1.0}$, when they exclude two large-scale structures in their sample. Novak et al. (2017) presented a radio selected sample of star-forming galaxies from deep VLA-COSMOS 3 GHz observations (Smolčić et al., 2017b) identifying 6040 galaxies, where the radio emission is not dominated by an AGN. Using this sample they derived radio LFs up to $z \sim 5$. The blue diamonds in Figure 3.7 show the Novak et al. (2017) LFs scaled down to 610 MHz. Their results are in agreement with our luminosity functions, with the their LF constraining the high luminosity end. By comparing their results with LFs derived using IR and UV selected samples and checking their robustness, they reported that their radio LF can be well described by a local LF evolved only in luminosity as $L_{1.4GHz} \propto (1+z)^{(3.2\pm0.2)-(0.33\pm0.08)z}$. These previous studies are broadly consistent with our radio derived PLE parameter and Table 3.5 presents a summary of the comparison.

TABLE 3.5: Best-fit evolution parameters obtained by fitting the local luminosity function to the redshift binned data assuming pure luminosity k_L evolution and the star formation rate density derived.

Med(z)	k_L	Total SFRD [$M_\odot\ yr^{-1}\ Mpc^{-3}$]	Lower limits
$0.18^{+0.05}_{-0.07}$	2.88±0.48	$0.021^{+0.004}_{-0.003}$	$0.014^{0.004}_{0.002}$
$0.39^{+0.09}_{-0.10}$	2.89±0.49	$0.026^{+0.004}_{-0.005}$	$0.018^{0.003}_{0.004}$
$0.66^{+0.16}_{-0.11}$	2.77±0.46	$0.035^{+0.009}_{-0.005}$	$0.023^{0.009}_{0.005}$
$1.08^{+0.08}_{-0.13}$	2.67±0.41	$0.046^{+0.006}_{-0.005}$	$0.016^{0.006}_{0.005}$
$1.28^{+0.13}_{-0.04}$	2.57±0.40	$0.066^{+0.012}_{-0.007}$	$0.013^{0.007}_{0.002}$

TABLE 3.6: Comparison of the current determinations of the evolution of the radio luminosity function.

Reference	Field	Wavelength	Redshift	Evolution Parameter (PLE)
Hopkins (2004)	-	1.4 GHz	~ 2.0	2.7 ± 0.6
Smolčić et al. (2009a)	COSMOS	1.4 GHz	~ 1.3	2.1 ± 0.2 OR 2.5 ± 0.1
Strazzullo et al. (2010)	DSF	1.4 GHz	~ 1.3	2.9 ± 0.3
Padovani et al. (2011)	CDFS	1.4 GHz	≤ 1.3	$3.5^{0.4}_{-0.7}$
Padovani et al. (2011)	CDFS	1.4 GHz	~ 2.3	$2.89^{+0.10}_{-0.15}$
Novak et al. (2017)	COSMOS	1.4 GHz	~ 5.0	(3.2 ± 0.2) − (0.33 ± 0.08)z
This work	ELAIS N1	610 MHz	~ 1.5	(2.95 ± 0.19) − (0.50 ± 0.14)z

COSMOS - Cosmological Evolution Survey.
CDFS - Chandra Deep Field South.
DSF - Deep SWIRE Field.

3.6 The Cosmic Star Formation History traced by the low-frequency SFG population

The relationship between the FIR luminosity and the SFR is complex, since stars with a variety of ages can contribute to the dust heating, and only a fraction of the bolometric luminosity of the young stellar population is absorbed by dust (e.g., see Lonsdale Persson & Helou 1987; Walterbos & Greenawalt 1996). By adopting the mean luminosity for 10-100 Myr continuous bursts, solar abundances, the Salpeter (1955) initial mass function (IMF) and assuming that the dust reradiates all of the bolometric luminosity yields:

$$\left(\frac{SFR_{IR}}{M_\odot\ yr^{-1}}\right) = \left(\frac{L_{IR}}{5.8\times10^9\ L_\odot}\right) \tag{3.12}$$

(see Kennicutt 1998; Bell 2003; Murphy et al. 2011). To compute the SFRs, we use the redshift dependent $q_{IR}(z)$ parameter. This should account for these intrinsic observational limitations under the assumption of a linear IR-radio correlation given by:

$$\left(\frac{SFR_{610\,MHz(z)}}{M_\odot\ yr^{-1}}\right) = \mathcal{F}_{IMF}\times10^{-24}\ 10^{q_{IR}(z)}\left(\frac{L_{610\,MHz}}{WHz^{-1}}\right) \tag{3.13}$$

where $\mathcal{F}_{IMF}$ = 1 for a Chabrier (2003) IMF and $\mathcal{F}_{IMF}$ = 1.7 for a Salpeter (1955) IMF. Novak et al. (2017) stresses that since low-mass stars do not contribute significantly to the total light of the galaxy, only the

mass-to-light ratio is changed when the IMF adopted is Chabrier (2003). We followed Novak et al. (2017) and used the Chabrier (2003) IMF.

In Figure 3.9 we show SFR from the total infrared luminosity as a function of radio luminosity at 610 MHz for SFGs. We color code the SFGs with redshift and dotted line shows the SFR, when a non-evolving q-value (i.e. median q-value in Section 3.3.1) is assumed. Converting the radio luminosity to SFR as shown in equation 3.12 to equation 3.13, before performing the integration will yield the star formation rate density (SFRD) of a given epoch as shown in equation 3.14 below, as presented as well by Novak et al. (2017).

$$\mathcal{SFRD} = \int_{L_{min}}^{L_{max}} \Phi_{(L,z,k_L,k_D)} \times \mathrm{SFR(L)}\, \mathrm{d}(\log\, L_{610\,\mathrm{MHz}}) \tag{3.14}$$

To derive the SFR density we need to compute the radio luminosity density and to convert our radio luminosities into SFRs, in Figure 3.10, we show the luminosity density for our 5 redshift bins. The curves are the PLE (solid red) best fit to the 610 MHz data in each redshift bin. We numerically integrated the expression in equation 3.14 by taking the analytical form of the LF in each redshift bin and using the best fit evolution parameters shown in Figure 3.7. We integrated over the entire luminosity range by setting $L_{min} = 0$ and $L_{max} = +\infty$. This ensures that the integral converges and that the major contribution to the SFRD arises from galaxies with luminosities around the turnover of the LF. From this approach, Novak et al. (2017) stresses that the entire radio emission is recovered and if the LF shape and evolution is well constrained, the SFRD estimate will be within the SFR calibration errors. We also performed the integration using the data constrained limits, where L_{min} and L_{max} correspond to the lowest and the highest value of the observed LF. This ensures that, any bias due to LF extrapolation toward higher or lower luminosities is removed (see Novak et al. 2017). We show our total SFRD derived by integrating the pure luminosity evolved LF in individual redshift bins as open black circles in Figure 3.11. Table 3.5 presents the best-fit evolution parameters obtained by the fitting local luminosity function to the redshift binned data assuming pure luminosity k_L evolution and the SFRD derived. We compare our SFRD results with other radio-based estimates in Figure 3.11. Smolčić et al. (2009a) derived the cosmic star formation history out to $z = 1.3$ using the local 20 cm LFs (Condon 1989; Sadler et al. 2002), purely evolved in luminosity, and best fit to the VLA-COSMOS data in four redshift bins (see yellow pluses and brown squares). SFRD obtained when L_{min} and L_{max} are data constrained limits (lower limits) are also shown (see lightblue squares). Lower limits obtained by Novak et al. (2017) are shown as green triangles. To create a consistent multi-wavelength picture, we also compare our work with results in the literature derived at infrared (IR) and ultraviolet (UV) wavelengths in Figure 3.11. All SFR estimates were rescaled to a Chabrier IMF where necessary, by multiplying by constant factors of 0.63 (i.e. as this is the conversion from literature). The curve from the review by Madau & Dickinson (2014), who performed a fit on a collection of previously published UV and IR SFRD data is shown as a solid black curve. The curve from Behroozi et al. (2013) who provide new fitting formulae for star formation histories based on a wide variety of observations is shown as dashed green curve is also shown. The constained SFRD by Burgarella et al. (2013) taking into account dust obscuration using combined IR and UV LFs reported in Gruppioni et al. (2013) and Cucciati et al. (2012), respectively are shown as red crosses for the total SFRD, red shaded area for the IR SFRD

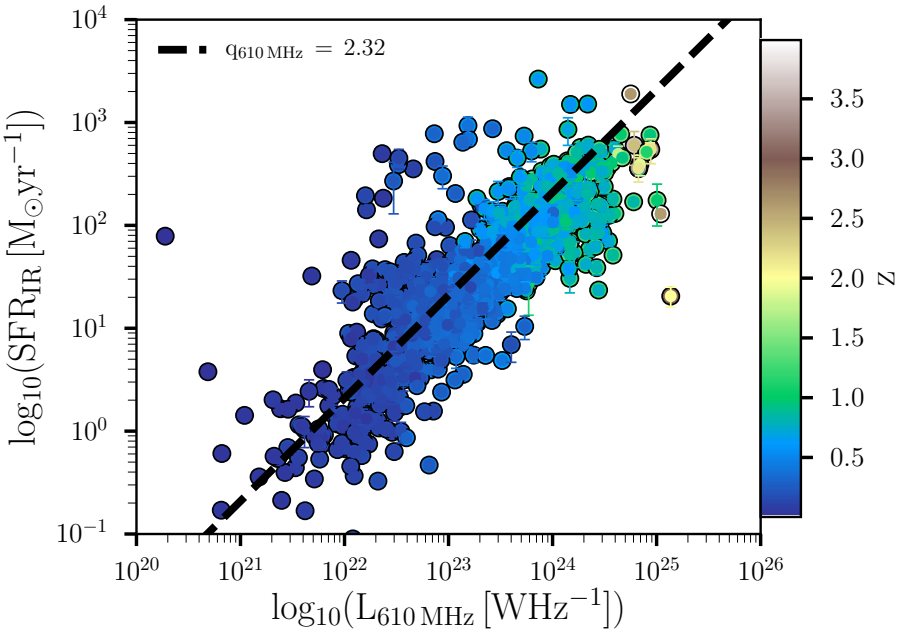

FIGURE 3.9: SFR from the total infrared luminosity as a function of radio luminosity at 610 MHz for SFGs. The SFGs are color coded with redshift. The dotted line shows the SFR, when a non-evolving q-value (i.e. median q-value at 610 MHz in Section 3.3.1) is assumed.

and green shaded area for the UV SFRD. The grey shaded area denote the 1σ uncertainty for the SFRD derived from integrated total IR LF by Gruppioni et al. (2013). SFRD estimates including the unobscured contribution based on the UV dust-uncorrected emission from local galaxies by Marchetti et al. (2016) are shown as magenta triangles. The expected steep decline in the star formation rate density since $z \sim 1$ seen by Smolčić et al. (2009a) and other previous studies is reproduced by our sample.

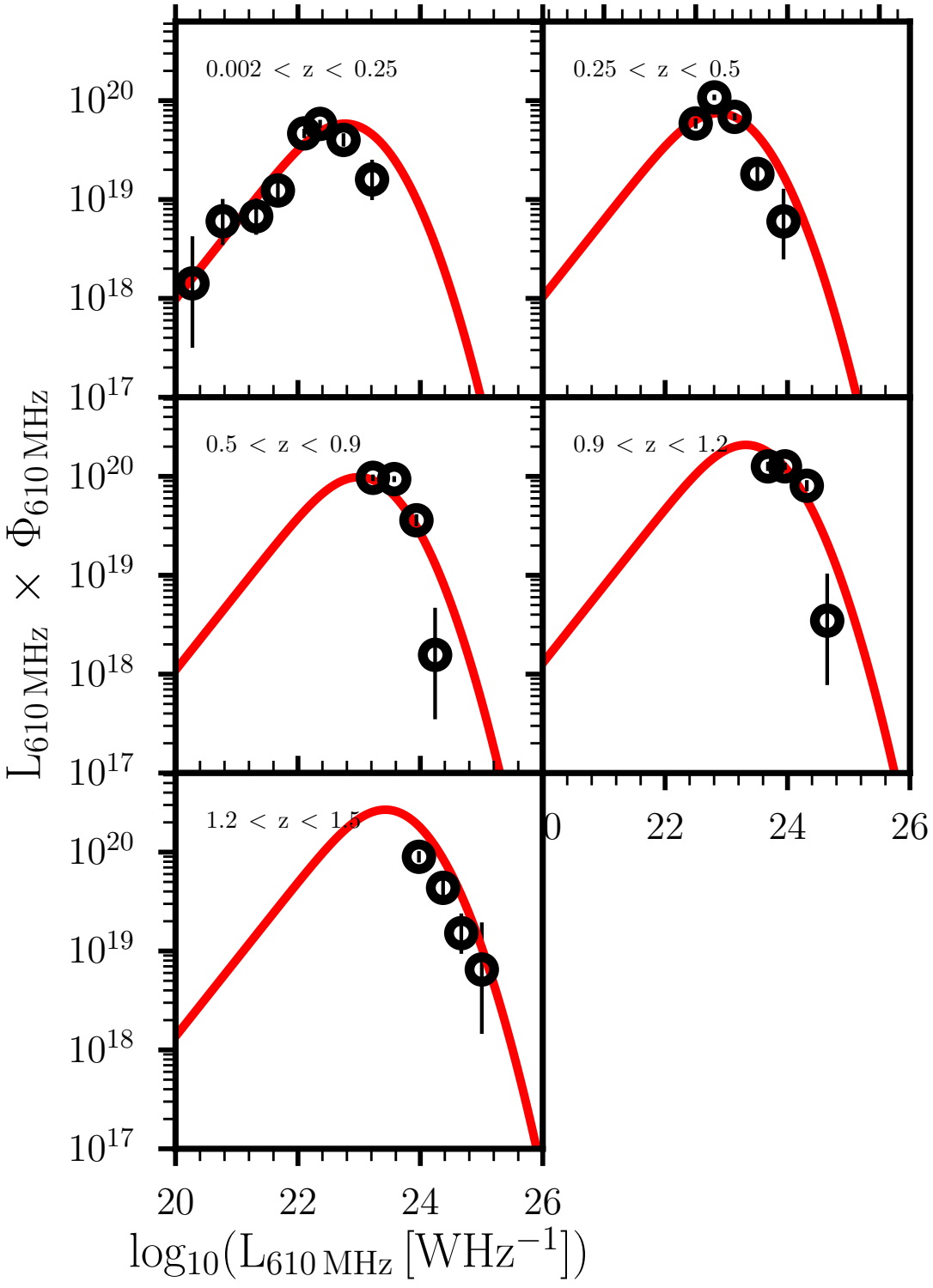

FIGURE 3.10: Luminosity density for 610 MHz GMRT star forming galaxies (open black circles) in 5 redshift bins. The solid red curves correspond to the best fit PLE LFs in each redshift bin.

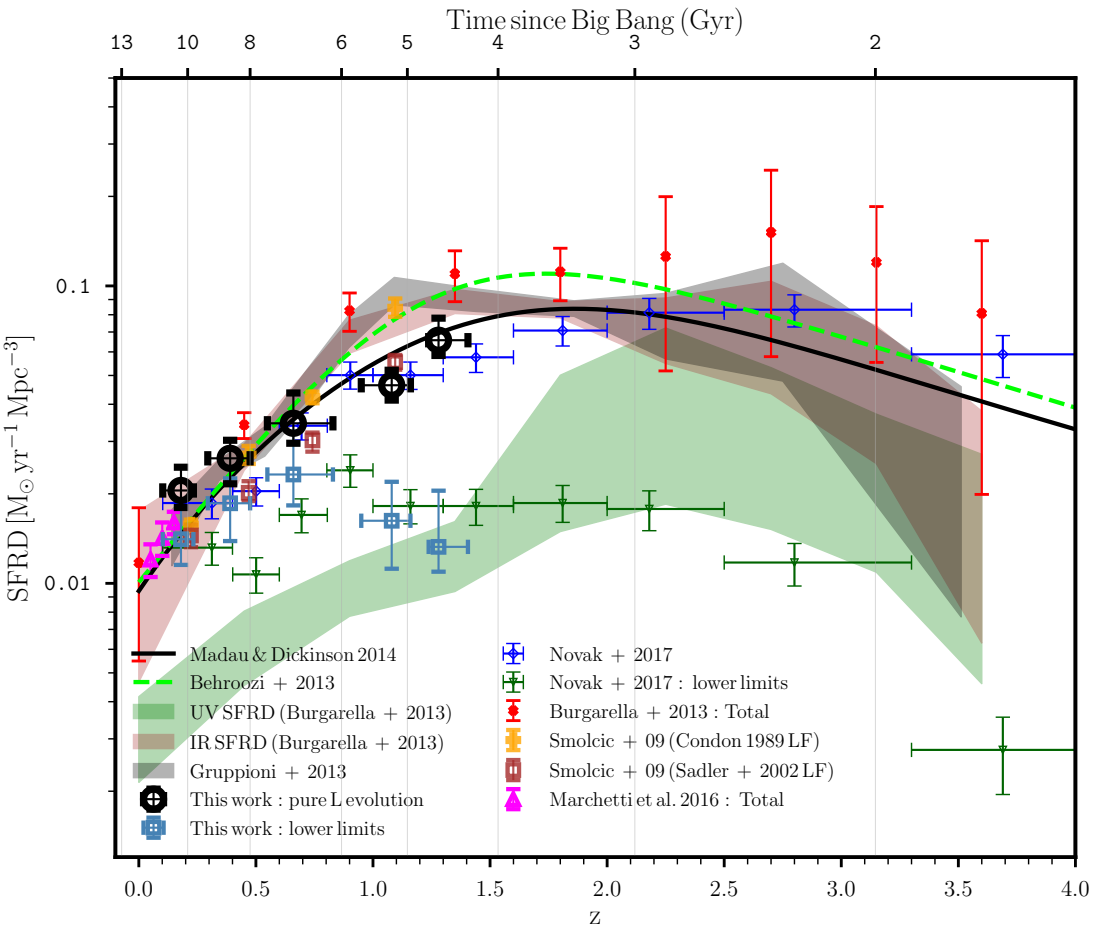

FIGURE 3.11: Cosmic star formation rate density history. Our total SFRD values estimated from the pure luminosity evolution in separate redshift bins are shown as open black circles. See text for details of the data points shown for comparison that are indicated in the legend. We limit the plot between $0 < z < 4$ redshift range.

3.7 Conclusions

Over the last few years Bonzini et al. (2013), Padovani et al. (2015) and Smolčić et al. (2017a) have for the first time managed to carry out a complete census of populations contributing to the faint radio sky at 1.4 and 3.0 GHz with the JVLA. These were done over a relatively small (0.5 deg^2 and 2 deg^2 for JVLA-ECDFS and JVLA-COSMOS respectively) contiguous area reaching rms sensitivities (i.e. 6μJy and 2.3μJy at 1.4 and 3.0 GHz respectively) comparable to our study. Such datasets that provide images of the radio flux density over small regions at these sensitivities are still rare but will be achieved by the MeerKAT and SKA1 albeit over much larger areas. We study a sample of 1685 SFGs covering ~1.86 deg^2 down to a a minimum noise of ~7.1 μJy / beam in the ELAIS N1 field at 610 MHz with the GMRT. The depth of our 610 MHz data represent a potentially very useful tool to address the role of SFGs in galaxy evolution. These SFGs were obtained from a combination of diagnostics from the radio and X-ray luminosity, optical spectroscopy, mid-infrared colors, and 24μm and IR to radio flux ratios. Of the 1685 SFGs from our sample, 496 have spectroscopic redshifts whereas 1189 have photometric redshifts.

Deep multi-wavelength spectrophotometric datasets with comparable resolutions and sensitivities to our radio data will be needed to improve our source classification. More specifically, mid-infrared multi-band photometry and optical/near-infrared spectroscopy are the limiting factor in our case. However, since no deep (wide-area) mid-infrared will not be carried out in the foreseeable future, the best avenue toward improving the diagnostics for such scientific work in the future is via multi-object wide-field optical/near-infrared spectroscopy.

We study the infrared-radio correlation (IRRC) for the star-forming galaxies. We measure an evolution with redshift of the IRRC for 1.4 GHz radio luminosities to be $q_{IR} = 2.86 \pm 0.04(1 + z)^{-0.20\pm0.02}$, where q_{IR} is the ratio between the total infrared luminosity ($L_{IR}, 8 - 1000\mu$ m) the 1.4 GHz radio luminosity ($L_{1.4\,GHz}$).

We have used the non-parametric V/Vmax test and the radio luminosity function to investigate the cosmic evolution of SFGs. Sadler et al. (2007) found evidence that low-luminosity radio sources experience mild evolution with an increase in their number density by a factor of ~ 2 at $z = 0.55$. Smolčić et al. (2009a) found a mild evolution of the SFGs in the VLA-COSMOS survey out to $z \sim 1.3$. We construct the RLF at 610 MHz for our SFGs and find positive evolution. This is consistent with previous studies, for the SFG RLF scaled to 610 MHz from 1.4 GHz assuming a spectral index of $\alpha = -0.8$. The exact shape of the radio spectral energy distribution (SED) of SFGs is usually assumed to be a superposition of the steep synchrotron spectrum, described by a power law (see Condon 1992), even so, there are processes which can alter the shape of the spectra. Recent work by Lacki (2013) and Tisanić et al. (2019) have developed theoretical models describing an alternative picture to the simple power-law shape which includes spectral curvature. However, deep multi-frequency radio observations of representative samples of galaxies are needed to study the radio SED and understand the physical processes shaping it across redshifts. We also compare our results to models from the literature and find that the Mancuso et al. (2017) and Wilman et al. (2008) models do compare well to our data. However, there is an exception for the lowest redshift bin, where none of the models is able to reproduce the low-luminosity observations. Our LFs behave very well at high luminosities, where other samples (see e.g. Smolčić et al. (2009b)) show an excess of sources with respect to models. This can be interpreted as contamination due to AGN. This can be better addressed with better multi-wavelength data and better-proven AGN diagnostics. Our radio LFs can be well described by a local LF evolved only in luminosity as $L_{610\,MHz} \propto (1 + z)^{(2.95\pm0.19)-(0.50\pm0.15)z}$.

We converted our radio luminosities to SFRs using a redshift dependent IR-radio correlation. By integrating over the entire luminosity range the LF fits in various redshift bins, we derived the cosmic star formation density out to $z = 1.5$ for our SFG sample. Our estimates of the SFRD is consistent with previous measurements from the literature when all the SFR estimates are rescaled to a Chabrier IMF. Novak et al. (2017) assumed pure luminosity evolution for their LF, consistent with the measurements by Smolčić et al. (2009b) (and recent result by Gruppioni et al. (2013) assuming the redshift dependent IR-radio correlation parameter). All these studies found broad agreement between the radio SFRD evolution and UV/IR surveys, observing a steep decline from $z = 1$ to 0. Our sample reproduces this expected steep decline in the star formation rate density since $z \sim 1$. This work represents a benchmark for studying the

evolution of the RLF and SFR function with cosmic time at the faint low-frequency regime in spite of our redshift limit.

In the near future we plan to undertake the exploitation of the MeerKAT International GHz Tiered Extragalactic Exploration (MIGHTEE) Survey (Jarvis et al., 2016) with the MeerkAT SKA precursor (Jonas & MeerKAT Team, 2016). MIGHTEE will survey well-studied extragalactic deep fields (E-CDFS, COSMOS, XMM-LSS and ELAIS-S1), totaling 20 square degrees at 1.4 GHz, to ∼2 μJy/beam rms. A survey matched in resolution and depth will be undertaken with the upgraded GMRT (Gupta, 2014), and the present work will thus be precious to make the most of such GMRT data. It is our hope that a complete and expansive review of this topic will be able to do justice to the wealth of current and ongoing measurements contributing to our understanding of this aspect of galaxy evolution. An extensive compilation from the literature of SFR density measurements as a function of redshift will be investigated in future works. This will provide rich compilation of SFR density evolution which will help with a robust constraint for many investigations of galaxy evolution.

Chapter 4

The evolution of the Low-Frequency Radio AGN Population to $z \simeq 1.5$

Abstract

The Faint Low-Frequency Radio Universe in Continuum: Exploitation of the Pre-SKA Deepest Survey

We investigate the cosmic evolution of radio sources with radio powers ($L_{610\,MHz} \sim 10^{20} - 10^{27}\,W\,Hz^{-1}$) out to z ~ 1.5 using a GMRT 610-MHz survey covering ~1.86 deg^2 of the ELAIS N1 field down to a minimum rms noise of ~7.1 μJy / beam. We divide our sample into star forming galaxies (SFGs), radio-quiet (RQ) and radio-loud (RL) Active Galactic Nuclei (AGN) using a combination of multi-wavelength diagnostics. We show that the radio rest-frame luminosity and the infrared bolometric rest-frame luminosity are equivalently good tracers of the Star Formation Rate (SFR) for our SFGs and RQ AGN. We study the SFR − $M_\star$ relation for our sample and find that RQ AGN occupy the same locus as SFGs in this plane, suggesting that the host galaxies of the majority of RQ AGN are not significantly different from SFGs. We then derive the 610-MHz luminosity functions for the overall AGN population up to $z \simeq 1.5$ and constrain its evolution via continuous models of pure density and pure luminosity evolution and find best-fit parametrizations of $\Phi^\star \propto (1+z)^{(2.25\pm0.38)-(0.63\pm0.35)z}$ and $L_{610\,MHz} \propto (1+z)^{(3.45\pm0.53)-(0.55\pm0.29)z}$ respectively. We also construct the radio luminosity function for RQ and RL AGN to $z \simeq 1.5$, and we find a fairly mild evolution with redshift which can be fitted with a pure luminosity evolution of the form $L_{610\,MHz} \propto (1+z)^{(2.81\pm0.43)-(0.57\pm0.30)z}$ for RQ AGN and $L_{610\,MHz} \propto (1+z)^{(3.58\pm0.54)-(0.56\pm0.29)z}$ for RL AGN.

4.1 Introduction

From an observational point of view, Active Galactic Nuclei (AGN) can be defined as apparent stellar sources with non-thermal spectra and high bolometric luminosity ($\gtrsim 10^{42}$ergs^{-1}) that can exceed that of the host galaxy (e.g. see Bower et al. 2006; Croton et al. 2006; Bonzini et al. 2013; Padovani 2016a). An AGN emits radiation at all wavelengths, from radio to X/γ-rays. The non-stellar nature of the radiation emitted by an AGN is understood to result from the accretion of matter by a supermassive black hole at the center of its host galaxy, with AGN properties depending on their evolutionary stage and on the rate of fuelling on their central engine. The main mechanism of radio continuum emission in both AGN and Star Forming Galaxies (SFGs) is synchrotron radiation. In AGN the electrons are accelerated in relativistic jets powered by the accretion of gas onto a supermassive black hole (e.g. see Condon 1992; Padovani et al. 2011; Bonzini et al. 2013).

The current unified theories of active galactic nuclei (AGN) postulate that there are two physically distinct classes of AGN: radio-loud (RL) and radio-quiet (RQ) AGN (see Wilson & Colbert 1995 and references therein). RL AGN produce large-scale radio jets and lobes, with the kinetic power of the jets being a significant fraction of the total bolometric luminosity whereas the weak radio ejecta of the RQ AGN are energetically insignificant (e.g. see Neugebauer et al. 1986; Steidel & Sargent 1991; Rawlings & Saunders 1991). Observationally, RQ AGN are thus radio sources that show signs of AGN activity at other bands (IR, optical or X-ray) and only a minority of them show the classical large-scale radio structures (jets and lobes) associated with RL AGN (Padovani et al. 1993; Padovani 1993). A multitude of studies have compared the properties of these two AGN classes in various bands to try and shed light on their inherent differences. It has been proposed that RQ AGN represent scaled-down versions of RL AGN with mini radio jets (Giroletti & Panessa 2009; Bonzini et al. 2013; Delvecchio et al. 2017). Other studies have argued that the radio emission of RQ AGN come from star formation in the host galaxy (Kimball et al., 2011; Padovani et al., 2011). Dunlop et al. (2003) found that the host galaxies of these two AGN classes are also different, with those of RL AGN mostly hosted by passive ellipticals while those of RQ AGN, excluding the most powerful ones, being spirals. Bonzini et al. (2013) showed that RQ AGN can have host galaxy properties very similar to SFGs, especially where the AGN emission is obscured by dust in so-called "type II" objects.

Measurement of the evolution of AGN underpins our understanding of galaxy evolution over cosmic time. In this context, radio continuum observations provide key information, mainly through the mechanical feedback produced by radio jets in AGN. Studying the properties of radio AGN over cosmic time and comparing the properties of the two RQ and RL sub-classes requires their identification and classification in deep ($\lesssim$ 1 m Jy) and wide (> 1 deg^2) radio surveys, which has been possible only recently (Padovani et al. 2009, 2011; Simpson et al. 2012; White et al. 2015, and references therein). Brown et al. (2001) found strong evolution in the low-luminosity radio population at 1.4-GHz out to z = 0.55, and by assuming pure luminosity density evolution of the form $L \propto (1 + z)^K$ found $3 < K < 5$ for AGN with $10^{23} < L_{1..4\,GHz} < 10^{25}$W Hz^{-1}. Sadler et al. (2007) found significant evolution for AGN with

$10^{24} < L_{1.4\,GHz} < 10^{25}\,W\,Hz^{-1}$ consistent with pure luminosity evolution where $L \propto (1+z)^{2.0\pm0.3}$ from $z = 0.7$, using the 2SLAQ Cannon et al. (2006) luminous red galaxy survey catalogue combined with Faint Images of the Radio Sky at Twenty-Centimeters (FIRST; Becker et al. (1995)) and NRAO VLA Sky Survey (NVSS; Condon et al. (1998)).

Prescott et al. (2016) determined radio luminosity functions at 325-MHz for a sample of radio-loud AGN by matching a 138 deg^2 radio survey conducted with the Giant Metrewave Radio Telescope (GMRT), with optical imaging and redshifts from the Galaxy And Mass Assembly survey (GAMA). By fitting the AGN radio luminosity function out to $z = 0.5$ as a double power law, and parametrizing the evolution as $\Phi \propto (1+z)^K$, they found evolution parameters of $K = 0.92 \pm 0.95$ assuming pure density evolution and $K = 2.13 \pm 1.96$ assuming pure luminosity evolution. Yuan et al. (2016b) proposed a mixture evolution scenario to model the evolution of the radio luminosity function (RLF) of steep spectrum AGN, based on a Bayesian method. In this scenario, the shape of the RLF is determined by both the density and luminosity evolution. Based on a sample of over 1800 radio AGN at redshifts out to $z \sim 5$ from 3 GHz radio data in the COSMOS field from the JVLA-COSMOS project, which have typical stellar masses within $\sim 3 \times (10^{10} - 10^{11}) M_\odot$, Smolčić et al. (2017b) derived the 1.4-GHz radio luminosity functions for radio AGN, out to $z \sim 5$. They defined their radio AGN as all the sources that show a significant radio excess with respect to what is expected from pure SF, independently from the properties of the host galaxies. They constrained the evolution of this population via continuous models of pure density and pure luminosity evolution and found best-fit parametrizations of $\Phi^\star \propto (1+z)^{(2.00\pm0.18)-(0.60\pm0.14)z}$ and $L^\star \propto (1+z)^{(2.88\pm0.82)-(0.84\pm0.34)z}$ respectively. Ceraj et al. (2018) studied a sample of 1604 moderate-to-high radiative luminosity active galactic nuclei (HLAGN) selected at 3 GHz by the JVLA-COSMOS project. By assuming pure density and pure luminosity evolution models they constrained their cosmic evolution out to $z \sim 6$, finding $\Phi^\star \propto (1+z)^{(2.64\pm0.10)-(0.61\pm0.04)z}$ and $L^\star \propto (1+z)^{(3.97\pm0.15)-(0.92\pm0.06)z}$. These several studies, while clearly showing evolution, yield different quantitative results and identify the AGN population with differing selection strategies and redshift range. Here we explore the evolution of AGN based on the the faint low-frequency radio population out to $z \simeq 1.5$, distinguish RQ and RL AGN and compare to the evolution of SFG from the same radio sample.

This is the third paper exploiting our deep 610-MHz GMRT observations of the ELAIS N1 field, covering $\sim$1.86 deg^2 down to a minimum noise of $\sim$7.1 μJy / beam. The ELAIS N1 field has deep extragalactic observations with the Infrared Space Observatory (ISO) due to its low infrared background (see Rowan-Robinson et al. 2004). From that time, ELAIS N1 has become one of the best-studied 1–10 deg^2 extragalactic fields. The wealth of mid-infrared and far-infrared wide-area imaging data, combined with a number of imaging surveys at far-ultraviolet to near-infrared wavelengths, has allowed the astronomical community to greatly improve estimates of the stellar masses and star formation rates of galaxies up to high redshift (Vaccari, 2015).

- The first publication presents a deep 610-MHz radio observation of the ELAIS N1 survey field using the GMRT. We present the source counts and classification of the radio sources by class. We also

conduct a study of the radio spectral properties of this sample.

- The second publication presents a study of star forming galaxies selected from the currently deepest low-frequency radio survey at 610-MHz. We derive the IR-radio correlation and luminosity functions of star-forming galaxies, as well as the cosmic star formation rate history up to $z \sim 1.5$.

Our previous study demonstrated the importance of using deep radio surveys as a tool to study the cosmic star formation history. In this work, we extend our analysis to the AGN population. Our AGN population comprises of RQ AGN and RL AGN populations classified using multi-wavelength data. We study the radio-IR correlation for the RQ AGN and RL AGN populations comparing them to the SFGs population. This paper exploits the evolution of AGN in the low-frequency faint radio source population to z $\sim$ 1.5. We investigate the well-established relation between star formation rates (SFR) and main sequence (MS) of our various classes of AGN as well as the SFGs presented in Ocran et al. (2020b) and also compare to literature. The layout of this paper is as follows: we first introduce the 610-MHz AGN data in Section 4.2. In Section 4.3, we present the analysis and results of the our AGN sample, comparing them to the SFGs we presented in Ocran et al. (2020a) and Ocran et al. (2020b). The sample selection for estimation of the radio AGN luminosity function and the method applied is discussed in Section 4.4. Also, we describe how we constrain the evolution of the AGN luminosity function out to $z \simeq 1.5$. We provide discussions on the evolution of our AGN sample in Section 4.5. We summarize our results and discuss future work in Section 4.6. We adopt throughout the paper a flat concordance Lambda cold dark matter (ΛCDM), with the following parameters: Hubble constant $H_0 = 70\,\mathrm{kms}^{-1}\,\mathrm{Mpc}^{-1}$, dark energy density $\Omega_\Lambda = 0.7$ and matter density $\Omega_\mathrm{m} = 0.3$.

4.2 Sample

4.2.1 GMRT 610-MHz Data

For our analysis we employ our 610-MHz radio survey covering $\sim$1.86 deg^2 of the ELAIS N1 field carried out with the GMRT. This is currently the deepest low-frequency radio survey at 610-MHz. We achieved a minimum noise of 7.1 μJy beam^{-1} and an angular resolution of 6 arcse $\times$ 6 arcsec with the median noise in the mosaic being 19.5μJy beam^{-1}. The higher noise values are attributed to enhanced rms in small regions around very bright sources and from the lower mosaic weights at the edge of the mosaic (see Ocran et al. 2020a). The ELAIS N1 field was originally chosen for a deep mid-infrared survey with the Infrared Space Observatory (Rowan-Robinson et al., 2004; Vaccari et al., 2005; Gonzalez-Solares et al., 2005), which has since led to a concerted multi-wavelength effort in the field (Vaccari, 2015; Shirley et al., 2019). The radio dataset, its reduction, the source extraction, multi-wavelength association and classification process is described in detail in Ocran et al. (2020a).

4.2.2 AGN Sample

Our AGN sample is defined as the sample of 610-MHz sources with at least one AGN indicator. In Ocran et al. (2020a,b) we used radio and X-ray luminosity, optical spectroscopy, mid-infrared colours, and IR to radio flux ratios to search for evidence of the presence of an AGN in our sub-sample with redshifts (see also Ocran et al. 2017). If an AGN is not present in the source according to any of the several criteria we adopted, then we inferred that the source was actually an SFG. While different diagnostics are by and large reliable, none of them is complete, hence the need to adopt a multi-wavelength approach. The sample used for the purposes of classification is therefore selected as providing at least one multi-wavelength AGN diagnostic and a redshift association. Since our criteria for classification of a source as an AGN is that any of the AGN indicators is positive, we would bias the population if we allowed AGN detected outside of the population of sources with redshifts to be included to the AGN list. Limiting our sample to the sources with redshift and at least one AGN diagnostic provides a rigorous control sample.

Once AGN are classified in this way, the distinction between RQ and RL AGN is only based on the mid-infrared radio flux ratio, quantified by q_{24}, which is the mid-infrared radio correlation criteria. This is based on the redshifted q_{24} value for the M82 local standard starburst galaxy template as implemented by Bonzini et al. (2013) to identify SFGs, RQ AGN and RL AGN. As detailed in Ocran et al. (2020a,b), the total number of sources with redshifts for which we can define at least one AGN indicator is 2305 (i.e. $\sim$ 54% of the whole 4290 sample and $\sim$ 74% of the 3105 sources with redshifts).

Redshift estimates used in this work are a combination of spectroscopic and photometric redshifts from (i.e. the Hyper Suprime-Cam (HSC) Photometric Redshift Catalogue (Tanaka et al., 2018b), the revised SWIRE Photometric Redshift Catalogue (Rowan-Robinson et al., 2013) and the Herschel Extragalactic Legacy Project (Vaccari, 2016; Shirley et al., 2019, HELP)).

We classified 1685 sources as SFGs, constituting ~73% of the 2305 sources with at least one AGN indicator, while 620 sources were classified as AGN, constituting ~27%. Within our AGN sample of 620 sources, 281 (45%) sources were classified as RQ AGN whereas 339 (55%) sources were classified as RL AGN.

Figure 4.1 shows the distribution of the total AGN (green histogram), RL AGN (red histogram) and RQ AGN (blue histogram) population with r_{AB} (left panel) and redshift (right panel). Figure 4.2 shows a mid-infrared colour-colour diagram for our sample of sources classified as radio AGN that have cataloged flux densities in all four Spitzer IRAC bands at 3.6, 4.5, 5.8, and 8.0 μm (left panel). This colour-colour diagram is based on the modeling of Sajina et al. (2005), who divided the diagram into different regions separated by dashed lines in Figure 4.2. Region 1 selects sources where the infrared emission is dominated by non-equilibrium emission of very small dust grains, which is interpreted as PAH destruction by the hard ultraviolet spectrum of an AGN. Region 2 is mainly populated by dusty star-forming galaxies at redshift $z < 0.5$ with strong polycyclic aromatic hydrocarbon (PAH) bands, as the 3.6 and 8.0 μm flux contain the strongest PAH features at low redshift. Region 3 can be divided into two as denoted by

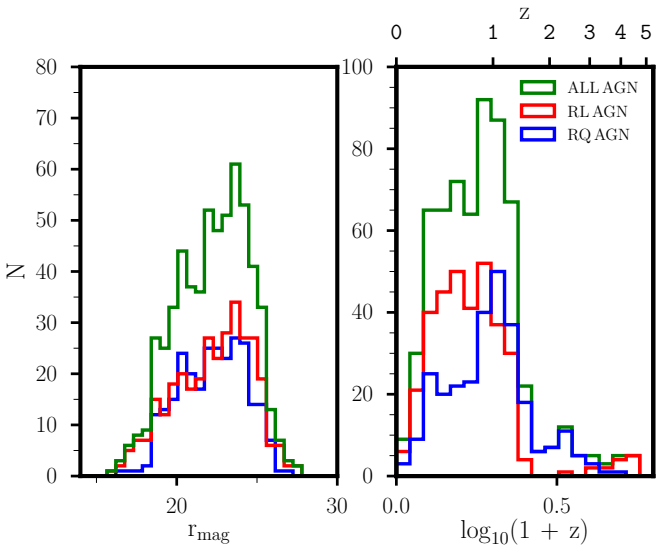

FIGURE 4.1: Distribution of the total AGN (green histogram), RL AGN (red histogram) and RQ AGN (blue histogram) with r_{AB} (left panel) and redshift (right panel).

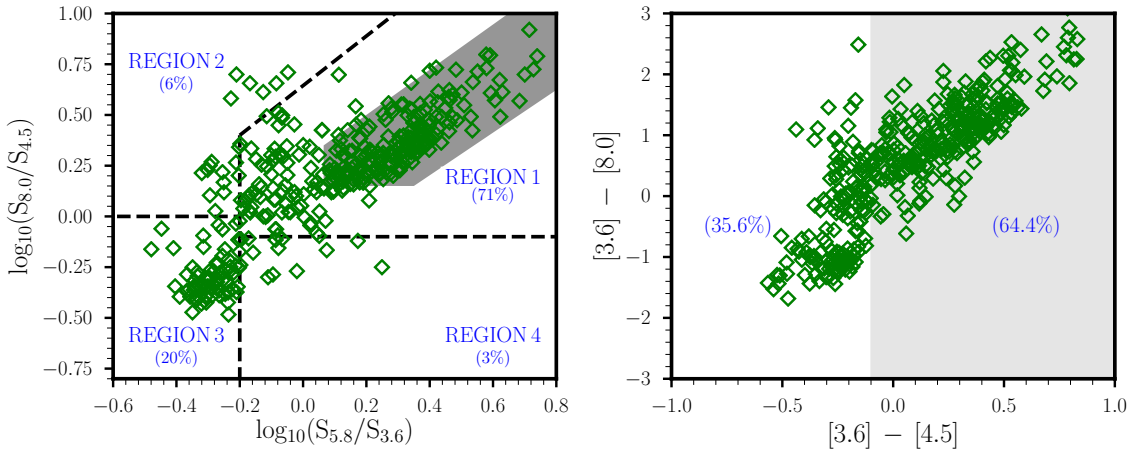

FIGURE 4.2: Left: IRAC colour-colour diagram for our full AGN sample with four-band IRAC detections. The four regions outlined by dashed lines are the ones defined by Sajina et al. (2005) with the fraction of AGN in each region given in the plot whilst the grey area defines the AGN criterion by Donley et al. (2012). Right: MIR [3.6μm] – [8.0μm] vs [3.6μm] – [4.5μm] colour-colour plot. The grey shaded region shows the location of the Richards et al. (2006) selection for Type 1 quasars.

Taylor et al. (2007) and Banfield et al. (2011): (a) where the region is populated by elliptical galaxies dominated by the starlight of old stellar populations (i.e $\log_{10}(S_{8.0}/S_{4.5}) \leq -0.5$); and (b) where the region is populated by galaxies with fainter PAH emission (i.e $\log_{10}(S_{8.0}/S_{4.5}) > -0.5$). The grey area in the left panel represents the more restrictive AGN selection criteria presented by Donley et al. (2012), which we adopted in our work. Richards et al. (2006) suggested that Type 1 quasars may be selected by taking $[3.6] - [4.5] = -2.5 \log(S_{3.6}/S_{4.5}) > -0.1$. We compare our selection of AGN to this criterion and find 263 sources corresponding to $\sim 65\%$ of sources with four color IRAC photometry would be classified as Type 1 AGN (see grey area in right panel of Figure 4.2).

TABLE 4.1: Table summarizing the median values of q_{IR} at 610-MHz for SFGs, RQ AGN and RL AGN.

Median $q_{IR\,SFG}$	Median $q_{IR\,RQ\,AGN}$	Median $q_{IR\,RQ\,AGN}$
2.32±0.30	2.10±0.34	1.75±0.40

4.3 Analysis and Results

4.3.1 The InfraRed-Radio Correlation (IRRC)

It has long been known that the ratio of infrared and radio luminosity in SFGs follows a tight empirical relation. This so-called IR/radio correlation (IRRC) is now well-established using a variety of ways to measure infrared and radio luminosities (see e.g. Dickey & Salpeter 1984; de Jong et al. 1985; Bell et al. 2003). In Ocran et al. (2020b), we studied the IRRC for our SFGs using the IR bolometric (i.e. integrated between 8 and 1000 μm) luminosity and the 1.4-GHz radio luminosity (see also Ocran et al. 2017). In this work, we extend our IRRC analysis to RQ and RL AGN as well as SFGs. The SFGs used in this work is based on the sub-sample presented in Ocran et al. (2020b). Throughout, we assume a fixed spectral index, $\alpha = -0.8$, and as such q_{IR} (610 MHz) is given by the simple conversion $q_{610\,MHz} = q_{1.4GHz} - 0.29$ (see Subsection 3.1 of Ocran et al. 2020b). We reported a median q_{IR} (610 MHz) of 2.32 for the SFGs. In Figure 4.3, we plot rest-frame 610-MHz luminosity versus the IR bolometric luminosity to show which sources follow the IRRC. The diagonal solid line in each panel shows the median q_{IR} given at 610-MHz for the SFGs since the IRRC is believed to be driven mostly by star formation (Condon, 1992; Yun et al., 2001). The dashed diagonal lines represent the $\pm 1\sigma$ limits given by the median absolute deviation (MAD) (Rousseeuw & Croux, 1993), $\sigma_{q_{IR\,SF}} = 0.30$, of the correlation. The contours levels are 1, 2, 3, and 4 σ. RQ AGN also show a tight correlation in agreement with the IRRC, with a median q_{IR} value of 2.10. RL AGN lie well above the IRRC for SFGs and RQ AGNs with a median q_{IR} value of 1.75. Table 4.1 summarizes the median values of q_{IR} at 610-MHz for SFGs, RQ AGN and RL AGN.

AGN-powered sources, by definition, lie above the IRRC because of the additional AGN component to radio emission. SFGs on the other hand reside close to the IRRC. The additional component to the radio luminosity for AGN-powered sources results in lower q_{IR} values (e.g. see Rawlings et al. 2015).

4.3.2 Radio emission in the faint low-frequency radio source population

The origin of the radio emission in RQ AGN is vigorously debated. Bonzini et al. (2015) compared the SFR computed from IR luminosity with the the SFR derived from radio luminosity for their 675 radio sources and observed a good agreement between SFR_{radio} and SFR_{IR} for RQ AGN. More recent work by Delvecchio et al. (2017) exploited multi-band information in the COSMOS field to derive accurate star SFR via SED fitting. They analyzed the ratio between the 1.4-GHz radio luminosity and the SFR for each source and found that ~30% of the sources with AGN signatures at non-radio wavelengths display a

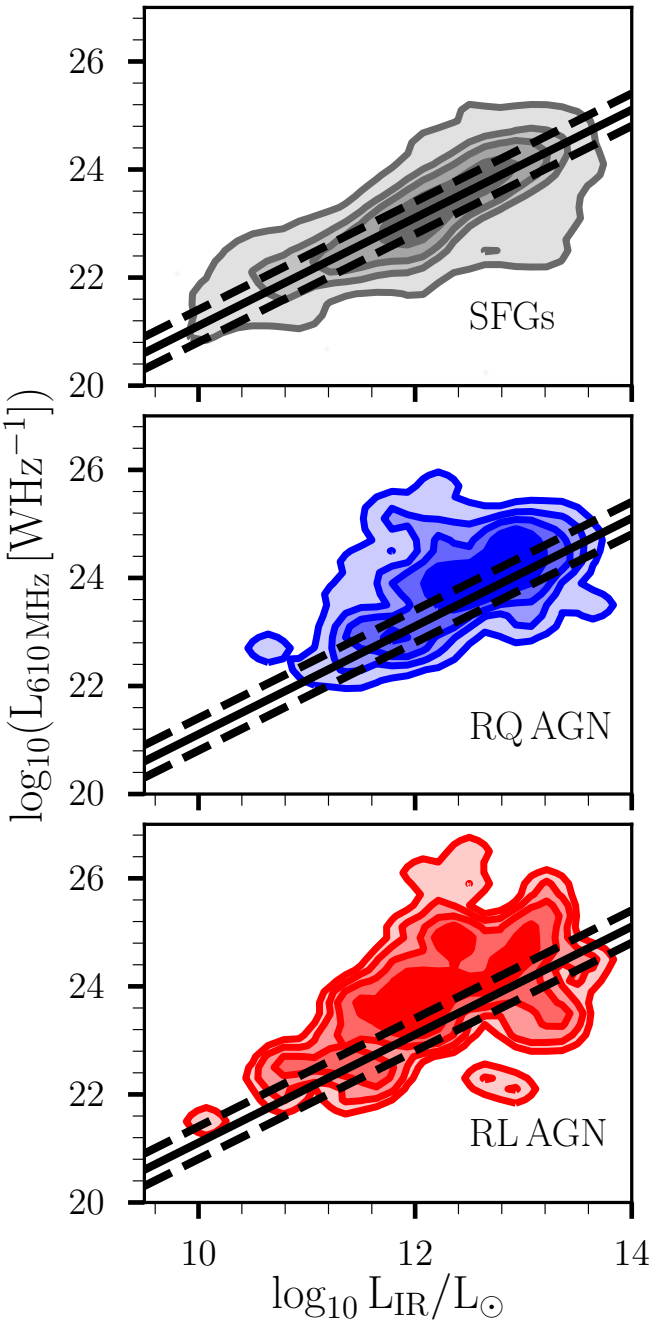

FIGURE 4.3: Rest-frame 610-MHz luminosity as a function of IR luminosity for SFGs (top panel), RQ AGN (middle panel) and RL AGN (bottom panel) represented as density contours. The solid line represents the IRRC with a q_{IR} value equal to the mean SF-powered q_{IR} of 2.32 (see Ocran et al. 2020b), while the dashed lines represent the $\pm 1\sigma$ limits, $\sigma_{q_{SF}} = 0.30$, of the correlation. The contours levels are 1, 2, 3, and 4 σ.

significant radio excess. Recent modeling work by Mancuso et al. (2017) supports the likely scenario that RQ AGN are composite systems where SF- and AGN-triggered radio emission can coexist over a wide range of relative contributions.

We characterize the star formation properties of the three types of sources by investigating IR and radio-based SFR, presented in Figure 4.4. The IR star formation rates were obtained by the Herschel Extragalactic Legacy Project (Vaccari, 2016; Hurley et al., 2017; Małek et al., 2018; Shirley et al., 2019, HELP), which collected multi-wavelength photometry and performed homogeneous physical modeling over roughly 1300 deg^2 of extragalactic sky covered by the Herschel Space Observatory's SPIRE Camera Griffin et al. (2010); Pilbratt et al. (2010), focusing on ELAIS N1 as a pilot field. Figure 4.4 shows the binned $\log_{10}(\mathrm{SFR_{IR}})$ vs $\log_{10}(\mathrm{SFR_{radio}})$ for SFGs, RQ AGN and RL AGN in bin width of 0.5 $\log_{10}(\mathrm{SFR_{IR}})$. It should be noted that $\mathrm{SFR_{radio}}$ is obtained under the assumption that the radio emission is entirely ascribed to star formation.

The radio and IR rest-frame luminosities correlates rather well across a wide range of luminosities for both SFGs and RQ AGN as shown in Figure 4.4 . This strongly suggests that the two quantities are equivalently good tracers of the SFR and that the main contribution to the radio emission in RQ AGN is due to the star-formation in the host galaxy rather than being powered by black hole activity. The behaviour of the RL AGN further supports this hypothesis since they scatter out from the one-to-one relation in Figure 4.4.

This is expected since the SFR computed from the radio luminosity is overestimated due to the jet contribution to the radio emission. Note that the comparison of the two SFR tracers can in principle also allow us to isolate sources that have been misclassified. At the high end of the radio-based SFR estimate (i.e. $\log_{10}\mathrm{SFR_{radio}} > 2.8$) the RQ AGN deviate from the one-to-one line. We state the possibility of a contamination to the RQ AGN population from RL AGN with a strong contribution from the AGN to the 24μm flux density that enhanced their q_{24} value into the SFGs locus since our distinction between RL and RQ AGN is based on q_{24} (see Ocran et al. 2017, 2020a. We note that the deviation from the IRRC (see subsection 4.3.1) seems to become larger going to higher luminosities. This may offer another interpretation, i.e. that only QSO-like objects host mini-jets while in lower luminosity sources radio emission is originated by star formation. This might be in line with recent results from White et al. (2017) on optically selected QSOs, where they found a radio luminosity excess with respect to SFGs that appears to be correlated with the optical luminosity. We see a similar trend in the RL AGN.

Figure 4.5 compares the SFR computed from IR luminosities with the expected SFR as derived from the radio luminosities for our individual SFGs, RQ AGN and RL AGN and performed bootstrapped linear regression.* fits to each sub-population. Different colours and symbols represent different classes of objects. The results of the linear regression fit are:

*A resampling method used to estimate the variability of statistical parameters from a dataset which is repeatedly sampled with replacement (Lopes et al., 2019).

TABLE 4.2: Median values of SFR_{IR} for the RQ AGN, RL AGN and SFGs in each redshift bin. The errors denote the difference between the 15.8 and 84.2 percentiles.

Redshift range	$N_{RQ\,AGN}$	RQ AGN $SFR_{IR}[M_\odot yr^{-1}]$	$N_{RL\,AGN}$	RL AGN $SFR_{IR}[M_\odot yr^{-1}]$	N_{SFG}	SFG $SFR_{IR}[M_\odot yr^{-1}]$
$0.002 < z < 0.25$	13	$1.06^{+0.25}_{-0.14}$	21	$0.66^{+0.52}_{-0.57}$	214	$0.52^{+0.74}_{-0.56}$
$0.25 < z < 0.5$	24	$1.57^{+0.29}_{-0.37}$	30	$1.06^{+0.48}_{-0.29}$	294	$1.21^{+0.28}_{-0.37}$
$0.5 < z < 0.9$	31	$1.98^{+0.40}_{-0.30}$	39	$1.69^{+0.92}_{-0.48}$	240	$1.61^{+0.42}_{-0.32}$
$0.9 < z < 1.5$	58	$2.27^{+0.30}_{-0.37}$	29	$2.13^{+0.33}_{-0.32}$	273	$2.15^{+0.35}_{-0.27}$

$$\log_{10}(SFR_{IR})_{SFG} = 0.81^{+0.03}_{-0.03} \times \log_{10}(SFR_{radio})_{SFG} + 0.20^{+0.04}_{-0.05} \quad (4.1)$$

$$\log_{10}(SFR_{IR})_{RQ\,AGN} = 0.50^{+0.07}_{-0.06} \times \log_{10}(SFR_{radio})_{RQ\,AGN} + 0.93^{+0.15}_{-0.15} \quad (4.2)$$

$$\log_{10}(SFR_{IR})_{RL\,AGN} = 0.52^{+0.08}_{-0.07} \times \log_{10}(SFR_{radio})_{RL\,AGN} + 0.40^{+0.19}_{-0.22} \quad (4.3)$$

The fits for the RL AGN (dashed red line) and RQ AGN (dashed blue line) from Figure 4.5 show a similar slope. Both fits are flatter than the SFG fit. This is not a surprise as in both cases deviations from the IRRC are stronger going to higher luminosities. This again supports the idea that there is a fraction of RQ AGN hosting mini radio jets. And this fraction increases with luminosity. Despite similar slopes, RL and RQ AGN fits differ by an offset, which points toward RQ AGN being hosted, on average, by higher SFR galaxies. This is further supported by Figure 4.6, which shows the host galaxy IR-derived SFR distribution in four different redshift bins for RL and RQ AGN. AGN host galaxies span a very wide range of SFRs, with RQ AGN generally hosted by higher SFR galaxies and RL AGN (which are mainly at low redshifts) hosted predominantly by galaxies with low SFRs. Table 4.2 presents median values of the SFR_{IR} for the RQ AGN, RL AGN and SFGs in each redshift bin . The errors denote the difference between the 15.8 and 84.2 percentiles.

4.3.3 SFR vs Stellar Mass

The SFR of SFGs is tightly correlated with the stellar mass of the galaxy by the so called "star formation main sequence" (SFMS). The correlation reveals interesting mechanisms of the star formation history. A high scatter in this correlation implies a stochastic star formation history with many discrete 'bursts',

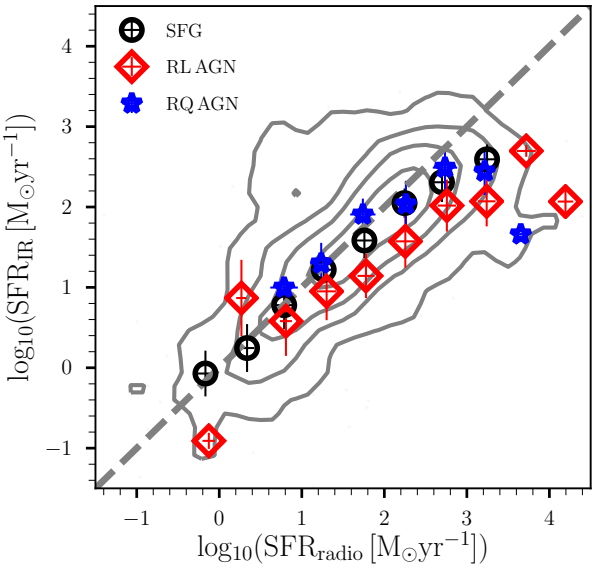

FIGURE 4.4: Binned $\log_{10}(\mathrm{SFR_{IR}})$ vs $\log_{10}(\mathrm{SFR_{radio}})$ for the SFGs, RQ AGN and RL AGN in bin width of $0.5\log_{10}(\mathrm{SFR_{IR}})$. The background contours represents the $\log_{10}(\mathrm{SFR_{IR}})$ vs $\log_{10}(\mathrm{SFR_{radio}})$ for our sub-sample (i.e both the SFGs and AGN) with SFR associations. The contours levels are 1, 2, 3, and 4 σ. The dashed grey line corresponds to $\log_{10}(\mathrm{SFR_{IR}}) = \log_{10}(\mathrm{SFR_{radio}})$.

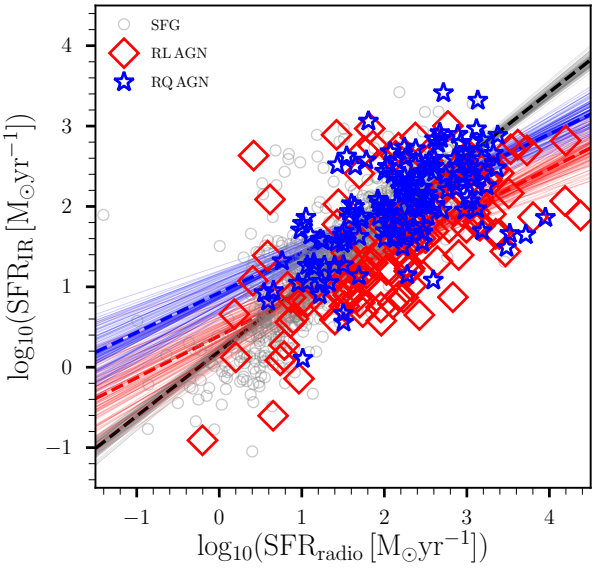

FIGURE 4.5: SFR derived from the IR luminosity versus the SFR from the radio luminosity. SFGs are plotted as open grey circles, RQ AGN as open blue stars and RL AGN as open red diamonds. A linear regression line that we get from each bootstrap replicate of the slope and intercept to each population are represented as light blue for RQ AGN, light red for RL AGN and grey for SFGs. The median of each bootstrap are represented as solid dashed lines.

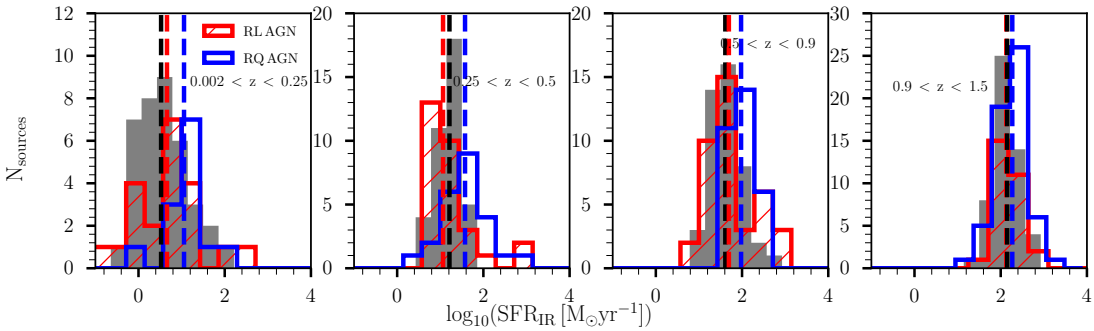

FIGURE 4.6: SFR distribution in four redshift bins for RQ AGN (blue histogram) and RL AGN (red histogram). The dashed blue and red vertical lines represents the median values of the SFR_{IR} for the RQ and RL AGN in each redshift bin. The filled grey histograms in each panel represents the SFR distribution for SFGs in each redshift bin scaled by a factor of five to ease the comparison to the RQ and RL distributions. The dashed lines vertical lines in each panel represents the median values of the SFR_{IR} for the SFGs.

while a tighter correlation implies a star formation history that traces stellar mass growth more smoothly (see e.g. Daddi et al. 2007; Renzini 2009; Lee et al. 2012). Previous studies have shown that the SFMS has near-constant slope but shifts towards higher SFRs as the redshift increases (see e.g. Noeske et al. 2007; Elbaz et al. 2007; Rodighiero et al. 2011; Johnston et al. 2015). The SFMS is largely linear and has remarkably small scatter at low redshifts (Brinchmann et al. 2004; Salim et al. 2007).

In Figure 4.7 we plot SFR_{IR}, which is relatively immune fron AGN contamination compared to SFR_{radio}, as a function of galaxy stellar mass for our objects divided in four redshift bins. Table 4.3 presents the median values of the stellar masses for the RQ AGN, RL AGN and SFGs in each redshift bin (see the dashed red and blue vertical lines in Figure 4.7 that represents the median values in Table 4.3). The black dashed lines indicates the expected position of the SFMS at the average redshift of the sources in each bin. Following Bonzini et al. (2015) we describe the redshift evolution of the SFMS as:

$$\log_{10}(\mathrm{SFR}(\mathrm{M},\mathrm{z})) = -7.77 + 0.79 \times \log_{10}(\mathrm{M})[\mathrm{M}_{\odot}] + 2.8 \times \log_{10}(1+\mathrm{z}) \tag{4.4}$$

where the slope and the redshift evolution are based on the results of Rodighiero et al. (2011) and M is the stellar mass expressed in units of solar masses. The dot-dashed lines in each panel above and below the SFMS correspond to ±0.6 dex (see Bonzini et al. 2015). The three populations occupy a similar locus in the $M_{\star}$ − SFR plane. There are a few outliers that make the RL AGN population show more scatter than the SFG population(and indeed for these the IR luminosities might be boosted by the AGN emission rather than reflecting true star formation alone). However, neglecting these outliers, the rest of the RL AGN population seem to show a similar distribution to both the SFGs and RQ AGN. This also suggests that the majority of the host galaxies of radio selected RQ AGN are not significantly different from the inactive star-forming galaxy population. However, our radio-selected sample lies a little above the SFMS. Bonzini et al. (2015) also found that their radio-selected SFGs and RQ AGN tend to have higher SFRs with respect to what is expected from the redshift evolution of the MS and attributed this bias toward high SFRs to their radio selection. Afonso et al. (2005) work on the multi-wavelength survey based on deep 1.4-GHz

TABLE 4.3: Median values of stellar mass for the RQ AGN, RL AGN and SFGs in each redshift bin. The errors denote the difference between the 15.8 and 84.2 percentiles.

Redshift range	$N_{RQ\,AGN}$	RQ AGN $\log_{10} M_\star(M_\odot)$	$N_{RL\,AGN}$	RL AGN $\log_{10} M_\star(M_\odot)$	N_{SFG}	SFG $\log_{10} M_\star(M_\odot)$
$0.002 < z < 0.25$	13	$10.83^{+0.29}_{-0.12}$	21	$10.45^{+0.42}_{-0.61}$	214	$10.28^{+0.58}_{-0.54}$
$0.25 < z < 0.5$	24	$11.06^{+0.21}_{-0.55}$	30	$10.71^{+0.48}_{-0.31}$	294	$10.83^{+0.28}_{-0.38}$
$0.5 < z < 0.9$	31	$11.11^{+0.38}_{-0.28}$	39	$11.11^{+0.25}_{-0.46}$	240	$11.05^{+0.23}_{-0.32}$
$0.9 < z < 1.5$	58	$11.23^{+0.25}_{-0.51}$	29	$11.13^{+0.27}_{-0.34}$	273	$11.20^{+0.26}_{-0.27}$

radio imaging of the Phoenix Deep showed that radio-selection is more sensitive to heavily-obscured populations of SFGs compared to optical selection (where the SFMS is defined). Given that there is a trend relating obscuration and luminosity or SFR (e.g., Gunawardhana et al. 2013; Hopkins et al. 2003b), we recognise that our radio-selected samples are indeed likely to include higher SFR systems on average than the optical-selected samples.

The open red, open blue and filled grey inset histogram in each panel shows the distribution for the RL AGN, RQ AGN and SFGs in each redshift bin respectively. The distribution of SFGs in each panel is scaled by a factor of five to ease the comparison to the RQ and RL AGN distributions. The three populations have by and large similar stellar mass distribution. We note that this is not what is typically expected, as RQ AGN (at least the ones found at bright > 1 mJy radio fluxes, e.g. see Kozieł-Wierzbowska et al. 2017) and SFGs are generally found in lower-mass host galaxies than RL AGN. However, perhaps because of our joint selection based on radio detection and SFR_{IR} estimate, particularly in the higher-redshift bins where most of our sample lies the range of SFRs and thus of SMs probed by our sample is limited and biased towards higher values, making it difficult to distinguish different populations. Our results may thus be affected by biases, due to the combination of the intrinsic source properties and selection effects.

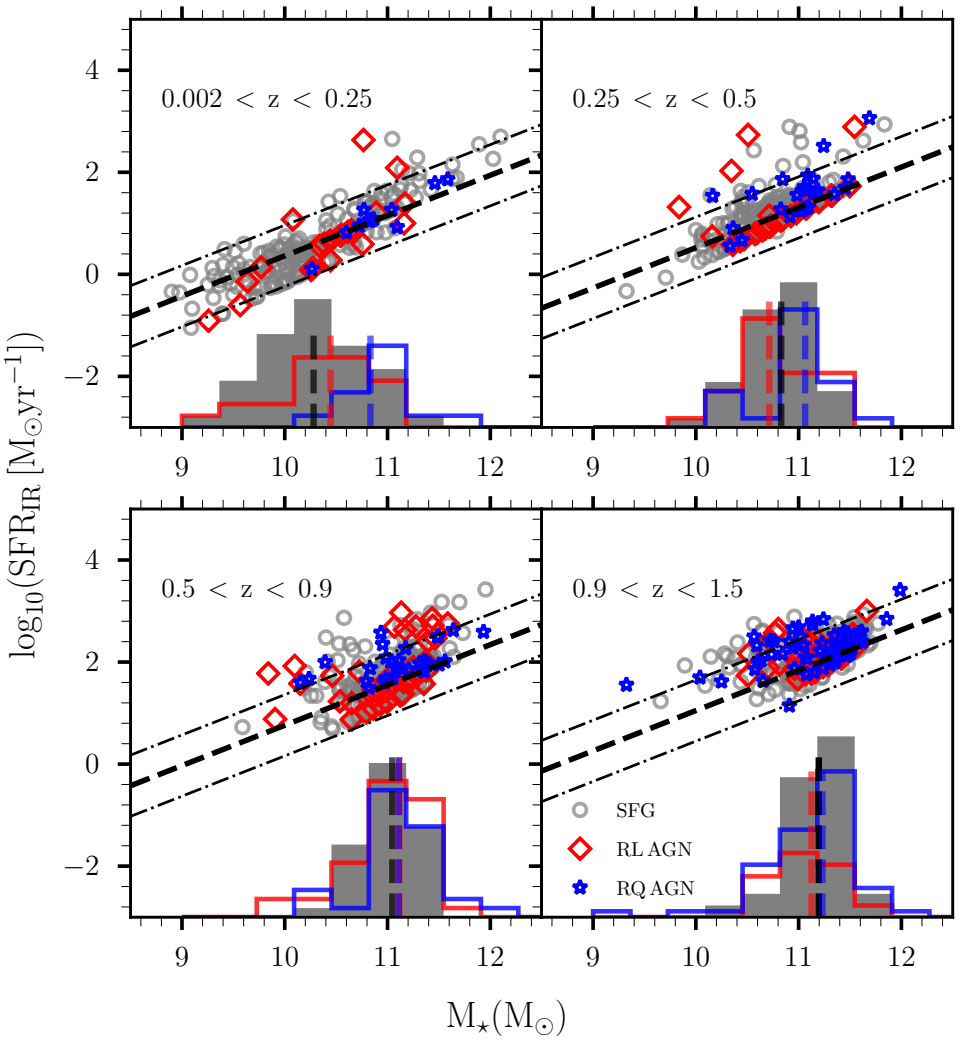

FIGURE 4.7: SFR versus stellar mass for different redshift bins. The open grey circles, open red diamonds and blue stars represent SFGs, RL AGN and RQ AGN respectively. The dashed lines indicates the position of the SFMS at the average redshift of the sources in each bin using equation 4.4. The dot-dashed lines above and below the SFMS correspond to ±0.6 dex. The grey, red and blue inset histograms in each panel shows the distribution for the SFGs, RL and RQ AGN in each redshift bin respectively. The dashed black, blue and red vertical lines in each panel represents the median values of the stellar masses for the SFGs, RQ AGN and RL AGN respectively.

4.4 AGN Radio Luminosity Function (RLF)

In this section we describe the AGN sample selection used for computing the RLF. We explain the method used in computing the AGN luminosity function and the reasoning behind adopting the analytic form of our local AGN luminosity function at 610-MHz to fit our data. We present the AGN RLF in different redshift bins. We further describe how the evolution of AGN luminosity function out to z $\sim$ 1.5 is constrained.

(A) All AGN (620 sources).

	RL AGN		RQ AGN	
	N	%	N	%
z_{phot}	220	35.5	149	24.0
z_{spec}	118	19.0	133	21.5

(B) AGN used for RLF (486 sources).

	RL AGN		RQ AGN	
	N	%	N	%
z_{phot}	177	36.4	107	22.0
z_{spec}	110	22.6	92	19.0

TABLE 4.4: Statistics of spectroscopic/photometric redshifts for the full AGN sample (a) and for the AGN sub-sample used to compute the RLF (b).

4.4.1 RLF Sample Selection

The number and percentage of AGN with spectroscopic and photometric redshifts without any redshift and $r_{AB} < 25$ cuts is summarized in Table 4.4 (a). However, we demonstrated in Ocran et al. (2020b) that the redshift distribution of the SFGs clearly shows that the sample is incomplete for $r_{mag} > 25$ and $z > 1.5$. This incompleteness, is driven by HSC/Subaru photometric redshifts, which start being incomplete at $z \sim 1.3$. It is recommended by Tanaka et al. (2018b) that photometric redshifts should only be used at $z \lesssim 1.5$ and $i \lesssim 25$.

Table 4.4 (b) summarizes the number and percentage of AGN with spectroscopic and photometric redshifts. In order to compute the AGN RLF, we select only AGN with $r_{AB} < 25$ and $0.002 < z < 1.5$. The total number of AGN satisfying these criteria is 486 sources of which 287 sources are RL AGN whilst the remaining 199 sources are RQ AGN (see Table 4.4 (b)). The r_{AB} magnitude distribution versus redshift for the RL and RQ AGN sample is plotted in the left panel of Figure 4.8. The $r_{AB} = 25$ limit is indicated by the dashed horizontal black line. The right panel of Figure 4.8 shows the 610-MHz luminosity distribution versus redshift for our sample (after applying the magnitude cut $r_{AB} < 25$).

4.4.2 Derivation of AGN RLF

We computed the volume densities (for a given redshift range) as described in detail in Ocran et al. (2020b). We followed the $\frac{1}{V_{max}}$ approach (Schmidt, 1968) and applied several corrections, including correcting for the incompleteness of our radio catalogue as well as optical identification and redshift incompletenesses which result from our sources not being identified or not being detected over a wide enough range of optical/IR wavelengths to compute a reliable (photometric) redshift. We refer to Subsection 4.1. in Ocran et al. (2020b) for a comprehensive description of the procedure. The rest-frame 610-MHz luminosities

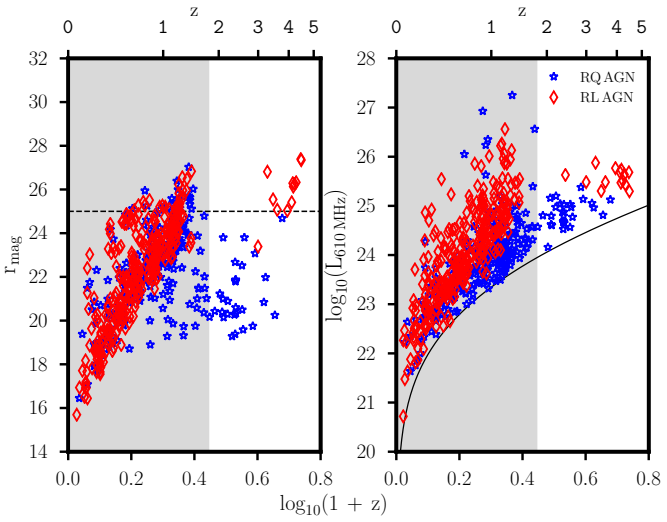

FIGURE 4.8: r_{AB} versus redshift for the AGN sample with redshift estimates and magnitude limit of $r = 25$ (the dashed horizontal red line) (left panel). 610-MHz luminosity versus redshift for the GMRT RL (open red diamonds) and RQ AGN (open blue stars) sample with redshift and magnitude limit of $r = 25$ (right panel). The luminosity limit implied by the GMRT sensitivity is shown by the solid black curve.

were computed using the observed-frame 610-MHz flux densities and assuming a radio spectral index of $\alpha = -0.8$ (Ibar et al., 2010).

4.4.3 Local AGN RLF

Following Dunlop & Peacock (1990), we assume for the RLF a double power law function, given by equation 4.5:

$$\Phi_0(\mathrm{L}) = \frac{\Phi_\star}{(\mathrm{L}_\star/\mathrm{L})^\alpha + (\mathrm{L}_\star/\mathrm{L})^\beta} \tag{4.5}$$

where $\Phi_\star$ is the normalization, $\mathrm{L}_\star$ is the luminosity corresponding to the break in the LF whereas α and β are the bright and faint end slopes. We used this analytic form for the local AGN RLF and adopted here the fit from Mauch & Sadler (2007) where the parameters are $\Phi_\star = \frac{1}{0.4}10^{-5.5}\,\mathrm{Mpc}^3\,\mathrm{dex}^{-1}$ (scaled to the base of dlog L), $\mathrm{L}_\star = 10^{24.59}\,\mathrm{W\,Hz}^{-1}$, $\alpha = -1.27$, and $\beta = -0.49$. We adopt the Mauch & Sadler (2007) for consistency with other studies in the literature. Mauch & Sadler (2007) constrain both the faint and bright end of the local AGN LF with a sample of 2661 detections in the 6dFGS-NVSS field with a median redshift of med(z) = 0.073 and a span of six decades in luminosities. Figure 4.9 shows our local 610-MHz AGN luminosity function (open green squares). We truncate our sample at $z < 0.1$ to minimize the effects of evolution. The yellow plus and blue stars represents Mauch & Sadler (2007) and Condon et al. (2002) AGN volume densities scaled to 610-MHz using an $\alpha = -0.8$. The dashed red line is the analytic fit to the local Mauch & Sadler (2007) AGN data converted to 610-MHz.

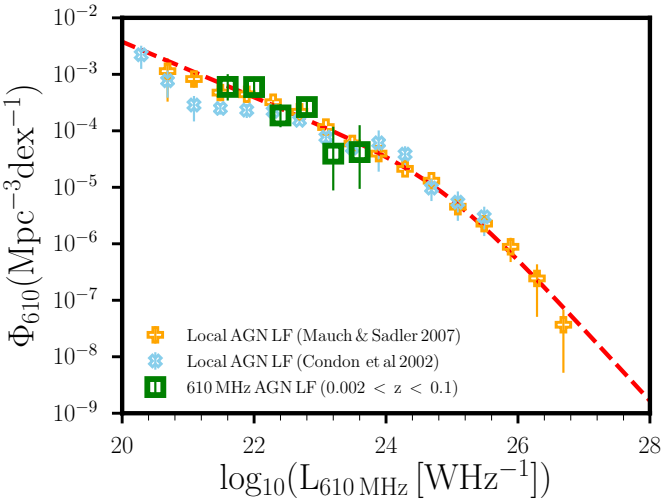

FIGURE 4.9: The local 610-MHz AGN luminosity function. The yellow plus and blue stars represents Mauch & Sadler (2007) and Condon et al. (2002) AGN volume densities scaled to 610-MHz assuming a spectral index of $\alpha = -0.8$. The dashed red line is the analytic fit to the local 610-MHz Mauch & Sadler (2007) AGN data.

4.4.4 AGN RLF as a function of z

The AGN fitted radio luminosity functions at $\nu = 610$ MHz in different redshift bins are presented in Table 4.5 (for all AGN and for RQ and RL AGN separately) and in Figure 4.10 (all AGN only; open green squares). Our data have small Poisson error bars due to the relatively large number of sources in each bin and as such the errors do not reflect all possible systematic effects. Scaled down luminosity functions from 1.4-GHz to 610-MHz (assuming $\alpha = -0.8$) by Smolčić et al. (2009b), McAlpine et al. (2013) and Smolčić et al. (2017b) are shown as yellow pluses, light blue diamonds and blue triangles respectively in each panel.

We also compare our AGN LFs with expectations from models and/or simulated radio catalogues, like e.g. the AGN models by Mancuso et al. (2017) (green line), the semi-empirical SKADS simulations by Wilman et al. (2008) (grey open pentagons), and the Tiered Radio Extragalactic Continuum Simulation (T-RECS) by Bonaldi et al. (2019) (black open diamonds) covering similar area and reaching similar depth in sensitivity and redshifts that we probe in this study. In general, our RLFs agree well with other estimates from the literature, as well as with models, especially with the Bonaldi et al. (2019) one, which better follows the data at high luminosities.

4.4.5 Evolution of AGN RLF

We model the evolution of the AGN RLF assuming pure luminosity evolution (PLE):

$$\Phi(\mathrm{L}, \mathrm{z}) = \Phi_0 \left[\frac{\mathrm{L}}{(1+\mathrm{z})^{k_L(z)}} \right] \tag{4.6}$$

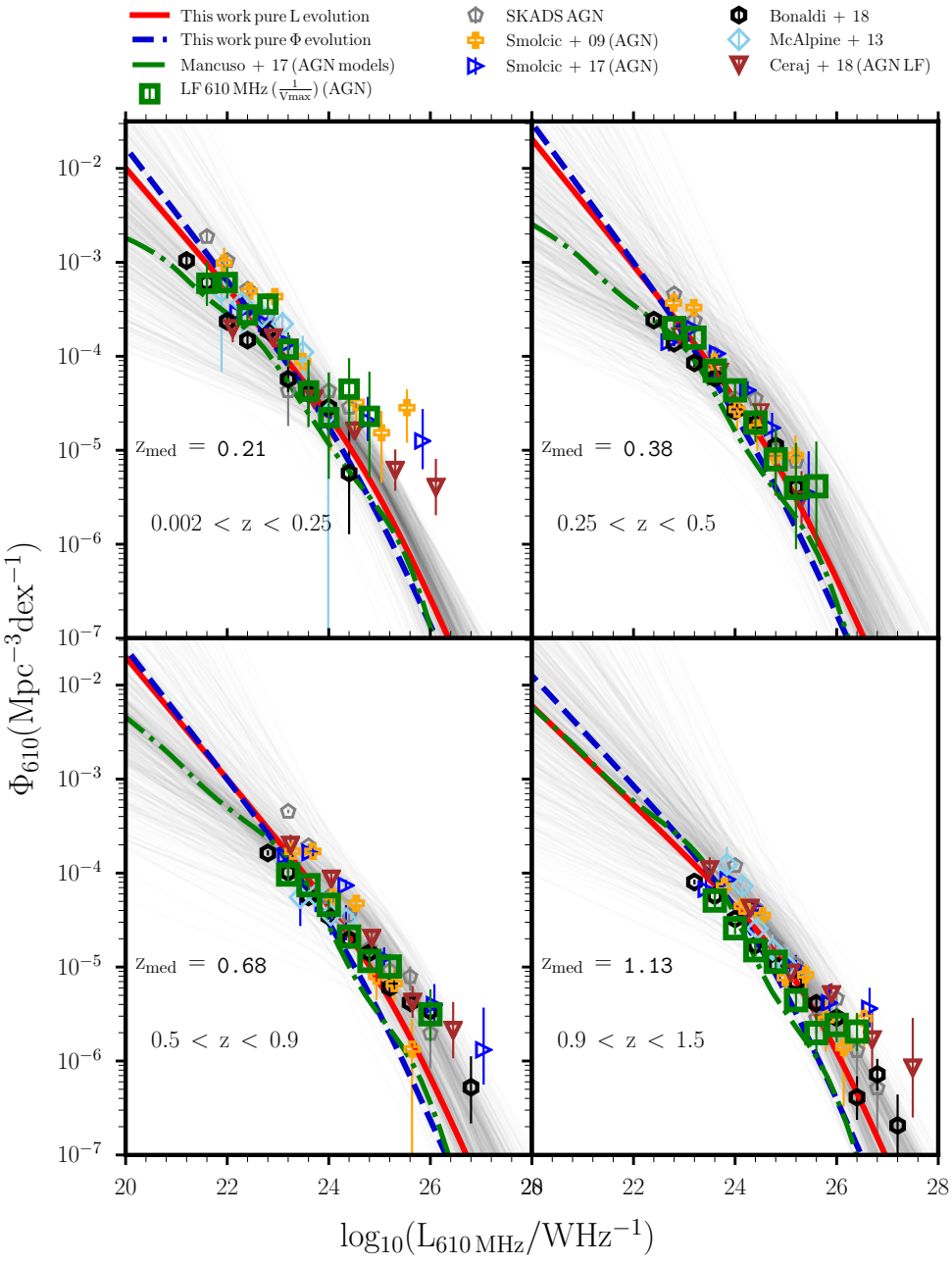

FIGURE 4.10: Radio luminosity functions of AGN at $\nu = 610$ MHz in different redshift bins (green open squares). The grey pentagons represent the total AGN LF from the semi-empirical simulation of the SKA (Wilman et al., 2008). The total AGN (i.e RS AGN+RL AGN + RQ AGN) from Mancuso et al. (2017) models are represented by the dotted dashed green lines. Luminosity functions computed for AGN from the T-RECS (Bonaldi et al., 2019) simulations are shown as open black diamonds. The redshift range and the median redshift are shown in each panel. Error bars are determined using the prescription of Gehrels (1986). Scaled down luminosity functions from 1.4-GHz to 610-MHz by Smolčić (2009), Smolčić et al. (2017b) and Ceraj et al. (2018) are shown as yellow pluses, right pointing blue triangles and downward pointing brown triangles respectively in each panel. The solid red and dashed blue lines in each panel correspond to the median values of the MCMC samples for the independent PLE and PDE fits in a given redshift bin respectively. The grey lines correspond to 1000 samples from the MCMC chain fits by a combination of PDE and PLE.

TABLE 4.5: Luminosity functions of the total AGN, RQ AGN and RL AGN obtained with the $1/V_{max}$ method.

Redshift z	Luminosity $\log_{10}(L_{610\,MHz}\,[WHz^{-1}])$	Number density $\Phi_{610}(Mpc^{-3}dex^{-1})$ ALL AGN	Number N	Number density RQ AGN	Number	Number density RL AGN	Number
$0.002 < z < 0.25$	21.6	$5.99^{+4.07}_{-2.55} \times 10^{-4}$	4	$2.25^{+2.57}_{-1.32} \times 10^{-4}$	2	$3.74^{+4.26}_{-2.20} \times 10^{-4}$	2
	22.0	$6.09^{+2.81}_{-1.97} \times 10^{-4}$	7	$1.66^{+1.89}_{-0.90} \times 10^{-4}$	2	$4.43^{+2.57}_{-1.69} \times 10^{-4}$	5
	22.4	$2.75^{+0.95}_{-0.71} \times 10^{-4}$	11	$6.74^{+7.68}_{-3.96} \times 10^{-5}$	2	$2.08^{+0.81}_{-0.59} \times 10^{-4}$	9
	22.8	$3.59^{+0.90}_{-0.72} \times 10^{-4}$	18	$2.00^{+0.73}_{-0.54} \times 10^{-4}$	10	$1.59^{+0.67}_{-0.48} \times 10^{-4}$	9
	23.2	$1.19^{+0.61}_{-0.42} \times 10^{-4}$	6	$3.93^{+4.47}_{-2.31} \times 10^{-5}$	2	$7.98^{+5.42}_{-3.40} \times 10^{-5}$	4
	23.6	$4.27^{+4.87}_{-2.51} \times 10^{-5}$	2	–	–	$4.27^{+4.87}_{-2.51} \times 10^{-5}$	2
	24.0	$2.22^{+4.43}_{-1.73} \times 10^{-5}$	1	–	–	$2.22^{+4.43}_{-1.73} \times 10^{-5}$	1
	24.4	$4.47^{+5.09}_{-2.63} \times 10^{-5}$	2	–	–	$2.24^{+4.46}_{-1.74} \times 10^{-5}$	1
	24.8	$2.29^{+4.57}_{-1.78} \times 10^{-5}$	1	–			
$0.25 < z < 0.5$	22.8	$2.00^{+0.40}_{-0.34} \times 10^{-4}$	26	$9.49^{+2.79}_{-2.17} \times 10^{-5}$	14	$1.05^{+0.34}_{-0.26} \times 10^{-4}$	12
	23.2	$1.58^{+0.24}_{-0.21} \times 10^{-4}$	41	$5.64^{+1.66}_{-1.29} \times 10^{-5}$	14	$1.01^{+0.20}_{-0.17} \times 10^{-4}$	27
	23.6	$7.03^{+1.66}_{-1.35} \times 10^{-5}$	20	$1.40^{+0.95}_{-0.60} \times 10^{-6}$	4	$5.63^{+1.53}_{-1.22} \times 10^{-5}$	16
	24.0	$4.34^{+1.41}_{-1.07} \times 10^{-5}$	12	$3.47^{+6.92}_{-2.70} \times 10^{-6}$	1	$4.00^{+1.37}_{-1.03} \times 10^{-5}$	11
	24.4	$1.97^{+1.15}_{-0.75} \times 10^{-5}$	5	–	–	$1.97^{+1.15}_{-0.75} \times 10^{-5}$	5
	24.8	$8.02^{+9.14}_{-4.71} \times 10^{-6}$	2	–	–	$8.02^{+9.14}_{-4.71} \times 10^{-6}$	2
	25.2	$3.99^{+7.95}_{-3.10} \times 10^{-6}$	1	–	–	$3.99^{+7.95}_{-3.10} \times 10^{-6}$	1
	25.6	$4.14^{+8.26}_{-3.22} \times 10^{-6}$	1	–	–	$4.14^{+8.26}_{-3.22} \times 10^{-5}$	1
$0.5 < z < 0.9$	23.2	$9.66^{+2.52}_{-2.01} \times 10^{-5}$	17	$6.50^{+2.01}_{-1.54} \times 10^{-5}$	13	$3.16^{+2.15}_{-1.35} \times 10^{-5}$	4
	23.6	$7.43^{+1.00}_{-0.88} \times 10^{-5}$	52	$3.04^{+0.74}_{-0.60} \times 10^{-5}$	13	$4.39^{+0.77}_{-0.65} \times 10^{-5}$	33
	24.0	$4.59^{+0.63}_{-0.55} \times 10^{-5}$	50	$1.58^{+0.41}_{-0.33} \times 10^{-5}$	17	$3.01^{+0.53}_{-0.45} \times 10^{-5}$	33
	24.4	$2.11^{+0.46}_{-0.38} \times 10^{-5}$	23	$5.42^{+2.78}_{-1.89} \times 10^{-5}$	6	$1.57^{+0.41}_{-0.33} \times 10^{-5}$	17
	24.8	$1.16^{+0.38}_{-0.29} \times 10^{-5}$	12	–	–	$1.16^{+0.38}_{-0.29} \times 10^{-5}$	12
	25.2	$1.01^{+0.37}_{-0.27} \times 10^{-5}$	10	–	–	$1.01^{+0.37}_{-0.27} \times 10^{-5}$	10
	26.0	$3.14^{+2.64}_{-1.54} \times 10^{-6}$	3	–	–	$2.07^{+2.36}_{-1.22} \times 10^{-6}$	2
$0.9 < z < 1.5$	23.6	$5.10^{+1.50}_{-1.17} \times 10^{-5}$	14	$4.70^{+1.45}_{-1.12} \times 10^{-5}$	13	–	–
	24.0	$2.59^{+0.42}_{-0.36} \times 10^{-5}$	38	$2.39^{+0.40}_{-0.34} \times 10^{-5}$	35	–	–
	24.4	$1.51^{+0.24}_{-0.20} \times 10^{-5}$	40	$7.24^{+1.77}_{-1.42} \times 10^{-6}$	19	$7.87^{+1.83}_{-1.47} \times 10^{-6}$	21
	24.8	$1.14^{+0.20}_{-0.17} \times 10^{-5}$	32	$4.61^{+1.42}_{-1.09} \times 10^{-6}$	13	$6.76^{+1.65}_{-1.33} \times 10^{-6}$	19
	25.2	$4.44^{+1.44}_{-1.10} \times 10^{-6}$	12	$7.36^{+8.39}_{-4.33} \times 10^{-7}$	2	$3.70^{+1.35}_{-1.00} \times 10^{-6}$	10
	25.6	$1.98^{+1.15}_{-0.76} \times 10^{-6}$	5	$4.02^{+8.01}_{-3.12} \times 10^{-7}$	1	$1.58^{+1.07}_{-0.67} \times 10^{-5}$	4
	26.0	$2.42^{+1.24}_{-0.84} \times 10^{-6}$	6	–	–	$2.42^{+1.24}_{-0.84} \times 10^{-6}$	6
	26.4	$2.06^{+1.19}_{-0.79} \times 10^{-6}$	5	–	–	$1.23^{+1.03}_{-0.59} \times 10^{-6}$	3

where $k_L = K_L + z\beta_L$; or pure density evolution (PDE):

$$\Phi(L, z) = (1 + z)^{k_D(z)} \times \Phi_0(L) \tag{4.7}$$

where $k_D = K_D + z\beta_D$. We used the Markov chain Monte Carlo (MCMC) algorithm module EMCEE (Foreman-Mackey et al., 2013), implemented in the LMFIT Python package (Newville et al., 2014) to perform a multi-variate fit to the data. The LMFIT Python package first does the fitting by performing a non linear least-squares χ^2 minimization to obtain the best fit k_L and k_D parameters. The EMCEE is then implemented to calculate the probability distribution for the parameters. From this we get the medians of the probability distributions and a 1σ quantile, estimated as half the difference between the 15.8 and 84.2 percentiles. The solid red and dashed blue lines in each panel of Figure 4.10 corresponds to the median values of the MCMC samples for the independent PLE and PDE fits in each redshift bin respectively. The shaded regions correspond to the 68% confidence region by combining PDE and PLE fitting to the samples.

4.5 Discussion

4.5.1 Evolution of the overall AGN Population

Figure 4.11 presents best fit parameters obtained from fitting PLE (top panel) and PDE (bottom panel) models to the AGN luminosity functions. The open green squares in the top and bottom panels show the evolution parameters obtained from independently fitting the assumed analytic form of the luminosity function in four redshift bins assuming, respectively, pure luminosity and pure density evolution scenarios. The vertical error bars in each panel represent the MAD of the MCMC samples. As shown in Figure 4.11 and reported in Table 4.6 best fit PLE and PDE parameters show no (or very mild) evolution when fitting the LF independently in each redshift bin. The solid red and blue lines in the two panels show, instead, the results obtained assuming that the PLE or PDE parameters in Eqs. 4.6 and 4.7 continuous fits assuming that both PLE and PDE evolve linearly with redshift. In this case we derive $L_{610\,MHz} \propto (1+z)^{(3.45\pm0.53)-(0.55\pm0.29)z}$ (i.e. $K_L = 3.45 \pm 0.53$) and $\Phi \propto (1+z)^{(2.25\pm0.38)-(0.63\pm0.35)z}$ (i.e. $K_D = 2.24 \pm 0.38$) for $0.002 < z < 1.5$.

Our measured 610-MHz RLF of AGN is in broad agreement with most scaled down 1.4-GHz RLF estimates from the literature. Using the VLA-COSMOS 1.4-GHz survey Smolčić (2009) have derived luminosity functions for their rest-frame colour selected AGN out to $z = 1.3$, which is also shown in Figure 4.10 as open yellow pluses. Overall, there is good agreement between the derivations based on this shallow 1.4-GHz survey and the deep 610-MHz survey presented here. They reported PLE and PDE evolution to be $L^\star \propto (1+z)^{0.8\pm0.1}$ and $\Phi^\star \propto (1+z)^{1.1\pm0.1}$ respectively[†]. Strazzullo et al. (2010) employed a method based on SED template fitting to separate their very faint radio sample ($5\sigma \sim 14\mu$Jy) RQ and RL AGN and found similar pure luminosity evolution parameters of $K_L \sim 3.0$ for their population. Padovani et al. (2011) measured pure luminosity evolution for their radio-quiet quasar samples. They found evidence that the low luminosity radio-loud AGN population undergoes no evolution in the redshift range probed by the Smolčić et al. (2009b) study and suggested that the evolution detected for low-luminosity AGN in the COSMOS study is driven by radio-quiet AGN included by their selection criteria. Smolčić et al. (2017b) constrained the evolution of this population via continuous models of pure density and pure luminosity evolutions, and found best-fit parametrizations of $\Phi^\star \propto (1+z)^{(2.00\pm1.8)-(0.60\pm0.14)z}$ and $L^\star \propto (1+z)^{(2.88\pm0.82)-(0.84\pm0.34)z}$ respectively, with a turnover in number and luminosity densities of the population at $z \approx 1.5$.

McAlpine et al. (2013) combined a 1 square degree VLA radio survey, complete to a depth of 100μJy, with accurate 10 band photometric redshifts from the VIDEO and CFHTLS surveys. Their evolution is best fitted by PLE with AGN evolving as $(1+z)^{1.18\pm0.21}$ out to $z \sim 2.5$. Prescott et al. (2016) detected mild but poorly constrained evolution from fits to their 325-MHz RLF for AGN out to $z = 0.5$, with evolution parameters of $K_D = 0.92 \pm 0.95$ for pure density evolution and $K_L = 2.13 \pm 1.96$ for pure

[†] $L^\star$ and $\Phi^\star$ represents the PLE and PDE fits

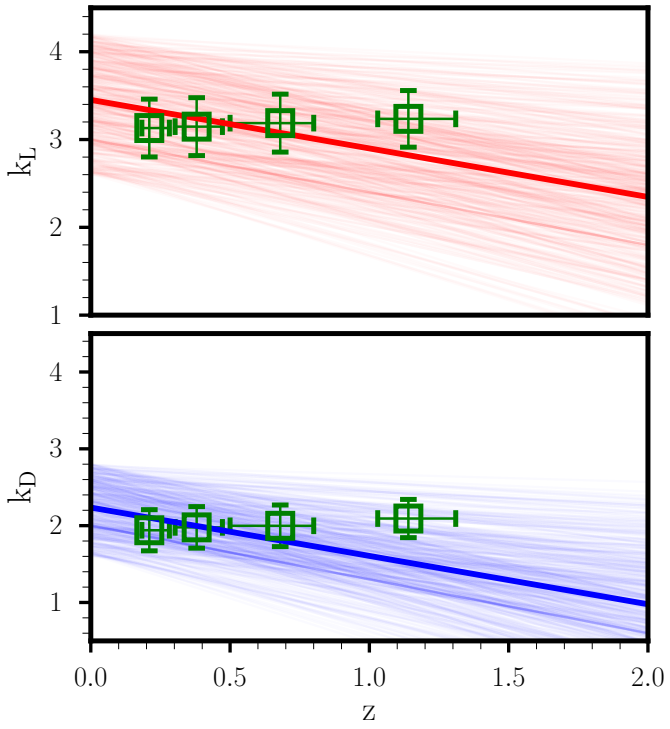

FIGURE 4.11: Parameters obtained by fitting PLE (top panel) and PDE (bottom panel) model to the AGN luminosity functions. Open green squares in both panels show the evolution parameters obtained from fitting the assumed analytic form of the luminosity function in four redshift bins assuming pure luminosity and density evolution scenario (see text for details). The vertical error bars represent the MAD of the MCMC samples. The horizontal error bars denote the inter-quartile range (IQR) of reshift in each bin. The solid red (top panel) and blue (bottom) lines show the results from the continuous fit assuming that both the PLE and PDE parameters evolves linearly with redshift.

luminosity evolution. Ceraj et al. (2018) derived the 1.4-GHz AGN luminosity function of the full VLA-COSMOS 3 GHz Large Project sample with COSMOS2015 counterparts out to $z \sim 6$ by (shown as downward pointing brown triangles in Figure 4.11), and found $\Phi^\star \propto (1+z)^{(1.24\pm0.08)-(0.25\pm0.03)z}$ and $L^\star \propto (1+z)^{(1.97\pm0.10)-(0.46\pm0.04)z}$ respectively. Most of these previous studies are broadly consistent with our radio derived PLE parameter and Table 4.7 presents a summary of the comparison.

We also compare with LFs derived from Wilman et al. (2008) (see grey pentagons in Figure 4.10) and Mancuso et al. (2017) models (see dot-dashed green line in each panel of Figure 4.10). Mancuso et al. (2017) model AGN in three components: radio silent (RS) AGN, RQ AGN and RL AGN. The RS and RQ AGN components are AGN clearly detectable in X-rays at luminosities $L_X \gtrsim 10^{42}\,\mathrm{erg\,s^{-1}}$, but the origin of their radio emission is mainly ascribed to the SFR in the host galaxy in the former and to the central AGN in the latter (see Mancuso et al. 2017 for more details). The star formation triggered radio emission in RS AGN is described using the model-independent approach by Mancuso et al. (2016a,b). The AGN-triggered RQ AGN were modeled by converting the bolometric power in X-rays via the Hopkins et al. (2007) correction, and then deriving the AGN radio power by using the relation between rest-frame X-ray and 1.4-GHz radio luminosity observed for samples of RQ AGN by Panessa et al. (2015) (see also Brinkmann et al. 2000).

TABLE 4.6: Best-fit evolution parameters obtained by fitting the local luminosity function to each redshift bin independently, assuming pure density K_D and pure luminosity K_L evolution.

Med(z)	K_D	K_L
$0.21^{+0.07}_{-0.03}$	1.94±0.27	3.13±0.33
$0.38^{+0.09}_{-0.08}$	1.98±0.27	3.15±0.33
$0.68^{+0.12}_{-0.18}$	1.99±0.26	3.19±0.34
$1.14^{+0.17}_{-0.11}$	2.09±0.25	3.24±0.32

TABLE 4.7: Comparison of the evolution parameters for radio AGN luminosity function determined from previous studies.

Reference	Field	Flux density limit	Wavelength	Redshift	Sample size	PLE	PDE
Brown et al. (2001)	SGP&F855	5mJy	1.4-GHz	$0.0 < z < 0.4$	230	3-5	-
Smolčić et al. (2009b)	COSMOS	50μJy	1.4-GHz	~ 1.3	601	0.8 ± 0.1	1.1 ± 0.1
Padovani et al. (2011)	CDFS	50μJy	1.4-GHz	≤ 1.3	86	$3.5^{+0.4}_{-0.7}$	-1.8 ± 0.4
McAlpine et al. (2013)	VIDEO	100μJy	1.4-GHz	$0 < z < 2.5$	951	1.18 ± 0.21	-
Padovani et al. (2015)	E-CDFS	50μJy	1.4GHz	$0.1 < z < 4.5$	136	-6.0 ± 1.4	-2.4 ± 0.3
Prescott et al. (2016)	Three GAMA fields	~5mJy	325-MHz	$0.0 < z < 0.5$	428	2.13 ± 1.96	0.92 ± 0.95
Smolčić et al. (2017b)	COSMOS	$\sim 10 - 15\mu$Jy	1.4-GHz	~ 5.0	1800	$(2.88 \pm 0.82) - (0.84 \pm 0.34)z$	$(2.00 \pm 1.8) - (0.60 \pm 0.14)z$
Ceraj et al. (2018)	COSMOS	$\sim 10 - 15\mu$Jy	1.4-GHz	~ 6.0	1604	$(3.97 \pm 0.15) - (0.92 \pm 0.06)z$	$(2.64 \pm 0.10) - (0.61 \pm 0.04)z$
This work (All AGN)	ELAIS N1	7.1μJy	610-MHz	~ 1.5	486	$(3.45 \pm 0.53) - (0.55 \pm 0.29)z$	$(2.24 \pm 0.38) - (0.63 \pm 0.35)z$
This work (RQ AGN)	-	-	-	-	199	$(2.81 \pm 0.43) - (0.57 \pm 0.30)z$	-
This work (RL AGN)	-	-	-	-	287	$(3.58 \pm 0.54) - (0.56 \pm 0.29)z$	-

SGP&F855 - South Galactic Pole (SGP) and UK Schmidt field 855 (F855).
COSMOS - Cosmological Evolution Survey.
CDFS - Chandra Deep Field South.
E-CDFS - Extended Chandra Deep Field South.
VIDEO - VISTA Deep Extragalactic Observations.

4.5.2 RL AGN Evolution

The RL AGN (open red diamonds) luminosity function is presented in Figure 4.12 at $\nu = 610$ MHz in different redshift bins. We compare our results to Mancuso et al. (2017) (see dotted dashed brown lines), who use the models derived by Massardi et al. (2010). Such models consider two flat-spectrum populations with different evolutionary properties, namely, flat-spectrum radio quasars (FSRQs) and BL Lacs, and a single steep-spectrum population (SSAGN); for sources of each population a simple power-law spectrum for their RL AGN LF models. The comoving luminosity function at a given redshift was described by a double power law (we defer the reader to Massardi et al. (2010) for a full description of this procedure). We also compare our RL AGN LF to the LFs computed for RL AGN by Bonaldi et al. (2019) (from the T-RECS simulations, shown as open black hexagons). Bonaldi et al. (2019) described the cosmological evolution of the LF of RL AGN by adopting an updated version of the Massardi et al. (2010) model, slightly revised by Bonato et al. (2017), which includes the three source populations of Mancuso et al. (2017), with different evolutionary properties: steep-spectrum sources, flat-spectrum radio quasars and BL Lacs. The best-fit values of the parameters were re-computed adding to the fitted data sets the 4.8 GHz number counts for the flat-spectrum population by Tucci et al. (2011). This addition resulted in a significant improvement of the evolutionary model for flat-spectrum sources. Our RL AGN LFs are consistent with the improved results by Bonaldi et al. (2019), whereas they are higher than the model predictions by Mancuso et al.

TABLE 4.8: Best-fit evolution parameters obtained by the fitting local luminosity function to the redshift binned data assuming pure luminosity evolution (i.e. $K_{L\,RQAGN}$ $K_{L\,RLAGN}$).

$Med(z)_{RQAGN}$	$K_{L\,RQAGN}$	$Med(z)_{RLAGN}$	$K_{L\,RLAGN}$
$0.22^{+0.07}_{-0.01}$	2.43±0.35	$0.19^{+0.05}_{-0.05}$	3.28±0.38
$0.36^{+0.04}_{-0.09}$	2.45±0.36	$0.39^{+0.08}_{-0.10}$	3.23±0.37
$0.74^{+0.18}_{-0.10}$	2.42±0.35	$0.67^{+0.19}_{-0.11}$	3.26±0.36
$1.14^{+0.17}_{-0.14}$	2.47±0.37	$1.12^{+0.10}_{-0.18}$	3.24±0.36

(2017). Ceraj et al. (2018) use the AGN-related 1.4-GHz emission to derive the 1.4-GHz AGN luminosity functions of moderate-to-high radiative luminosity active galactic nuclei (HLAGN[‡]) out to $z \sim 6$ (see downward pointing green triangles in Figure 4.11) selected at 3 GHz within the VLA-COSMOS 3 GHz Large Project. They reported best-fit parameters obtained with a continuous fit of the analytic form of $L^{\star} \propto (1+z)^{(3.97\pm0.15)-(0.92\pm0.06)z}$ in the case of pure luminosity evolution (i.e. $K_d = \beta_d = 0$).

The open red diamonds in Figure 4.13 represent best fit k_L parameters obtained from fitting the PLE model to the RL AGN luminosity functions, independently in each redshift bin. From the independent PLE parameters in the redshift $z \sim 0.002-0.25$, $z \sim 0.25-0.5$, $z \sim 0.5-0.9$ and $z \sim 0.9-1.5$ ranges, we see a fairly mild evolution in radio luminosity (see also values in the third and fourth columns of Table 4.8).

We also derived a best fit k_L parameter obtained by continuous fitting of the PLE model to the redshift-dependent RL AGN luminosity functions. The light red lines show the results of 1000 MCMC realisations from the continuous fit assuming that the PLE parameter evolves linearly with redshift by using Equation 4.6. The solid red line represents the median value of the MCMC samples. The vertical error bars are as described in Section 4.5.1. We derive $L_{610\,MHz} \propto (1+z)^{(3.58\pm0.54)-(0.56\pm0.29)z}$ (i.e. $K_L = 3.58 \pm 0.54$) for $0.002 < z < 1.5$, in good agreement with Ceraj et al. (2018) results.

4.5.3 RQ AGN Evolution

In subsections 4.3.2 and 4.3.3, we have shown that RQ AGN are quite similar to SFGs in that they obey the relation between star formation rate and radio emission, even though the presence of outliers indicates that they can also host an active nucleus contributing to the radio emission. Indeed, the processes responsible for the emission of RQ AGN, as well as their dichotomy with the RL AGN population, are still vigorously debated. At the core of the problem is the understanding of the interaction between black-hole accretion and star-formation in galaxies, which in turn constrains the relative emission levels (see Padovani et al. 2015; Mancuso et al. 2017; White et al. 2017 and references therein). We provide an estimate of the evolution of RQ AGN in the radio band at 610-MHz, by modelling it as a PLE $L(z) \propto (1+z)^{K_L + z\beta_L}$. The RQ AGN (blue stars) luminosity function is presented in Figure 4.12 at $\nu = 610$ MHz in different redshift bins. The open blue stars in Figure 4.13 presents best fit parameters obtained from independently fitting

[‡]HLAGN were identified by Ceraj et al. (2018) using a combination of X-ray (Civano et al., 2016) ($L_X > 10^{42} ergs^{-1}$) and MIR (Steinhardt et al., 2014) (color-color diagram; Donley et al. 2012) criteria and template fitting to the optical-to-millimeter spectral energy distributions (SED; Delvecchio et al. 2017)

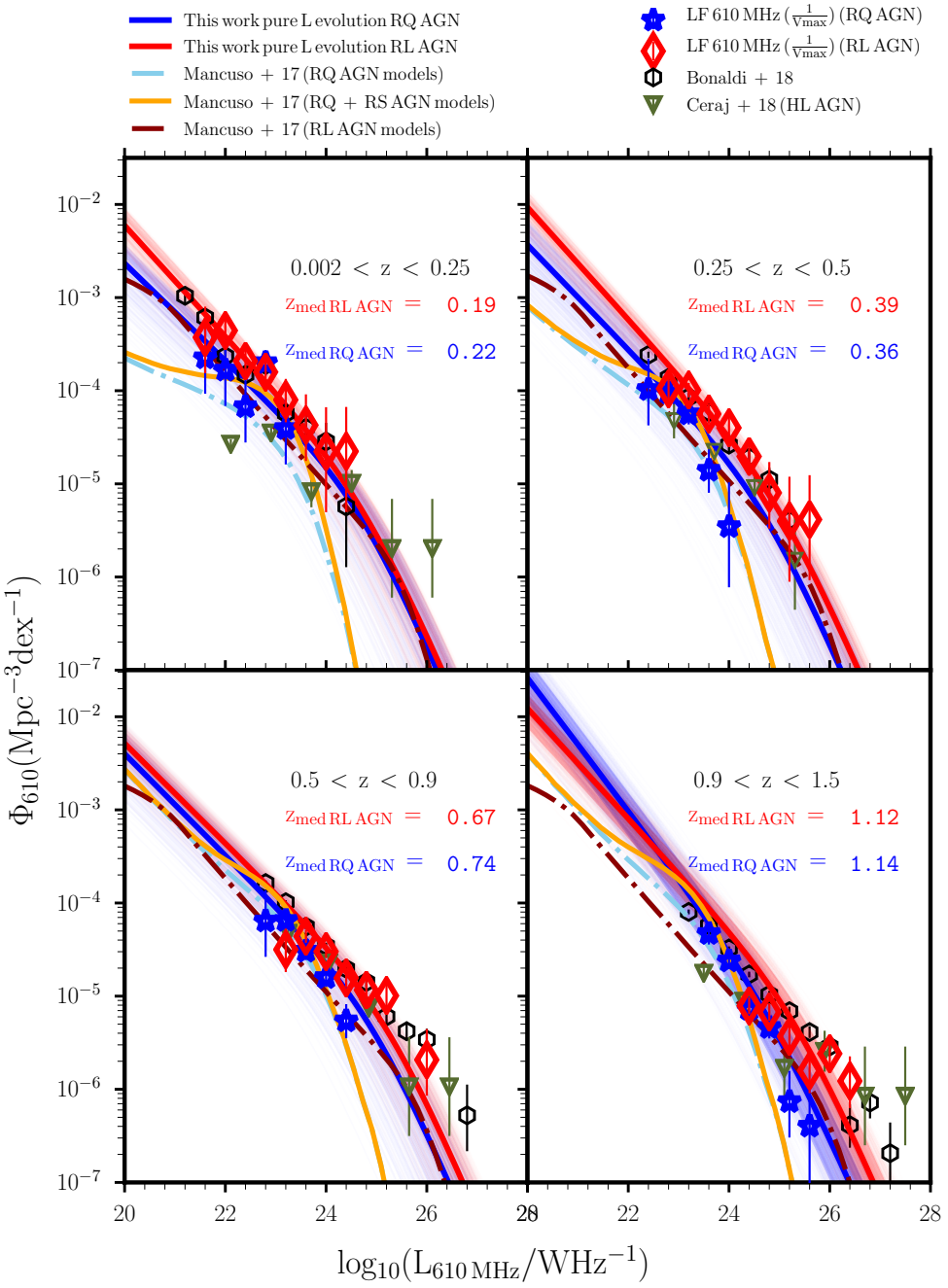

FIGURE 4.12: Radio luminosity functions of RL AGN (open red diamond) and RQ AGN (blue stars) at ν = 610 MHz in different redshift bins. Luminosity functions computed for AGN from the T-RECS (Bonaldi et al., 2019) simulations are shown as open black hexagons. RL AGN and RQ AGN models from Mancuso et al. (2017) are represented, respectively, by the dot-dashed brown and light blue lines. The solid orange lines in each panel represents RS AGN+RQ AGN models from Mancuso et al. (2017). Error bars are determined using the prescription of Gehrels (1986). Scaled down HLAGN (see text for details) luminosity functions from 1.4-GHz to 610-MHz by Ceraj et al. (2018) are shown as downward pointing green triangles in each panel. The solid red and blue lines in each panel correspond to the median values of the MCMC samples from the PLE fits to the RL and RQ AGN. The light red and blue lines in each panel corresponds 1000 MCMC realisations from the PLE fits.

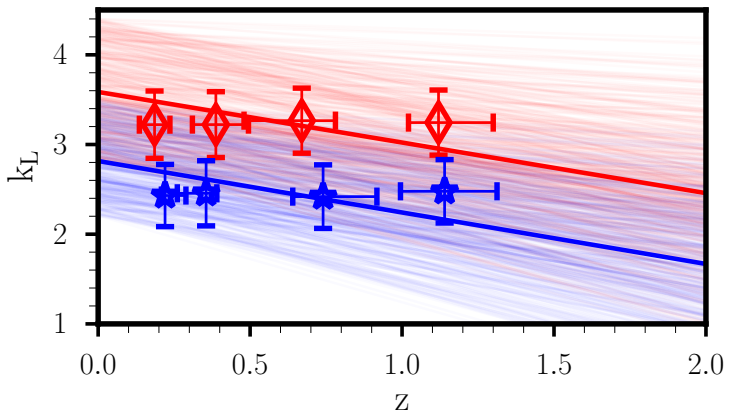

FIGURE 4.13: Parameters obtained by fitting PLE model to the RL and RQ AGN luminosity functions. The open red diamonds and blue stars show the evolution parameters obtained from fitting the assumed analytic form of the luminosity function in four redshift bins assuming pure luminosity evolution scenario for both the RL and RQ AGN (see text for details). The vertical error bars represent the MAD of the MCMC samples. The horizontal error bars denote the inter-quartile range (IQR) of reshift in each bin. The same colour line shows the results from the continuous fit assuming that the PLE parameter evolves linearly with redshift.

PLE model to the RQ AGN luminosity functions in each redshift bin. The RQ AGN exhibit a trend similar to that of RL AGN, with a fairly evolution in radio luminosity (see also K_L values in the first and second columns of Table 4.8). Figure 4.13 also presents the best-fit evolution parameters obtained by continuously evolving the local luminosity function assuming PLE. The light blue lines in this Figure correspond to 1000 MCMC realisations whereas the solid blue line represents the median value of the MCMC samples assuming that the PLE parameter evolves linearly with redshift (as mentioned in previous Sections). We derive $L_{610\,MHz} \propto (1+z)^{(2.81\pm0.43)-(0.57\pm0.30)z}$ (i.e. $K_L = 2.81 \pm 0.43$) for $0.002 < z < 1.5$. Padovani et al. (2011) estimated the evolution of RQ AGN in the radio band, modeling it as a PLE and obtaining $K_L = 2.5^{+0.4}_{-0.5}$, in the range $0.2 \lesssim z \lesssim 3.9$. Following upon the estimate of the evolution of RQ AGN in the radio band derived in Padovani et al. (2011), Padovani et al. (2015) reported a PLE fit to their RQ AGN LF of $K_L = 3.0 \pm 0.2$ from the V_e/V_a [§] analysis and $K_L = 2.5 \pm 0.2$ from their maximum likelihood analysis, over a $0.2 - 3.66$ redshift range. Our results are broadly consistent with these previous findings from the literature.

We compare our results to both the RQ AGN LF (see dot-dashed light blue lines) and also RQ+RS AGN (see solid orange lines) models derived by Mancuso et al. (2017). The available statistics does not allow to clearly discriminate between the two models, but a contribution of SF-driven AGN at low redshift ($0.002 < z < 0.25$) and low luminosities ($\log(L) < 22$) is certainly present. At higher redshifts and higher luminosities this contribution seems to drop and become less significant. Larger samples of radio-selected, radio-quiet samples will put stronger constraints on the evolution of these sources. We place emphasis on the fact that the scale of the PLE evolution found for the RQ AGN evolution is highly consistent with the

[§] V_e/V_a is the ratio between *enclosed* and *available* volume, when there is not a single flux density limit

PLE evolution found in Chapter 3 for the SFG population (see subsection 3.5.3). Thus this is consistent with our argument that the radio luminosity in these systems arises predominantly from star formation.

4.6 Summary and Conclusions

We study a sample of 620 AGN covering ~1.86 deg^2 down to a a minimum noise of ~7.1 μJy / beam in the ELAIS N1 field at 610-MHz observed with the GMRT. The AGN sample was defined via a combination of diagnostics from the radio and X-ray luminosity, optical spectroscopy, mid-infrared colours, and 24μm to radio flux ratios. Of the 620 AGN from our sample, 251 have spectroscopic redshifts whereas 369 have photometric redshifts. The AGN sub-sample is constructed based on a source having at least one multi-wavelength AGN diagnostic and a redshift association. Sources meeting these criteria were further classified into RQ AGN (281 sources, or 45% of the sample) and RL AGN (339 sources, or 55% of the sample).

We measure a median value for the IRRC at 610-MHz luminosity, $q_{610\,\mathrm{MHz}}$, for our RQ AGN population to be 2.10 ± 0.34. This is comparable that of our SFGs we measured in Ocran et al. 2020b which was 2.32 ± 0.30. This suggests that the radio emission from RQ AGN host galaxies results primarily from star formation activity. The RL AGN on the other hand are systematically above the IRRC correlation for SFG and RQ AGN, with a median qIR of 1.75 ± 0.40, indicating the presence of additional AGN-powered radio emission. We have shown that the radio and the IR are equivalently good tracers of the SFR for our SFGs and RQ AGN but not for the RL AGN. This further supports our argument that in RQ AGN the radio power is tracing the SF activity in the host galaxy rather effectively but that in RL AGN the radio emission is highly contaminated by jets. Nevertheless, kpc-scale jets can contaminate also the radio emission in RQ AGN, especially at high radio luminosity, where we see an increasing fraction of outliers with respect to the radio – FIR correlation.

We derived the luminosity function of radio AGN out to $z \sim 1.5$ using the $\frac{1}{V_{max}}$ method by limiting the AGN sample to sources satisfying a cut of $r_{AB} < 25$ and $0.002 < z < 1.5$. We further constrained the evolution of this population with continuous models of pure density and pure luminosity evolution finding best-fit parameters of $\Phi^\star \propto (1+z)^{(2.25\pm0.38)-(0.63\pm0.35)z}$ and $L_{610\,\mathrm{MHz}} \propto (1+z)^{(3.45\pm0.53)-(0.55\pm0.29)z}$. The AGN as a whole do not appear to evolve significantly in both PLE and PDE in the individual redshift bins we consider for this study. We assumed the local AGN RLF Mauch & Sadler (2007) of these two distinct populations and constrained the evolution of both the RQ and RL AGN population via continuous models of pure luminosity evolution. RL AGN exhibit a weak evolution with redshift in radio luminosity as $\propto (1+z)^{(3.58\pm0.54)-(0.56\pm0.29)z}$, up to $z \sim 1.5$. RQ AGN also evolve mildly with redshift in radio luminosity as $\propto (1+z)^{(2.81\pm0.43)-(0.57\pm0.30)z}$, up to $z \sim 1.5$. The fitted PLE evolution of our RQ AGN is comparable to that of our SFGs (i.e. $\propto (1+z)^{(2.95\pm0.19)-(0.50\pm0.15)z}$, see Ocran et al. 2020b).

Comparing our RLF for both the RQ AGN and RL AGN population to models by Mancuso et al. (2017) and Bonaldi et al. (2019), we find that our RQ AGN LFs in the different redshift bins for which the LFs

are computed, are mostly consistent with the models predicted by Mancuso et al. (2017), while models by Bonaldi et al. (2019) seem to over-predict our RQ AGN LFs. On the other hand, the RL AGN LFs are higher than the Mancuso et al. (2017) estimates but agrees well with Bonaldi et al. (2019) models in different redshift bins. With regards to radio power, the LFs of the RL AGN objects extends to higher radio luminosities whereas the RQ AGN dominates at lower radio luminosities.

In future studies, we will use the ongoing MeerKAT International GHz Tiered Extragalactic Exploration (MIGHTEE) Survey (Jarvis et al., 2016) which has been planned with the goal of studying the formation and evolution of galaxies and AGN over cosmic time. MIGHTEE will greatly improve upon radio studies to date by providing dust-unbiased radio-based star formation rate estimates for large samples of individually-detected SFGs at the peak of the cosmic star-formation history (CSFH) as well as deep radio maps for stacking studies (Karim et al., 2011; Zwart et al., 2015b). A parallel effort, known as superMIGHTEE, is also underway to obtain matched-resolution 610-MHz imaging of the MIGHTEE fields with the uGMRT. The upcoming deep surveys mentioned here will be complemented by very-wide-area surveys like the Evolutionary Map of the Universe (EMU) at 1.4-GHz and the VLA Sky Survey (VLASS) at 3 GHz, which will sample brighter and rarer populations.

Chapter 5

Investigating the infrared-radio correlation and radio spectral indices at μJy fluxes with stacking

Abstract

The Faint Low-Frequency Radio Universe in Continuum: Exploitation of the Pre-SKA Deepest Survey

We probe the infrared-radio correlation and radio spectral indices using stacking. We stack in total intensity as a means to study the average properties of radio sources that are too faint to be detected individually. We stack based on infrared sources in the ELAIS N1 field using the MIPS 24 micron mid-infrared survey and radio images created at 325 MHz, 610 MHz and 1.4 GHz. Our stacking experiment shows a variation in the absolute strength of the infrared-radio correlation between these three different frequencies and the MIPS 24 micron band. We find tentative evidence of a small deviation from the correlation at the faintest infrared flux densities. We also carry out radio spectral index analyses using the median stacked radio images from from 325 MHz to 610 MHz and 610 MHz to 1.4 GHz to characterize the radio spectral index. The majority of the median stacked sources exhibit steep spectra, with a spectral index that steepens with frequency between α_{610}^{325} and α_{1400}^{610}.

5.1 Introduction

One of the tightest correlations known amongst observed parameters of galaxies is the so called Far-Infrared/Radio Correlation (FIRC) (de Jong et al. 1985; Helou et al. 1985). This correlation between the far-infrared and radio emission are tightly and linearly correlated in a broad variety of star-forming (SF) systems (e.g. see Condon 1992; Yun et al. 2001; Garrett 2002, and references therein). The correlation was initially based on comparisons between challenging ground-based observations of 10μm/radio correlations of small samples of galaxies (van der Kruit 1973; Condon et al. 1982; Rickard & Harvey 1984). However, the distinctive nature of the FIRC correlation became more apparent with larger IR-samples obtained from the Infrared Astronomical Satellite (IRAS) all sky survey (Dickey & Salpeter 1984; de Jong et al. 1985; Helou et al. 1985; Wunderlich et al. 1987; Fitt et al. 1988).

The correlation spans a wide range of galaxy types and seems to be valid both for the local and distant Universe. The reasons why the thermal dust emission at far-infrared wavelengths should be so tightly coupled to the non-thermal radio emission are not clear. One simple explanation assumes that UV and optical radiation from the most massive stars are completely absorbed by dust and re-radiated in the far-infrared, these massive stars end their lives as supernovae explosions the remnants of which accelerate the relativistic electrons that power synchrotron radio emission (Voelk, 1989). The far-infrared and radio emission are thus both related to the level of massive star-formation taking place in the galaxy (Lacki & Thompson 2010). The universality of the FIR/radio correlation is interesting because the interstellar extinction, cosmic ray transport, star formation rate, magnetic field strength vary significantly between galaxies. The radio emission from these galaxies are mostly produced from the synchrotron emission of cosmic-ray electrons accelerated in supernova shocks whereas the infrared emission is due to ultraviolet light from young massive stars that is absorbed and re-radiated by dust (Condon, 1992).

The FIRC has been explored mostly at GHz frequencies in the past, particularly at 1.4 GHz. Yun et al. (2001) studied the NRAO Very Large Array (VLA) Sky Survey (NVSS) 1.4-GHz radio counterparts of IR galaxies selected from the IRAS Redshift survey out to $z \sim 0.15$ and found the correlation is well described by a linear relation over five orders of magnitude with a scatter of only 0.26 dex. The *Spitzer* Space Telescope (Lonsdale et al., 2003) has increased the sensitivity of mid-infrared (MIR) observations and hence increased our potential to study the MIR-radio correlation. Early results, such as from the Spitzer First Look Survey (FLS), have confirmed that the MIR-radio correlation holds for relatively bright star-forming galaxies ($S_{20\,cm} > 115\,\mu$Jy) out to at least $z = 1$ (Appleton et al., 2004).

Stacking is a statistical approach to measure the mean or median flux density of a class of sources that cannot be detected individually in a survey (see White et al. 2007; Stil et al. 2014; Zwart et al. 2015a). This can be done by the co-addition of maps at the positions of sources detected in another map or catalogue. That is, if the position of a sample of sources is known, the intensities at the recorded positions can be combined by taking the average or the median (Stil et al., 2014). For an input sample of N galaxies its background noise level in a stacked image should correspond to $\sim 1/\sqrt{N}$ of the noise measured in a single radio image.

Stacking has previously been carried out by selecting sources in the near infra-red and measuring their 1.4 GHz fluxes and using photometric redshifts to convert those fluxes into star-formation rates (e.g. Garn & Alexander 2009; Dunne et al. 2009; Zwart et al. 2014) via calibration to the infrared-radio correlation (Condon et al., 2002).

Many stacking experiments have been performed to study the mid-infrared-radio correlation for galaxies which are detected in the infrared, but are below the detection limits of their radio surveys. The mid-infrared radio correlation, defined by the q_{24} index, which quantifies the FIRC as the logarithmic ratio of a monochromatic MIR 24μm flux ($S_{\nu,\mathrm{IR}}$) to the 1.4 GHz radio flux ($S_{\nu,1.4\mathrm{GHz}}$). Boyle et al. (2007) found a significantly higher value of q_{24} than is observed in sources which are detected in both mid-infrared and radio. Beswick et al. (2008) also found a significantly lower value of q_{24}, and a tentative evidence of evolution in the value of q_{24} with 24μm flux density. Garn & Alexander (2009) used stacking experiment to study the infrared-radio correlation for μJy radio sources from optical-IR catalogues that has allowed statistical correlations such as the average radio-IR correlation to be explored to lower radio flux densities.

Previous stacking studies of the infrared-radio correlation have mostly been carried out at 1.4 GHz. In this study, we aimed to explain this relation and compare with literature by performing stacking experiments of radio observations of the European Large Area ISO Survey N1 (ELAIS N1 hereafter) field. The ELAIS N1 field was originally chosen for deep extragalactic observations with the Infrared Space Observatory (ISO) due to its low infrared background (see Rowan-Robinson et al. 2004; Vaccari et al. 2005). Hence there is a wealth of mid-infrared and far-infrared wide-area imaging data, combined with a number of imaging surveys at far-ultraviolet to near-infrared wavelengths for the ELAIS N1 field (Vaccari, 2015, 2016). ELAIS N1 field contains very low amounts of Galactic emission (Lonsdale et al., 2003) and is ideal for studying the Extragalactic Universe because of its low level diffuse foreground (Baran et al., 2010).

We extend the analysis to also investigate the α_{610}^{325} and α_{1400}^{610} spectral indices of different samples. The aim is to reach much lower noise levels, providing a statistical detection of samples whose elements are individually undetected in the original images. This paper is divided as follows: we first introduce the various datasets we use in Section 5.2. In Section 5.3.1, we present the stacking method we employ in this study. Section 5.5 presents the analyses of the infrared-radio correlation extending this work to the 610-MHz and 325-MHz ELAIS N1 survey fields.

For calculation of intrinsic source properties we assume a flat cold dark matter (ΛCDM) cosmology with $\Omega_\Lambda = 0.7$, $\Omega_\mathrm{m} = 0.3$ and $\mathrm{H_o} = 70\ \mathrm{km\,s^{-1}\ Mpc^{-1}}$ and $S \propto \nu^\alpha$.

TABLE 5.1: Table showing the summary of the properties of the multi-frequency samples used in this work.

Survey	Frequency (MHz)	Resolution (arcsec)	Area covered (deg^2)	noise level (μJy beam^{-1})	Reference
ELAIS N1 GMRT Deep	325	10	1.5	~70	Sirothia et al. (2009)
ELAIS N1 GMRT Deep	610	6	1.8	~19.5	Ocran et al. (2020a)
ELAIS N1 JVLA Wide	1400	3.9	10	~87	Banfield et al. (2011)

Note, the noise level quoted for the 610 MHz is the median rms reported by Ocran et al. (2020a)

5.2 Observations and data

5.2.1 Radio data

Our primary data is the GMRT deep ELAIS N1 field observed at 610 MHz during several observing runs from 2011 to 2013 first presented by Ocran et al. (2017) and more recently by Ocran et al. (2020a). From that time, ELAIS N1 has become one of the best-studied 1–10 deg^2 extragalactic fields in a hexagonal configuration centred on $\alpha = 16^h\ 10^m\ 30^s$, $\delta = 54°\ 35\ 00''$, covering an area of 1.86 deg^2 of the ELAIS N1. The survey consists of 7 closely-spaced GMRT pointings, with on source integration time of $\sim$ 18 hours per pointing. The visibility data were calibrated, imaged and mosaicked using the CASA (Common Astronomy Software Applications) processing software. Further details regarding the observations and data processing are described in Ocran et al. (2020a). The minimum rms noise in the central region of the image is 7.1 μJy beam^{-1}. The median noise in the mosaic is 19.5 μJy beam^{-1} (see Ocran et al. 2020a).

We also use radio images are drawn from the ELAIS N1 GMRT Deep Survey 325 MHz and ELAIS N1 JVLA Wide Survey at 1400 MHz. The 325 MHz data used in this work is from Sirothia et al. (2009), who observed using the GMRT, with the objective of identifying active galactic nuclei and starburst galaxies and examining their evolution with cosmic epoch. The JVLA Wide Survey is from Banfield et al. (2011), who observed 10 deg^2 at 1.4 GHz with the JVLA in B configuration to a minimum noise of 87 μJy beam^{-1} in total intensity. Table 5.1 presents the radio surveys used in this work, their resolution, area covered and their corresponding sensitivity limits. The ELAIS N1 GMRT Deep Survey at 325 MHz is centred on $\alpha = 16^h\ 9^m\ 59^s$, $\delta = 54°\ 66\ 00''$ whereas the ELAIS N1 JVLA Wide Survey at 1400 MHz is centred on $\alpha = 16^h\ 15^m\ 37^s$, $\delta = 53°\ 77\ 00''$.

5.2.2 Mid-Infrared data

The Spitzer Space Telescope (Werner et al., 2004) has revolutionised galaxy formation and evolution studies. The telescope has provided nearly optical-quality imaging over wide areas at mid-infrared wavelengths in its IRAC (Fazio et al., 2004) 3.6, 4.5, 5.8, 8.0 μm channels and in its Multiband Imaging Photometer for Spitzer (MIPS) (Rieke et al., 2004) 24 μm channel as well as lower-resolution imaging

in its MIPS 70 and 160 μm far-infrared channels. The 24μm array has excellent photometric properties, and measurements with rms relative errors of about 1% can be obtained. The Spitzer Wide-Area Infrared Extragalactic Survey (Lonsdale et al., 2003, SWIRE) covered nearly 50 deg^2 in six different fields, including ELAIS N1, in all IRAC and MIPS channels. In this work we use the 24μm maps and catalogs produced by the Spitzer Data Fusion Project Shupe et al. (2008); Vaccari (2015)* for our stacking analysis. The Spitzer Extragalactic Representative Volume Survey (Mauduit et al., 2012, SERVS) obtained deeper IRAC 3.6 and 4.5 μm observations than SWIRE. In this work we use the SERVS catalogs produced by the SERVS Data Fusion project Vaccari (2015)† to obtain accurate positions of SWIRE 24 μm sources. Specifically, we require that a SWIRE 24 μm source is detected at 3.6 or 4.5 μm by SERVS.

5.3 Stacking Analysis

5.3.1 Method

We stacked radio flux density at 325 MHz, 610 MHz and 1.4 GHz of infrared-selected galaxies. As a starting point, galaxies were selected in the 24μm MIPS and binned according to their 24μm flux density. Positional information for the infrared sources was taken from the 24μm source catalogue from the Spitzer Data Fusion. This catalogue which contains 85 394 extragalactic point sources with a 24 μm flux density limit of 286.6μJy for the ELAIS N1 region. Of the total sources in the catalogue, 19 591 are located within the 610 MHz image. These sources were within the central region of the mosaic, so that any edge effects and increasing noise levels due to the varying primary beam would not affect the flux density calibration. Ocran et al. (2020a) computed a small median astrometric offset for second cross-matching to be $+0.055 \pm 0.447$ arcsec in RA and -0.026 ± 0.435 arcsec in DEC between the GMRT and SERVS catalogues. These positional offsets between the 24μm catalogue and the radio image were removed before performing any stacking.

Stacking was done with the `genstack.py` program developed at the University of Calgary by Ben Keller and Jeroen Stil‡ (Keller & Stil, 2018). The code takes a list of targets, extracts postage stamp images for each target from the survey images, and creates median and mean images of the postage stamps. Genstack has powerful options to assist in sample selection and produces statistics for each postage stamp for detailed analysis of the sample. In practice, we hardly ever use the mean image because it is sensitive to interloping sources in crowded fields and to image artefacts around bright sources.

The median image provides a compelling visual impression of the statistical significance of the sample median compared to nearby off positions. White et al. (2007) performed detailed calculations that show that a median stacking analysis is superior to a mean stacking, since it is robust to small numbers of bright sources, and it does not require any maximum allowed flux density cutoff prior to stacking. It also shows

*http://mattiavaccari.net/df/m24
†http://www.mattiavaccari.net/df
‡https://github.com/bwkeller/PASTA

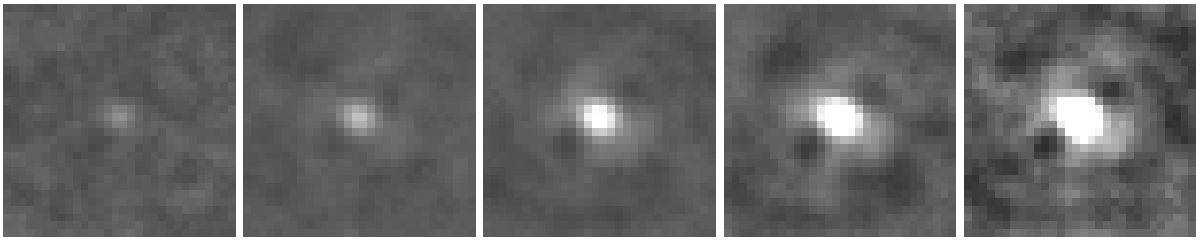

FIGURE 5.1: Median stacked 325 MHz radio images for the 24μm faintest six flux density bins. All images have a size of 30×30 arcsec^2. The grey-scale ranges between -30 and 60μJy beam^{-1}

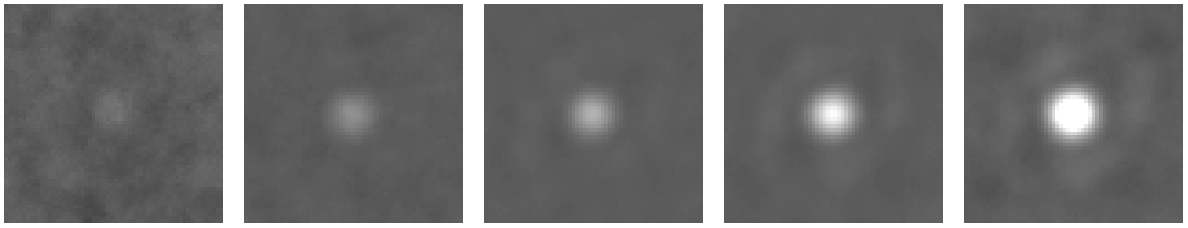

FIGURE 5.2: Median stacked 610 MHz radio images for the 24μm faintest six flux density bins. All images have a size of 60×60 arcsec^2. The grey-scale ranges between -7 and 40μJy beam^{-1}

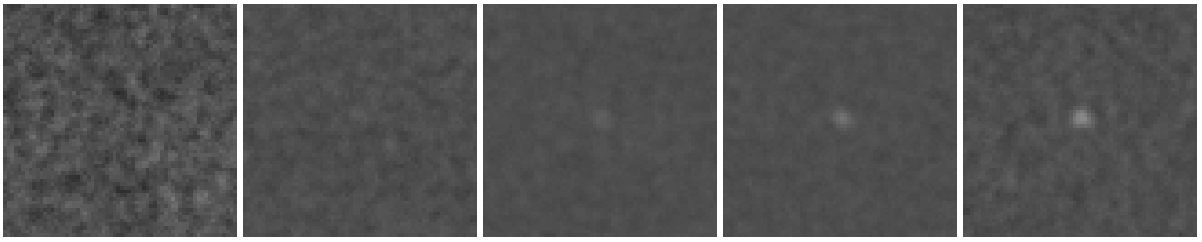

FIGURE 5.3: Median stacked 1.4 GHz radio images for the 24μm faintest six flux density bins. All images have a size of 60×60 arcsec^2. The grey-scale ranges between -7 and 60μJy beam^{-1}

patterns like the side lobes of the dirty beam that must be present around real sources of any flux density in the image.

One would rarely be satisfied with a single stack. Some of the more powerful applications of stacking involve differential measurements where the differences between samples are highlighted alongside the absolute flux measurements.

At the time that the stamps are created, if they are found to have no error flags, they are added to the stack. This stack is simply a 3-dimensional matrix of intensity values, with the first two dimensions of the postage stamps holding spatial information. Once the stack has been fully populated with stamps, 2-dimensional matrices are generated which are the median and mean output images. Figures 5.1, 5.2, and 5.3 presents the median stacked 325 MHz 610 MHz and 1.4 GHz radio images for the 24μm faintest six flux density bins (also see Figures D.1, D.2 and D.3 which presents the mean stacked 325 MHz 610 MHz and 1.4 GHz radio images for the 24μm faintest six flux density bins in Appendix D). There is a visible point which is remarkably faint in the first bin (i.e. $22 - 39\mu$Jy) for the median 325 MHz radio image. This point remains blurred in the second and third bins but becomes distinct in the fourth bin. Similar to this, Figure 5.2 shows this visible point which starts to be distinct in the fourth bin. The circular appearance of the point in

Figure 5.2 is given by the source seen in each image, with a circular appearance given by the 6×6 arcsec^2 resolution of the original GMRT mosaic. In contrast to Figures 5.1 and 5.2, the point remains faint in Figure 5.3 and starts to appear in the fourth bin.

It is not possible, however, to do meaningful aperture photometry on a median-stacked image. The premise of median stacking a survey is that the radio emission is unresolved, and that the central pixel represents the flux density of the source. We can verify this after the stack be fitting a two-dimensional Gaussian to the stacked image and verify that its width is consistent with the size of the synthesized beam. Figure 5.4 shows the angular size of the median stacked image detection (in arcsec) as a function of infrared flux compared with the beam (dashed black lines in each panel) of the 325 MHz (top panel), 610 MHz (middle panel) and 1.4 GHz (bottom panel) images.

The fitted angular size is over-all closely consistent with the beam size. Differences may occur for various reasons. A Gaussian fit to a source convolved with a non-Gaussian point spread function can give rise to systematic errors. Errors in the positions of the input source catalog can lead to blurring of the stacked image. The same effect can occur if the radio emission is systematically offset from the IR emission for some reason. Errors in the SWIRE positions can only have a minor effect, because the fitted angular sizes are most consistent with the beam size for the 1.4 GHz survey, which has the smallest beam. The systematically larger source size at 325 MHz is then more likely due to the higher side lobes of the dirty beam (see Figure 5.1). The systematic behaviour of the angular size in the 610 MHz survey may be due to a small negative bias in off-source values in the median-stacked images.

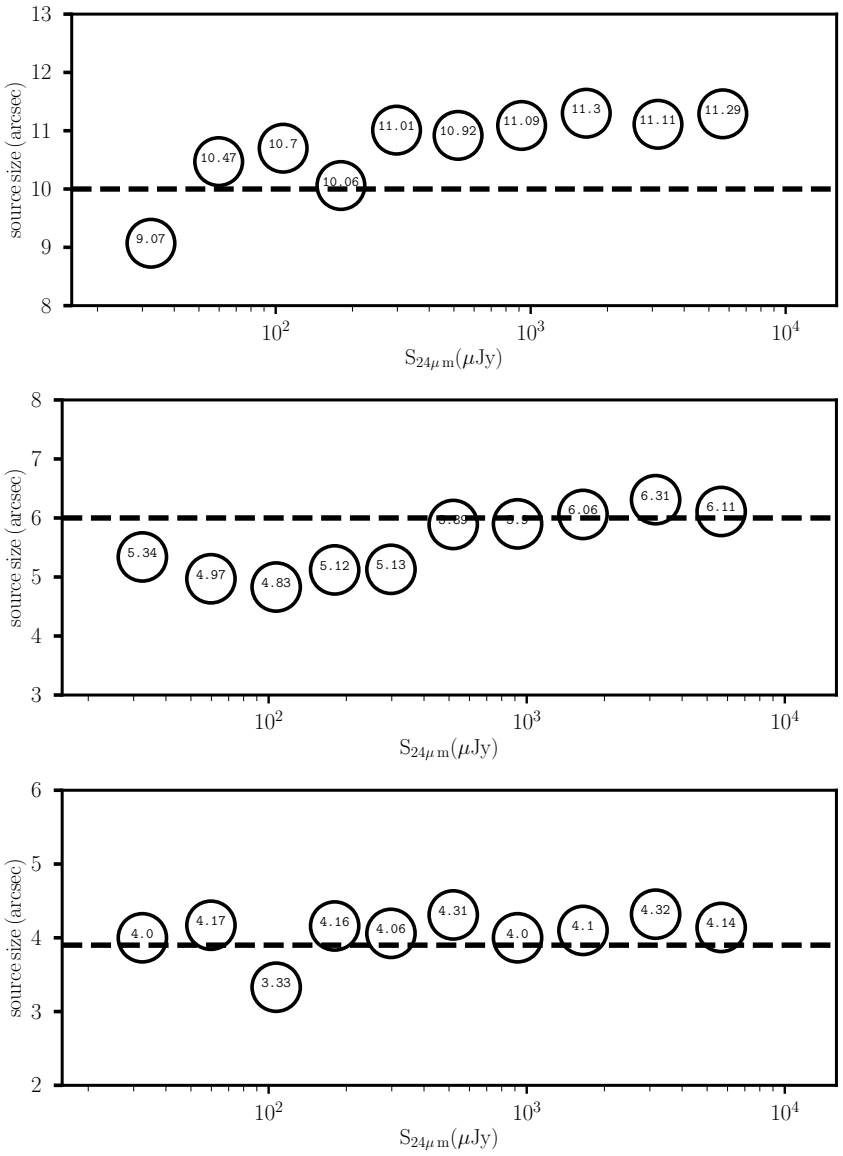

FIGURE 5.4: Angular size (in arcsec) as a function of infrared flux compared with the size of the beam (dashed black lines in each panel) of the 325 MHz (top panel), 610 MHz (middle panel) and 1.4 GHz (bottom panel) images.

5.4 Results and discussion

5.4.1 Flux density of individual sources

We first measure the radio flux density at the individual source positions and bin the sources by their infrared flux density (see Garn & Alexander 2009). We then use the statistical distribution of radio flux density for sources within an infrared flux density bin to estimate quantities that can be inferred from observations. White et al. (2007) showed that while the individual measurements will be very uncertain, particularly for sources near to or below the noise level, the statistical properties of the distribution should be robust.

TABLE 5.2: Table showing the infrared flux density range, number of sources in each bin N, the median flux and the noise level σ for the stacked images as 610 MHz, 325 MHz and 1.4 GHz

Bin	S_{24} (μJy)	N_{610}	S_{610} (μJy)	σ_{610} (μJy beam^{-1})	N_{325}	S_{325} (μJy)	σ_{325} (μJy beam^{-1})	$N_{1.4}$	$S_{1.4}$ (μJy)	$\sigma_{1.4}$ (μJy beam^{-1})
1	22 -39	91	3.81	3.36	96	2.58	12.77	108	2.44	11.88
2	39 - 71	392	4.71	1.85	400	5.06	6.69	452	9.19	5.45
3	71 - 129	2110	14.49	0.66	2140	17.79	2.44	2403	3.36	2.19
4	129 - 232	6518	25.74	0.63	6660	35.69	1.52	6937	8.46	1.50
5	232 - 418	6178	48.92	0.97	6293	74.47	1.91	6038	19.94	1.32
6	418 - 754	2576	91.05	1.33	2648	132.60	3.65	2441	32.09	2.52
7	754 - 1356	759	146.89	2.31	782	220.30	6.12	728	53.92	4.02
8	1356 - 2450	287	246.36	2.95	292	350.34	9.74	276	93.42	7.72
9	2450 - 4412	109	305.20	4.81	113	495.75	13.31	105	126.28	10.30
10	4412 - 7892	48	600.76	6.18	49	751.25	17.92	45	201.73	16.13

Table 5.2 presents the infrared central flux density of the bin, number of sources in each bin N, the median flux and the noise level σ for the stacked images as 610 MHz, 325 MHz and 1.4 GHz. We choose fixed (in log space) bin sizes and non-overlapping in flux (statistically independent) bins. We had eleven bins with flux density range from 22 to 7892 μJy . Each bin's upper limit is ~1.8 times the lower limit. The expected noise level of a stacked image composed of N stamps, with measured RMS noise of σ_0 is roughly:

$$\sigma = \frac{\sigma_0}{\sqrt{N}} \tag{5.1}$$

The background RMS noise versus number of sources stacked for the 325 MHz (top panel) 610 MHz (middle panel) and 1.4 GHz (bottom panel) data is presented in Figure 5.5. The solid line in each panel shows the noise level measured from each survey divided by the square root of the number of sources in each bin (see Equation 5.1). The open black circles in each panel represents the measure RMS noise listed in Table 5.2.

Figure 5.6 shows the radio flux density for each source in the 24μm catalogue, measured as described in subsection 5.3.1 (open green circles). The values of noise in each radio image are shown as horizontal dashed lines in each panel. The 325, 610 and 1400 MHz samples are represented by the top, center and bottom panels respectively. The figure is plotted on a log-linear scale in order to show the range of radio flux density that is measured, which can be negative due to the effects of noise (see, Garn & Alexander 2009). The sources are binned logarithmically by their 24μm flux densities and we calculate the median infrared and radio flux density in each bin so that one may explore the statistical properties of sources. This is demonstrated by the open black circles in Figure 5.6. These median values of flux density within each bin are plotted as open black circles with errors. The error bars show the size of the inter-quartile range (IQR) of radio flux density in each bin.

It can be inferred from Figure 5.6, especially at low 24μm flux densities, the extracted total radio flux density of individual sources is close to or even below the radio sensitivity of these data. At the positions of the majority of the faintest 24μm sources, the radio emission is significantly lower than the image noise demonstrating that stacking is a powerful tool to measure the flux density of sources that cannot be detected

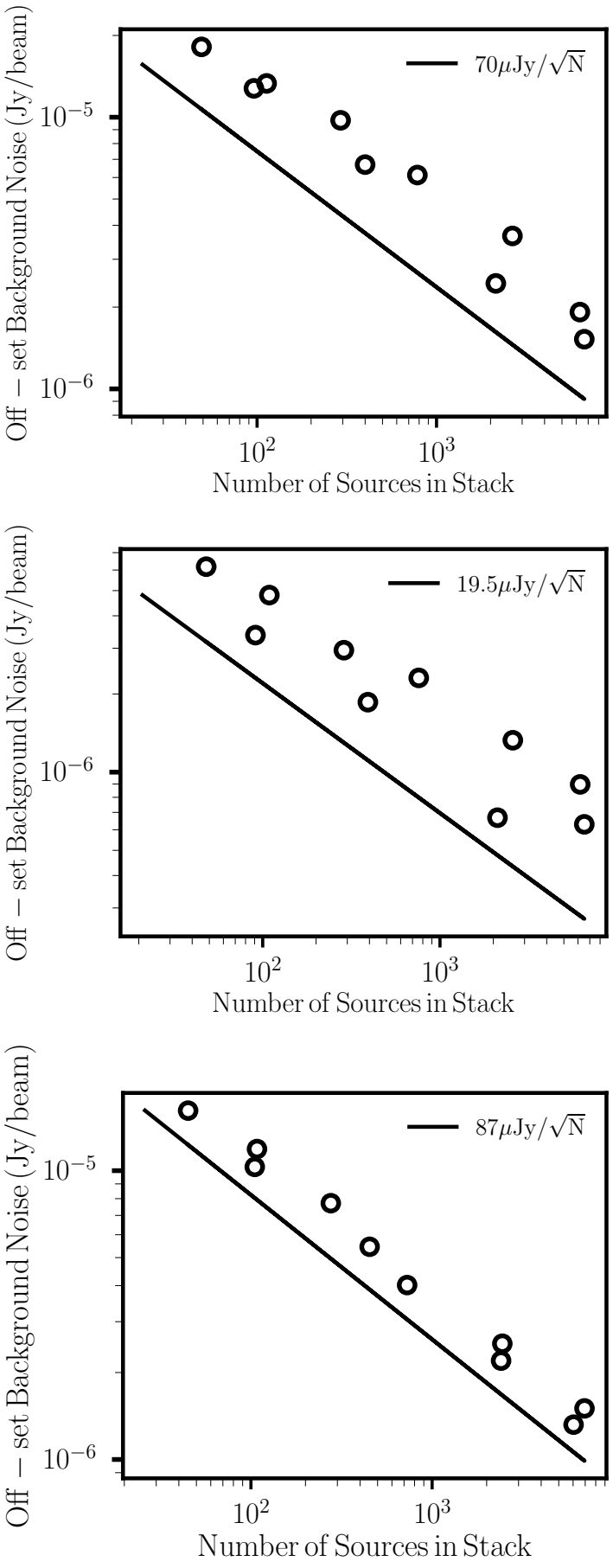

FIGURE 5.5: The background RMS noise versus number of sources stacked for the 325 MHz (top panel) 610 MHz (middle panel) and 1.4 GHz (bottom panel) data. The solid line in each panel shows the noise level measured from the each survey divided by the square root of the number of sources in each bin.

individually in a survey. There is a large dispersion in the individual values of flux density being measured, and the IQR of radio flux density for each bin is bigger as a result of the increased and varying noise level across the 610 MHz image. Results from Boyle et al. (2007) CDFS and Boyle et al. (2007) ELAIS-S1 at 1.4 GHz are overlaid as dashed red line and brown stars respectively. The orange plus represent results from Beswick et al. (2008). Results from Garn & Alexander (2009) are overlaid on the middle and bottom panels as a blue solid line.

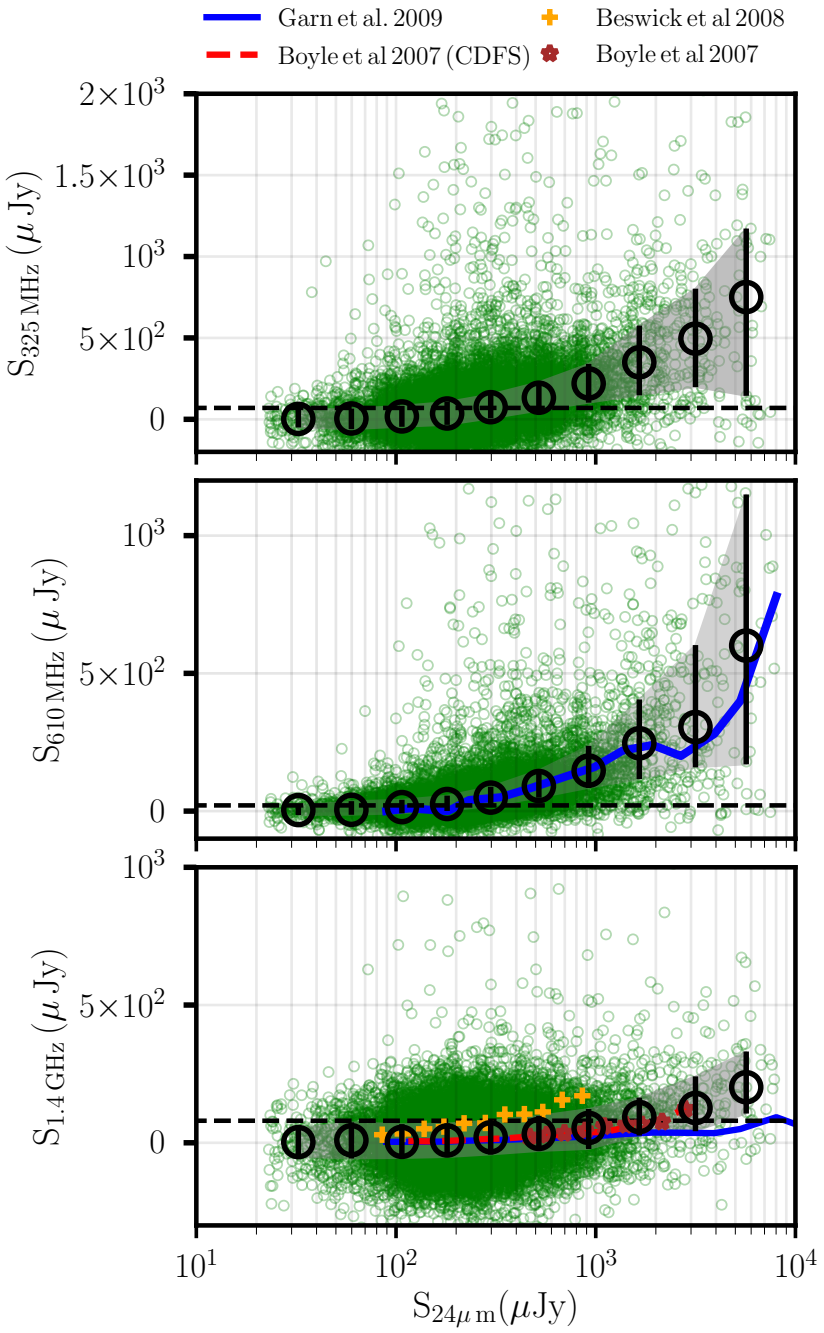

FIGURE 5.6: The median radio flux density for each source in the 24μm catalogue as a function of 24μm flux density. The error bars show the size of the inter-quartile range (IQR) of radio flux density in each bin. Bins containing fewer than 20 sources have been excluded from the figure. The 325, 610 and 1400 MHz samples are represented by the top, middle and bottom panels respectively. Results from Boyle et al. (2007) CDFS and Boyle et al. (2007) ELAIS-S1 are overlaid as dashed red line and brown stars respectively. The orange pluses in represent results from Beswick et al. (2008). Results from Garn & Alexander (2009) are overlaid on the middle and bottom panels as blue solid line.

5.5 The Mid-Infrared Radio flux ratio

The logarithmic flux density ratio between the infrared and radio is quantified by q_{IR} (Appleton et al., 2004) given by:

$$q_{IR} = \log_{10}\left(\frac{S_{IR}}{S_{radio}}\right) \tag{5.2}$$

where S_{IR} is the infrared flux density detected within any of the Spitzer IR bands (e.g. 24μm) and S_{radio} is the radio flux density. We measure the strength of the infrared-radio correlation quantified at 325 and 610 MHz in a similar way to 1.4 GHz. We represent the strength of the infrared/radio correlation quantified at 325 MHz and 610 MHz in a similar way to at 1.4 GHz, using the notations $q'_{24\,325}$ and $q'_{24\,610}$ respectively.

The top left panel of Figure 5.7, the value of q'_{24} for each source in the 24μm catalogue is shown, along with the median binned, value of 24μm, which is calculated directly from the median values of infrared and radio flux density within each flux density bin using the 325 MHz sample. The top left panel of Figure 5.7 shows a comparison between q'_{24} calculated from all sources within the 610 MHz ELAIS N1 field. The bottom panel shows the q_{24} versus 24μm flux for our 1.4 GHz sample. The shaded region in each plot denotes the inter-quartile range (IQR) for each bin, a more robust measurement of the range than the standard deviation. We estimated the error bars on the median using the median absolute deviation (MAD) estimator (Rousseeuw & Croux, 1993).

5.5.1 Comparison to literature

Appleton et al. (2004) carried out the first study of the infrared-radio correlation in the extragalactic First Look Survey (xFLS) field, using a 1.4 GHz radio catalogue (Condon et al., 2003), and early 24μm *Spitzer* data. 508 sources were found with both 24μm and 1.4 GHz detections. Appleton et al. (2004) calculated a mean value of $q_{24} = 0.84 \pm 0.28$ for these sources. The horizontal black line in the bottom panel of Figure 5.7 represents the mean value, whilst the dashed horizontal black lines represents the error reported by Appleton et al. (2004). Garn & Alexander (2009) found a variation in the absolute strength of the correlation between the xFLS and SWIRE regions, but no evidence for significant evolution in the correlation over the 24μm flux density range 150μJy to 2mJy. They reported that their sources are more radio-quiet than was found by Appleton et al. (2004). The Garn & Alexander (2009) results at 610 MHz are overlaid on the middle panel of Figure 5.7 as blue solid line.

Boyle et al. (2007) presented stacking analysis, using 24μm sources detected in the SWIRE survey, in the Chandra Deep Field South (CDFS) and ELAIS-S1 fields. They reported a q_{24} value of 1.39, and no significant variation with S_{24} over the range 100 – 2800 μJy. We overlay results from Boyle et al. (2007) CDFS, Boyle et al. (2007) ELAIS-S1 as dashed red line and brown stars respectively. Beswick et al. (2008) detected a small deviation from the correlation at the faintest infrared flux densities and attributed the small observed change in the gradient of the correlation as a result of a suppression of the MIR emission in faint star-forming galaxies. They stressed that the deviation potentially has significant implications for using

TABLE 5.3: Table summarizing the mean and median values of $q_{24\mu m}$ measured at the different frequencies studied in this work.

Frequency	Mean q_{24}	Median q_{24}
325 MHz	0.47±0.40	0.42±0.27
610 MHz	0.83±0.46	0.78±0.23
1.4 GHz	0.66± 0.50	0.59±0.33

either the MIR or non-thermal radio emission as a star formation tracer of very low luminosity galaxies. The orange pluses in Figure 5.7 represent results from Beswick et al. (2008). Boyle et al. (2007) stacking results appear systematically higher than our results, and those of Appleton et al. (2004), Beswick et al. (2008) and Garn & Alexander (2009). In their discussions, Boyle et al. (2007) acknowledged that although their value of q_{24} is derived from stacked data, whilst that Appleton et al. (2004) value is derived from detected sources, this discrepancy is nevertheless a surprising result and merits further scrutiny. They attributed this discrepancy might be caused by a difference in k-correction between their analysis and that of Appleton et al. (2004).

The curves in each panel in Figure 5.7 highlight the dramatic change in $q'_{24\,325}$, $q'_{24\,610}$ and q_{24} over the 24μm flux density range. All the plots in Figure 5.7 show a tentative trend for low q_{IR} (i.e. $q'_{24\,325}$, $q'_{24\,610}$ and q_{24}) with declining 24μm flux density. It is clear that our stacking results give a value of q_{24} that is lower than the Appleton et al. (2004) mean value. Our results indicate that the radio emission from host galaxies in the faint flux density regime result primarily from star formation activity.

Table 5.3 summarizes the mean and median values of q_{24} measured at the different frequencies studied in this work. The solid black horizontal line in each panel of Figure 5.7 represents the median q_{24} (i.e. computed at different frequencies presented in this work) for all sources within the ELAIS N1 field over the entire 24μm flux density range. We report a mean and median value of $q_{24\mu m}$ for all of the ELAIS N1 sources at 325 MHz to be 0.47±0.40 and 0.42±0.27 respectively. The mean and median value of $q_{24\mu m}$ for all of the ELAIS N1 sources at 610 MHz presented in this study is 0.83±0.46 and 0.78±0.23, respectively. At 1.4 GHz we report the mean and median value to be 0.66±0.50 and 0.59±0.33 respectively. The errors on the mean denote the standard deviation whereas the errors on the median represent the MAD. Beswick et al. (2008) reported a mean and median value of $q_{24\mu m}$ for all their HDF-N sources to be 0.52 and 0.48, respectively 24mum flux densities ranging from 80.1 to 1480 μJy. Ibar et al. (2008) reported a K-corrected value out to $z \sim 3$ of $q_{24} = 0.71$ with a dispersion of 0.47.

5.5.2 Is there evolution in the MIR-radio correlation?

The increasing sensitivity of deep radio surveys to the distant Universe has enabled the probe both AGN and SFGs. A major question that arises is, are we probing a regime where AGN are less important? Thus, by determining the nature of the faint radio population we can learn about the relationship between AGN and SFGs.

Previous stacking experiments at 1.4 GHz have suggested that the IR-radio correlation may evolve at lower flux densities (see Boyle et al. 2007; Beswick et al. 2008). This suggestion is also backed theoretically by Bell (2003) who assembled a diverse sample of galaxies from the literature with far-ultraviolet (FUV), optical, infrared (IR) and radio luminosities to explore the origin of the radio-IR correlation. The average value of q_{24} shows a small decrease as a function of lower values of $S_{24\mu m}$ (see the bottom panel of Figure 5.7). This trend is also seen for $q'_{24\,325}$ and $q'_{24\,610}$

Beswick et al. (2008) outlined biases introduced by flux density thresholds of observations, the application or non-application of k-corrections and possible AGN contamination of sample galaxies as contributing factors which could affect these results. Previous studies, such as Appleton et al. (2004), showed that the application of k-corrections to individual sources below z = 1 only introduces a small change to the average value of q_{24} as a function of redshift. We have not applied k-correction to the flux densities of these ELAIS N1 sources because in many cases the spectral shapes and redshifts of objects are not known adequately enough to apply any k-correction with confidence.

5.5.3 Stacked radio spectral indices

The radio spectral index can be used as a probe of a galaxy's nature, star-forming galaxies are usually considered to have a mean spectral index between -0.8 and -0.7 with a relatively small dispersion, 0.24 (e.g. see Condon 1992; Jarvis et al. 2001; Ibar et al. 2009). Thus the radio spectral energy distributions provide valuable information which can be used to differentiate between sources types according to their dominant emission mechanisms (e.g. Marsden et al. (2014)). Work combining 610 MHz and 1.4 GHz data, have found evidence for flatter spectral indices (Bondi et al., 2007; Garn et al., 2008) at sub-mJy radio fluxes , suggesting that core-dominated radio-quiet AGN are playing a key role in the sub-mJy radio population. To estimate the radio spectral index we used the median flux reported for each S_{24} bin for the 325 MHz, 610 MHz and 1.4 GHz sample. We investigate the spectral index between α_{610}^{325} and α_{1400}^{610} of the stacked sources to give us a better indication on how the spectra changes going to higher frequency.

The top panel of Figure 5.8 shows the 2-point spectral index from 325 MHz to 610 MHz (i.e. median spectral index computed from the median stacks of the 325 MHz and 610 MHz image). We see a clear spectral steepening of the median stacked spectral index as we go down towards low 610 MHz flux densities. However, the first two median stacks corresponding to a 610 MHz flux densities of 3.81 and 4.71 μJy respectively (i.e. first 2 bins see Table 5.2), have a flatter median spectral index. A spectral index α = -0.5 divides in a remarkably clean way flat-spectrum/compact sources from steep spectrum /extended sources (e.g., Massardi et al. 2011; Padovani 2016b). Thus, at these two low flux density median stacks, the individual sources may be populated by compact sources hence the flatter median stacked spectral indices. Ocran et al. (2020a) reported the 2-point spectral index from 325 MHz to 610 MHz for sources in their ELAIS N1 deep sample sample range from -2.7 to 1.8 with a median value of -0.80 ± 0.29. Restricting their statistical analyses to a much brighter sub-sample for the spectral index from 325 MHz to 610 MHz for sources with a flux range corresponding to $S_{610\,\mathrm{MHz}} > 0.5$ mJy, they reported a median α -0.71 ± 0.27.

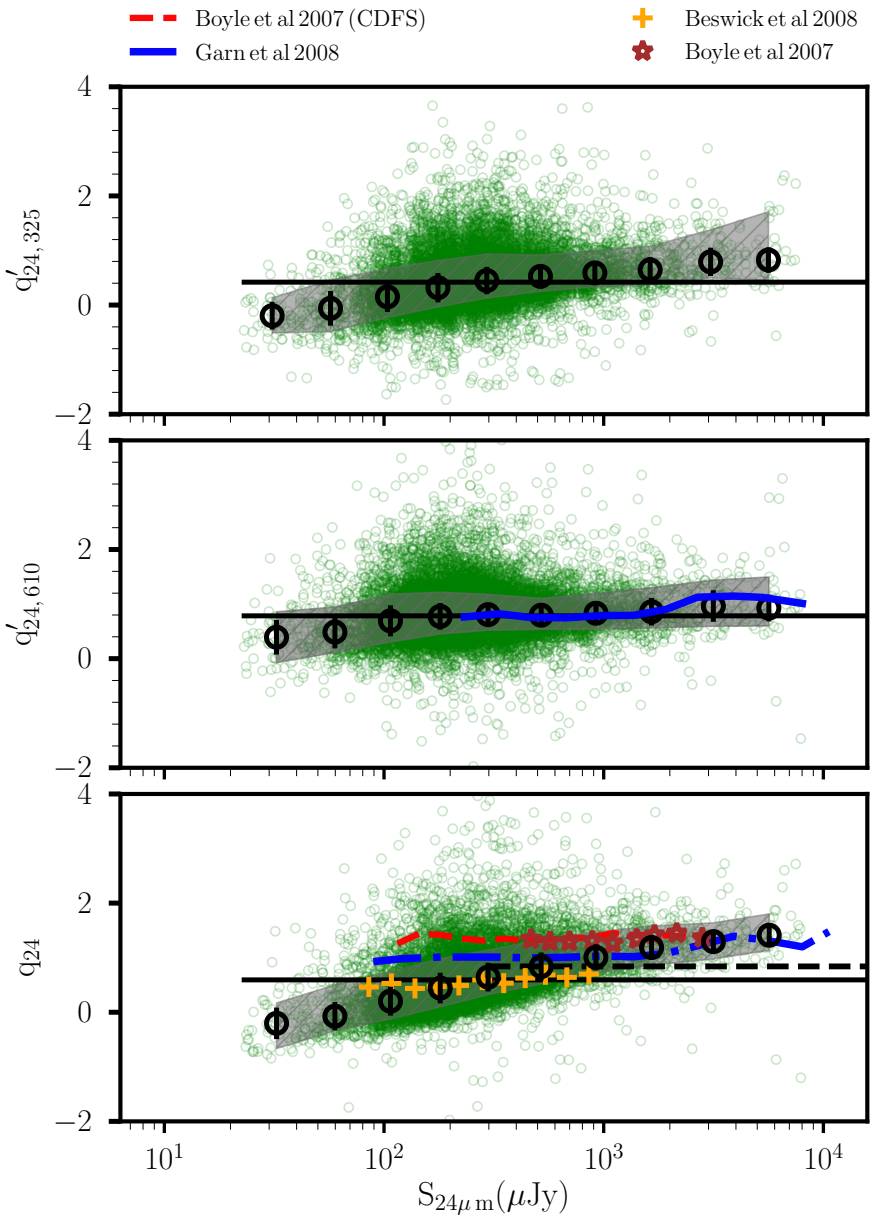

FIGURE 5.7: The 24μm flux density versus q_{24} for all sources within the ELAIS N1 field (light green circles). The median values of q_{24} in each flux density bin are shown as open black circles in each panel. The error bars denote the size of the IQR of radio flux density in each bin. The 325, 610 and 1400 MHz samples are represented by the top, middle and bottom panels respectively. The solid black horizontal line in each panel represents the median for all sources within the ELAIS N1 field over the entire 24μm flux density range. Results from Boyle et al. (2007) CDFS and Boyle et al. (2007) ELAIS-S1 are overlaid as dashed red line and brown stars respectively. The orange pluses in represent results from Beswick et al. (2008). Results from Garn & Alexander (2009) are overlaid on the middle and bottom panels as blue solid line.

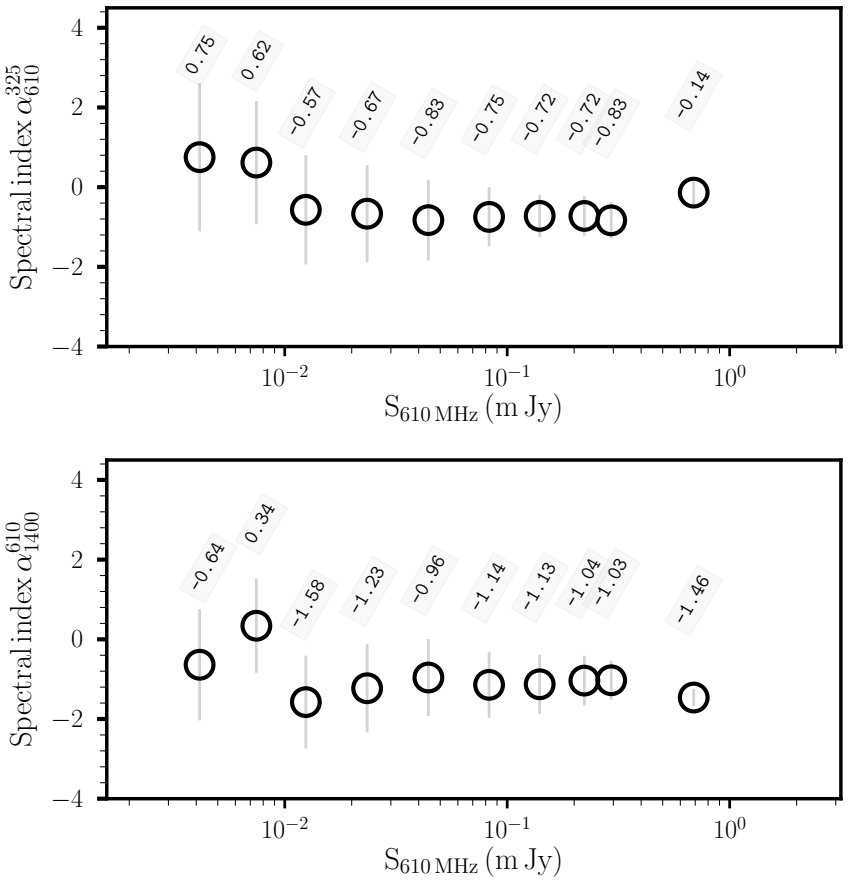

FIGURE 5.8: colour-flux diagrams comparing the 325-610 MHz (top) and 1400-610 MHz (bottom) spectral indices

The bottom panel of Figure 5.8 shows the 2-point spectral index from 610 MHz to 1.4 GHz The open black represent the median spectral index computed from the median stacks of the 610 MHz and 1.4 GHz image. Similarly to the top panel, we write the measured spectral index on top of each circle to provide a graphic representation of the change in the spectral index over the 610 MHz flux densities. Based on the spectral indices between 610 MHz and 1.4 GHz, there is also a small spectral steepening with the third and fourth median stacks (i.e. bins) of the 610 MHz and 1.4 GHz spectral index becoming ultra-steep (i.e. α < -1.2 see Argo et al. 2013; Herzog et al. 2016). Unlike the nature of spectral index from the first two median stack from corresponding to a 610 MHz flux densities of 3.81 and 4.71 μJy for α_{610}^{325}, only the second bin spectral index for α_{1400}^{610} is flat. In the first bin of the median stacked radio images, we measure a steep median spectral index from 610 MHz to 1.4 GHz of -0.64.

5.6 Conclusions and future work

Stacking offers high sensitivity to the median signal of a class of radio sources. Using the deepest sensitive 610 MHz observations together with other radio surveys drawn at 325 MHz and 1.4 GHz, and in conjunction with deep 24μm Spitzer source catalogues from ELAIS N1 field, we have investigated the μJy

radio counterparts of faint MIR sources. We have calculated q'_{24} and q_{24} for sources within the ELAIS N1 field. We find that the population of objects at μJy flux densities obey the mid-infrared radio correlation which indicates that they are powered by star formation rather than by AGN. Previous work on statistically stacking the radio emission from many tens of faint 24μm sources has been used to characterize the size and nature of the radio emission at very faint IR galaxies well below the nominal radio sensitivity of these data. Using these same methods, we have further extended the MIR-radio correlation at very low 24μm flux densities than these previous studies and found a tentative deviation in correlation. We estimate the radio spectral index using the median flux reported for each S_{24} bin for the 325 MHz, 610 MHz and 1.4 GHz sample. We have investigated the spectral index between α_{610}^{325} and α_{1400}^{610} of the stacked sources. The primary results of this work demonstrate that our sample of individual 24μm selected sources follow the MIR-radio correlation down to radio flux densities of a few μJy for the radio surveys drawn at 325 MHz and 1.4 GHz. Our findings are consistent with shallower independent radio surveys of previous studies with stacking, as we extend the MIR-radio correlation down to lower flux densities.

With available multi-wavelength ancillary data one can proceed from noisy flux measurements to studies of radio number counts, galaxy luminosity functions, star-formation rates and their cosmic densities, as a function of environment, stellar mass, redshift (e.g. see Glenn et al. 2010; Padovani et al. 2011; Heywood et al. 2013a; Zwart et al. 2014 and references therein for more comprehensive introductions to the science available via stacking). In future, we plan to select galaxy samples at 3.6μm with panchromatic (FUV to mid-IR) ancillary data and mapping in 610 MHz radio continuum emission in the ELAIS N1 field, we will measured stellar mass-dependent average (specific) star formation rates ((S)SFR) in the redshift range exploited by Ocran et al. 2020b following work by Karim et al. (2011). They explored the redshift evolution of the specific star formation rate (SSFR) for galaxies of different stellar mass by drawing on a deep 3.6μm selected sample of $> 10^5$ galaxies in the 2 deg^2 COSMOS field. These were obtained using a median image stacking technique that is best applied in the radio regime where the angular resolution is high and the fraction of direct detections is comparatively low such that blending of sources is negligible (see Karim et al. (2011)).

The advent of MeerKAT complemented by low-frequency surveys such as those being planned with the uGMRT, will enable us to study the infrared-radio correlation over a large range of radio frequencies, including where the contribution from thermal free-free emission is less important than at 1.4-GHz. We also plan to undertake stacking polarized intensity as a means to study the polarization of sources that are too faint to be detected individually in surveys of polarized radio sources. This technique is very useful at higher flux densities where a significant fraction of sources is detectable in polarization. Stil et al. (2014) presented a procedure for stacking polarized intensity that uses the shape of the distribution of data values going into the stack as an additional constraint to solve for the unknown intrinsic distribution of polarized intensity of the sample.

Chapter 6

Conclusions and Future Work

In this Chapter, I summarize the main results of my Thesis and outline some possible further developments of this research. This thesis presents the study of the nature of the microJy radio source population, based on a deep GMRT survey of the ELAIS N1 field. Our sample consists of 4920 sources observed at 610 MHz over an area of ∼1.86 deg^2, and down to a minimum noise of 7.1 μJy/beam. In Chapter 2, I present the deep 610 MHz radio observation, I extract the source catalogue and present the source counts and classification of the radio sources by type (AGN or star-forming galaxy). I also conduct a study of the radio spectral properties of this sample. I present a study of star forming galaxies selected from the currently deepest low-frequency radio survey at 610 MHz in Chapter 3. I derive the IR-radio correlation and the luminosity functions , as well as the cosmic star formation rate history of star-forming galaxies up to $z \sim 1.5$. In Chapter 4, I shed further light on the properties of the AGN in the sample comparing them to the SFG sample discussed in Chapter 3. Chapter 5 focuses on the stacking analysis of the GMRT ELAIS N1 image data at 325 MHz, 610 MHz and 1.4 GHz to explain the IR-radio correlation and spectral index properties to even fainter flux densities. In the following sections I present results and conclusions for each chapter.

6.1 Deep GMRT 610 MHz Observations of ELAIS N1 field: Catalogue and Source Counts

I report deep 610 MHz GMRT observations of the ELAIS N1 field, a well studied region of sky with a wealth of multi-wavelength data. The nominal sensitivity of the image is ∼7.1 μJy/beam in the central region of the field. From the mosaicked image, which covers approximately 1.86 deg^2, I recover a catalogue of 4290 sources down to a flux density limit of 35.5 μ Jy.

I derive the 610 MHz source counts applying corrections for completeness, resolution bias and Eddington bias. The counts are within the scatter of most previous source counts from other surveys at 610 MHz and agree with extrapolated models of the low-frequency source population counts. The counts show

a flattening below $\sim$ 1 mJy which is believed to be a result of the increasing contribution of SFGs as well as RQ AGN which can also contribute to the flattening. This corresponds well with the flux density regime where this feature has been detected at 1.4 GHz. To that end, this is the confirmation detection of this feature in the differential source counts at 610 MHz. I provide classification of the radio sources with redshift using radio and X-ray luminosity, optical spectroscopy and mid-infrared colours to search for evidence of the presence of an AGN. I compare my identifications to predictions of the flux density distributions of SFGs and AGN from models of galaxy evolution, and find a good agreement assuming the majority of the sources without redshift are SFGs.

I conduct a study of the radio spectral properties of this sample by matching the 610 MHz catalogue with catalogues from other surveys at different frequencies. This forms a sample with which to study the spectral index properties of low-frequency radio sources. I measure the median spectral index between 610 - 325 MHz, 610 - 1400 MHz and 610 - 5000 MHz. The results suggest that the 610 MHz sample is dominated by steep-spectrum sources as expected for low-frequency selected sources. Adopting the definition of a USS object as a radio source with $\alpha < -1.3$ (as is typically the case in the literature) I find a total of two candidate USS radio sources which have counterparts at 325 MHz and 1.4 GHz (FIRST). The two candidate USS sources have no corresponding spectroscopic and photometric redshift association from the multi-wavelength catalogue, therefore remain unclassified.

6.1.1 Future work

Future work on Chapter 2 could be taken in many directions. The sample used for the purposes of classification is selected based on the availability of at least one multi-wavelength (i.e. not based on radio properties alone) AGN diagnostic. Deep multi-wavelength spectro-photometric datasets with comparable resolutions and sensitivities to our radio data will be needed to improve our source classification. In future, I will employ multi-object wide-field optical/near-infrared spectroscopy, as this is the best avenue toward improving the diagnostics for such scientific work. I have compiled possible candidate giant radio sources (GRS) in the 610 MHz sample. This work extends the GRS detections to the faint radio universe. I plan to compare the properties of my selected candidate GRS with those of a complete sample of 3CR (Laing et al., 1983) radio sources with sizes between 50 kpc and 1 Mpc. From this, I will investigate the evolution of the giant sources, and test their consistency with the unified scheme for radio galaxies and quasars.

While modern source counts approach flux density sensitivities of $\lesssim 10\mu$Jy in total intensity (Windhorst 2003; Hopkins et al. 2003a), very little is known about the polarization properties of the faint radio source population. Taylor et al. (2007) presented deep polarimetric observations at 1420 MHz of the ELAIS N1 region as part of the Dominion Radio Astrophysical Observatory Planck Deep Fields project (DRAO) achieving a maximum sensitivity in Stokes Q and U of 78μJybeam^{-1}. They found that the polarized differential source counts are mostly constant down to p $> 500\mu$Jy, and that the brighter source population are much less polarized than the faint polarized radio sources. Future work will include radio

polarization studies of the ELAIS N1 region at 610 MHz, allowing to explore the polarization properties of the population down to deeper flux density limits.

6.2 Cosmic evolution of star-forming galaxies to $z \simeq 1.8$ in the faint low-frequency radio source population

This work represents the second paper exploiting the currently deepest low-frequency radio survey at 610 MHz (see Ocran et al. 2020a). I study the properties of star forming galaxies in the ELAIS N1 GMRT field. Source classification was performed by relying heavily on radio and X-ray luminosity, optical spectroscopy and mid-infrared colours. The sources classified as SFGs are those sources in our redshift sample in Ocran et al. 2020a that do not show evidence of AGN activity in any of the diagnostics. I study the infrared-radio correlation (FIRC) for the star-forming galaxies with redshift. Investigating the V/V_{max} statistics to quantify the evolution of the co-moving space density of the SFG sample, I find that averaged over luminosity, my results indicate $\langle V/V_{max} \rangle$ is consistent with no evolution. Using this sample we derived radio luminosity functions up to z $\sim$ 1.5. I compare our results to galaxy evolution models from the literature and find that the Mancuso et al. (2017), Wilman et al. (2008) and the T-RECS (Bonaldi et al., 2019) models do compare well to our data. I fit the SFG radio LF with pure luminosity evolution models that depend on redshift. Calibrating the 610 MHz rest-frame luminosity as a SFR indicator using FIR-derived SFRs from HELP allowed us to turn radio luminosity estimates into SFR function estimates. I then derive the cosmic star formation rate history up to redshift of 1.5. Through my study of the SF properties of the GMRT sample, I have demonstrated that radio selected samples at low frequency are powerful tools to investigate the cosmic SF history, alternative or complementary to FIR and UV surveys.

6.2.1 Future work

The low-frequency radio continuum emission of galaxies, if it can be distinguished from AGN activity, provides a direct measure of star formation (e.g., Yun, Reddy & Condon 2001). The multi-wavelength analysis of this GMRT 610 MHz deep ELAIS N1 data down to flux densities of 50 μJy clearly shows the transition from an AGN-dominated to a star-formation dominated population, allowing to estimate the cosmic star formation rate density (SFRD) in separate redshift bins up to z $\sim$ 1.5. At the sensitivity of MeerKAT MIGHTEE, this work can be extended and the SFRD measured up to and through the peak star formation epoch at $1 < z < 4$. The depth and width of the MIGHTEE survey will allow to substantially improve the calibration of radio luminosity as a SFR indicator provided in this work, enabling further radio-based studies of the SFRD.

The increased bandwidth and sensitivity of the upgraded GMRT (uGMRT) which provides similar capability to the MeerKAT, will achieve noise levels of $\sim 2\mu$ Jy. The uGMRT data will allow ground-breaking radio spectral index studies. Thus the uGMRT data can be used as a powerful tool for investigating the

evolution of starburst galaxies. Work by Thomson et al. (2014) demonstrated the potential of combining GMRT 610 MHz observations with deep 1.4 GHz data to derive radio spectral indices for samples of z ∼ 2.5 starburst galaxies in E-CDFS. They detected ∼ 70% of their sample of ALMA-identified submillimetre galaxies (SMGs) in their 7μJy rms, 1.4 GHz map, but only half of these are detected at 610 MHz in a map with rms of 45μJy. However, these observations already indicate the variety of spectral indices exhibited by high redshift starbursts, which preclude the adoption of a single canonical spectral index.

6.3 The evolution of the Low-Frequency Radio AGN Population to $z \simeq 1.5$

This work represents the third paper based on the deep 610 MHz survey of the ELAIS N1 field. Analyses of the deep 610 MHz extragalactic radio survey of the ELAIS N1 field in the previous chapters, have revealed two dominant galaxy populations, namely SFGs and AGN are observed in the faint radio universe. Using the sub-sample of radio AGN, I explore the evolution and composition of the radio AGN population out to a redshift of z $\sim$ 1.5. The AGN sub-sample with a redshift association and at least one multi-wavenlength AGN diagnostic consists of over 600 AGN covering an area of ∼1.86 deg^2 of ELAIS N1 of which RL AGN constitute ∼15% whereas RQ AGN constitute ∼12%. The distinction between RQ and RL AGN is indeed only based on the mid-infrared radio flux ratio, q_{24} criteria. The relative contribution of the two classes of sources to the sub-sample of radio sources with redshifts and at least one multi-wavelength diagnostic is as follows: ∼12% RQ AGN and ∼15% RL AGN (the remaining sources being SFGs). I compare the SFR (derived from the FIR) with the radio luminosity to demonstrate that the main contribution to the radio emission in RQ AGN is due to the SF in their hosts. Indeed I found good agreement between FIR-derived and radio luminosity derived SFRs for both SFGs and RQ AGNs over about four orders of magnitude in SFR and in the redshift range $0.002 < z < 1.5$.

I also constrained the evolution of the AGN population with continuous models of pure density and pure luminosity evolution.

6.3.1 Future work

Future samples of radio selected AGN will be sufficiently numerous to allow detailed studies of their SF activity as a function of AGN luminosity or BH accretion rate. As upcomming surveys will go even deeper than we present in this Thesis, many more RQ AGN will be detected. Hence one can apply this as a robust tool to study the star-forming properties of quasars hosts. It will also be interesting to characterize the accretion properties of these BHs and their excitation state. Studies on low and high-excitation RL AGN have been so far limited to the local Universe or to higher radio powers than those probed by this sample. I plan to estimate the kinetic luminosity for the AGN presented in this thesis in order to understand how the kinetic feedback of AGN changes through cosmic time (e.g. Willott et al. 1999; Merloni & Heinz 2007; Godfrey & Shabala 2016).

Another thrust in this work will be to explore more advanced, automated approaches to estimating the AGN fractional contribution to the bolometric energy output. By fitting SFG and AGN spectral energy distribution templates to photometric observations, it may be possible to define the AGN contribution to the bolometric luminosity and to use Bayesian model selection techniques to establish an AGN fraction for each object and hence examine trends and redshift evolution for different underlying populations. The method can be calibrated against standard spectroscopic observations for some subsets of objects. There are also opportunities for applying machine-learning techniques by way of comparison.

6.4 Investigating the infrared-radio correlation and radio spectral indices at μJy fluxes with stacking

I have used the deepest sensitive 610 MHz observations together with other available radio surveys at 325 MHz and 1.4 GHz, and in conjunction with deep 24μm Spitzer source catalogues of the ELAIS N1 field, to investigated the average properties of μJy radio counterparts of faint MIR sources using stacking. Galaxies were selected in the 24 μm MIPS and binned according to their 24 μm flux density. Stacking these samples into a deep radio images has enabled us to determine their average radio properties at flux densities an order of magnitude fainter than had previously been possible with flux-limited radio surveys. I compute the mid-infrared radio correlation, defined by the 'q_{24}' index, which quantifies the IRRC as the logarithmic ratio of a monochromatic MIR flux ($S_{\nu,\mathrm{IR}}$) to the 1.4 GHz radio flux ($S_{\nu,1.4\mathrm{GHz}}$). I also, study the strength of the mid-infrared radio correlation quantified at 325 MHz and 610 MHz in a similar way to at 1.4 GHz, denoted by $q'_{24\,325}$ and $q'_{24\,610}$ for sources within the ELAIS N1 field. I find that the population of objects at μJy flux densities obey the mid-infrared radio correlation which indicates that they are powered by star formation rather than by AGN. The results are consistent with previous work on statistically stacking the radio emission from many tens of faint 24μm sources has been used to characterize the size and nature of the radio emission at very faint IR galaxies well below the nominal radio sensitivity of these data. I have further extended and found a tentative deviation in the MIR-radio correlation at very low 24μm flux densities than these previous studies. I estimate the radio spectral index using the median flux reported for each S_{24} bin for the 325 MHz, 610 MHz and 1.4 GHz sample.

6.4.1 Future work

I plan to study the average star formation rate (SFR) for subsets of the galaxies presented in this thesis using their estimated stacked 610 MHz radio continuum emission. Hence through stacking analysis, I can estimate the general radio properties for a specific galaxy population. Another future work on Chapter 5 will be the stacking in polarized intensity as a mean to study the polarization properties of sources that are too faint to be detected individually in surveys of polarized radio sources. Stacking polarized intensity allows one to investigate the faint polarized signal of radio sources, using large samples obtained from

wide-area radio surveys. This technique has been explored at higher flux densities where a significant fraction of sources is detectable in polarization.

6.5 General Perspectives

Future large surveys with the SKA pathfinders and precursor telescopes will detect tens of millions of radio sources down to sub-mJy fluxes, and the SKA itself will detect hundreds of millions of objects down to the microJy levels, that we explore in this thesis. This work allowed a study of the evolution of the properties of the radio emission with cosmic time, including changes in the distribution of luminosities of the objects and in the rates of star formation. Therefore thesd data have provided a first look at the faint radio sky at sensitivities that will be achieved by key programs on the South African MeerKAT radio telescope, and hence taken the first step in the exploration of the radio universe that will be made by the SKA.

The MIGHTEE Survey project is one of eight approved Large Survey Projects (LSPs) with the MeerKAT SKA precursor. A joint MeerKAT and uGMRT project will provide complete spectral coverage from 250 MHz to 3 GHz at several-arcsecond angular resolution. Such a data set will have a profound impact on our understanding of how AGN and star-forming galaxies evolve over cosmic time, as a function of stellar mass and environment. Therefore, the science investigated in this thesis provides a contribution to the science cases that will be pursued by MeerKAT and SKA1. Smolcic et al. (2015) outlined that the SKA1 is expected to detect about 3×10^7, whereas the SKA1 deep survey is expected to detect 4×10^5 AGN at 1 GHz assuming an rms of 0.2 μJy/beam over 30 deg^2 for 2000 hours of observations. Thus, the SKA2 will provide 10× higher sensitivities at this frequency. Due the unique combination of high resolution imaging and sensitivity to obscured star-formation and AGN activity, the SKA itself will be the a leading facility to resolve the interplay between AGN and star-formation over a large fraction of cosmic time and thoughout the epoch of peak star formation and AGN activity.

The redshift depth and luminosity depth of this study is limited by the sensitivity of the survey. Future surveys will go several factors deeper and cover 10s of square degrees, extending this research to very early universe.

Chapter A

Deep GMRT 610 MHz Observations of the ELAIS N1 Field : Catalogue and Source Counts

Figure A.1 show the distribution of 610-MHz flux densities for the GMRT sample according to their S_{int} (black histogram) and S_{peak} (grey histogram).

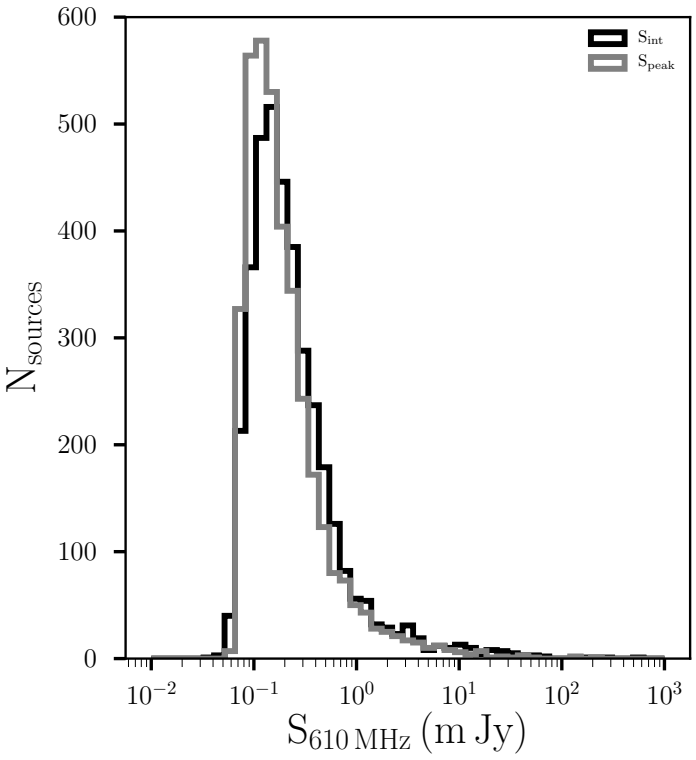

FIGURE A.1: The distribution of 610-MHz flux densities for the GMRT sample according to their S_{int} (black histogram) and S_{peak} (grey histogram).

A.1 POSTAGE STAMPS

Below we present postage stamps of extended sources, including those merged into single sources, in Figure A.2. The greyscale shows IRAC band 1 images. The green contours represents the GMRT 610 MHz whereas the blue contours represents VLA FIRST.

From Figure A.3, the vast majority of sources in the GMRT catalogue have very little offset with respect to the sources against the Spitzer Extragalactic Representative Volume Survey (SERVS) DR2 catalogue.

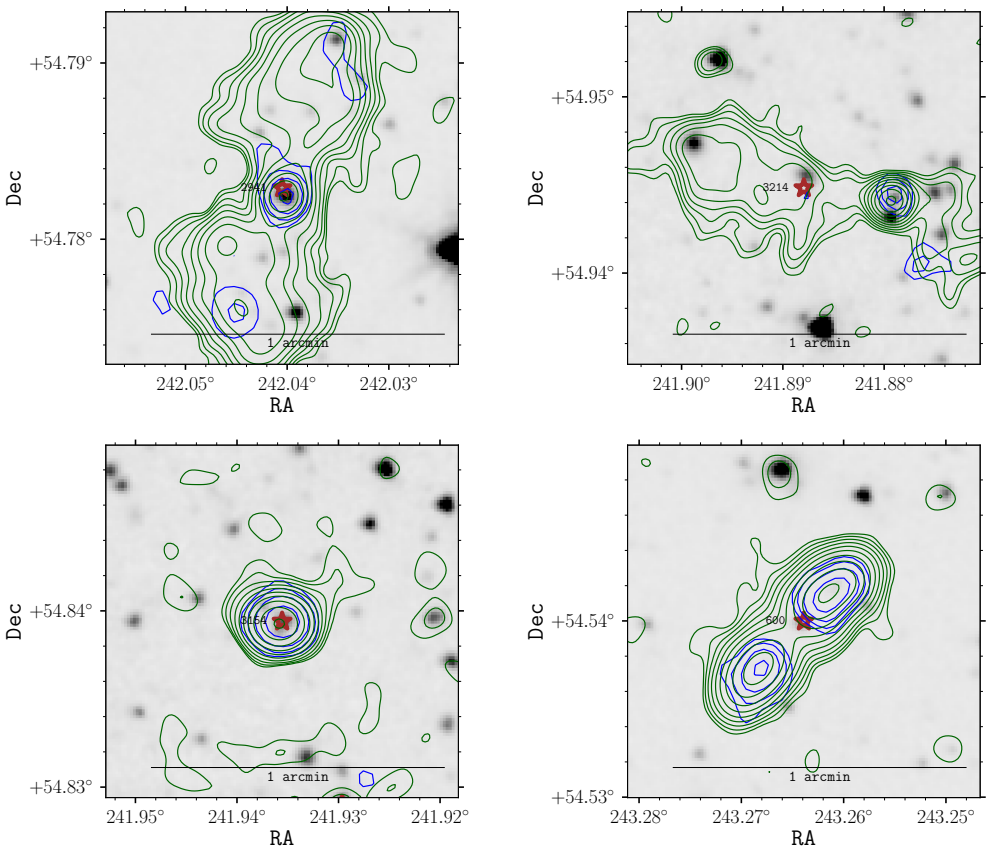

FIGURE A.2: Postage stamps showing examples of extended sources in the GMRT 610 MHz catalogue. The greyscale shows IRAC band 1 images. The green contours represents the GMRT 610 MHz whereas the blue contours represents VLA FIRST.

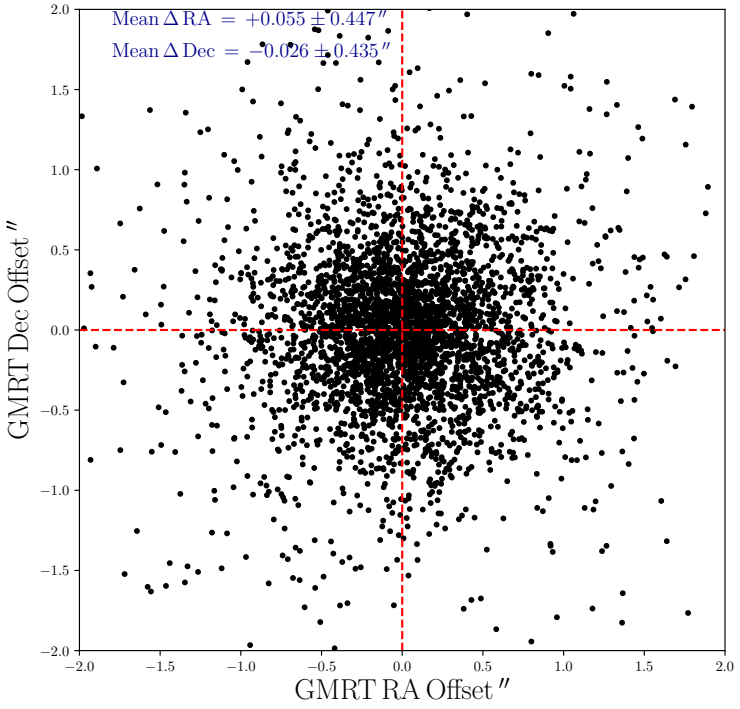

FIGURE A.3: Offset in RA and DEC of the sources in the GMRT field of view that have matches in the NVSS catalogue. The mean ΔRA (ΔDEC) is +0.055 ± 0.447 (−0.026 ± 0.435) arcsec, and is indicated by the red dashed lines.

Chapter B

SFGs evolution at 610 MHz

B.1 LF

The LFs obtained from the $\frac{1}{V_{max}}$ method for SFGs for the entire redshift range we consider (i.e. $0.002 < z < 1.5$) is shown in Figure B.1 as open black circles. The local RLF from Mauch & Sadler (2007) is represented as black solid line in this figure for comparison. The total SFG RLF for our sample is higher than the SFG RLF of Mauch & Sadler (2007) scaled to 610 MHz assuming $\alpha = -0.8$. This is evident especially at the high luminosity end and can be attributed to cosmic evolution of the SFGs known to positively evolve with redshift (Mao et al., 2012). Also, this may be attributed to the sensitivity of our radio observations which allows us to probe the source population up to high redshifts. The open brown diamonds show LF's computed for SFGs from T-RECS (Bonaldi et al., 2019) simulations. The faded black squares are RLF computed from the semi-empirical simulation of the SKA (Wilman et al., 2008). This is in good agreement with the RLF we compute for the SFG sample over the same redshift range. The breakdown of the results obtained for the 610 MHz RLF for SFGs from $0.002 < z < 1.5$ is presented in Table B.1.

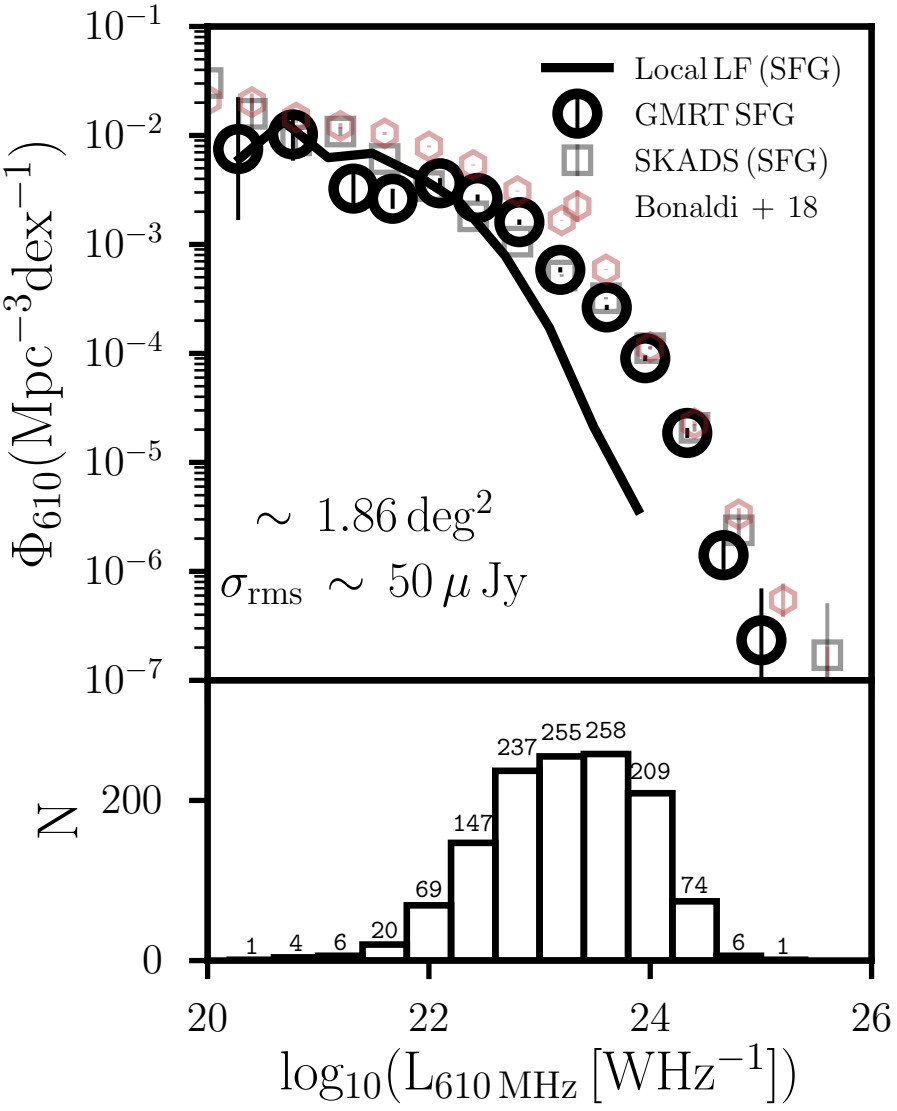

FIGURE B.1: The 610 MHz RLF for SFGs in the redshift range 0.002 < z < 1.5 shown in open black circles. The local RLF of Mauch & Sadler (2007), which has been converted to 610 MHz from 1.4 GHz assuming a spectral index of $\alpha = -0.8$, is shown in black line. The LF's computed for SFGs from T-RECS (Bonaldi et al., 2019) simulations are shown as open brown diamonds. Error bars are determined using the prescription of Gehrels (1986). The lower panel shows the luminosity distribution with the number of sources in each bin indicated on the bar.

TABLE B.1: 610 MHz RLF for SFGs from $0.002 < z < 1.5$. The listed luminosity values represent the median luminosity of the sources in the corresponding luminosity bin.

Luminosity $\log_{10}(L_{610\,\mathrm{MHz}}\,[\mathrm{WHz}^{-1}])$	Number density $\Phi_{610}(\mathrm{Mpc}^{-3}\mathrm{dex}^{-1})$	Number
20.28	$7.51^{+14.64}_{-5.70} \times 10^{-3}$	1
20.77	$1.02^{+6.67}_{-3.34} \times 10^{-2}$	4
21.32	$3.25^{+2.61}_{-1.52} \times 10^{-3}$	6
21.67	$2.63^{+0.50}_{-0.54} \times 10^{-3}$	20
22.09	$3.64^{+0.28}_{-0.24} \times 10^{-3}$	69
22.44	$2.67^{+0.17}_{-0.15} \times 10^{-3}$	147
22.82	$1.60^{+0.68}_{-0.63} \times 10^{-3}$	237
23.19	$5.85^{+0.27}_{-0.25} \times 10^{-4}$	255
23.61	$2.64^{+0.09}_{-0.09} \times 10^{-4}$	258
23.95	$9.04^{+0.42}_{-0.39} \times 10^{-5}$	209
24.33	$1.86^{+0.18}_{-0.16} \times 10^{-5}$	74
24.66	$1.41^{+5.10}_{-2.63} \times 10^{-6}$	6
25.00	$2.33^{+5.10}_{-2.63} \times 10^{-7}$	1

Chapter C

The evolution of the Low-Frequency Radio AGN Population to $z \simeq 1.5$

C.1 Stellar mass vs Radio power

Figure C.1 shows the stellar mass versus radio power for SFGs (left) RQ AGN (middle) and RL AGN (right). Colours correspond to redshifts. The SFGs appear much less anomalous in this figure. However, above a stellar mass of $\sim 10^{10}\,M_{\odot}$ we see an abrupt increase in the typical radio luminosity for a given stellar mass despite the fact that their radio luminosities are still below $10^{25}WH^{-1}$. We note that majority of the SFGs have redshifts below $z < 2$: see Figure C.1 . The RQ and RL AGN appear much more anomalous, given that we observe a large spread in stellar mass with radio power for both RQ and RL AGN. Above a stellar mass of $\sim 10^{10}\,M_{\odot}$ we see an increase in the typical radio luminosity for a given stellar mass. Also, the most powerful RL AGN are only found in the most massive objects at $z > 2$.

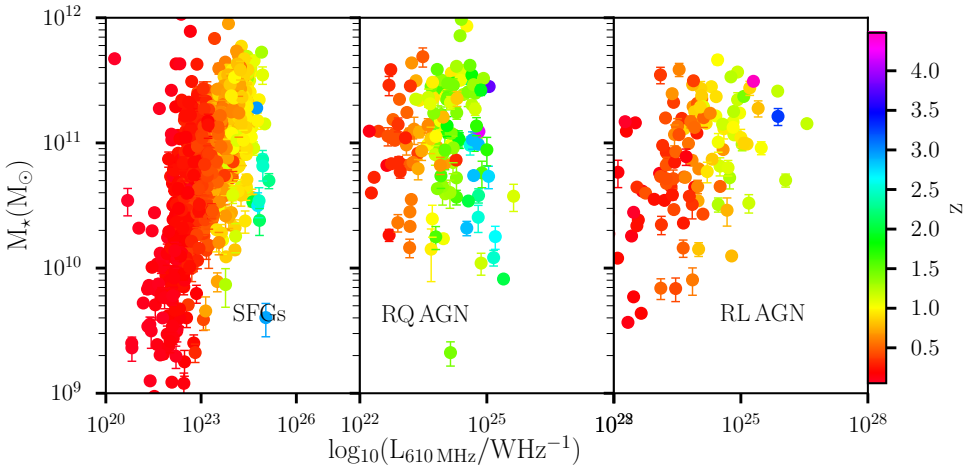

FIGURE C.1: Stellar mass versus radio power for SFGs (left) RQ AGN (middle) and RL AGN (right). Colour scale tracks redshift.

C.2 Giant Radio Galaxies

Giant Radio Galaxies (GRGs) are the largest single galaxies in the Universe (Ishwara-Chandra & Saikia, 1999). A radio galaxy is usually classified as a giant if its projected linear size is greater than a Mpc. The two largest surveys of GRGs to date are those of Ishwara-Chandra & Saikia (1999) and Schoenmakers et al. (1999), 04372244 and 10252229, from the Molonglo Complete Sample with these sources having a well defined FR II radio structure.

Our 610 MHz GMRT sample includes some giant radio galaxies. Figure C.2 shows postage stamps of some examples of sources identified as AGN in our sample plotted on SDSS colour composite (left panel). Following Dabhade et al. (2020) we define a galaxy as a GRG in our sample if the projected linear size is greater than 0.7 Mpc. The projected linear sizes of the candidate GRGs shown in the left panel of Figure C.2 are ∼1.49, ∼0.76 and ∼0.95 Mpc respectively (from top to bottom). Examples of spectra for these candidate GRGs that are classified as AGN are also shown in Figure C.2 (see right panel). These were obtained from the four additional Baryon Oscillation Spectroscopic Survey (BOSS) plates granted to obtain spectra for the radio sources detected by our GMRT observations as well as by other shallower radio surveys in the ELAIS N1 field. The observations were obtained and reduced by the SDSS team and publicly available as part of the SDSS DR12 (Tarr et al. in preparation).

Three of the candidate GRGs have BOSS/SDSS optical spectra with z = 0.71396 ± 0.00003, z = 0.23080 ± 0.00003, z = 0.31293 ± 0.00003. These correspond to radio galaxies which have already been identified as SWIRE_J161116.67+543224.3, ELAISR _J161320+541637 and ELAISR_J16133+54118. The three sources are identified as RL AGN by their mid-infrared to radio flux ratio, following the Bonzini et al. (2013). This is obtained by computing the $q_{24\mu m}$ for the radio sources with MIPS 24μm detections and redshifts. The study of the radio spectral index maps of these potential GRGs will be the subject of another paper.

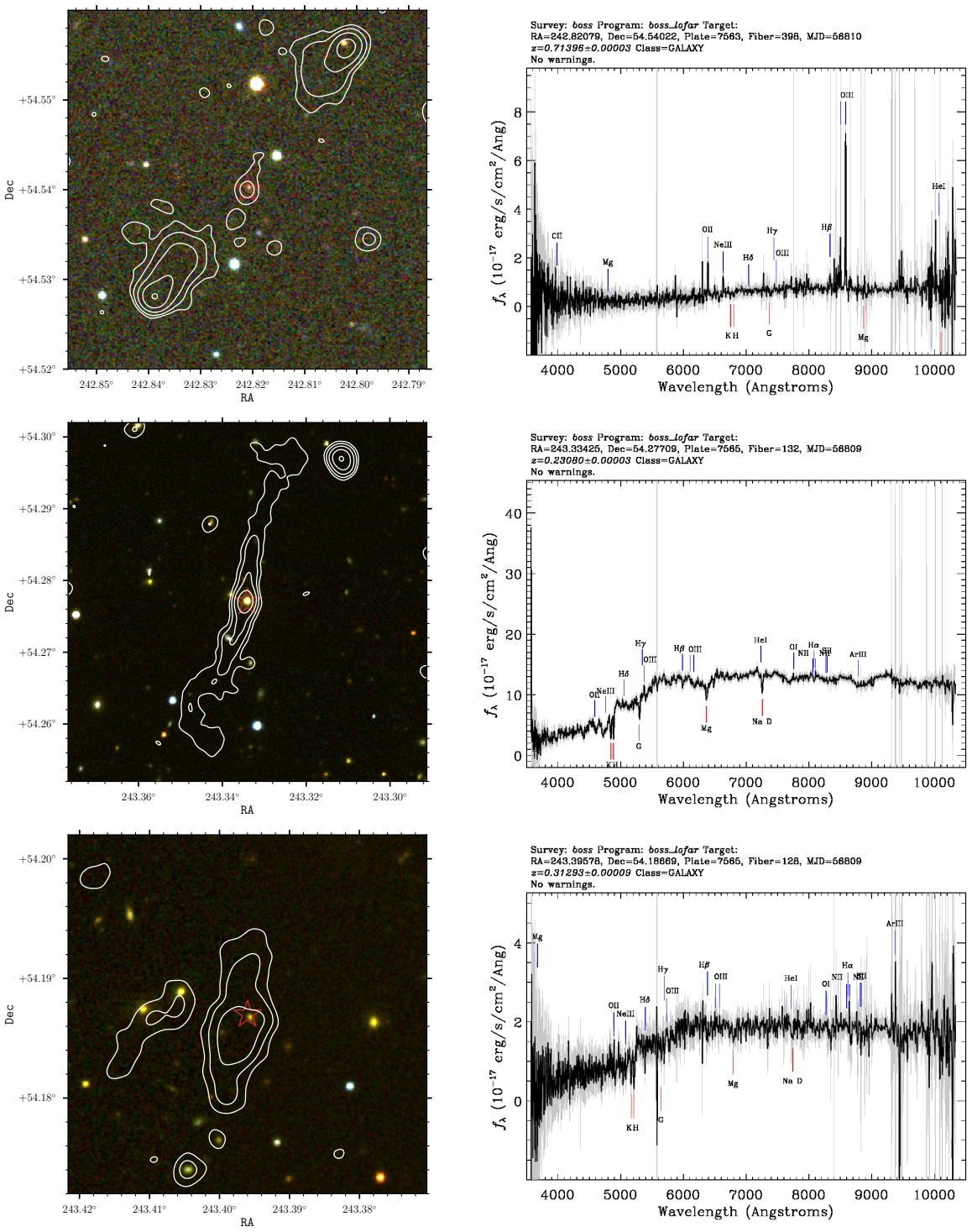

FIGURE C.2: Left panel: Postage stamps of some examples of sources identified as AGN in our sample plotted on SDSS colour composite (i.e. g, r and i). Overlaid are radio contours from the GMRT at 610 MHz represented in white. The contours levels are 1, 2, and 3σ. The red stars show the central position of the GMRT source. Right panel: Example optical spectra and position of the main spectral features found in our GMRT matched sample (black lines).

Chapter D

Investigating the infrared-radio correlation and radio spectral indices at μJy fluxes with stacking

D.1 Mean Stacked Images

In contrast to Figures 5.1, 5.2 and 5.3, Figures D.1, D.2 and D.3 show the mean stacked images for the same 24μm faintest six flux densitybins for the 325 MHz 610 MHz and 1.4 GHz radio images. All images are uniquely noisier than their median equivalents. There are bright sources away from the centre of the cut-out images have a much greater effect on the stacked images. The noise level of the mean images is $\sim 1.5-3$ times the noise of the median images, and the mean images are not representative of the typical sources within each flux density bin, but are strongly biased by a few bright radio sources.

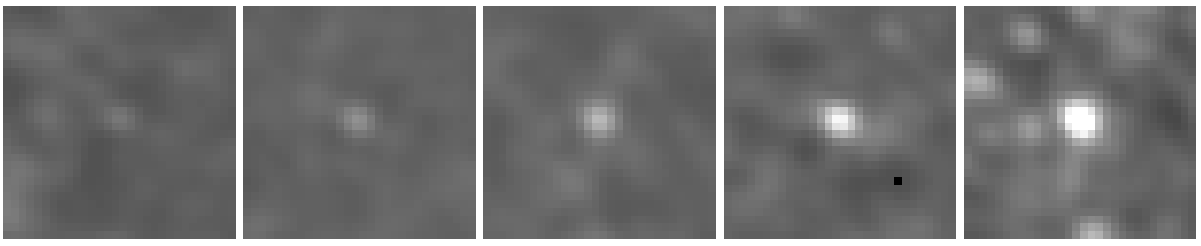

FIGURE D.1: Mean stacked 325 MHz radio images for the 24μm faintest six flux density bins. All images have a size of 30×30 arcsec^2. The grey-scale ranges between -30 and 60μJy beam^{-1}

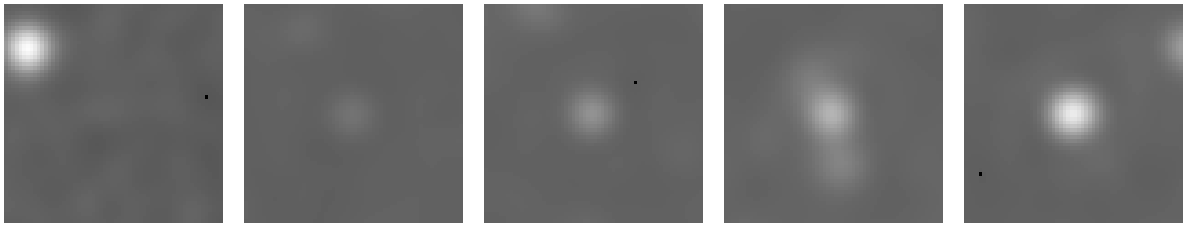

FIGURE D.2: Mean stacked 610 MHz radio images for the 24μm faintest six flux density bins. All images have a size of 60×60 arcsec^2. The grey-scale ranges between -7 and 40μJy beam^{-1}

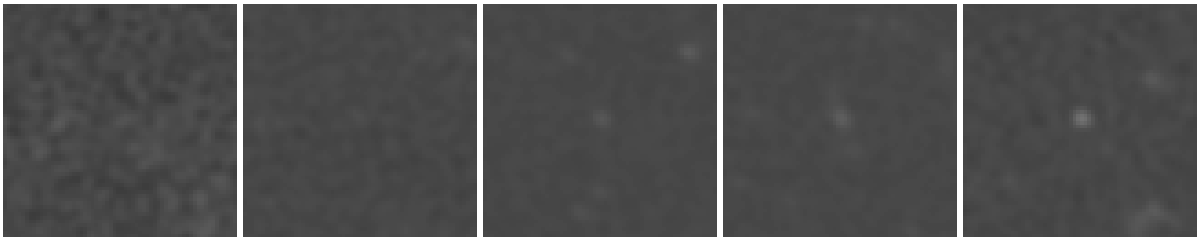

FIGURE D.3: Mean stacked 1.4 GHz radio images for the 24μm faintest six flux density bins. All images have a size of 60×60 arcsec^2. The grey-scale ranges between -7 and 60μJy beam^{-1}

D.2 The Mid-Infrared Radio flux ratio

Table D.1 summarizes various range of the IR and radio luminosity ratios mean and median values found in the literature. Radio stacking of 24 μm sources are denoted by ^{a}.

TABLE D.1: Table summarizing various range of the IR and radio luminosity ratios mean and median values found in the literature. This table is a modified version of the non-exhaustive list of papers presented by Randriamampandry et al. (2015).

Reference	Redshift	Mean q_{24}	Median q_{24}
Boyle et al. (2007)^a	$\leqslant$2.5	1.39±0.02	-
Beswick et al. (2008)^a	$0 < z < 1.2$	0.52±0.20	0.48±0.20
Rieke et al. (2009)	$\leqslant$0.088	1.22± 0.02	-
Bourne et al. (2011)	$0 < z < 2$	1.47±0.03	-
Ibar et al. (2008)	$\leqslant$3.5	0.71±0.47	-
Appleton et al. (2004)	$\leqslant$2	10	-
Murphy et al. (2006)	$\leqslant$0.002	10	-
Sargent et al. (2010a)	$0 < z < 5$	1.26±0.13	-
Randriamampandry et al. (2015)	~0.54	0.69±0.55	-
Ocran et al. (2017)	$0 < z \leqslant 5$	-	0.86±0.01

Note. ^{a} Radio stacking of 24 μm sources.

Bibliography

Afonso J., Georgakakis A., Almeida C., Hopkins A. M., Cram L. E., Mobasher B., Sullivan M., 2005, ApJ, 624, 135

Alexander D. M., Hickox R. C., 2012, New Astronomy Reviews, 56, 93

Antonucci R., 1993, ARA&A, 31, 473

Appleton P. N., et al., 2004, ApJS, 154, 147

Argo M. K., Paragi Z., Rottgering H., Klockner H. R., Miley G., Mahmud M., 2013, MNRAS, 431, L58

Athreya R. M., Kapahi V. K., 1998, Journal of Astrophysics and Astronomy, 19, 63

Avni Y., Bahcall J. N., 1980, ApJ, 235, 694

Baldwin J. A., Phillips M. M., Terlevich R., 1981, PASP, 93, 5

Banfield J. K., George S. J., Taylor A. R., Stil J. M., Kothes R., Scott D., 2011, ApJ, 733, 69

Baran A., Fiege J., Taylor A. R., Foster T., Landecker T. L., 2010, in Kothes R., Landecker T. L., Willis A. G., eds, Astronomical Society of the Pacific Conference Series Vol. 438, Astronomical Society of the Pacific Conference Series. p. 303

Becker R. H., White R. L., Helfand D. J., 1995, ApJ, 450, 559

Behroozi P. S., Wechsler R. H., Conroy C., 2013, ApJ, 770, 57

Bell E. F., 2003, ApJ, 586, 794

Bell E. F., McIntosh D. H., Katz N., Weinberg M. D., 2003, ApJS, 149, 289

Bell E. F., Zheng X. Z., Papovich C., Borch A., Wolf C., Meisenheimer K., 2007, ApJ, 663, 834

Bennett A. S., 1962, MNRAS, 125, 75

Best P. N., et al., 1998, MNRAS, 301, L15

Best P. N., Arts J. N., Röttgering H. J. A., Rengelink R., Brookes M. H., Wall J., 2003, MNRAS, 346, 627

Best P. N., Kauffmann G., Heckman T. M., Brinchmann J., Charlot S., Ivezić Ž., White S. D. M., 2005, MNRAS, 362, 25

Beswick R. J., Muxlow T. W. B., Thrall H., Richards A. M. S., Garrington S. T., 2008, MNRAS, 385, 1143

Blandford R. D., Znajek R. L., 1977, MNRAS, 179, 433

Blanton M. R., et al., 2003, AJ, 125, 2348

Blumenthal G., Miley G., 1979, A&A, 80, 13

Blundell K. M., Kuncic Z., 2007, ApJ, 668, L103

Bolton A. S., et al., 2012, AJ, 144, 144

Bonaldi A., Bonato M., Galluzzi V., Harrison I., Massardi M., Kay S., De Zotti G., Brown M. L., 2019, MNRAS, 482, 2

Bonato M., et al., 2017, MNRAS, 469, 1912

Bondi M., et al., 2007, A&A, 463, 519

Bonzini M., Padovani P., Mainieri V., Kellermann K. I., Miller N., Rosati P., Tozzi P., Vattakunnel S., 2013, MNRAS, 436, 3759

Bonzini M., et al., 2015, MNRAS, 453, 1079

Bornancini C. G., De Breuck C., de Vries W., Croft S., van Breugel W., Röttgering H., Minniti D., 2007, MNRAS, 378, 551

Bourne N., Dunne L., Ivison R. J., Maddox S. J., Dickinson M., Frayer D. T., 2011, MNRAS, 410, 1155

Bouwens R. J., Illingworth G. D., Franx M., Ford H., 2007, ApJ, 670, 928

Bouwens R. J., et al., 2012a, ApJ, 752, L5

Bouwens R. J., et al., 2012b, ApJ, 754, 83

Bower R. G., Benson A. J., Malbon R., Helly J. C., Frenk C. S., Baugh C. M., Cole S., Lacey C. G., 2006, MNRAS, 370, 645

Boyle B. J., Cornwell T. J., Middelberg E., Norris R. P., Appleton P. N., Smail I., 2007, MNRAS, 376, 1182

Brammer G. B., van Dokkum P. G., Coppi P., 2008, ApJ, 686, 1503

Braun R., Bourke T., Green J. A., Keane E., Wagg J., 2015, Advancing Astrophysics with the Square Kilometre Array (AASKA14), p. 174

Brinchmann J., Charlot S., White S. D. M., Tremonti C., Kauffmann G., Heckman T., Brinkmann J., 2004, MNRAS, 351, 1151

Brinkmann W., Laurent-Muehleisen S. A., Voges W., Siebert J., Becker R. H., Brotherton M. S., White R. L., Gregg M. D., 2000, A&A, 356, 445

Brown M. J. I., Webster R. L., Boyle B. J., 2001, AJ, 121, 2381

Burgarella D., et al., 2013, A&A, 554, A70

Calistro Rivera G., Lusso E., Hennawi J. F., Hogg D. W., 2016, ApJ, 833, 98

Calistro Rivera G., et al., 2017, MNRAS, 469, 3468

Cannon R., et al., 2006, MNRAS, 372, 425

Caputi K. I., et al., 2007, ApJ, 660, 97

Ceraj L., et al., 2018, A&A, 620, A192

Chabrier G., 2003, PASP, 115, 763

Choloniewski J., 1987, MNRAS, 226, 273

Civano F., et al., 2016, ApJ, 819, 62

Clewley L., Jarvis M. J., 2004, MNRAS, 352, 909

Cohen A. S., et al., 2003, ApJ, 591, 640

Condon J. J., 1984, ApJ, 287, 461

Condon J. J., 1989, ApJ, 338, 13

Condon J. J., 1992, ARA&A, 30, 575

Condon J. J., Condon M. A., Gisler G., Puschell J. J., 1982, ApJ, 252, 102

Condon J. J., Cotton W. D., Greisen E. W., Yin Q. F., Perley R. A., Taylor G. B., Broderick J. J., 1998, AJ, 115, 1693

Condon J. J., Cotton W. D., Broderick J. J., 2002, AJ, 124, 675

Condon J. J., Cotton W. D., Yin Q. F., Shupe D. L., Storrie-Lombardi L. J., Helou G., Soifer B. T., Werner M. W., 2003, AJ, 125, 2411

Croom S. M., Smith R. J., Boyle B. J., Shanks T., Miller L., Outram P. J., Loaring N. S., 2004, MNRAS, 349, 1397

Croom S. M., et al., 2009, MNRAS, 399, 1755

Croton D. J., et al., 2006, MNRAS, 365, 11

Cucciati O., et al., 2012, A&A, 539, A31

Dabhade P., et al., 2020, A&A, 635, A5

Daddi E., et al., 2007, ApJ, 670, 156

Dadina M., 2008, A&A, 485, 417

Dahlen T., Mobasher B., Dickinson M., Ferguson H. C., Giavalisco M., Kretchmer C., Ravindranath S., 2007, ApJ, 654, 172

Dahlen T., et al., 2013, ApJ, 775, 93

Delhaize J., et al., 2017, A&A, 602, A4

Delvecchio I., et al., 2017, A&A, 602, A3

Di Matteo T., Springel V., Hernquist L., 2005, Nature, 433, 604

Dickey J. M., Salpeter E. E., 1984, ApJ, 284, 461

Donley J. L., et al., 2012, ApJ, 748, 142

Dopita M. A., Kewley L. J., Heisler C. A., Sutherland R. S., 2000, ApJ, 542, 224

Duncan K. J., Jarvis M. J., Brown M. J. I., Röttgering H. J. A., 2018, MNRAS, 477, 5177

Dunlop J. S., Peacock J. A., 1990, MNRAS, 247, 19

Dunlop J. S., McLure R. J., Kukula M. J., Baum S. A., O'Dea C. P., Hughes D. H., 2003, MNRAS, 340, 1095

Dunne L., et al., 2009, MNRAS, 394, 3

Dye S., Eales S., Moncelsi L., Pascale E., 2010, MNRAS, 407, L69

Eddington A. S., 1913, MNRAS, 73, 359

Edge D. O., Shakeshaft J. R., McAdam W. B., Baldwin J. E., Archer S., 1959, MmRAS, 68, 37

Efstathiou A., Rowan-Robinson M., 1995, MNRAS, 273, 649

Eisenstein D. J., et al., 2011, AJ, 142, 72

Elbaz D., et al., 2007, A&A, 468, 33

Elvis M., et al., 1994, ApJS, 95, 1

Fazio G. G., et al., 2004, ApJS, 154, 10

Fitt A. J., Alexander P., Cox M. J., 1988, MNRAS, 233, 907

Fomalont E. B., Kellermann K. I., Wall J. V., Weistrop D., 1984, Science, 225, 23

Fomalont E. B., Kellermann K. I., Partridge R. B., Windhorst R. A., Richards E. A., 2002, AJ, 123, 2402

Foreman-Mackey D., Hogg D. W., Lang D., Goodman J., 2013, PASP, 125, 306

Fried J. W., et al., 2001, A&A, 367, 788

Garn T., Alexander P., 2009, MNRAS, 394, 105

Garn T., Green D. A., Riley J. M., Alexander P., 2008, MNRAS, 383, 75

Garrett M. A., 2002, A&A, 384, L19

Gehrels N., 1986, ApJ, 303, 336

Genzel R., et al., 2011, ApJ, 733, 101

Giroletti M., Panessa F., 2009, ApJ, 706, L260

Glenn J., et al., 2010, MNRAS, 409, 109

Godfrey L. E. H., Shabala S. S., 2016, MNRAS, 456, 1172

Gonzalez-Solares E. A., et al., 2005, MNRAS, 358, 333

Grant J. K., Taylor A. R., Stil J. M., Land ecker T. L., Kothes R., Ransom R. R., Scott D., 2010, ApJ, 714, 1689

Greve T. R., et al., 2010, ApJ, 719, 483

Griffin M. J., et al., 2010, A&A, 518, L3

Gruppioni C., et al., 1999, MNRAS, 305, 297

Gruppioni C., et al., 2010, A&A, 518, L27

Gruppioni C., et al., 2013, MNRAS, 432, 23

Gruppioni C., et al., 2020, arXiv e-prints, p. arXiv:2006.04974

Gunawardhana M. L. P., et al., 2013, MNRAS, 433, 2764

Gupta Y., 2014, in Astronomical Society of India Conference Series. pp 441–447

Haarsma D. B., Partridge R. B., Windhorst R. A., Richards E. A., 2000, ApJ, 544, 641

Helou G., Soifer B. T., Rowan-Robinson M., 1985, ApJ, 298, L7

Herzog A., et al., 2016, A&A, 593, A130

Heywood I., Bielby R. M., Hill M. D., Metcalfe N., Rawlings S., Shanks T., Smirnov O. M., 2013a, MNRAS, 428, 935

Heywood I., Jarvis M. J., Condon J. J., 2013b, MNRAS, 432, 2625

Heywood I., et al., 2016, MNRAS, 460, 4433

Hoaglin D. C., 2003, Statistical Science, 18, 311

Hopkins A. M., 2004, ApJ, 615, 209

Hopkins A. M., Afonso J., Chan B., Cram L. E., Georgakakis A., Mobasher B., 2003a, AJ, 125, 465

Hopkins A. M., et al., 2003b, ApJ, 599, 971

Hopkins P. F., Richards G. T., Hernquist L., 2007, ApJ, 654, 731

Hopkins P. F., Hernquist L., Cox T. J., Kereš D., 2008a, ApJS, 175, 356

Hopkins A. M., McClure-Griffiths N. M., Gaensler B. M., 2008b, ApJ, 682, L13

Hurley P. D., et al., 2017, MNRAS, 464, 885

Ibar E., et al., 2008, MNRAS, 386, 953

Ibar E., Ivison R. J., Biggs A. D., Lal D. V., Best P. N., Green D. A., 2009, MNRAS, 397, 281

Ibar E., Ivison R. J., Best P. N., Coppin K., Pope A., Smail I., Dunlop J. S., 2010, MNRAS, 401, L53

Ilbert O., et al., 2010, ApJ, 709, 644

Ilbert O., et al., 2013, A&A, 556, A55

Intema H. T., van Weeren R. J., Röttgering H. J. A., Lal D. V., 2011, A&A, 535, A38

Intema H. T., Jagannathan P., Mooley K. P., Frail D. A., 2017, A&A, 598, A78

Ishwara-Chandra C. H., Saikia D. J., 1999, MNRAS, 309, 100

Ishwara-Chandra C. H., Taylor A. R., Green D. A., Stil J. M., Vaccari M., Ocran E. F., 2020, MNRAS, 497, 5383

Ivison R. J., et al., 2010, A&A, 518, L31

Jarvis M. J., Rawlings S., Willott C. J., Blundell K. M., Eales S., Lacy M., 2001, MNRAS, 327, 907

Jarvis M., et al., 2016, in Proceedings of MeerKAT Science: On the Pathway to the SKA. 25-27 May. p. 6 (arXiv:1709.01901)

Jiang L., Fan X., Ivezić Ž., Richards G. T., Schneider D. P., Strauss M. A., Kelly B. C., 2007, ApJ, 656, 680

Johnston R., Vaccari M., Jarvis M., Smith M., Giovannoli E., Häußler B., Prescott M., 2015, MNRAS, 453, 2540

Jonas J., MeerKAT Team 2016, in Proceedings of MeerKAT Science: On the Pathway to the SKA. 25-27 May. p. 1

Karim A., et al., 2011, ApJ, 730, 61

Kartaltepe J. S., et al., 2010, ApJ, 709, 572

Katgert J. K., 1979, A&A, 73, 107

Katgert J. K., Spinrad H., 1974, A&A, 35, 393

Kauffmann G., et al., 2003, MNRAS, 346, 1055

Keller B. W., Stil J. M., 2018, PASTA: Python Astronomical Stacking Tool Array (ascl:1809.003)

Kellermann K. I., Wall J. V., 1987, in Hewitt A., Burbidge G., Fang L. Z., eds, IAU Symposium Vol. 124, Observational Cosmology. pp 545–562

Kellermann K. I., Sramek R., Schmidt M., Shaffer D. B., Green R., 1989, AJ, 98, 1195

Kennicutt Robert C. J., 1998, ApJ, 498, 541

Kewley L. J., Dopita M. A., Sutherland R. S., Heisler C. A., Trevena J., 2001, ApJ, 556, 121

Kewley L. J., Groves B., Kauffmann G., Heckman T., 2006, MNRAS, 372, 961

Kiepenheuer K. O., 1950, Physical Review, 79, 738

Kimball A. E., Kellermann K. I., Condon J. J., Ivezić Ž., Perley R. A., 2011, ApJ, 739, L29

Knopp G. P., Chambers K. C., 1997, ApJ, 487, 644

Kormendy J., Ho L. C., 2013, ARA&A, 51, 511

Kozieł-Wierzbowska D., Vale Asari N., Stasińska G., Sikora M., Goettems E. I., Wójtowicz A., 2017, ApJ, 846, 42

Lacki B. C., 2013, MNRAS, 431, 3003

Lacki B. C., Thompson T. A., 2010, ApJ, 717, 196

Lacy M., et al., 2004, ApJS, 154, 166

Lacy M., Sajina A., Petric A. O., Seymour N., Canalizo G., Ridgway S. E., Armus L., Storrie-Lombardi L. J., 2007, ApJ, 669, L61

Laigle C., et al., 2016, ApJS, 224, 24

Laing R. A., Riley J. M., Longair M. S., 1983, MNRAS, 204, 151

Lapi A., et al., 2011, ApJ, 742, 24

Lawrence A., et al., 2007, MNRAS, 379, 1599

Ledlow M. J., Owen F. N., 1996, AJ, 112, 9

Lee K.-S., et al., 2012, ApJ, 752, 66

Lilly S. J., Le Fevre O., Hammer F., Crampton D., 1996, ApJ, 460, L1

Liu D., et al., 2018, ApJ, 853, 172

Loiacono F., et al., 2020, arXiv e-prints, p. arXiv:2006.04837

Lonsdale Persson C. J., Helou G., 1987, ApJ, 314, 513

Lonsdale C. J., et al., 2003, Publications of the Astronomical Society of the Pacific, 115, 897

Lopes M. E., Wang S., Mahoney M. W., 2019, Journal of Machine Learning Research, 20, 1

Machalski J., Godlowski W., 2000, A&A, 360, 463

Machalski J., Jamrozy M., Konar C., 2010, A&A, 510, A84

Madau P., Dickinson M., 2014, ARA&A, 52, 415

Madau P., Ferguson H. C., Dickinson M. E., Giavalisco M., Steidel C. C., Fruchter A., 1996, MNRAS, 283, 1388

Magliocchetti M., Andreani P., Zwaan M. A., 2008, MNRAS, 383, 479

Magnelli B., Elbaz D., Chary R. R., Dickinson M., Le Borgne D., Frayer D. T., Willmer C. N. A., 2009, A&A, 496, 57

Magnelli B., et al., 2010, A&A, 518, L28

Magnelli B., Elbaz D., Chary R. R., Dickinson M., Le Borgne D., Frayer D. T., Willmer C. N. A., 2011, A&A, 528, A35

Magnelli B., et al., 2013, A&A, 553, A132

Magnelli B., et al., 2015, A&A, 573, A45

Mahony E. K., et al., 2016, MNRAS, 463, 2997

Małek K., et al., 2018, A&A, 620, A50

Mancuso C., Lapi A., Shi J., Gonzalez-Nuevo J., Aversa R., Danese L., 2016a, ApJ, 823, 128

Mancuso C., Lapi A., Shi J., Cai Z. Y., Gonzalez-Nuevo J., Béthermin M., Danese L., 2016b, ApJ, 833, 152

Mancuso C., et al., 2017, ApJ, 842, 95

Mao M. Y., et al., 2012, MNRAS, 426, 3334

Marchetti L., et al., 2016, MNRAS, 456, 1999

Marsden D., et al., 2014, MNRAS, 439, 1556

Massardi M., Bonaldi A., Negrello M., Ricciardi S., Raccanelli A., de Zotti G., 2010, MNRAS, 404, 532

Massardi M., et al., 2011, MNRAS, 412, 318

Mauch T., Sadler E. M., 2007, MNRAS, 375, 931

Mauduit J.-C., et al., 2012, PASP, 124, 714

McAlpine K., Jarvis M. J., 2011, MNRAS, 413, 1054

McAlpine K., Jarvis M. J., Bonfield D. G., 2013, MNRAS, 436, 1084

McCarthy P. J., et al., 2001, ApJ, 560, L131

Merloni A., Heinz S., 2007, MNRAS, 381, 589

Middelberg E., et al., 2008, AJ, 136, 519

Miley G., De Breuck C., 2008, A&A Rev., 15, 67

Mills B. Y., 1984, Radio sources and the log N-log S controversy. Cambridge University Press, p. 147

Mills B. Y., Slee O. B., 1957, Australian Journal of Physics, 10, 162

Mills B. Y., Slee O. B., Hill E. R., 1958, Australian Journal of Physics, 11, 360

Mohan N., Rafferty D., 2015, PyBDSF: Python Blob Detection and Source Finder, Astrophysics Source Code Library (ascl:1502.007)

Molnár D. C., et al., 2018, MNRAS, 475, 827

Morris S. L., Stocke J. T., Gioia I. M., Schild R. E., Wolter A., Maccacaro T., della Ceca R., 1991, ApJ, 380, 49

Moss D., Seymour N., McHardy I. M., Dwelly T., Page M. J., Loaring N. S., 2007, MNRAS, 378, 995

Murphy E. J., et al., 2006, ApJ, 651, L111

Murphy E. J., et al., 2011, ApJ, 737, 67

Narayan R., Yi I., 1994, ApJ, 428, L13

Nenkova M., Ivezić Ž., Elitzur M., 2002, ApJ, 570, L9

Nenkova M., Sirocky M. M., Ivezić Ž., Elitzur M., 2008a, ApJ, 685, 147

Nenkova M., Sirocky M. M., Nikutta R., Ivezić Ž., Elitzur M., 2008b, ApJ, 685, 160

Neugebauer G., Miley G. K., Soifer B. T., Clegg P. E., 1986, ApJ, 308, 815

Newville M., Stensitzki T., Allen D. B., Ingargiola A., 2014, LMFIT: Non-Linear Least-Square Minimization and Curve-Fitting for Python, doi:10.5281/ZENODO.11813, https://zenodo.org/record/11813

Noeske K. G., et al., 2007, ApJ, 660, L43

Norberg P., et al., 2002, MNRAS, 336, 907

Norris R. P., et al., 2006, AJ, 132, 2409

Norris R. P., et al., 2013, PASA, 30, e020

Novak M., et al., 2017, A&A, 602, A5

Novak M., Smolčić V., Schinnerer E., Zamorani G., Delvecchio I., Bondi M., Delhaize J., 2018, A&A, 614, A47

O'Dea C. P., 1998, PASP, 110, 493

Ocran E. F., Taylor A. R., Vaccari M., Green D. A., 2017, MNRAS, 468, 1156

Ocran E. F., Taylor A. R., Vaccari M., Ishwara-Chandra C. H., Prandoni I., 2020a, MNRAS, 491, 1127

Ocran E. F., Taylor A. R., Vaccari M., Ishwara-Chandra C. H., Prandoni I., Prescott M., Mancuso C., 2020b, MNRAS, 491, 5911

Oesch P. A., et al., 2010, ApJ, 725, L150

Oliver S. J., et al., 2012, MNRAS, 424, 1614

Osterbrock D. E., 1978, PhyS, 17, 137

Ouchi M., et al., 2009, ApJ, 706, 1136

Padovani P., 1993, MNRAS, 263, 461

Padovani P., 2016a, in Active Galactic Nuclei 12: A Multi-Messenger Perspective (AGN12). p. 14, doi:10.5281/zenodo.163592

Padovani P., 2016b, A&A Rev., 24, 13

Padovani P., 2017, Frontiers in Astronomy and Space Sciences, 4

Padovani P., Ghisellini G., Fabian A. C., Celotti A., 1993, MNRAS, 260, L21

Padovani P., Mainieri V., Tozzi P., Kellermann K. I., Fomalont E. B., Miller N., Rosati P., Shaver P., 2009, ApJ, 694, 235

Padovani P., Miller N., Kellermann K. I., Mainieri V., Rosati P., Tozzi P., 2011, ApJ, 740, 20

Padovani P., Bonzini M., Miller N., Kellermann K. I., Mainieri V., Rosati P., Tozzi P., Vattakunnel S., 2014, in Mickaelian A. M., Sanders D. B., eds, IAU Symposium Vol. 304, Multiwavelength AGN Surveys and Studies. pp 79–85 (arXiv:1401.1342), doi:10.1017/S1743921314003391

Padovani P., Bonzini M., Kellermann K. I., Miller N., Mainieri V., Tozzi P., 2015, MNRAS, 452, 1263

Panessa F., et al., 2015, MNRAS, 447, 1289

Pascarelle S. M., Windhorst R. A., Keel W. C., Odewahn S. C., 1996, Nature, 383, 45

Pei Y. C., Fall S. M., Hauser M. G., 1999, ApJ, 522, 604

Phillips A. C., Guzmán R., Gallego J., Koo D. C., Lowenthal J. D., Vogt N. P., Faber S. M., Illingworth G. D., 1997, ApJ, 489, 543

Pierre M., et al., 2004, JCAP, 2004, 011

Pilbratt G. L., et al., 2010, A&A, 518, L1

Prandoni I., Gregorini L., Parma P., de Ruiter H. R., Vettolani G., Wieringa M. H., Ekers R. D., 2001, A&A, 365, 392

Prandoni I., Parma P., Wieringa M. H., de Ruiter H. R., Gregorini L., Mignano A., Vettolani G., Ekers R. D., 2006, A&A, 457, 517

Prandoni I., de Ruiter H. R., Ricci R., Parma P., Gregorini L., Ekers R. D., 2010, A&A, 510, A42

Prandoni I., Guglielmino G., Morganti R., Vaccari M., Maini A., Röttgering H. J. A., Jarvis M. J., Garrett M. A., 2018, MNRAS, 481, 4548

Prescott M., et al., 2016, MNRAS, 457, 730

Randriamampandry S. M., Crawford S. M., Cress C. M., Hess K. M., Vaccari M., Wilcots E. M., Bershady M. A., Wirth G. D., 2015, MNRAS, 447, 168

Rawlings S., Jarvis M. J., 2004, MNRAS, 355, L9

Rawlings S., Saunders R., 1991, Nature, 349, 138

Rawlings S., Eales S., Lacy M., 2001, MNRAS, 322, 523

Rawlings J. I., et al., 2015, MNRAS, 452, 4111

Reddy N. A., Steidel C. C., 2009, ApJ, 692, 778

Rees M. J., 1984, ARA&A, 22, 471

Renzini A., 2009, MNRAS, 398, L58

Reuland M., Röttgering H., van Breugel W., De Breuck C., 2004, MNRAS, 353, 377

Richards G. T., et al., 2004, ApJS, 155, 257

Richards G. T., et al., 2006, ApJS, 166, 470

Rickard L. J., Harvey P. M., 1984, AJ, 89, 1520

Rieke G. H., et al., 2004, ApJS, 154, 25

Rieke G. H., Alonso-Herrero A., Weiner B. J., Pérez-González P. G., Blaylock M., Donley J. L., Marcillac D., 2009, ApJ, 692, 556

Riseley C. J., et al., 2016, MNRAS, 462, 917

Rodighiero G., et al., 2011, ApJ, 739, L40

Roettgering H. J. A., West M. J., Miley G. K., Chambers K. C., 1996, A&A, 307, 376

Rousseeuw P. J., Croux C., 1993, Journal of the American Statistical Association, 88, 1273

Rowan-Robinson M., 1968, MNRAS, 138, 445

Rowan-Robinson M., et al., 2004, MNRAS, 351, 1290

Rowan-Robinson M., et al., 2008, MNRAS, 386, 697

Rowan-Robinson M., Gonzalez-Solares E., Vaccari M., Marchetti L., 2013, MNRAS, 428, 1958

Rujopakarn W., et al., 2010, ApJ, 718, 1171

Ryle M., Scheuer P. A. G., 1955, Proceedings of the Royal Society of London Series A, 230, 448

Sadler E. M., Jenkins C. R., Kotanyi C. G., 1989, MNRAS, 240, 591

Sadler E. M., et al., 2002, MNRAS, 329, 227

Sadler E. M., et al., 2007, MNRAS, 381, 211

Sajina A., Lacy M., Scott D., 2005, ApJ, 621, 256

Sajina A., Yan L., Lacy M., Huynh M., 2007, ApJ, 667, L17

Sajina A., et al., 2008, ApJ, 683, 659

Salim S., et al., 2007, ApJS, 173, 267

Salpeter E. E., 1955, ApJ, 121, 161

Sargent M. T., et al., 2010a, ApJS, 186, 341

Sargent M. T., et al., 2010b, ApJ, 714, L190

Saunders W., Rowan-Robinson M., Lawrence A., Efstathiou G., Kaiser N., Ellis R. S., Frenk C. S., 1990, MNRAS, 242, 318

Saxena A., et al., 2018a, MNRAS, 475, 5041

Saxena A., et al., 2018b, MNRAS, 480, 2733

Schechter P., 1975, PhD thesis, California Institute of Technology, Pasadena, CA USA

Schechter P., 1976, ApJ, 203, 297

Schiminovich D., et al., 2005, ApJ, 619, L47

Schmidt M., 1968, ApJ, 151, 393

Schmitt J. H. M. M., Kahabka P., Stauffer J., Piters A. J. M., 1993, A&A, 277, 114

Schoenmakers A. P., de Bruyn A. G., Röttgering H. J. A., van der Laan H., 1999, A&A, 341, 44

Schweitzer M., et al., 2008, ApJ, 679, 101

Serjeant S., Gruppioni C., Oliver S., 2002, MNRAS, 330, 621

Seymour N., et al., 2008, MNRAS, 386, 1695

Shakeshaft J. R., Ryle M., Baldwin J. E., Elsmore B., Thomson J. H., 1955, MmRAS, 67, 106

Shirley R., et al., 2019, MNRAS, 490, 634

Shupe D. L., et al., 2008, AJ, 135, 1050

Simpson J. M., et al., 2012, MNRAS, 426, 3201

Singh V., et al., 2014, A&A, 569, A52

Sirothia S. K., Dennefeld M., Saikia D. J., Dole H., Ricquebourg F., Roland J., 2009, MNRAS, 395, 269

Smolcic V., et al., 2015, in Advancing Astrophysics with the Square Kilometre Array (AASKA14). p. 69 (arXiv:1501.04820)

Smolčić V., 2009, ApJ, 699, L43

Smolčić V., et al., 2008, ApJS, 177, 14

Smolčić V., et al., 2009a, ApJ, 690, 610

Smolčić V., et al., 2009b, ApJ, 696, 24

Smolčić V., et al., 2017a, A&A, 602, A1

Smolčić V., et al., 2017b, A&A, 602, A6

Snellen I. A. G., Schilizzi R. T., van Langevelde H. J., 2000, MNRAS, 319, 429

Somerville R. S., Primack J. R., Faber S. M., 2001, MNRAS, 320, 504

Springel V., Di Matteo T., Hernquist L., 2005, MNRAS, 361, 776

Steidel C. C., Sargent W. L. W., 1991, ApJ, 382, 433

Steinhardt C. L., et al., 2014, ApJ, 791, L25

Stern D., et al., 2005, ApJ, 631, 163

Stil J. M., Keller B. W., George S. J., Taylor A. R., 2014, ApJ, 787, 99

Strazzullo V., Pannella M., Owen F. N., Bender R., Morrison G. E., Wang W.-H., Shupe D. L., 2010, ApJ, 714, 1305

Swinbank A. M., et al., 2007, MNRAS, 379, 1343

Szokoly G. P., et al., 2004, ApJS, 155, 271

Tanaka M., et al., 2018a, PASJ, 70, S9

Tanaka M., et al., 2018b, PASJ, 70, S9

Tasse C., et al., 2006, A&A, 456, 791

Tasse C., Röttgering H. J. A., Best P. N., Cohen A. S., Pierre M., Wilman R., 2007, A&A, 471, 1105

Tasse C., Le Borgne D., Röttgering H., Best P. N., Pierre M., Rocca-Volmerange B., 2008, A&A, 490, 879

Taylor A. R., et al., 2007, ApJ, 666, 201

Taylor A. R., et al., 2014, in Astronomical Society of India Conference Series. pp 99–104 (arXiv:1405.0117)

Thomson A. P., et al., 2014, MNRAS, 442, 577

Tisanić K., et al., 2019, A&A, 621, A139

Tucci M., Toffolatti L., de Zotti G., Martínez-González E., 2011, A&A, 533, A57

Vaccari M., 2015, in Proceedings of "The many facets of extragalactic radio surveys: towards new scientific challenges" (EXTRA-RADSUR2015). 20-23 October 2015. Bologna. p. 27 (arXiv:1604.02353)

Vaccari M., 2016, The Many Facets of Extragalactic Radio Surveys: Towards New Scientific Challenges (EXTRA-RADSUR2015), p. 27

Vaccari M., et al., 2005, MNRAS, 358, 397

Vaccari M., et al., 2010, A&A, 518, L20

Veilleux S., Osterbrock D. E., 1987, in Lonsdale Persson C. J., ed., NASA Conference Publication Vol. 2466, NASA Conference Publication. pp 737–740

Villarroel B., Korn A. J., 2014, Nature Physics, 10, 417

Vito F., Gilli R., Vignali C., Comastri A., Brusa M., Cappelluti N., Iwasawa K., 2014, MNRAS, 445, 3557

Voelk H. J., 1989, A&A, 218, 67

Walterbos R. A. M., Greenawalt B., 1996, ApJ, 460, 696

Webb T. M. A., Brodwin M., Eales S., Lilly S. J., 2004, ApJ, 605, 645

Werner M. W., et al., 2004, ApJS, 154, 1

White S. D. M., Frenk C. S., 1991, ApJ, 379, 52

White R. L., Helfand D. J., Becker R. H., Glikman E., de Vries W., 2007, ApJ, 654, 99

White S. V., Jarvis M. J., Häußler B., Maddox N., 2015, MNRAS, 448, 2665

White S. V., Jarvis M. J., Kalfountzou E., Hardcastle M. J., Verma A., Cao Orjales J. M., Stevens J., 2017, MNRAS, 468, 217

Whittam I. H., Green D. A., Jarvis M. J., Riley J. M., 2017, MNRAS, 464, 3357

Williams W. L., et al., 2016, MNRAS, 460, 2385

Willott C. J., Rawlings S., Blundell K. M., Lacy M., 1999, MNRAS, 309, 1017

Willott C. J., Rawlings S., Blundell K. M., Lacy M., Eales S. A., 2001, MNRAS, 322, 536

Willott C. J., Rawlings S., Archibald E. N., Dunlop J. S., 2002, MNRAS, 331, 435

Wilman R. J., et al., 2008, MNRAS, 388, 1335

Wilman R. J., Jarvis M. J., Mauch T., Rawlings S., Hickey S., 2010, MNRAS, 405, 447

Wilson A. S., Colbert E. J. M., 1995, ApJ, 438, 62

Windhorst R. A., 1984, PhD thesis, Ph. D. thesis, University of Leiden (1984)

Windhorst R. A., 2003, New Astronomy Reviews, 47, 357

Windhorst R., Mathis D., Neuschaefer L., 1990, in Kron R. G., ed., Astronomical Society of the Pacific Conference Series Vol. 10, Evolution of the Universe of Galaxies. pp 389–403

Windhorst R. A., et al., 2011, ApJS, 193, 27

Wunderlich E., Klein U., Wielebinski R., 1987, A&AS, 69, 487

Wyder T. K., et al., 2005, ApJ, 619, L15

Yuan Z. S., Han J. L., Wen Z. L., 2016a, MNRAS, 460, 3669

Yuan Z., Wang J., Zhou M., Mao J., 2016b, ApJ, 820, 65

Yuan Z., Wang J., Zhou M., Qin L., Mao J., 2017, ApJ, 846, 78

Yun M. S., Reddy N. A., Condon J. J., 2001, ApJ, 554, 803

Zheng X. Z., Bell E. F., Rix H.-W., Papovich C., Le Floc'h E., Rieke G. H., Pérez-González P. G., 2006, ApJ, 640, 784

Zwart J. T. L., Jarvis M. J., Deane R. P., Bonfield D. G., Knowles K., Madhanpall N., Rahmani H., Smith D. J. B., 2014, MNRAS, 439, 1459

Zwart J., et al., 2015a, Advancing Astrophysics with the Square Kilometre Array (AASKA14), p. 172

Zwart J. T. L., Santos M., Jarvis M. J., 2015b, MNRAS, 453, 1740

de Gasperin, F. et al., 2012, A&A, 547, A56

de Jong T., Klein U., Wielebinski R., Wunderlich E., 1985, A&A, 147, L6

de Zotti G., Massardi M., Negrello M., Wall J., 2010, A&A Rev., 18, 1

van der Kruit P. C., 1971, A&A, 15, 110

van der Kruit P. C., 1973, A&A, 29, 263